



Wojewodka, Michael M. (2020) *Complex flow physics & active plasma flow control in convoluted ducts*. PhD thesis.

<http://theses.gla.ac.uk/81885/>

Copyright and moral rights for this work are retained by the author

A copy can be downloaded for personal non-commercial research or study, without prior permission or charge

This work cannot be reproduced or quoted extensively from without first obtaining permission in writing from the author

The content must not be changed in any way or sold commercially in any format or medium without the formal permission of the author

When referring to this work, full bibliographic details including the author, title, awarding institution and date of the thesis must be given

Enlighten: Theses

<https://theses.gla.ac.uk/>  
[research-enlighten@glasgow.ac.uk](mailto:research-enlighten@glasgow.ac.uk)

# **Complex flow physics & active plasma flow control in convoluted ducts**

Michael M. Wojewodka

Submitted in fulfilment of the requirements for the  
Degree of Doctor of Philosophy

Aerospace Sciences Research Division  
James Watt School of Engineering  
College of Science and Engineering  
University of Glasgow



University  
of Glasgow

August 2020



# Abstract

Convolutd, s-shaped ducts form an integral part of many subsystems in engineering applications and specifically the aviation industry. They are used, for example, as inlet ducts for fuselage embedded jet engines and as connector pipes between high and low pressure turbine or compressor stages. With a strong curvature and a diffusive nature, the geometry acts on the throughflow making it prone to separate and experience significant cross-stream pressure gradients. The geometry and resulting flow phenomena lead to a non-uniform and highly unsteady flow field in the duct aft the inflection point. Those effects are detrimental to the overall performance of the convoluted duct, reducing the pressure recovery and increasing the distortion parameters.

S-shaped ducts have been studied by a large number of researchers for many years. Traditionally, many studies rely on steady state simulations and time averaged experimental data to characterise the flow in convoluted ducts and analyse their performance. However, more recent findings point to the need of transient data to fully understand the dynamic nature of the throughflow and discuss the complex flow physics. This is something that is lacking from many studies reported in the current literature.

This is addressed with computational fluid dynamics (CFD) studies of the throughflow in the s-duct using the open source tool OpenFOAM. First low fidelity, steady state simulations are set up before higher fidelity, transient delayed detached eddy simulations (DDES) are conducted. Baseline s-duct throughflow computations are validated against experimental data from literature with very good agreement of pressure recovery values, wall static pressure contours, and flow structures. CFD data is next post processed with statistical and modal decomposition methods. Coherent structures and phase information are obtained from the proper orthogonal decomposition (POD) and the dynamic mode decomposition (DMD) methods.

Modal decomposition analysis of DDES data confirms the existance of the horizontal shifting mode. Contrary to previous findings, the presence of a second vertical shifting mode is observed from DDES data. Occurance rates and phase information are determined from the DMD analysis.

The recent surge of interest in plasma actuators is clearly illustrated by the high research output that has been reported in literature. Dielectric barrier discharge (DBD) plasma actuators have been studied and successfully applied to control external aerodynamics on aerofoils and

bluff bodies. However, successful flow control in convoluted ducts has not been reported with this technology for realistic Reynolds numbers.

The DBD plasma characterisation is conducted on two types of actuators: alternating current (ac) and nanosecond (ns) DBD plasma actuators. The Schlieren imaging technique is used with ns-DBD plasmas to record density changes and establish the shock front strength and propagation speed with changing ambient pressure. Higher ambient pressures result in stronger shock waves; this has been observed irrespective of the actuator thickness. This might be explained with fewer air molecules to ionize at lower ambient pressures and hence a lower temperature from the exothermal recombination reactions.

For ac-DBD actuators, thinner dielectric materials outperformed thicker ones in terms of ionisation strength with constant voltage input. The smallest dielectric constant of the materials tested resulted in higher induced velocities. Using particle image velocimetry (PIV), a high gradient of velocity reduction with streamwise distance was recorded in the plasma jet. This is significant, as it shows plasma actuators have mostly localised effects.

Experimental campaigns are set up such that the DBD experiments are coherent studies in their own right. However, the main purpose of plasma experiments in the context of this thesis is to collect data to validate numerical plasma models. Those phenomenological plasma models are subsequently used for numerical flow control studies on the s-shaped duct. Phenomenological plasma models match the experimental data well when tuned. However, the flow control studies did not show a performance improvement in the convoluted duct.

# Acknowledgements

First and foremost, I would like to acknowledge my primary supervisor Dr Craig White who gave me the opportunity to embark on this journey. Thank you for guiding me through the process and allowing me to take turns in the direction I wanted this PhD to move forward. Thanks also go to my second supervisor Prof Konstantinos Kontis and Dr Shahrokh Shahpar of Rolls-Royce for their support and guidance.

I would also like to thank David Pickles, Richard Dunlop, and Craig Nolan for keeping me company and providing a much needed distraction during long hours at university and the many social activities when motivation was stretched thin. I also want to acknowledge David Pickles and Richard Dunlop for proof reading my thesis.

Completing the thesis would not have been possible without the continuous help and support I received from my family. Special mention goes to my sister Colette for her support. I want to express my gratitude and thank my parents for their encouragement throughout my PhD research and the write up period. To mum and dad, dziękuje!

To my significant other, thank you for motivating me during the final part of my PhD journey and pushing me towards the finish line.



# Declaration

“I declare that, except where explicit reference is made to the contribution of others, that this dissertation is the result of my own work and has not been submitted for any other degree at the University of Glasgow or any other institution.”

Printed Name: Michael Wojewodka

Signature: Michael Wojewodka

Date: 31.08.2020



# Preface

This thesis presents work carried out by the author in the Aerospace Sciences Research Division part of the James Watt School of Engineering at the University of Glasgow during the period from October 2015 to May 2020, including a three month leave of absence. The work was mainly supervised by Dr Craig White as the principal supervisor with additional guidance from Prof Konstantinos Kontis.

Two separate experimental campaigns were carried out. One was conducted under the supervision of Dr Takahiro Ukai while the other was completed with the help and guidance from Dr Richard Green. Both experimental campaigns were conducted at the National Wind Tunnel Facility at Glasgow University. Regular, monthly scheduled meetings to discuss the progress and research outcomes were held with Dr Shahrokh Shahpar of Rolls-Royce. Annual progression meetings and review discussions were held with Dr Kiran Ramesh and Dr Rene Steijl.

Numerical simulations were performed on two high performance computing centres. Initial computational studies were conducted on the Buckethead cluster at the University of Glasgow with more extensive simulations being run on Archie-WeST at Strathclyde University.

Funding of the PhD project was obtained from the Engineering and Physical Sciences Research Council (EPSRC) with grant numbers as follows: EP/M506539/1 ENG 70374 and EP/M508056/1 EN.



# Contents

<b>Abstract</b>	<b>i</b>
<b>Acknowledgements</b>	<b>iii</b>
<b>Declaration</b>	<b>v</b>
<b>Preface</b>	<b>vii</b>
<b>Nomenclature</b>	<b>xxi</b>
<b>1 Introduction</b>	<b>1</b>
1.1 Background . . . . .	2
1.2 Research objectives & scope . . . . .	3
1.3 Thesis outline . . . . .	4
1.4 Originality & contribution . . . . .	4
1.5 Research outcomes . . . . .	5
<b>2 Literature survey</b>	<b>7</b>
2.1 Performance and geometrical parameters . . . . .	8
2.2 Flow physics in s-ducts . . . . .	9
2.3 Passive flow control . . . . .	13
2.3.1 Working principle of common passive flow control devices . . . . .	13
2.3.2 Passive flow control devices employed in s-shaped ducts . . . . .	15
2.3.3 Optimisation studies . . . . .	19
2.4 Active flow control . . . . .	25
2.5 Hybrid flow control . . . . .	30
2.6 Conclusions . . . . .	31
<b>3 Wellborn s-duct baseline CFD simulations</b>	<b>33</b>
3.1 Performance criteria . . . . .	34
3.2 Simulation set-up . . . . .	35
3.2.1 Geometry . . . . .	36

3.2.2	Computational grid . . . . .	38
3.2.3	CFD code . . . . .	39
3.2.4	Boundary conditions, initial conditions, and numerical schemes . . . . .	41
3.3	Steady flow properties and performance criteria . . . . .	42
3.4	Unsteady flow properties and performance criteria . . . . .	48
3.5	Modal decomposition and frequency spectrum . . . . .	52
3.6	Conclusions . . . . .	61
<b>4</b>	<b>Dielectric barrier discharge plasma actuators</b>	<b>63</b>
4.1	Introduction . . . . .	63
4.2	Experimental set-up . . . . .	67
4.2.1	ns-DBD experiments . . . . .	67
4.2.2	ac-DBD experiments . . . . .	70
4.3	Results & discussion . . . . .	73
4.3.1	ns-DBD plasma actuators . . . . .	73
4.3.2	ac-DBD plasma actuators . . . . .	79
4.4	Conclusions . . . . .	87
<b>5</b>	<b>DBD plasma numerical models</b>	<b>89</b>
5.1	ns-DBD model . . . . .	89
5.1.1	ns-DBD model implementation . . . . .	90
5.1.2	Results . . . . .	91
5.1.3	Discussion . . . . .	94
5.2	ac-DBD model . . . . .	96
5.2.1	ac-DBD model implementation . . . . .	96
5.2.2	Results . . . . .	97
5.2.3	Discussion . . . . .	99
5.3	Conclusions . . . . .	100
<b>6</b>	<b>Plasma flow control</b>	<b>103</b>
6.1	Plasma flow control in convoluted ducts . . . . .	103
6.1.1	Meshing: new cell set for plasma functionality . . . . .	103
6.1.2	CFD code . . . . .	104
6.1.3	ac-DBD flow control . . . . .	105
6.1.4	ns-DBD flow control . . . . .	117
6.1.5	Conclusions . . . . .	124
6.2	Practical considerations . . . . .	125
6.2.1	Control authority . . . . .	125
6.2.2	Effect of ambient conditions . . . . .	125

6.2.3	Power source . . . . .	126
6.2.4	Control system . . . . .	126
6.2.5	Conclusions . . . . .	126
<b>7</b>	<b>Conclusions &amp; Future work</b>	<b>127</b>
7.1	Conclusions . . . . .	127
7.1.1	OpenFOAM CFD validation for convoluted duct test case . . . . .	127
7.1.2	Analysis of transient phenomena and coherent structures . . . . .	128
7.1.3	ac- and ns-DBD plasma characteristion . . . . .	128
7.1.4	Numerical models of ac and ns DBD plasma actuation . . . . .	128
7.1.5	Flow control studies with plasma actuators . . . . .	128
7.2	Future work . . . . .	128
<b>A</b>		<b>131</b>
A.1	fvOption file ns-DBD numerical model . . . . .	131
A.2	fvOption file ac-DBD numerical model . . . . .	132
A.3	blockMeshDict file . . . . .	134
A.4	controlDict file . . . . .	138
A.5	fvSchemes file . . . . .	139
A.6	fvSolution file . . . . .	140
A.7	refineMeshdict . . . . .	141
A.8	topoSetDict file . . . . .	142
A.9	radialStripToCell.C . . . . .	145
A.10	radialStripToCell.H . . . . .	147



# List of Tables

2.1	Summary of passive flow control techniques employed on s-ducts . . . . .	20
2.2	Summary of optimisation techniques employed on s-ducts . . . . .	24
2.3	Summary of active flow control techniques employed on s-ducts . . . . .	29
4.1	Dielectric materials used with corresponding physical properties. . . . .	71
4.2	Set up for PIV flow field measurements. . . . .	73
4.3	Best performing surface PA and their properties. . . . .	82
5.1	Temperature values added to the near wall region for the simulation of ns-DBD generated shock waves. . . . .	95
6.1	Details of cell set regions for flow control cases. . . . .	107
6.2	Input details of numerical ac-DBD model. . . . .	109
6.3	Input details of numerical ns-DBD model. . . . .	119



# List of Figures

1.1	Throughflow snapshot of velocity magnitude ( $ms^{-1}$ ) along the symmetry plane as well as the s-duct inlet and outlet planes. Simulation conducted in OpenFOAM.	1
2.1	S-shaped duct.	7
2.2	S-duct flow schematic.	10
2.3	Flow separation in convoluted duct at a Mach number of 0.6.	11
2.4	Swirl intensity vs inlet Mach number.	12
2.5	Swirl coefficient SC60 at AIP vs inlet Mach number.	12
2.6	Average and standard deviation of pressure recovery and swirl at AIP of Well-born duct based on DDES simulation.	13
2.7	Switching and vertical modes (SM and VM respectively) at Mach number of 0.27.	14
2.8	Schematic representation of various VG types.	15
2.9	Oil flow visualisation of baseline, co and counter-rotating vane VG.	17
2.10	Coefficient of total pressure loss along the duct length.	18
2.11	Normalised total pressure recovery contours for convoluted duct without (left) and with (right) vortex generator array.	21
2.13	Sketch of synthetic jet actuation positions.	25
2.14	Average secondary (cross-flow) velocity vs nondimensionalised duct length.	26
2.15	Pressure recovery at AIP vs injection mass flow as % of inlet flow.	27
2.16	Improvement of pressure recovery at AIP in % vs injection mass flow as % of inlet flow.	28
2.17	Time averaged total pressure contours at AIP for a) baseline s-duct, b) vane type VG, c) synthetic jets, and d) hybrid flow control.	30
2.18	Society of Automotive Engineers circumferential distortion descriptor (DPCP) with Mach number for baseline flow, passive (vane type VG), active (synthetic jets), and hybrid flow control.	31
3.1	S-shaped duct.	37
3.2	S-shaped duct numerical domain.	37
3.3	RANS simulations mesh convergence study with total pressure recovery: (3.3a) with average $Y+$ value of mesh; (3.3b) with total cell size of mesh.	39

3.4	Computational mesh: structured, multi block grid cut along the symmetry plane of the geometry with a close up view of the prism layers near the wall. . . . .	40
3.5	Wall $Y^+$ values in computational domain for final mesh (3.5a) with corresponding convergence history for steady state RANS simulation with two iterations for pressure correction (3.5b) in OpenFOAM. . . . .	40
3.6	Wall static pressure coefficient along (3.6a) three streamwise lines of 10, 90, and 170 degrees and (3.6b) three cross-stream planes for Wellborn's experimental results ([1]) and OpenFOAM rhoSimpleFoam CFD results. . . . .	43
3.9	Contour plots: (3.9a-3.9b) Wellborn's data, (3.9c-3.9d) RANS rhoSimpleFoam, time mean rhoPimpleFoam CFD of (3.9e-3.9f) URANS, and (3.9g-3.9h) DDES. . . . .	47
3.10	Total pressure distortion coefficient with sectors of 30, 45, 60, 90, and 120 degrees for RANS, URANS, and DDES simulations compared to experiments by [2,3]. . . . .	48
3.14	Total and static pressure recovery with snapshots of URANS (3.14a-3.14b) and DDES (3.14c-3.14d) simulations. The average PR is shown by the continuous line. Results are compared to experimental data recorded by [2,3]. Numerical DDES results published by [4] are also presented. . . . .	53
3.15	Reconstruction of flow statistics ( $ms^{-1}$ ) at AIP with POD modes: (3.15a) target snapshot secondary flow statistics; (3.15b) reconstruction based on first 5 modes; (3.15c) reconstruction based on first 10 modes; (3.15d) reconstruction based on first 20 modes; (3.15e) reconstruction based on first 40 modes; (3.15f) reconstruction based on first 60 modes. . . . .	54
3.16	POD energy content for modes of the streamwise velocity component snapshot data set from DDES computations. . . . .	55
3.17	Horizontal shedding mode: (3.17a) mode for maximum temporal coefficient; (3.17b) mode for minimum temporal coefficient; (3.17c) mode for maximum temporal coefficient with superimposed average flow field; (3.17d) mode for minimum temporal coefficient with superimposed average flow field ( $ms^{-1}$ ). . . . .	55
3.18	First vertical shedding mode: (3.18a) mode for maximum temporal coefficient; (3.18b) mode for minimum temporal coefficient; (3.18c) mode for maximum temporal coefficient with superimposed average flow field; (3.18d) mode for minimum temporal coefficient with superimposed average flow field ( $ms^{-1}$ ). . . . .	56
3.19	Second vertical shedding mode: (3.19a) mode for maximum temporal coefficient; (3.19b) mode for minimum temporal coefficient; (3.19c) mode for maximum temporal coefficient with superimposed average flow field; (3.19d) mode for minimum temporal coefficient with superimposed average flow field ( $ms^{-1}$ ). . . . .	57
3.20	Eigenvalue unit circle plot for dynamic mode decomposition of streamwise velocity DDES data. . . . .	58

3.21	DMD first vertical mode (coupled DMD modes 2 and 3 in 3.21a and 3.21b, respectively) representing same dynamics as POD first vertical shifting mode. DMD horizontal mode (coupled DMD modes 4 and 5 in 3.21c and 3.21d, respectively) representing same dynamics as POD horizontal shifting mode. DMD second vertical mode (coupled DMD modes 6 and 7 in 3.21e and 3.21f, respectively) representing same dynamics as POD second vertical shifting mode. . . .	59
3.22	Example of dominant frequency extraction process: (3.22a) non-normalised and normalised FFT spectrum for point 14700; (3.22b) peak detection on normalised FFT spectrum. . . . .	60
4.1	Schematic representation of typical dielectric barrier discharge plasma actuator configuration for ac and ns operation. . . . .	64
4.5	Example of the actuator used (not to scale). . . . .	68
4.6	Schematic representation of experimental Schlieren set up. . . . .	69
4.7	Schematic representation of experimental set up. . . . .	71
4.8	Design and layout of surface plasma actuator used. Left: side view, right: top view. . . . .	72
4.9	Schematic representation of PIV set up including field of view (FoV) and plasma actuator positioning. . . . .	72
4.10	Voltage signal supplied to plasma actuators . . . . .	74
4.11	Schlieren image of characteristic, cylindrical, and planar shock waves generated from the ns-DBD actuator. . . . .	74
4.12	Shock propagation based on shock front location: time vs velocity. Actuator thickness: 0.4 mm. . . . .	75
4.13	Shock propagation based on shock front location: time vs velocity. Actuator thickness: 0.8 mm. . . . .	75
4.14	Shock propagation based on shock front location: time vs velocity. Actuator thickness: 1.6 mm. . . . .	76
4.15	Example of output from Matlab code: Normalised shock strength $I/I_b$ vs vertical distance from actuator surface. . . . .	77
4.16	Normalised intensity profiles, $I/I_b$ , along vertical line across ten shock wave propagation images. . . . .	77
4.17	Normalised shock strength $I/I_b$ with vertical distance from actuator for a pressure range of 30 to 100 kPa. Actuator thickness is 0.4 mm. . . . .	78
4.18	Normalised shock strength $I/I_b$ with vertical distance from actuator for a pressure range of 30 to 100 kPa. Actuator thickness is 0.8 mm. . . . .	78
4.19	Normalised shock strength $I/I_b$ with vertical distance from actuator for a pressure range of 30 to 100 kPa. Actuator thickness is 1.6 mm. . . . .	79

4.21	Induced velocity with x-y location along centreline ( $z = 0mm$ ) downstream of plasma actuator. . . . .	81
4.25	Time averaged velocity vector plot from PIV for surface PA with a 0.5 mm GRE dielectric material. Units are in $ms^{-1}$ with the horizontal and vertical axes showing the FoV. . . . .	84
4.26	Time averaged velocity vector plot from PIV for surface PA with a 0.5 mm PTFE dielectric material. Units are in $ms^{-1}$ with the horizontal and vertical axes showing the FoV. . . . .	84
5.1	Gaussian distribution of temperature profile prescribed to heated region. . . . .	90
5.2	Mesh independence study. . . . .	91
5.4	Progression of shock wave with the ns-DBD model implemented in OpenFOAM. Black coloured region at the bottom of the computational domain schematically depicts the heated volume region. This is not to scale. Dimensions of the heated volume are $10 \times 1 \times 10^{-5} \times 1$ mm in the $x$ , $y$ , and $z$ direction, respectively. . . . .	92
5.6	Effect of parameter $\chi$ on Mach number of shock front at ambient conditions. . . . .	93
5.7	Comparison of experimental and numerical shock wave propagation for ambient pressure of 30 kPa. . . . .	94
5.8	Comparison of experimental and numerical shock wave propagation for ambient pressure of 70 kPa. . . . .	94
5.9	Comparison of experimental and numerical shock wave propagation for ambient pressure of 100 kPa. . . . .	95
5.10	Numerically modelled ac-DBD plasma actuator: resultant horizontal jet velocity with dielectric thickness used in numerical model. . . . .	97
5.11	Numerically modelled ac-DBD plasma actuator: resultant horizontal jet velocity with driving frequency ( $f_v = 10$ kHz) used in numerical model. . . . .	98
5.12	Resulting streamwise jet velocities with peak-to-peak voltage input for ac-DBD numerical model. . . . .	98
5.13	Horizontal velocity component ( $ms^{-1}$ ) of resultant wall bounded jet. . . . .	99
5.14	Experiments compared to ac-DBD model body force with dielectric thickness. . . . .	99
5.15	PTFE dielectric experiments compared to tuned ac-DBD model body force with dielectric thickness. . . . .	100
5.16	Kapton dielectric experiments compared to tuned ac-DBD model body force with dielectric thickness. . . . .	101
5.17	GRE dielectric experiments compared to tuned ac-DBD model body force with dielectric thickness. . . . .	101
6.1	Mesh of heated region at $x=0.18$ in numerical domain. . . . .	104
6.2	S-shaped duct flow control locations. . . . .	106

6.3 Heated regions in numerical domain of s-shaped duct. . . . . 107

6.11 Pressure distortion coefficient at AIP. . . . . 117

6.12 Pressure distortion coefficients for baseline and ac-DBD actuated cases: (6.12a)  
30° sector; (6.12b) 45° sector; (6.12c) 60° sector; (6.12d) 90° sector. . . . . 118



# Nomenclature

## UNITS

All units of measurement throughout this thesis conform to the Systeme Internationale, with deviations from this rule noted where appropriate.

## SYMBOLS

The following symbols are used throughout this thesis. Where a symbol is used only briefly, it is defined at the appropriate point in the text.

## GREEK SYMBOLS

symbol	description	units
$\beta$	ns-DBD model Gaussian profile parameter	
$\delta$	boundary layer thickness	
$\varepsilon$	dielectric constant / relative permittivity	
$\gamma$	ns-DBD model Gaussian profile parameter	
$\omega$	specific dissipation rate	1/s
$\lambda$	eigenvalues	
$\rho$	density	kg/m <sup>3</sup>
$\sigma$	standard deviation	
$\chi$	ambient temperature multiplication factor	

## ABBREVIATIONS

symbol	description	units
AIP	aerodynamic interface plane	
BL	boundary layer	
CAD	computer aided design	
CFD	computational fluid dynamics	

CI	confidence interval	
$C_p$	static pressure coefficient	
DAQ	data acquisition system	
DBD	dielectric barrier discharge	
DC	direct current	
$DC_\theta$	total pressure distortion coefficient	
DDES	delayed detached eddy simulation	
DES	detached eddy simulation	
DFT	discrete Fourier transform	
DMD	dynamic mode decomposition	
DNS	direct numerical simulation	
DoE	design of experiment	
EHD	electrohydrodynamics force	
EMI	electromagnetic interference	
fft	fast fourier transform	
GRE	glass reinforced epoxy	
HPC	high performance computing	
k	turbulent kinetic energy	$m^2/s^2$
LES	large eddy simulation	
Ma	Mach number	
MAM	mid-point approximation method	
MOGA	multi objective genetic algorithm	
NWTF	national wind tunnel facility	
PA	plasma actuator	
$P_s$	static pressure	Pascals
$P_t$	total pressure	Pascals
PIV	particle image velocimetry	
POD	proper orthogonal decomposition	
$PR_s$	static pressure recovery	
$PR_t$	total pressure recovery	
PTFE	polyimide Kapton / Polytetrafluoroethylene	
q	dynamic pressure	Pascals
RANS	Reynolds averaged Navier-Stokes	
Re	Reynolds number	
RMS	root mean square	
RSM	response surface model	
s	entropy	$\frac{J}{K}$
$s_c$	distance along duct centreline	m

$SC_{\theta}$	swirl distortion coefficient	
SGS	sub grid scale	
sPIV	stereoscopic particle image velocimetry	
St	Strouhal number	
SQP	sequential quadratic programming	
SST	shear stress transport	
$T_g$	glass transition temperature	$K$
$u, v, w$	velocity components	$m/s$
UAV	unmanned aerial vehicle	
URANS	unsteady RANS	
UV	ultra violet	
VG	vortex generator	



# Chapter 1

## Introduction

The s-shaped duct is a key component on air breathing engines being used as an inlet for fuselage embedded jet engines or as a connecting duct between turbine stages. Turbine connecting ducts are annular in design and are not considered in detail for this work. With detrimental flow physics dominating the duct throughflow an effort is made to understand the complex flow physics in more detail and improve the performance parameters of the throughflow. To that end plasma actuators, a novel active flow control technique, are used in various numerical studies to characterise their effect. Computational simulations are conducted to first characterise the baseline throughflow and apply active plasma flow control next. Figure 1.1 shows a snapshot of the velocity magnitude along the symmetry plane in the baseline, convoluted duct geometry used for this work. The geometry is adapted from Wellborn [1]. This thesis aims to investigate the use of plasma actuators as active flow control techniques in s-shaped, convoluted ducts.

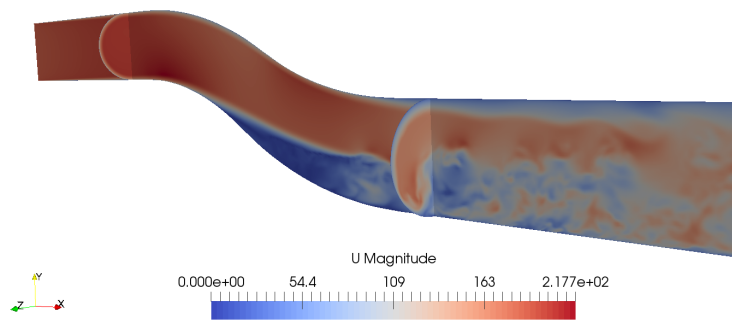


Figure 1.1: Throughflow snapshot of velocity magnitude ( $ms^{-1}$ ) along the symmetry plane as well as the s-duct inlet and outlet planes. Simulation conducted in OpenFOAM.

## 1.1 Background

Performance is key in the aviation sector, now more so than ever with growing pressures on the industry due to a changing climate, greater scrutiny by the public and shareholders, and awareness of the footprint the sector leaves on the planet. Operational costs, fuel efficiency, and noise levels of modern airplane engines are a prime concern for environmental and business reasons. The European Commission has launched a research and innovation programme, Clean Sky, with ambitious environmental goals for the aviation industry. The programme provides emission reduction targets, research funding, and collaboration opportunities for academia and industrial partners. Following the success of the initial Clean Sky Programme, its successor, Clean Sky 2, was launched in 2014 as part of the Horizon 2020 research and innovation initiative. Clean Sky 2 aims to be the main contributor to the Flightpath 2050 goals. These goals and targets are:

- A 75% reduction in carbon dioxide ( $CO_2$ ) emissions;
- A 90% reduction in mono-nitrogen oxides (NOX);
- A noise reduction of flying aircraft of 65%;
- Mitigate the environmental impact of the lifecycle of aircraft and related products by designing and manufacturing aircraft to be recyclable.

In line with the current business climate, new ideas and old approaches are being looked at for potential performance benefits. One possibility to achieve a higher performance in aviation is through reducing losses in the system and improving the quality of the air flow. This can be achieved directly by reducing the weight of components or indirectly by increasing the pressure in jet engine systems allowing a more efficient operation.

A key component of many air breathing engines is the convoluted, s-shaped duct. Guiding the air flow to aft engine components, the s-shaped duct has a high potential for performance improvements due to inherent detrimental flow physics. These are mostly driven by the centreline curvature, the diffusion ratio, and centrifugal pressure gradients. The interplay of those characteristics leads to strong secondary flows and a separated flow region. This in turn results in a high level of unsteadiness and nonuniformity of the flowfield at the aerodynamic interface plane (AIP). For this work, the s-shaped duct geometry was taken from literature. The decision was made as there is detailed experimental data available in the public domain. This data is used for validation and comparison. More detailed analysis of the flow physics in convoluted ducts and the performance criteria is given in chapter 2.

Detrimental flow physics is traditionally tackled by various means of flow control to influence the fluid and improve a chosen performance parameter. The s-shaped, convoluted duct has

also been subject to many flow control studies with both passive as well as active flow control methods. What has not been investigated, however, is the suitability of active plasma flow control devices in s-shaped ducts.

Plasma actuators are a relatively novel form of flow control devices. Dielectric barrier discharge (DBD) plasma actuators operate with high voltage waveforms to ionise the air layer near the actuator. Depending on the mode of operation two distinct types can be characterised. The nanosecond (ns) DBD plasma actuator is fed with nanosecond voltage pulses generating a sonic pressure wave in the discharge region. The alternating current (ac) DBD actuator discharge occurs on a longer timescale resulting in a wall bounded jet. The primary aim for using plasma actuators as flow control devices is to delay or suppress the separation onset in the s-duct by influencing the boundary layer upstream of the separation onset. If successful, this would significantly decrease the non-uniform velocity profile at the AIP and reduce transient fluctuation levels of flow phenomena. More details on plasma actuators are given in chapter 4.

Numerical simulations of the throughflow are performed with OpenFOAM. OpenFOAM (Open Field Operation and Manipulation) is a computational fluid dynamics (CFD) toolbox used to simulate many complex fluid flows involving chemical reactions, turbulence modelling, and heat transfer. The core technology is a set of efficient C++ modules. This software package is available open source which allows users to add their own functionality to the code and tailor solution approaches to each specific problem.

In this work the suitability of plasma actuators to control the flow through an s-shaped duct is investigated numerically.

## 1.2 Research objectives & scope

The main research question of this work is to evaluate the effect of active plasma flow control on the throughflow and performance parameters in the s-shaped duct. Particular interest is put on the transient flow properties.

The objectives addressing the main research question and the scope of the investigation are summarised in bullet form:

- validate OpenFOAM computational fluid dynamics software for simulations of convoluted ducts;
- characterise flow physics & fluid structures in convoluted duct;
- characterise plasma actuators experimentally for active flow control;
- create & validate plasma flow control numerical model in OpenFOAM;
- apply active plasma flow control to convoluted duct.

## 1.3 Thesis outline

Following the introduction, chapter 2 is dedicated to the literature survey on convoluted ducts. It outlines past and current literature on the topic of flow physics in s-shaped ducts as well as flow control research conducted on it. There are separate sections on passive and active flow control studies including optimisation campaigns of both geometry and flow control devices.

In chapter 3 the baseline convoluted duct throughflow is presented and analysed with novel and traditional performance criteria. Numerical simulations are validated against experimental data from literature and compared to other numerical studies from the public domain. This chapter is based on compressible, transient numerical simulations and uses modal decomposition techniques to gain insight into dominant modes and their influence on the throughflow.

Chapter 4 introduces the reader to the operating principles of plasma actuators with the two main types used in this work. The experimental campaigns undertaken to characterise the performance of plasma actuators is outlined. Two experimental campaigns are presented: one for the ac-DBD actuator and one for the ns-DBD actuator.

Chapter 5 follows up on the results of chapter 4 by presenting numerical models that simulate plasma actuators. The simulation results are compared to experimental data gathered during the experimental campaigns described in chapter 4. For each of the two plasma actuator types one numerical model is introduced, discussed, and validated.

Next, in chapter 6, the numerical functionalities of ac-DBD and ns-DBD plasma actuators from chapter 5 are applied to the throughflow simulations of the baseline, convoluted duct geometry from chapter 3. Initially numerical studies were conducted with four different placements of the plasma actuators within the duct for ac-DBD actuators to establish the actuator location with the most impact on the flow. Those simulations are performed with a steady state solver. The selected location is then used for both ns-DBD and ac-DBD actuator flow control with transient simulations and a selected actuation frequency.

## 1.4 Originality & contribution

The research undertaken for this work resulted in a number of contributions to the current state of knowledge. The main contributions were also presented separately in journal publications.

An experimental campaign on the pressure dependency of ns-DBD plasma actuators was conducted. Results were published in the Journal Physics of Plasmas. This study established the effect of ambient pressure from 30 kPa to atmospheric levels on the shock wave propagation speed and strength, showing clear trends with decreasing ambient pressure. Higher ambient pressures result in stronger shock waves; this has been observed irrespective of the actuator thickness.

The effect of permittivity and frequency on induced velocity in ac-DBD plasma actuators

was established experimentally with results published in the Journal Sensors and Actuators A: Physical. Both surface and channel plasma actuators were used with three different dielectric materials and five thicknesses of dielectric material. Surface plasma actuators with thinner dielectric materials outperformed thicker ones for a given high voltage input. For the channel actuator a high gradient of velocity reduction with streamwise distance from the exposed electrode was also observed.

Furthermore, the numerical computations were conducted in an open source CFD solver which has not previously been reported in literature. Simulation snapshots were then analysed with modal decomposition techniques. The proper orthogonal decomposition (POD) is a well established analysis tool, but the dynamic mode decomposition (DMD) has not been applied to convoluted duct throughflow snapshots. With the DMD, phase information and frequency of occurrence of coherent structures can be extracted from data. Findings from the numerical study have been submitted to the Journal of Fluid Mechanics for publication.

## 1.5 Research outcomes

The following list points out the research outcomes based on the work undertaken as part of the PhD project.

Published work:

- Michael M. Wojewodka, Craig White, Shahrokh Shahpar, Konstantinos Kontis, A review of flow control techniques and optimisation in s-shaped ducts, *International Journal of Heat and Fluid Flow*, Volume 74, December 2018
- Michael M. Wojewodka, Craig White, Takahiro Ukai, Andrew Russell, Konstantinos Kontis, Pressure dependency on a nanosecond pulsed dielectric barrier discharge plasma actuator, *Physics of Plasmas*, Volume 26(6), June 2019
- Michael M. Wojewodka, Craig White, Konstantinos Kontis, Effect of permittivity and frequency on induced velocity in ac-DBD surface and channel plasma actuators, *Journal of Sensors and Actuators*, Elsevier Press, Volume 303, January 2020

Submitted work:

- Michael M. Wojewodka, Craig White, Konstantinos Kontis, Shahrokh Shahpar, Numerical study of complex flow physics and coherent structures of the flow through a convoluted duct

Conferences:

- Michael M. Wojewodka, Craig White, Konstantinos Kontis, Complex flow physics and fluid structures in convoluted ducts, ASME Turbomachinery Exhibition and Conference, Phoenix Arizona, 2019

# Chapter 2

## Literature survey

The s-shaped duct, an example of which is shown in Figure 2.1, has a number of distinct advantages. Due to the curvature in the duct, the incoming air is slowed down much faster than in conventional straight ducts which leads to shorter designs and considerable weight savings [5,6]. It is estimated that the net weight of an aircraft would decrease by 15% if the length of the fuselage is reduced by one inlet diameter [7]. This has particular relevance only when propulsion systems are integrated within the airframe and not pod mounted under an aircraft's wing. Moreover, the curved inlet is a line-of-sight blockage to the engine fan/compressor and thus effectively lowers the noise level as well as radar and infrared signatures [5, 7]. Further weight saving potential exists for unmanned aerial vehicles (UAVs) as their total size is often determined by the propulsion system [6]: a shorter propulsion system would directly relate to a smaller UAV.

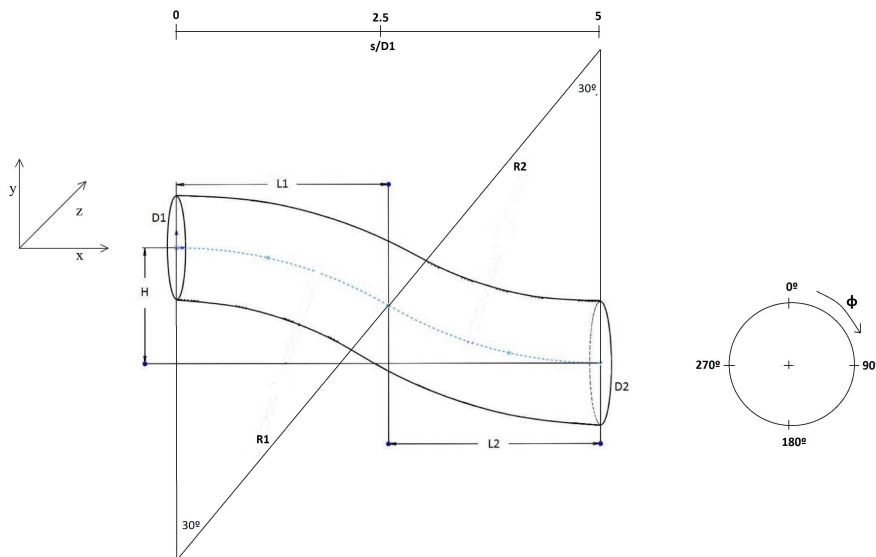


Figure 2.1: S-shaped duct. Geometry adapted from Wellborn [1]. Symbols denote:  $H$  = vertical offset;  $D_1$  = inlet diameter,  $D_2$  = outlet diameter;  $L_1$  = horizontal distance to inflection point from inlet;  $L_2$  = horizontal distance to outlet from inflection point;  $R_1$  = radius of first arc;  $R_2$  = radius of second arc. Figure taken from [8].

S-shaped ducts have been used as intakes on a number of commercial and military airplanes (engines) such as the Boeing 727 (P&W JT8D), the Lockheed Tristar L-1011 (RR-RB211), the General Dynamics F-16 (P&W F100), and the McDonnell-Douglas F-18 (GE F404) with the engine buried in the fuselage. The convoluted s-duct has also been employed to join compressor and turbine stages in turbomachinery. However, the duct design introduces a number of undesirable flow features, such as a non-uniform pressure distribution at the aerodynamic interface plane (AIP), i.e. the plane between the exit of the intake and the compressor/fan of the engine, and flow separation for particularly aggressive convoluted ducts. These undesirable flow features reduce the efficiency of the s-shaped inlets, increase the pressure loss, cause higher levels of fatigue, and hence decrease the operational lives of the engine compressor/fan [7]. Non-uniform flow conditions at the AIP also lower engine surge and stall limits [3].

## 2.1 Performance and geometrical parameters

S-shaped ducts are commonly characterised by their diffusion ratio, their radius ratio as well as their length-to-diameter, LDR, and length-to-offset, LOR, ratios. The diffusion ratio depends on the inlet and outlet diameters denoted by  $D_1$  and  $D_2$ , respectively in Figure 2.1. The duct's centreline is specified by two arcs with respective radii  $R_1$  and  $R_2$ . The radius ratio is defined by the ratio of the arc radius to the inlet radius.

The two main criteria for evaluating the performance of engine intakes are total pressure recovery and distortion coefficient. The latter one is described by various parameters as it is defined in a number of ways [9, 10]. Total pressure recovery (PR) is defined as the mean value of total pressure at the AIP  $\langle P_{t-AIP} \rangle$  divided by the total pressure of the inlet freestream  $P_{t-o}$  [11], i.e.,

$$PR = \frac{\langle P_{t-AIP} \rangle}{P_{t-o}}. \quad (2.1)$$

The distortion coefficient used in this work is denoted  $DC_\theta$ . Here  $\theta$  represents the in-plane angle in a chosen cross-section of the circular s-duct. This parameter is an indicator of the non-uniformity of a flow property at a cross-section plane in the flow. The distortion coefficient  $DC_\theta$  is computed by subtracting the minimum mean total pressure of all sectors of extent  $\theta$ ,  $\langle P_{t-\theta,AIP} \rangle_{min}$ , (usually equal to 60 degrees) at the AIP from the mean total pressure at the AIP,  $\langle P_{t-AIP} \rangle$ , and dividing the result by the dynamic pressure,  $q$ , at the AIP [11],

$$DC_\theta = \frac{\langle P_{t-AIP} \rangle - \langle P_{t-\theta,AIP} \rangle_{min}}{q}. \quad (2.2)$$

The swirl flow parameter,  $SC_\theta$ , is based on  $DC_\theta$  and is defined as the maximum average circumferential component of the cross-flow velocity in a given theta degree sector  $\text{MAX} \langle U_{crossflow-\theta-AIP} \rangle$ . The cross-flow velocity is the magnitude of the in-plane velocities in the y and z directions. This parameter is non-dimensionalised by dividing by the velocity on the

centreline of the duct at the throat  $U_{centreline-throat}$  [12],

$$SC_{\theta} = \frac{MAX \langle U_{crossflow-\theta-AIP} \rangle}{U_{centreline-throat}}. \quad (2.3)$$

Another swirl flow parameter, the swirl intensity, SI, is defined as the area weighted average of absolute swirl angles for each measurement sector [13]:

$$SI = \frac{\sum_{k=1}^m SS_k^+ * \theta_k^+ + \sum_{k=1}^m SS_k^- * \theta_k^-}{360}, \quad (2.4)$$

where  $\theta_k^-$  and  $\theta_k^+$  define the size of the swirl flow regions and  $SS_k^-$  and  $SS_k^+$  are symbols for the negative and positive sector swirls, respectively.

Ideally, an s-shaped duct would have small LDR and LOR ratios (i.e. an aggressive design), have a high PR for minimal losses, as well as low pressure and swirl distortion coefficients for a uniform pressure distribution at the AIP with little swirl flow.

## 2.2 Flow physics in s-ducts

First, a schematic drawing (Figure 2.2) of widely accepted flow features in s-ducts is presented. Figure 2.2 was created based on findings in the literature.

Depending on the diffusion rate, the radius of curvature and the strength of secondary flows, flow separation is expected near the inflection point [1, 14]. The radius of curvature generates centrifugal pressure gradients that, helped by the diffusion rate, develop into secondary flows and promote a complex three-dimensional flow field [14–16].

The centrifugal body force creates a gradient of pressure between the concave and convex sections of the duct walls [17]. Therefore, the higher velocity fluid is dragged from the top to the bottom wall in the first bend and from the bottom to the top wall in the second bend. This accounts for the low velocity region in the lower section of the AIP as slow moving fluid is less affected by the centrifugal pressure gradients.

In the curving duct, the static pressure increases at the outer wall, contrary to the inner wall, thickening the boundary layer (BL) [1, 15, 18]. Total pressure losses are most prominent in the lower central region of the AIP and a smaller area at the top of the interface plane [13, 15, 19]. These pressure losses are caused by the secondary flow structures and flow separation in the first bend and the adverse pressure gradient in the second bend, respectively [19].

Contrary to the reported results by Bensod and Bradshaw [20], it is generally agreed that the time-averaged flow is symmetric about the symmetry plane of the s-duct. This was concluded in studies by Taylor et al. [21,22] for low to medium Reynolds numbers ( $Re = 790$  and  $Re = 48000$ ) as well as Vakili et al. [23] and Wellborn [1] for higher Reynolds numbers ( $Re = 3.25 \times 10^6$  and  $Re = 2.6 \times 10^6$ , respectively). This finding has been used extensively in numerical simulations

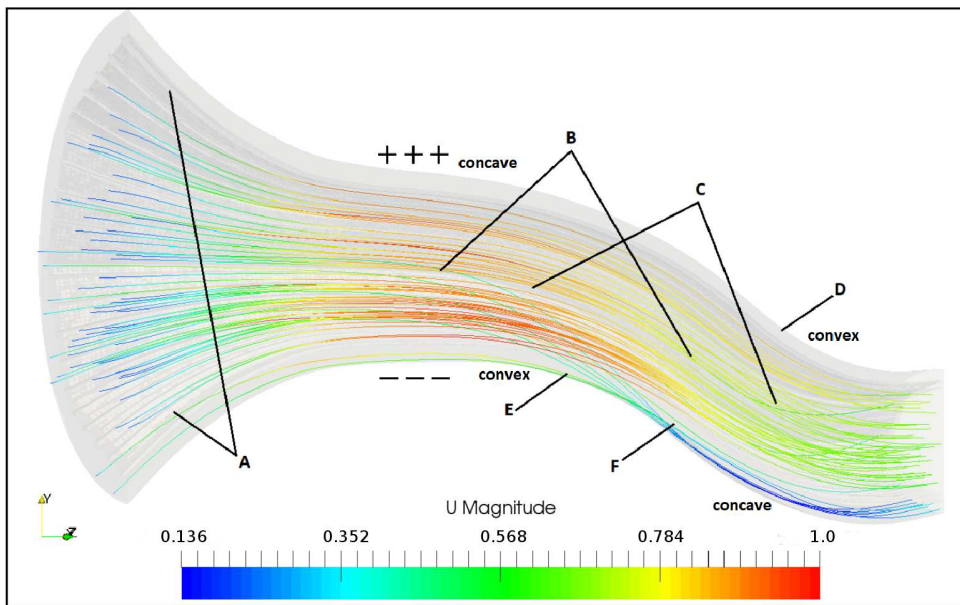


Figure 2.2: S-duct flow schematic, labelled with the major and widely accepted flow features. On the top side, the +++ indicate a high pressure region and the --- a low pressure region on the bottom side. Streamlines are coloured with the normalised velocity magnitude. The centreline velocity magnitude at the throat of the duct is used for normalising. Regions: A) Favourable pressure gradient, thin BL; B) Diffusion causing cross-stream pressure gradients, secondary flow, thickening of BL, and rising static pressure values; C) Radius of curvature promotes centrifugal pressure gradients, cross-stream flow, and swirl formation; D) low energy flow swept to inner wall in second bend; E) Low energy flow swept to inner wall in first bend; F) Separation dependent on diffusion rate, secondary flows, and pressure gradient. Figure adapted from [8].

and analysis of the through-flow with only half of the geometry being modelled. In steady, time-averaged computations this results in a realistic representation of the flow. However, unsteady flow phenomena are asymmetric by nature and hence, this assumption is void for detailed, time-varying simulations of the flow field as demonstrated by Berens et al. [24].

This symmetric flow pattern is dominated by a pair of counter-rotating vortices that form in the duct and propagate to the AIP. Guo and Seddon [25] report a double vortex pattern forming after the second bend. As does Wellborn, stating that a large pair of counter-rotating vortices evolves due to secondary flows dragging fluid from the BL into the core and thus degrading the uniformity of the pressure profile [1]. Swirling flow also develops because the flow along the centreline in a duct moves fastest and hence is subjected to a larger centrifugal force compared to the flow along the duct walls [26]. Blockage, due to flow separation at the duct's inflection point, is responsible for the accelerated core flow [14].

Separation at the inflection point, an example of which is shown in Figure 2.3, is aided by the adverse pressure gradient, diffusion, and secondary flows. Diffusion causes stream-wise pressure gradients [27], resulting in a non-uniform pressure distribution that promotes separation. The low energy flow in the separated region is affected more than any other part of the flow by

the centrifugal pressure gradient associated with the bend, it is hence swept across the duct to the inner wall as is reported by Guo and Seddon [25]. Brear et al. note that separation creates large unsteady structures, with two vortices being the most distinctive features [28], leading to a reduction in pressure recovery and a high level of unsteadiness. The exact mechanism, cause, and effect of unsteadiness and flow phenomena such as separation, diffusion, and secondary flows is not yet fully understood. However, recent studies have shed some light on the unsteady features of flows in convoluted ducts [13, 16, 29].

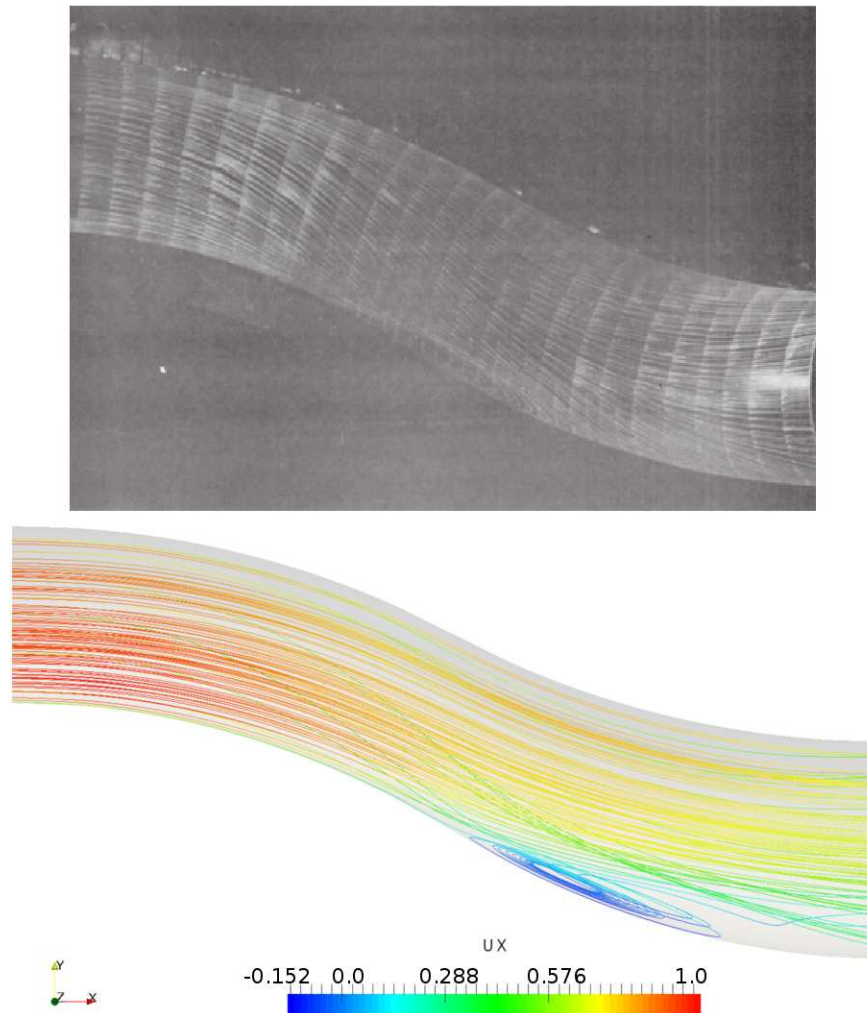


Figure 2.3: Flow separation in convoluted duct at a Mach number of 0.6. Top: Wellborn’s experimental oil-flow results [1]. Bottom: Authors’ CFD simulation with OpenFOAM. Streamlines are coloured with the normalised streamwise velocity. The centreline streamwise velocity at the throat of the duct is used for normalising. Figure adapted from [8].

A study by Luers [30] suggests that the distortion coefficient, in this case  $DC_{60}$ , does not change with the inlet Mach number. Zachos et al. [13], look at swirl, investigating the flow through an s-duct at Mach numbers in the range 0.27-0.6 [13]. This study concludes that the Mach number has little effect on the flow parameters. Both swirl descriptors,  $SI$  and  $SC_{60}$ , increase very weakly with higher Mach numbers as is shown in Figures 2.4 and 2.5.

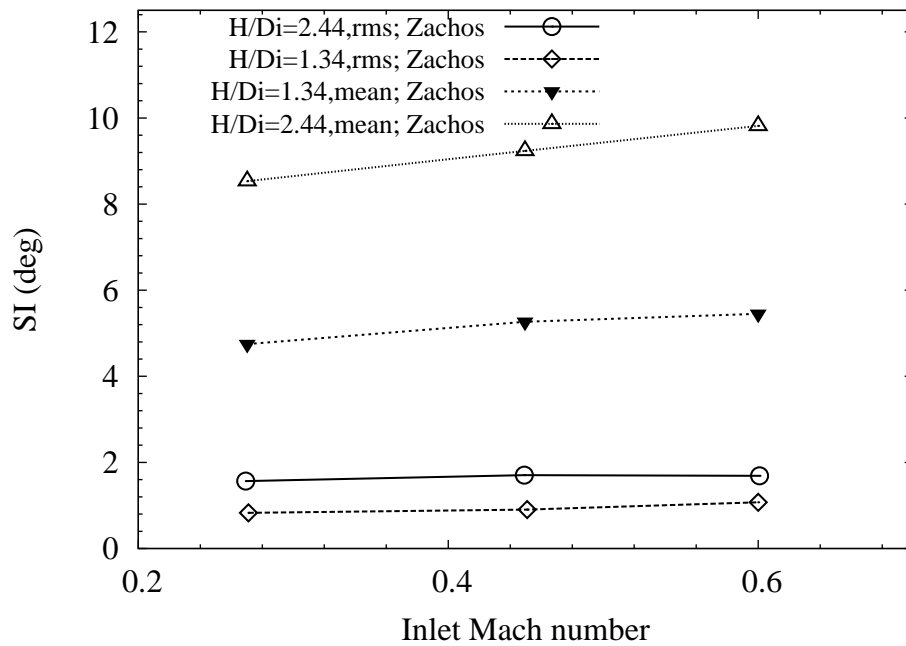


Figure 2.4: Swirl intensity vs inlet Mach number. Data replotted from [13].

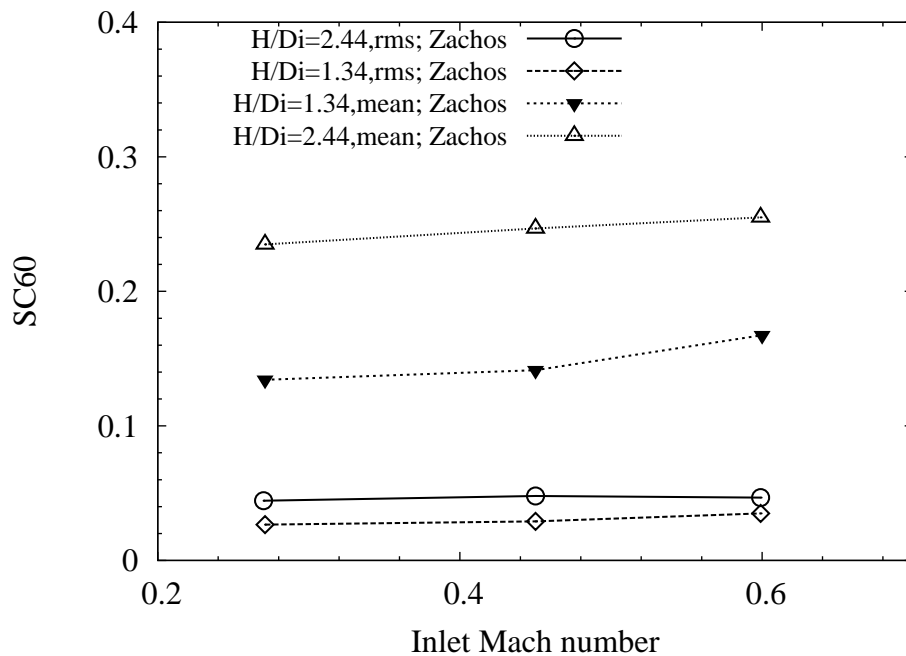


Figure 2.5: Swirl coefficient SC60 at AIP vs inlet Mach number. Data replotted from [13].

Unsteady flow measurements were conducted by Gil-Prieto et al.6 [16] in two circular s-shaped ducts at Mach numbers of 0.27 and 0.6 [16]. They compared two ducts with two height-to-length ratios  $H/L$ , of 0.5 and 0.27, respectively. It has to be noted that the snapshots of the flow were under resolved temporally and the unsteadiness was quantified by a sample of statistically representative data. Results show that the instantaneous flow features are different from the time-

averaged properties. The difference in peak values of swirl distortion, for example, can be one order of magnitude higher. Figure 2.6 shows the time averaged field and the standard deviation of the pressure recovery and swirl at the AIP. The results are based on numerical analysis of Delayed Detached Eddy Simulation (DDES) and are adapted from MacManus [29].

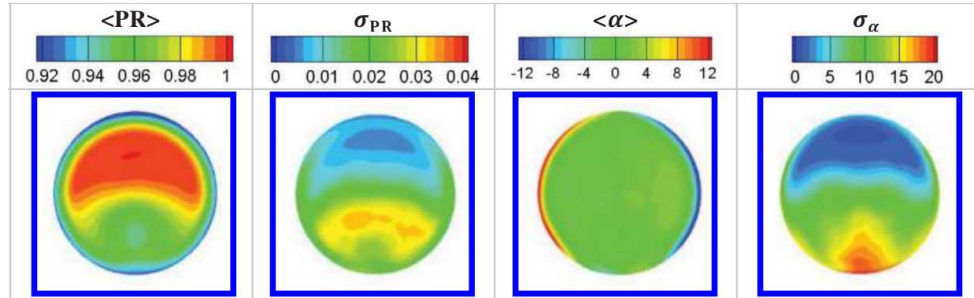


Figure 2.6: Average and standard deviation of pressure recovery and swirl at AIP of Wellborn duct based on DDES simulation. Figure adapted from MacManus [29].

The literature survey on the subject of convoluted ducts did not show any numerical studies with the large eddy simulation (LES) or direct numerical simulation (DNS) techniques. Such studies would fill a gap in the literature and provide benchmark data lower fidelity numerical studies and experimental findings can be compared against. However, due to the required mesh resolution and computational expense for the LES and DNS techniques this is not readily achievable.

Based on the analysis of stereoscopic PIV data, dominant modes of flow structures are identified in a follow-up study by Gil-Prieto et al. [31]. The results clearly show a switching as well as a vertical mode. In the switching mode, the vortices observed in the mean flow alternate in strength with either one dominating the flow pattern at the AIP - perturbing the circumferential flow field. Gil-Prieto et al. [31] postulate that the vertical mode is associated with unsteadiness of the centreline shear layer. Its effect is to shift the vortical structures, and hence the main loss region, vertically from its time-averaged position (see Figure 2.7).

The described flow features are undesirable and much research has focussed on ways to improve the flow at the AIP, using flow control devices, or geometry optimisation.

## 2.3 Passive flow control

### 2.3.1 Working principle of common passive flow control devices

Spoilers are commonly used as a swirl control device. The spoiler trips the flow which causes separation and a decrease of the total pressure. A reduction in pressure gradients has a direct effect on swirl formation. Fences and rails are also used to the same effect.

Vortex generators (VG) are mainly used to control separation. They re-energise the low momentum fluid in the boundary layer by generating vortical structures that draw higher mo-

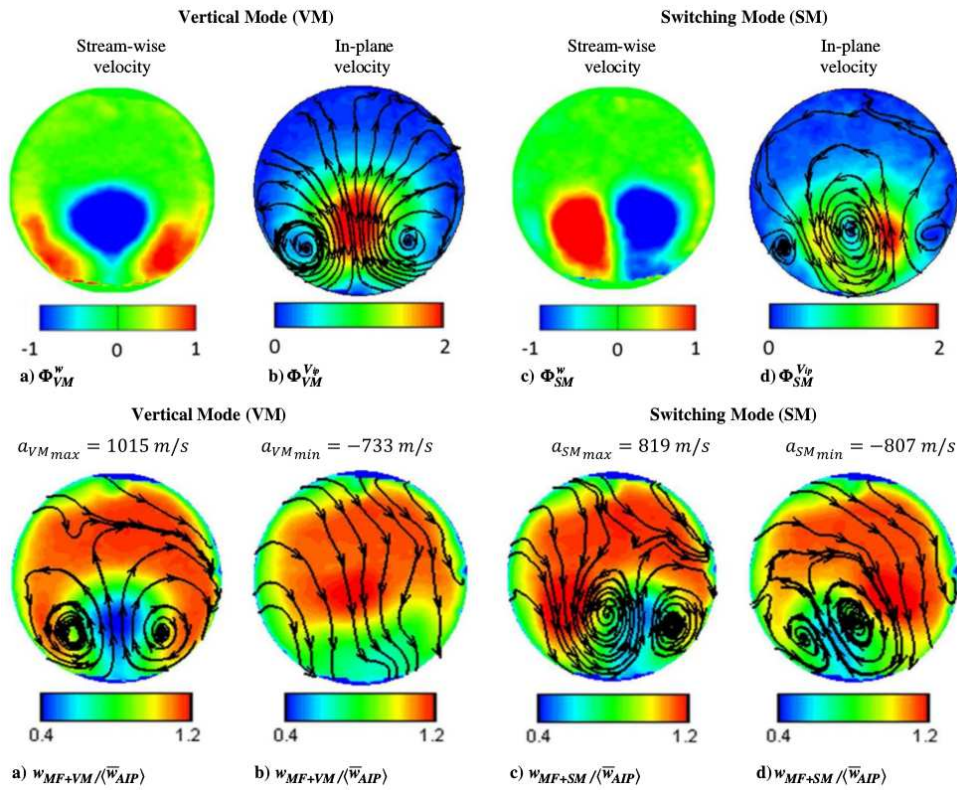


Figure 2.7: Switching and vertical modes (SM and VM respectively) at Mach number of 0.27. Figure taken from [31]. Top: Proper orthogonal decomposition (POD) modal shapes with a) symmetric distribution for the streamwise velocity component of the VM; b) vertical in-plane perturbation (VM); c) anti-symmetric distribution of the switching mode; d) swirling perturbation of the in-plane velocity. Bottom: Snapshots of vertical and switching modes superimposed on the mean flow in the duct with a) showing the effect of the VM on the mean flow with a positive temporal coefficient, and b) with a negative temporal coefficient. The superimposed SM on the mean flow is shown in c) and d) for a positive and negative temporal coefficient, respectively.

mentum fluid from the core flow in to the boundary layer. This mechanism delays the onset or prevents separation of the BL. Vortex generators also introduce a secondary flow pattern within the BL that, ideally, counters the naturally occurring one and prevents the formation of the pair of counter rotating vortices [32]. Vortex generators come in different shapes and sizes. Schematic diagrams of vane type, tapered-fin, and wishbone vortex generators are shown in Figure 2.8.

Submerged VGs have a much lower device drag than conventional VGs [33] - Lin [32] reports a difference of an order of magnitude. Conventional VGs can produce vortices that are too strong, due to their relative height compared to the boundary layer thickness ( $\delta$ ), that do not attenuate and disturb the flow past their intended range. However, in s-ducts a high rate of vortex decay is desirable once short-range flow control is achieved. The effectiveness of submerged VGs is in part attributed to the turbulent BL they are placed in. As the turbulent BL has a fuller velocity profile than a laminar one, the submerged VGs have a higher velocity to work with and hence create stronger vortices than in a laminar BL of similar height. The local velocity at 20% height in a typical turbulent BL is already 75% of the freestream value [34].

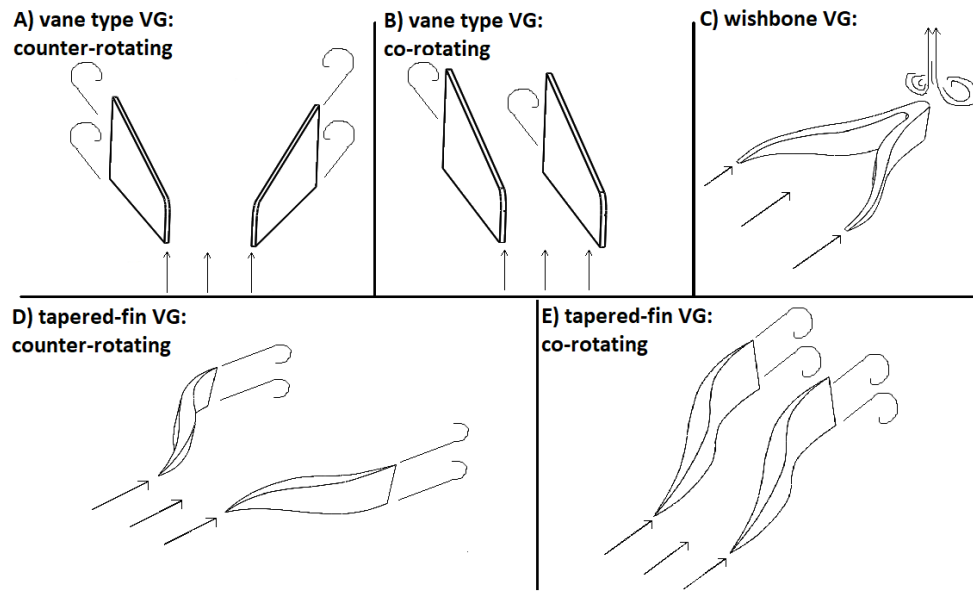


Figure 2.8: Schematic representation of various VG types: Counter and co-rotating configurations of vane type VG in a) and b) respectively. Wishbone VG in c). Counter and co-rotating configurations of tapered-fin VG in d) and e) respectively. Figure taken from [8].

Detrimentially, vortex generators, spoilers, fences, and rail devices cause an obstruction to the flow, and have an associated drag penalty. From these four devices only the VG are positioned axially, i.e. in the streamwise direction, so that the drag penalty is the smallest as they cause the smallest obstruction to the flow.

### 2.3.2 Passive flow control devices employed in s-shaped ducts

Spoilers can be used to alter the swirl pattern and create a zero swirl flow as demonstrated in a rectangular-to-circular cross-section s-duct by Guo and Seddon at  $40 \text{ ms}^{-1}$ . A solid spoiler of  $0.13w$  (where  $w$  is the ratio of spoiler width to duct width at throat) gives a zero swirl coefficient [12]. However, its side-area results in high drag at low incidence flows, and hence high pressure losses. In a similar study, swirl reduction by using spoilers was also demonstrated in convoluted ducts ( $U=38 \text{ ms}^{-1}$ ,  $Re = 3.8 \times 10^5$ ), with both horizontal and vertical offsets [35]. Vakili et al. used a thick rail device of thickness equal to the BL height, to successfully control swirl formation and eliminate flow separation [23] in an s-duct of circular cross-section ( $Ma = 0.6$ ,  $Re = 3.25 \times 10^6$ ). As in Guo and Seddon's study [12], this also resulted in losses due to a high induced drag and blockage to the flow. The distortion coefficient,  $DC_{60}$ , at the AIP was degraded (from 0.559 to 0.772) by the rail device.

Reichert and Wendt [2] used arrays of wishbone VG in the Wellborn s-duct. The study looked at VG streamwise location, their spacing, and their height (40%, 100%, and 160% of BL height). Even though some configurations were effective in improving pressure recovery, no configuration tested managed to reduce pressure distortion values at the AIP. This may be partly

due to the counter-rotating vortices produced by each wishbone VG. Counter-rotating vortices interfere with one another resulting in vortex interference and a reduction in vortex strength [36]. Marginal effects on the flow of wishbone VG of height equal to 60% of the BL thickness have also been reported by Sullerey [27] as they are best suited for flows with non-zero sideslip angle which is not the case in s-ducts upstream of the separation point. Lin, also, concludes that co-rotating configurations tend to yield better results in s-ducts [32].

Vane type vortex generators were used by a number of researchers [23, 37–41]. Two publications embedded counter-rotating configurations and report beneficial effects on the flow such as a suppressed separation region and reduced total pressure losses [39] or a more uniform flow at the AIP [23]. However, the former study was conducted on a constant-area cross-section s-duct which does not take into account the added complexity of the flow due to diffusion. The latter does not provide essential information on the location of the actuators, their number, and their height with respect to the BL thickness.

Five co-rotating VG configurations were tested by Delot et al. [38] with varying angle to the incoming flow and of various heights (6, 4, and 2 mm - BL thickness information is not provided). The greatest reduction in  $DC_{60}$  is achieved with the highest VG and a constant orientation to the incoming flow of 18 degrees. Zhang et al. compared counter and co-rotating vane type VG in the same convoluted duct at a Reynolds number of  $1.5 \times 10^5$  [40] with heights of 25% and 15% of the BL thickness, respectively. Other geometric parameters and their number (2 pairs in the counter-rotating set-up and 4 single VG in the co-rotating set-up) were identical for both configurations. Zhang and colleagues report that both configurations were successful in eliminating separation (based on oil flow visualisations and surface pressures) and resulted in an identical distribution of static pressure. This is also evident from oil flow visualisations presented in Figure 2.9. However, the counter-rotating VG array produced higher near-wall losses and a less uniform flow at the AIP. The co-rotating array decreased the pressure loss at the AIP by 5%, 1% more than the counter-rotating configuration.

Paul et al. [17, 42] have managed to use counter-rotating vane type VG, called fishtail VG in the publication, in s-ducts and improve performance parameters - flow uniformity improved at the AIP (16% lower distortion [17]), higher static pressure recovery and reduced total pressure loss [42]. Submerged VG of height of  $0.2\delta$  were placed at the inlet at both the bottom and top surfaces of the convoluted duct. With the height of the VG being a fraction of the BL thickness, counter-rotating VG gain effectiveness as their vortices remain within the BL, re-energising the low-momentum fluid, but do not disturb the flow past their short-range flow control objective. Combining submerged VG with a chamfered inlet area (23% at inlet and 12% at exit is blocked with a fillet) Paul et al. showed that flow uniformity is improved significantly [17] as is the pressure loss coefficient (Figure 2.10). This might be due to the fact that the rectangular cross-section is made more circular by the fillets which reduces corner losses through the s-duct.

Reichert and Wendt employed arrays of tapered fin VG of height equal to the BL thickness

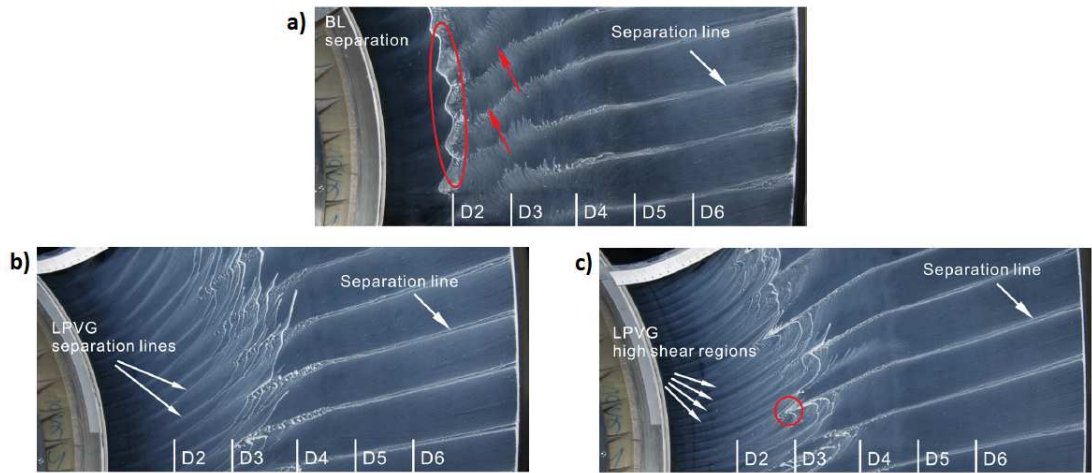


Figure 2.9: Oil flow visualisation of baseline (a), co and counter-rotating vane VG (b) and (c), respectively. In a) flow separation is clearly visible (marked with red oval). This separation region is eliminated by the co and counter-rotating VG configurations in (b) and (c), respectively. Figure taken from [40].

in the Wellborn s-duct at a Mach number of 0.6 [3]. The study investigated narrow and wide spacings between consecutive VG. Based on the results, configurations of narrow spaced VG shed vortices that did overcome the natural secondary flows and are better equipped to improve pressure recovery and eliminate separation. This is believed to be the case as vortices of narrow configurations experience interference effects and merge into a single pair of vortices. Wide spaced arrays, however, retain their separate vortices and have an effect on a wider circumferential extent, hence the uniformity was highest with wide spaced configurations. Wendt et al. explain in their study on structure and development of streamwise vortex arrays that the downstream interaction depends on the VG spacing. Tight arrays provide best local mixing hence are better equipped to suppress flow separation, but their vortices attenuate rapidly downstream [37].

Tanguy employed vane type VG in an experiment with unsteady measurements to control the flow through an s-duct [19]. This study ( $Ma = 0.27$  &  $0.6$ ), which is temporally underresolved and bases its conclusions on statistics of flow snapshots, examines the effect of the circumferential extent, the VG height, and the axial location. All configurations were successful in improving the pressure recovery and decreasing pressure losses, but four designs increased the distortion levels at the AIP [19]. It was found that the smallest VG height (equal to  $0.63$  of BL thickness), and an axial placement of  $14\delta$  upstream from the separation point (i.e. configuration VG5 in the publication), resulted in the best performance improvement.

The effect on swirl at the AIP is also quantified in the study by swirl descriptors [19]. The study shows that dynamic levels of swirl angle can be significantly reduced. Tanguy et al. explain the beneficial effect with the increased secondary flow field which confines the swirling flow to their respective regions, reducing unsteadiness across the AIP. For example, one of the VG configurations decreased the mean swirl intensity, SI, by 49% with a significantly lower

standard deviation and maximum SI values.

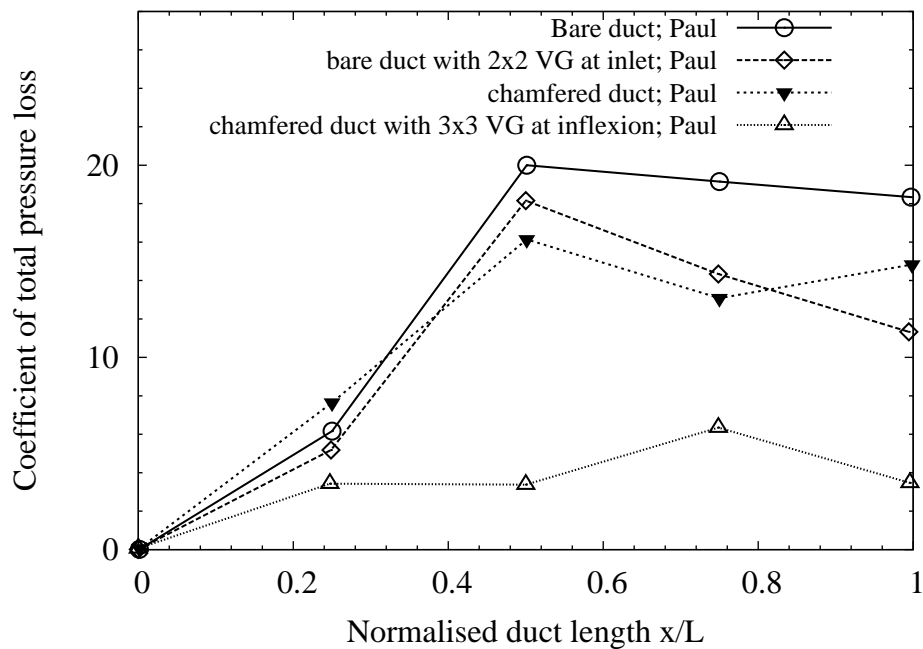


Figure 2.10: Coefficient of total pressure loss along the duct length. Data replotted from [17].

Conventional VGs are usually placed further downstream than submerged VGs,  $5\delta$  and  $2\delta$  upstream of the baseline separation location, respectively [32]. Jenkins et al. [43] report that the location of submerged VG should be 5-30 device heights upstream of the separation location. It is widely agreed that the optimum location for vortex generators is upstream of the separation point just ahead of the high adverse pressure gradient [27,39]. At this location the boundary layer grows rapidly before detaching from the surface and separating. Sub VGs lose effectiveness for heights smaller than  $0.1\delta$ . The smaller its height, the stronger the influence of the wall and the shear stress on the produced vortices. This promotes faster vortex strength decay and hence less flow control authority. Joint vane type VG, or VG in close proximity to one another producing counter-rotating vortices, experience interference effects and a reduction in vortex strength [36]. Therefore, co-rotating configurations tend to work better in s-duct geometries [32].

Table 2.1 is a summary of all the passive flow control techniques considered in this literature review. The summary indicates which techniques were found to improve or deteriorate flow phenomena such as separation, distortion at AIP, swirl flow, pressure loss, and pressure recovery. The table also shows the flow regime, characterised by the Reynolds number or Mach number of the flow, as well as the publication the results were reported in. The column labelled “study” indicates through the letters “E” and “N” whether a study was performed experimentally, numerically, or both. The percentage values given indicate the change of a certain parameter with respect to the baseline value as reported in the publications.

Different geometries and flow regimes for the studies presented in Table 2.1 prevent the results from being directly comparable to each other, but, a comprehensive overview is obtained.

Reducing the extent of separation usually has a positive effect on pressure loss and pressure recovery, however, this is not assumed in the summary so that only explicitly stated results from the corresponding publications are included.

### 2.3.3 Optimisation studies

Optimisation techniques were used by a number of researchers to alter flow control actuators [45–48] or the geometry [49–52] of convoluted ducts and thus mitigate undesirable flow features. Optimisation algorithms can be broadly split into three groups: evolutionary based algorithms, local search methods, and mid-range approximation methods.

Evolutionary based optimisation methods are based on natural selection principles of evolution and mutation [53]. Different designs are rated according to their goodness criteria, i.e. depending on the value of their corresponding cost function. The higher a particular design is rated the greater its chance to ‘reproduce’ and influence the next generation of designs. These algorithms are generally able to find a global optima, however, a considerable number of design evaluations are required to reach a final answer. An example of evolutionary optimisation algorithms is the adaptive range multi-objective genetic algorithm, ARMOGA [54].

Local search methods make use of adjoint gradients which are used to compute the sensitivity of a baseline design with respect to local changes. As pointed out by Shahpar et al. [55], the sensitivity of a parameter can be divided into parts relating to changes in the flow and of the geometry. For the adjoint method to work, an existing, well-converged computational fluid dynamics (CFD) solution is required, as the gradients are computed on this basis.

Mid-point approximation methods (MAM) are based on the trust region approach in which the optimiser searches for an optimum solution. The trust regions are gradually reduced in size during the optimisation process as the design space is narrowed down. Approximate models are built on each trust region with a response surface model (RSM) forming the basis for the next design evaluations [56]. An advantage of using the combination of approximate models is that this method is considerably faster (between 6 to 10 times) than genetic algorithms [57]. Examples of such algorithms are multi-point approximation methods [58, 59] (MAM1 and MAM2) that are being developed.

Sequential quadratic programming (SQP) algorithms are iterative optimisers for non-linear problems. The algorithm solves a number of sub-problems optimising a quadratic model [60]. The solution approximations are used to create a more appropriate solution in the next step. Convergence is achieved by iterating through the process until a solution cannot be improved upon further. As the solution is based on the initial approximation to the algorithm, SQP works best with a good initial guess, but does not handle noisy data well.

Usually, the numerical cost of an optimisation study increases with increasing number of design parameters (d.p.), as a bigger design space has to be searched and evaluated by the algorithm.

Table 2.1: Summary of passive flow control techniques employed on s-ducts

flow control	flow regime	separation	distortion	PR	pressure loss	swirl	E/N	publication
spoilers	Re=4.2x10 <sup>5</sup>	↓	/	↓	↓	↑	E	[12]
rail	Re=3.25x10 <sup>6</sup>	↑	↓ 38%	↓ 13%	/	↓	E	[23]
wing type VG	Re=3.25x10 <sup>6</sup>	↑	↑ 18%	↑ 9.9%	/	↑	E	[23]
vane type VG (const. area)	Re=4.73x10 <sup>4</sup>	↑	/	/	↑	↓	E	[39]
tapered fin VG	Re=2.6x10 <sup>6</sup>	↑	↑ 50%	↑ 0.65%	/	↑	E	[3]
tapered fin VG (duct1)	Re=0.78x10 <sup>6</sup>	/	↑ 9%	↑ 8.4%	↑ 11%	/	E	[27]
tapered fin VG (duct2)	Re=0.78x10 <sup>6</sup>	/	↑ 17%	↑ 20%	↑ 38.8%	/	E	[27]
wishbone VG (duct2)	Re=0.78x10 <sup>6</sup>	/	↑ 5%	↑ 0.7%	↑ 13.5%	/	E	[27]
fences (duct2)	Re=0.78x10 <sup>6</sup>	/	↑ 10%	↑ 12%	↑ 28.8%	/	E	[27]
fences (duct1)	Re=0.78x10 <sup>6</sup>	/	↑ 11%	↑ 18.6%	↑ 37.5%	/	E	[27]
VG	Re=2.6x10 <sup>6</sup> , Ma=0.6	↑	↑	↑	↑	/	E	[2]
VG vanes	Re=1.5x10 <sup>6</sup>	↑	↑ 50%	↑	↑	/	E	[38]
subm. VG + chamfered corners	Re=1.34x10 <sup>5</sup>	/	↑ 16%	↑	↑	/	E	[17]
subm. vane type VG	Re=0.68x10 <sup>5</sup>	↑	↑ 27%	↑ 27%	↑ 14%	/	E&N	[42]
VG	Ma=0.27	/	---	↑	↑ 25%	↑	E	[19]
VG	Ma=0.6	/	---	↑	↑ 30%	↑	E	[19]
BL fences	Ma=0.85	/	↑ 11%	/	↓ 52%	/	E&N	[44]

Symbols indicate: ↑ = improvement by flow control technique; / = not reported; ↓ = deterioration by flow control technique; - - - = no effect.

### VG optimisation

Geometrical features of VG and their location (5 d.p.) in a circular s-duct ( $Ma = 0.66$ ) were optimised using a RSM search based on 27 CFD runs by Jirasek [46]. The RSM search indicated that the most important parameters with respect to minimising the pressure distortion are the VG height and their distance from the separation region. With respect to increasing the pressure recovery, the angle of inclination and square of the VG height are the most important terms. Performance parameters were improved significantly based on the optimisation study with distortion reduced to 7% from 56% and pressure recovery increased by 0.66%. An earlier study by Hamstra et al. [45] utilised a design of experiment (DoE) approach based on 45 CFD Reynolds Averaged Navier-Stokes (RANS) simulations for micro-jet and micro-vane VG (6 d.p.) at an inlet Mach number of 0.6, improving both the distortion and pressure recovery in the duct.

Anderson et al. [47] also employed the DoE - RSM combination to investigate micro-vane and micro-jet actuators at a Mach number of 0.7. Their optimisation strategy allowed for identifying two-factor synergistic effects of the three variables used: number of micro-vane actuators ( $n$ ), their height ( $h$ ), and cord length ( $c$ ). The results suggest that there is a coupling effect between the number of actuators and their height ( $n$  &  $h$ ), as well as their cord length ( $n$  &  $c$ ), that is important for controlling the inlet total pressure recovery. Three two-factor interactions ( $n$  &  $h$ ,  $n$  &  $c$ , and  $h$  &  $c$ ) were found to influence the  $DC_{60}$  coefficient at the AIP.

Another study optimising VGs by Yi et al. [48] used an adjoint code to optimise an array of 11 VGs resulting in 55 d.p. in total (5 d.p. per VG: chord length, height, angle of incidence, axial position, circumferential position) in an s-duct of circular cross-section. The objective was to minimise the distortion coefficient, with the baseline total pressure recovery defined as a constraint (lower limit) to ensure pressure loss would not be increased. The optimised configuration improved distortion by 79% and also yielded improvements at a number of off-design conditions. Total pressure recovery also improved as is evident from the contours presented in Figure 2.11.

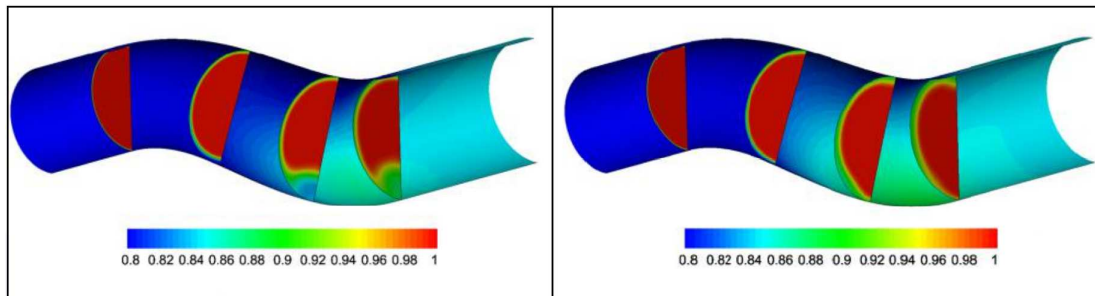


Figure 2.11: Normalised total pressure recovery contours for convoluted duct without (left) and with (right) vortex generator array. Figure taken from [48].

## Geometry optimisation

Zhang et al. [49] conducted an optimisation study using an SQP algorithm with two design parameters and distortion at the AIP as the objective function. The two design parameters were controlling the height and width of a perturbation introduced just ahead of the onset of flow separation. The perturbation in the duct geometry introduces a separated flow region, reducing the cross-flow, and resulting in a reduction of distortion of 63% at the AIP. The pressure recovery remained unchanged as the separation in the bump behaved like a closed bubble and was confined to that region [49]. The final geometry presented in the research is shown in Figure 2.12.

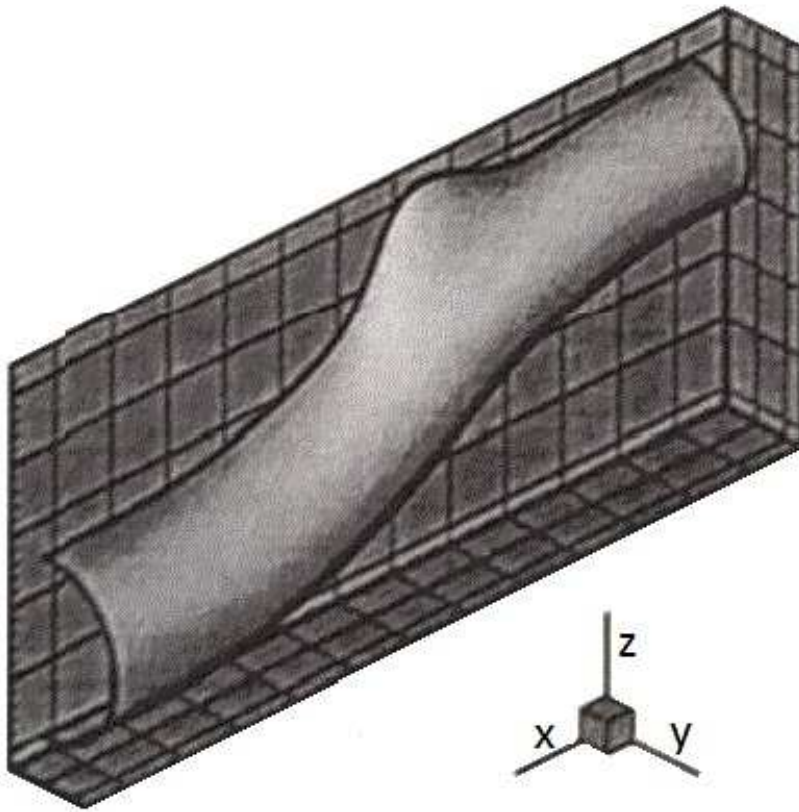


Figure 2.12: S-shaped duct with bump in geometry. Figure taken from [49].

In a similar study, the Wellborn s-duct was used for an optimisation study of a bump with two design parameters (height and stream-wise width of bump) and one objective function (minimising distortion), using a gradient based feasible SQP optimiser [50]. Reducing the distortion by 37%, the optimised design has an increased bump ahead of the separation region similar to the one presented in reference [49]. This leads to an area increase and a reduction of secondary flow as reported by Lefantzi and Knight [50]. This is consistent with other optimisation studies that base the performance criteria on RANS simulations.

However, as noted previously, RANS simulations are not suitable to capture the full dynamics of the complex flow field in diffusing, s-shaped ducts. By inspection of the optimised duct

geometries in [49] and [50], it is highly likely that the benefits would be outweighed by the expected unsteady distortion such designs would naturally promote. Moreover, unless embedded in the fuselage, the external aerodynamics over such geometries would be highly susceptible to separation and increased drag, making such design solutions not acceptable from an applications perspective.

Geometry optimisation based on a multi-objective genetic algorithm (MOGA) was used by Aranake et al. on an s-duct ( $Ma = 0.3$ ) including two design objectives: maximisation of total pressure recovery and minimisation of distortion [51]. The optimisation was only partly successful, as the total pressure recovery of the optimised designs was of the same order of magnitude as for the baseline case. However, the distortion coefficient was significantly reduced by 56% and 50%, according to numerical and experimental data, respectively. The lowest distortion was achieved for the largest area ratio at mid span leading to the following design suggestion: "The flow in the approximate midpoint of the bends should be over-expanded, i.e. the cross-sectional area should be greater than the outlet cross-sectional area." [51]. Due to the over-expansion, the BL separates earlier, generating more mixing of the flow, which, together with the favorable pressure gradient resulting from the contraction, leads to a smaller distortion coefficient at the duct outlet [51].

A combined low and high fidelity optimisation was conducted by Ghate et al. [52]. The low fidelity study used a SQP algorithm optimising pressure recovery, while the high fidelity optimisation minimised distortion through a DoE and RSM search. The low fidelity optimisation produced designs with area expansion over the first one third of the duct's length, with constant area thereafter and a 1.5% increase in pressure recovery. The high fidelity optimisation reduced the distortion coefficient from 6.19 to 1.7, with a much more uniform pressure distribution at the exit plane.

It is important to note that all of the research studies presented in this section are based on steady-state RANS simulations. While it has been established that the time-dependant flow field properties are important in convoluted ducts, unsteady simulations still seem to be too computationally expensive to be employed in optimisation studies due to the high number of CFD runs required. However, with computational resources becoming more readily available, optimisation studies should not only include the uniformity of the flow at the AIP but also the unsteadiness. As a compromise, to minimise the computational expense of the simulations, at least the optimised geometries should be analysed with unsteady CFD.

Table 2.2 gives a summary of all optimisation studies reported in this section in a similar fashion to Table 2.1. The percentage values given indicate the change of a certain parameter with respect to the datum as reported in the publications.

Table 2.2: Summary of optimisation techniques employed on s-ducts

flow control	flow regime	separation	distortion	PR	pressure loss	swirl	E/N	publication
microvane VG	Ma=0.6	↑	↑ 50%	↑ 5%	↑	/	E&N	[45]
microjet VG	Ma=0.6	↑	↑ 20%	↑ 2.5%	↑	/	E&N	[45]
VG and location	Ma=0.6	/	↑ 87.5%	↑ 0.66%	/	/	N	[46]
VG	Ma=0.27	/	↑ 79%	---	/	/	N	[48]
bump in geometry	Re=2.6x10 <sup>6</sup> , Ma=0.6	/	↑ 63%	---	/	↑	N	[49]
geometry	Ma=0.3	/	↑ 56%	---	/	/	E&N	[51]
cross-sectional area	Ma=0.52	/	↑ 72.5%	↑ 1.5%	/	/	N	[52]
bump in geometry	Re=2.6x10 <sup>6</sup> , Ma=0.6	/	↑ 37%	---	/	↑	N	[50]

Symbols indicate: ↑ = improvement by flow control technique; / = not reported; ↓ = deterioration by flow control technique; - - - = no effect.

## 2.4 Active flow control

One of the earliest studies to employ active flow control in s-ducts was conducted by Ball in 1985 [61], using wall suction and blowing at a Mach number of 0.7. Pressure measurements suggest that separation was eliminated and effective boundary layer control achieved, using a slot blowing a mass flow equal to 2% of the inlet flow. Automatic adjustable blades (AABs) were used as a swirl control mechanism by Weng and Guo in 1991 [62]. This method reduced the bulk swirl to the point of elimination at 7.5 degree AAB angle in a rectangular-to-square cross-section s-duct, without changing the pressure distribution along the walls. However, AABs also resulted in a slightly higher pressure loss in the core flow [62].

Synthetic jets (blowing velocity =  $11 \text{ ms}^{-1}$ , frequency = 1032 Hz) were employed in an s-duct by Amitay, with results suggesting complete flow reattachment and higher pressure at the AIP for  $\text{Ma} < 0.2$  and faster flow reattachment for  $0.2 < \text{Ma} < 0.3$  [63]. In another study, synthetic jets were also found to suppress flow separation and decrease pressure distortion in an s-duct at a Mach number of 0.43 [7]. Figure 2.13 shows the three actuation cases tested. The results show that 3D actuation in the middle of the duct, i.e. Figure 2.13c, is more effective than the 3D actuation along the sides of the duct (Figure 2.13d), or the 2D actuation (Figure 2.13b) along the whole span. The cross-flow velocity presented in Figure 2.14 is lowest for the 3D actuation case with synthetic jets applied in the middle of the duct closely followed by the 2D actuation. It is worth pointing out that the 3D actuation along the sides of the duct (Figure 2.13d) does not reduce the cross-flow velocities which stay at the same level as for the bare duct.

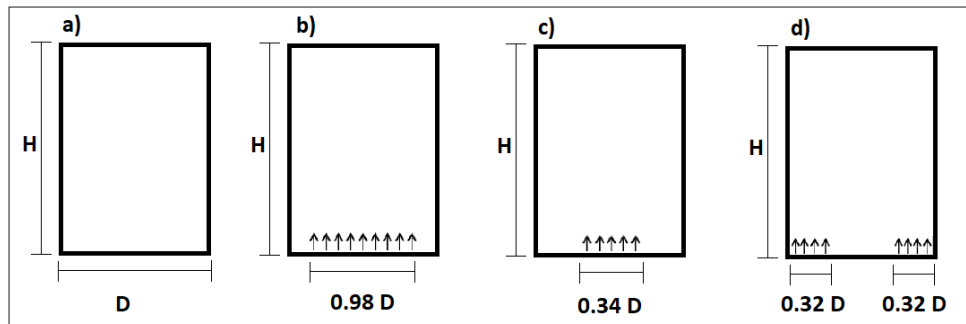


Figure 2.13: Sketch of synthetic jet actuation positions: (a) no control, (b) up, (c) up-mid, and (d) up-side [7].

Luers [30] investigated wall jet injection (as a percentage of inlet mass flow) at the separation point and upstream of this, in an s-duct ( $\text{Ma} = 0.5\text{-}0.7$ ), for different inlet mass flow conditions. Pulsed actuation proved to be the most effective with a frequency equal to the shedding frequency of vortices in the undisturbed flow. Increased values of pressure recovery and lower distortion were measured [30]. Figures 2.15 and 2.16 show the pressure recovery, and improvement in pressure recovery, for a number of jet injection mass flows and two inlet mass flow conditions, respectively. It is clear that the beneficial effect of the wall jet on the pressure

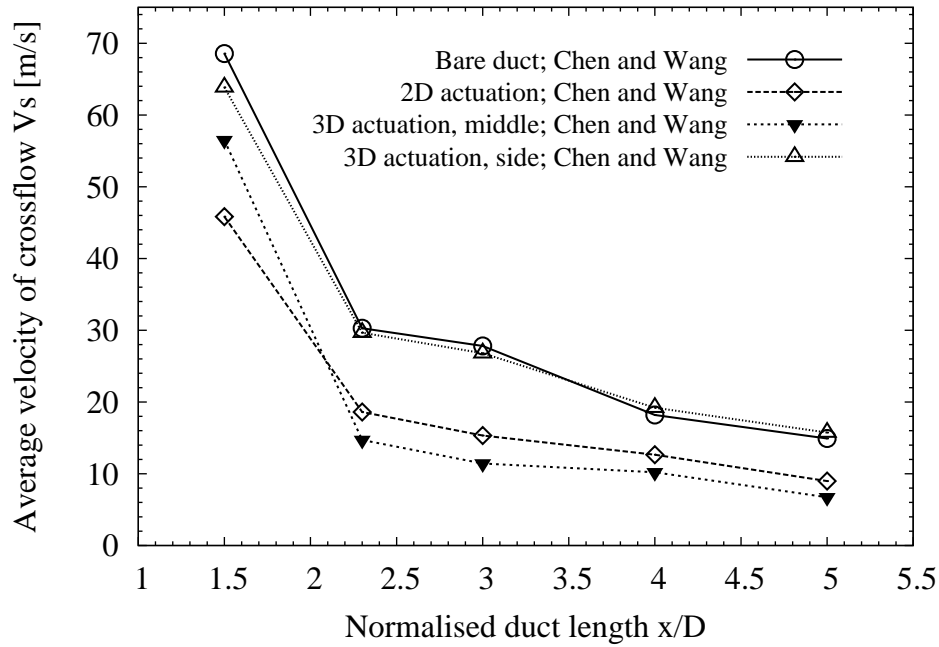


Figure 2.14: Average secondary (cross-flow) velocity [ $\text{ms}^{-1}$ ] vs nondimensionalised duct length for control cases a, b, c, and d as in Figure 2.13. Data replotted from [7].

recovery increases initially with percentage injection mass flow, but saturates for 3-4% of the inlet mass flow.

VG jets in circular and rectangular-to-circular cross-section s-ducts ( $\text{Ma} = 0.1$ ,  $\text{Re} = 7.8 \times 10^5$ ) were used with a fixed pitch angle of 45 degrees and a range of skew angle [64]. A skew angle of 135 degrees resulted in the best performance. Jet-to-freestream-velocity ratios of 1.6 and 1.7 in the two circular and rectangular-to-circular ducts respectively give the best pressure recovery values. For the circular s-duct, Pradeep and Sullerey record a 20% reduction in total pressure loss and a 30% reduction of turbulence intensities at the AIP [64]. Tangential blowing (14 tubes, blowing velocity 12.5 to 24.5  $\text{ms}^{-1}$ ) and VG jets with the same momentum coefficient as the tangential blowing, were investigated by Ng et al. [39] in a constant area s-duct ( $R = 4.73 \times 10^4$ ) and were placed on the near-side wall. They suppressed flow separation successfully, but also lead to an increased swirl in the flow at the AIP. As stated by Vaccaro et al. [65], a 2D control jet actuator in an s-duct ( $\text{Ma} = 0.43$ ) can affect centreline reattachment, but cannot influence the formation of secondary flows, and does not reduce pressure losses at off-centreline locations of the AIP. Vaccaro et al. suspect that the two-dimensional jet does not influence the three-dimensional flow features enough to have a significant effect on the performance parameters of the flow.

Another study by the same researcher, using 2D steady blowing through a continuous slit spanning 90% of the duct along the lower surface of an s-duct with a similar Mach number ( $\text{Re} = 0.75 \times 10^6$ ,  $\text{Ma} = 0.44$ ), managed to reattach the flow along the centreline, decreasing the flow speed and improving the flow at the AIP. Pressure recovery increased by 1.7%, there was a 13.3%

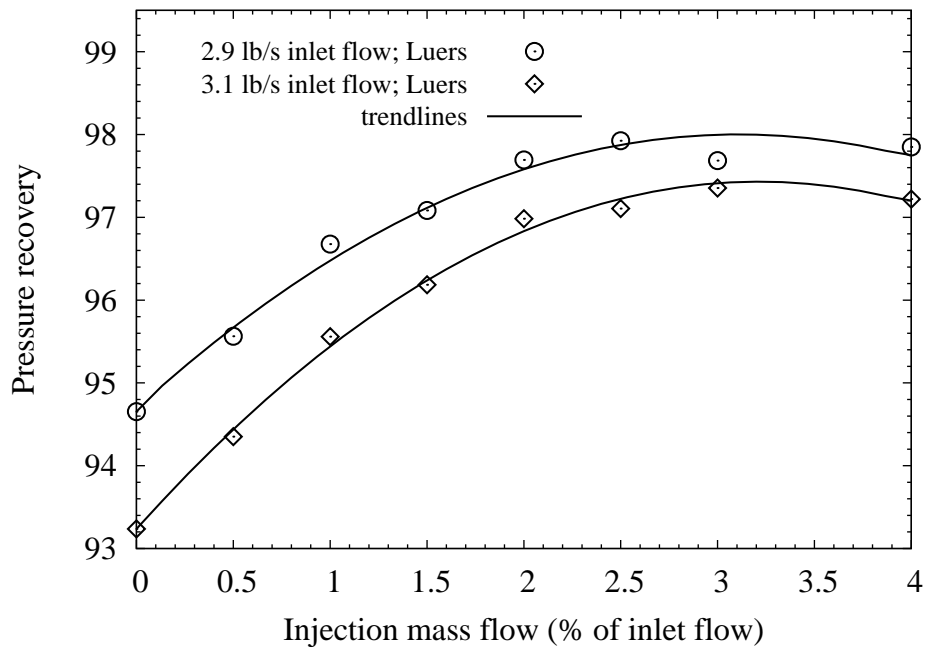


Figure 2.15: Pressure recovery at AIP vs injection mass flow as % of inlet flow. Data replotted from [30].

reduction of standard deviation in the pressure signal, and elimination of the dominant frequency of Strouhal number ( $St$ ) of 0.26 [6]. The study also shows that unsteady forcing, at frequencies of  $St$  of 0.26, 0.59, and 0.88, did not have the same beneficial effect as steady actuation. Supersonic pulsed jets (7 jets per half configuration) in an s-duct ( $Re = 1.5 \times 10^6$ ) resulted in fully reattached flow in a study by Garnier et al. [66], with jets of  $Ma$  1.4 out-performing jets with  $Ma$  2. Garnier et al. recommend the use of higher pulsed actuation frequencies than those present in the flow at the separation region.

In a further study, actuation with pulsed jets (14 actuators, 0 to 1000 Hz) in an s-duct ( $Re_{max} = 1.5 \times 10^6$ ,  $Ma = 0.2 - 0.4$ ) show that the efficiency of actuators decreases with increasing Mach number [67]. Nonetheless, a 1% gain in efficiency was achieved for the Mach 0.4 case. A zero-net-mass-flow jet was created with a 4.5mm displacement of the oscillating piston and a frequency of 28.8 Hz. This is a momentum influx device that does not add more mass to the flow. Mathis et al. [68] employed this technique in an s-duct ( $Re = 4.1 \times 10^4$ ) for a low Reynolds number flow eliminating the separation region completely. However, drawbacks of this technique include added complexity through moving parts and weight addition.

Electrohydrodynamic (EHD) glow discharge plasma (no additional mass flow or moving parts) was used in an s-duct ( $Ma=0.3$  to 0.7) by Hui et al. in a numerical study, resulting in a maximum improvement of 6.7% for pressure distortion and 0.34% for pressure recovery [5]. Another study that demonstrated the suitability of plasma for internal flow control was conducted by Xu [69]. The author successfully used ac-DBD plasma actuation (dielectric barrier discharge plasma powered with an alternating current wave form) in an s-duct to reduce the

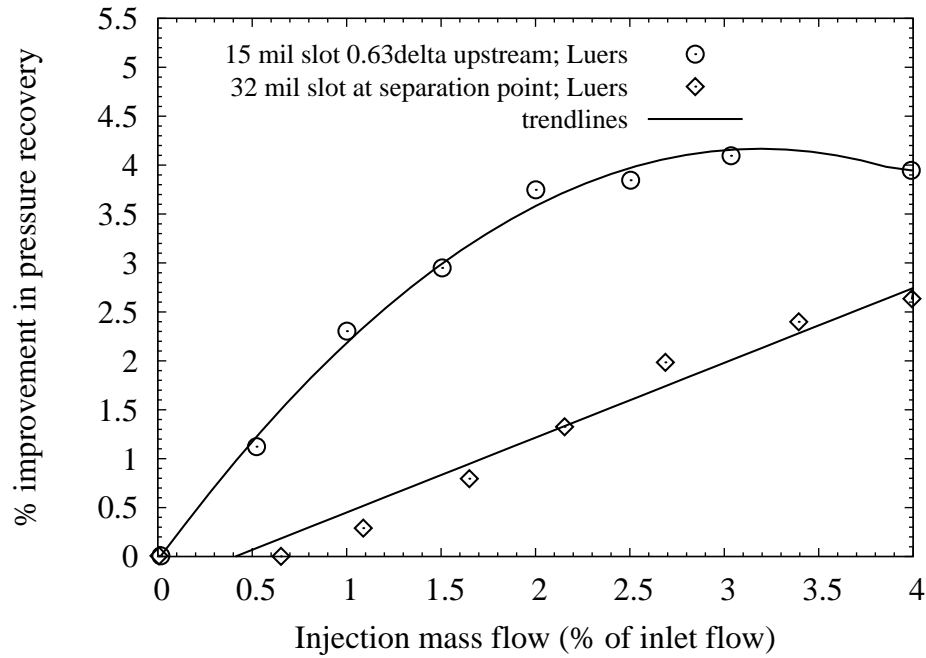


Figure 2.16: Improvement of pressure recovery at AIP in % vs injection mass flow as % of inlet flow. Data replotted from [30].

extent of the separation region. The optimal location for actuators was found to be near the separation point for both continuous and pulsed actuation. As expected, separation reduction increases with increasing actuator strength [69]. Ac-DBD plasma, however, is self-limiting, with the highest recorded values of induced flow being of the magnitude of  $10 \text{ ms}^{-1}$  [70], which is not fast enough to influence the flow structure in s-shaped ducts and prevent separation at high subsonic flow speeds.

A different form of plasma generation, referred to as ns-DBD plasma (dielectric barrier discharge plasma powered with a nano-second pulse wave form) does not exhibit this self-limiting behaviour [71]. No publications of ns-DBD plasma actuation in s-shaped ducts were found during the literature review. However, its applicability to flow control in general has been demonstrated in a number of studies on aerofoils [71–73].

Finally, a study comparing passive to active flow control in the same s-duct was performed by Delot and Garnier [38] from the Onera Group in France. In their work, an array of VG vanes and micro-jet actuators ( $10\text{--}120 \text{ ms}^{-1}$ , 14 continuous or pulsed jets) were used on the lower part of an s-duct ( $\text{Re} = 1.5 \times 10^6$ ) showing that VGs (50% or more improvement for  $0.15 < \text{Ma} < 0.45$  at AIP) are more effective in reducing flow distortion than continuous jets (30% improvement, for  $\text{Ma} 0.2$  at AIP) or pulsed jets (50% improvement, for  $\text{Ma} 0.2$  at AIP) and yield better results for a wider range of Mach numbers [38].

Table 2.3 gives a summary of active flow control techniques discussed in this section. The percentage values given indicate the change of a certain parameter with respect to the baseline value as reported in the publications.

Table 2.3: Summary of active flow control techniques employed on s-ducts

flow control	flow regime	separation	distortion	PR	pressure loss	swirl	E/N	publication
wall suction & blowing	Ma=0.7	↑	↑	↑	/	/	E	[61]
automatic adjustable blade	/	/	/	/	↓	↑	E	[62]
synthetic jets	Ma=0.3	↑	/	/	↑	/	E	[63]
3D synthetic jet	Ma=0.43	↑	↑	↑	↑	↑	N	[7]
2D synthetic jets	Ma=0.43	↑	↑	/	/	↑	N	[7]
VG jets	Ma=0.1, Re=7.8x10 <sup>5</sup>	↑	↑ 25%	↑	↑ 30%	/	E	[64]
tang. blowing (const. area)	Re=4.73x10 <sup>4</sup>	↑	/	/	↑	↓	E	[39]
VG jets (const. area)	Re=4.73x10 <sup>4</sup>	↑	/	/	↑	↓	E	[39]
3D control jet	Ma=0.43	↑	↑	↑	/	/	E	[65]
2D control jet	Ma=0.43	↑	↑	---	/	/	E	[65]
2D steady blowing	Ma=0.44, Re=7.5x10 <sup>5</sup>	↑	↑ 13.3%	↑ 1.7%	/	/	E&N	[6]
supersonic pulsed jets	Re=1.5x10 <sup>6</sup>	↑	↑	↑	/	/	E	[66]
zero-net-mass-flow jet	Re=4.1x10 <sup>4</sup>	↑	/	/	/	/	E	[68]
Electro-hydrodynamic EHD	Ma=0.3-0.7	↑	↑ 6.7%	↑ 0.34%	/	/	N	[5]
AC-DBD plasma	/	↑	/	/	/	/	E&N	[69]
pulsed micro jet	Re=1.5x10 <sup>6</sup>	↑	↑ 50%	---	/	/	E	[38]
continuous micro jet	Re=1.5x10 <sup>6</sup>	↑	↑ 30%	---	/	/	E	[38]

Symbols indicate: ↑ = improvement by flow control technique; / = not reported; ↓ = deterioration by flow control technique; - - - = no effect.

## 2.5 Hybrid flow control

A few researchers have combined passive and active flow control techniques in an attempt to control both the steady and time-dependant flow properties in s-shaped intake ducts. This combination of active and passive flow control methods is called a hybrid system.

Gissen et al. [41, 74] proved that hybrid systems can have an additional benefit on performance parameters, compared to passive or active flow control alone. In [41], the authors employ vane-type VG and synthetic jets at a Mach number of 0.55 in an s-duct with no flow separation in the baseline case. Vane-type VG and synthetic jets both improve the performance parameters when used alone, and decrease the circumferential distortion descriptor by 20% each. The combination of both in the hybrid system has a more profound effect, reducing the distortion by as much as 35%. This is shown in Figure 2.18. Total pressure contours at the AIP, presented in Figure 2.17, also demonstrate the combined effect of passive and active flow control. However, as the authors note in their work, caution has to be exercised as some hybrid configurations had a detrimental effect on the performance of the duct.

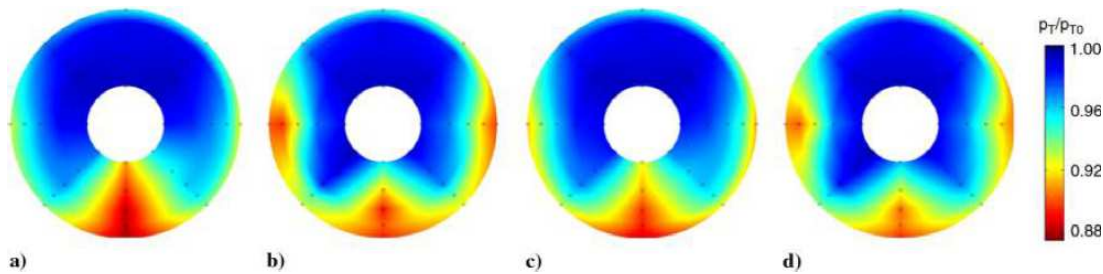


Figure 2.17: Time averaged total pressure contours at AIP for a) baseline s-duct, b) vane type VG, c) synthetic jets, and d) hybrid flow control. Figure taken from [41].

A second publication [74] explains the dynamics of the hybrid flow control model. As expected, the vane-type VG only have a steady effect, but the synthetic jets, operated at 133 Hz, have a cyclic contribution. Initially, at the beginning of the duty cycle, the synthetic jets cause an increase of distortion followed by a stark decrease. Being a viability study, Gissen et al. [74] have not optimised the jet operation for frequency which may result in improving the initial response at the onset of the active flow control.

Owens et al. also investigated the suitability of hybrid flow control [75]. Their design of vane-type VG and air jets achieved an additional benefit, too. The same decrease of circumferential distortion coefficient at the AIP was recorded for lower air jet mass flows with the hybrid system. This suggests that passive-active hybrid flow control can be a means of making the active part more efficient, by having the passive flow control device improve the steady performance and the active one the time-dependant performance.

Further research is necessary to show that hybrid systems can eliminate flow separation, as existing studies only quantified the improvement in circumferential distortion at the AIP.

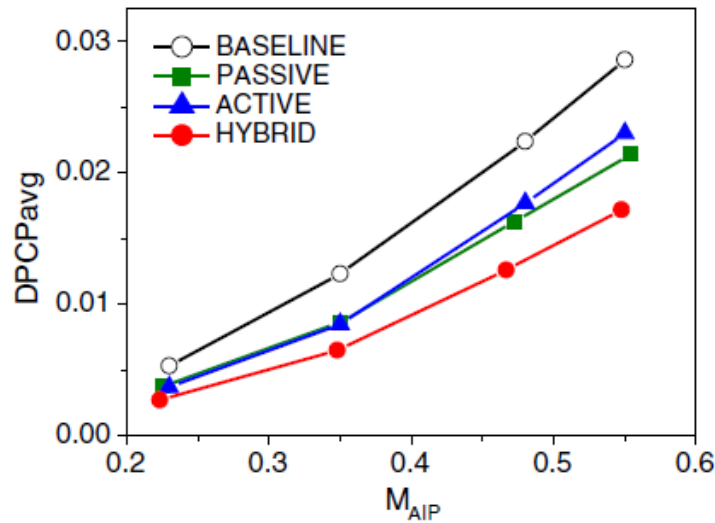


Figure 2.18: Society of Automotive Engineers circumferential distortion descriptor (DPCP) with Mach number for baseline flow, passive (vane type VG), active (synthetic jets), and hybrid flow control. Figure taken from [41].

## 2.6 Conclusions

Passive flow control devices have been heavily studied by a number of researchers and show promising results improving, by large, the performance parameters. From the passive flow control devices reviewed, tapered fin vortex generators and submerged vortex generators improved pressure loss and distortion by double digit percentages. It is widely agreed that the optimum location for vortex generators is upstream of the separation point just ahead of the high adverse pressure gradient. At this location the boundary layer grows rapidly before detaching from the surface and separating. Most early active flow control devices were derived from their passive counterparts (i.e. VG jets) and employed in both continuous and pulsed mode. Three-dimensional synthetic jets and pulsed micro-jets show the greatest promise amongst active flow control devices. While the biggest improvements in flow parameters at first appear to be achieved with optimisation techniques - decreasing distortion values of pressure by as much as 80% - there is doubt over the accuracy of reported benefits because transient features have not been accounted for.

Given the recent findings on the unsteadiness of the flow in convoluted ducts and the significant variation to flow parameters as compared to time-averaged data, it is believed that the effect of flow control techniques should also be obtained with unsteady measurements - both experimentally and numerically.

Only limited work with ac-DBD plasma actuators and none with ns-DBD plasma actuators in s-shaped ducts was found in the public domain. Plasma actuators have not previously been used as a transient, active flow control technique for internal flows in convoluted ducts.



# Chapter 3

## Wellborn s-duct baseline CFD simulations

Extensive steady state analysis of the flow through convoluted ducts was conducted both numerically and experimentally by a number of researchers [1,12,28,76–79]. Those efforts established the non-uniformity of the flow at the AIP and the existence of the double, counter-rotating vortex pattern forming downstream of the separation region. More recent work has focused on the unsteadiness, highlighting new aspects of the flow through an s-duct. Transient fluid flow simulations through convoluted ducts were performed, among others, by Berens [24]. Their study showed that time dependent flow statistics and unsteadiness of flow properties varied greatly between steady state and transient Detached Eddy Simulation (DES) computations. Delot [80] notes that unsteady Reynolds Averaged Navier-Stokes (URANS) solutions did not capture the dynamic behavior of the s-duct throughflow accurately.

This is expected as the nature of URANS simulations implies an averaging process that does not allow for large deviations from the mean flow properties. RANS and URANS simulations are based on statistical averaging where the effect of turbulence is simulated through modelling of the Reynolds stresses. In eddie-resolved numerical approaches, however, the turbulence is resolved up to a certain length scale. Only very small length eddies are averaged with a sub-grid scale model.

Other studies [13,29] look at swirl, investigating the flow through an s-duct at Mach numbers in the range 0.27 to 0.6. Results show that the instantaneous flow features are considerably different from the time-averaged properties. The difference in peak values of swirl distortion, for instance, can be one order of magnitude higher. Based on the analysis of stereoscopic particle image velocimetry (sPIV) data and Delayed Detached Eddy Simulation (DDES), dominant modes of flow structures are identified in a follow-up study by Gil-Prieto [31] for a Reynolds number of  $7.1 \times 10^5$  and an inlet Mach number of 0.27. The results clearly show a switching as well as a vertical mode. This has been earlier documented in [81] and [82] for pipes with bends. In the switching mode, the vortices observed in the mean flow alternate in strength with either one dominating the flow pattern at the AIP - perturbing the circumferential flow field.

In this chapter, in order to better understand the transient effects of the flow and how best to

model it numerically, the Wellborn convoluted duct case was used and studied with unsteadiness resolved. DDES and URANS formulations in the open source computational fluid dynamics (CFD) toolbox OpenFOAM are presented. Steady flow properties and transient results are compared to existing experimental data for validation of the OpenFOAM CFD results in the first part of this chapter. Next, the transient nature of the flow is characterised through modal decomposition techniques and the frequency spectrum of flow properties at the AIP. While Proper Orthogonal Decomposition (POD) was previously used in analysing flow snapshots of convoluted duct throughflows [16, 29, 83], dynamic mode decomposition (DMD) is employed in such flows for the first time. Moreover, maps of dominant frequencies of flow properties at the AIP are presented and discussed for the first time.

Phase information and frequency domain analysis is often key to a successful flow control strategy. As reported in literature, active flow control often has the biggest effect when it is influencing frequencies found in the baseline flow. A number of researchers, [84, 85], proposed coupling the actuation frequency to global instabilities in the flow field. With this line of thought, it is argued that actuation is most effective when its period scales with the advection time over the length of the flow domain downstream of separation.

The test case is run at a realistic cruise condition with a Reynolds number of  $2.6 \times 10^6$  and a Mach number at the inlet of 0.6.

### 3.1 Performance criteria

Traditional and more novel performance criteria are applied to characterise the flow field in detail. The two main traditional criteria for evaluating the performance are static and total pressure recovery, and the pressure distortion coefficient. Those parameters were introduced in the literature review in Chapter 2. Less common methods of analysing convoluted duct throughflows are presented next.

The proper orthogonal decomposition snapshot method by Sirovich [86] is employed to extract dominant modes from the data using second order flow statistics of flow properties,

$$V_i = \sum_{j=0}^i a_j(t) \phi_j(y, z), \quad (3.1)$$

where  $\phi_j$  is the nondimensionalised POD modal distribution set of orthonormal bases, and  $a_j$  are the POD temporal coefficients associated with each mode. The POD representation of the velocity field can be obtained as the linear sum of a finite number  $i$  of modal contributions [86, 87].

Phase information of dominant modes is given by the dynamic mode decomposition as proposed by Schmid [88, 89]. This formulation allows for the evaluation of phase information and varies from a POD analysis such that it does not produce orthogonal modes. The DMD algo-

rithm as proposed by Tu [90] is used. A set of flow field snapshots,  $V_i$ , separated by a constant timestep is arranged as follows:

$$V_1^i = v_1, v_2, v_3, \dots, v_n. \quad (3.2)$$

A linear mapping matrix is then constructed that maps  $V_i$  onto  $V_{i+1}$ :

$$V_{i+1} = AV_i. \quad (3.3)$$

This is used to formulate the following problem which is solved for the matrix  $S$  by minimising  $r$ :

$$AV_1^{n-1} = V_2^n = V_1^{n-1}S + re_{n-1}^T. \quad (3.4)$$

The eigenvectors and eigenvalues of  $S$  give the dynamic modes of flow properties and their temporal behaviour.

Moreover, fast fourier transforms (FFT) are used to show the frequency spectrum of the time series of data at the AIP.

## 3.2 Simulation set-up

Compressible flow solvers in OpenFOAM are used for both steady and transient simulations given the flow is subsonic with an inlet Mach number of 0.6. For transient simulations a timestep of  $1\mu\text{s}$  was used resulting in a maximum Courant number of 0.24 in the domain with a mean value of 0.06. Simulations were conducted for 24 convective timescales. One convective timescale is defined by the ratio of the s-duct length and the inlet centreline velocity. Gil-Prieto [16] showed that there is only 1% difference of averaged flow properties between 20 and 50 convective timescales. Due to the volume of data generated, flow solutions were saved every  $500\mu\text{s}$  of physical time. For faster run times transient simulations were initialised from a converged RANS calculation. To account for the transitional flow the first 20 snapshots were discarded. The ARCHIE-WeST high performance computing machine in Glasgow was used to run the simulations in parallel on 40 cores. ARCHIE-WeST uses Intel Xeon Gold 6138 20 core 2.0 GHz CPU chips.

Compressible flow solvers are used for both steady and transient simulations given the flow is subsonic with an inlet Mach number of 0.6. For transient simulations a timestep of  $1\mu\text{s}$  was used resulting in a maximum Courant number of 0.24 in the domain with a mean value of 0.06.

The Navier-Stokes Fourier equations are solved in OpenFOAM. Those equations are presented next through the mass, momentum, and total energy conservation equations:

$$\frac{\partial \rho}{\partial t} + \nabla \cdot (\rho \vec{U}) = 0 \quad (3.5)$$

$$\frac{\partial(\rho \vec{U})}{\partial t} + \nabla \cdot (\rho \vec{U} \times \vec{U}) + \nabla P + \nabla \vec{\tau} - \rho \vec{g} = 0 \quad (3.6)$$

$$\frac{\partial(\rho E)}{\partial t} + \nabla \cdot (\rho \vec{U} (e + \frac{\rho |\vec{U}|^2}{2})) + \nabla \cdot (\vec{q}) - \rho (\vec{U} \cdot \vec{g}) + \nabla \cdot (P \vec{U}) + \nabla \cdot (\vec{\tau} \cdot \vec{U}) = 0 \quad (3.7)$$

where  $\rho$  is the density;  $\vec{U}$ ,  $\vec{q}$ , and  $P$  denote the velocity field, the heat flux vector, and the total pressure, respectively. The gravity is denoted by  $\vec{g}$ . The total energy  $\rho E = \rho e + \frac{\rho |\vec{U}|^2}{2}$  with  $e$  being the internal energy. Finally,  $\vec{\tau}$  represents the shear rate tensor.

### 3.2.1 Geometry

The Wellborn s-duct [1] design is used for this study as there are detailed experimental results available in the public domain. The test case was first designed in the NASA Glenn Research Centre and more recently also used by the research group at Cranfield University [13, 16, 19, 29, 83, 91]. The geometry, schematically shown in Figure 3.1, was created using the parametric equations for radius and duct centreline given in Wellborn's initial work and repeated here for clarity. The duct centreline comprises of two circular arc sections of  $\frac{\theta_{max}}{2} = 30^\circ$ . That is, the arc sector from the inlet to the inflection point and from the inflection point to the exit each have an angle of  $30^\circ$ .

The duct has a diffusivity ratio of 1.52 based on the inlet and outlet areas, inlet and outlet diameters of  $D1 = 0.2042$  m and  $D2 = 0.2514$  m, respectively, and a total vertical centreline offset  $H$  equal to  $0.2757$  m. Consistent with Wellborn's experimental set-up, pipes with constant diameter of length  $0.762$  m are added to the front and aft of the convoluted duct. The total s-duct length is made of two equal parts,  $L1 + L2$ , and is  $1.021$  m. This length does not include the duct sections added to the aft and front parts. Figure 3.2 shows the full numerical domain used for CFD simulations in this chapter.

The centreline coordinates of the s-duct are defined as:

$$x_{cl} = 1.021 \sin(\theta), \quad (3.8)$$

$$y_{cl} = 1.021 \cos(\theta) - 1.021, \quad (3.9)$$

$$z_{cl} = 0, \quad (3.10)$$

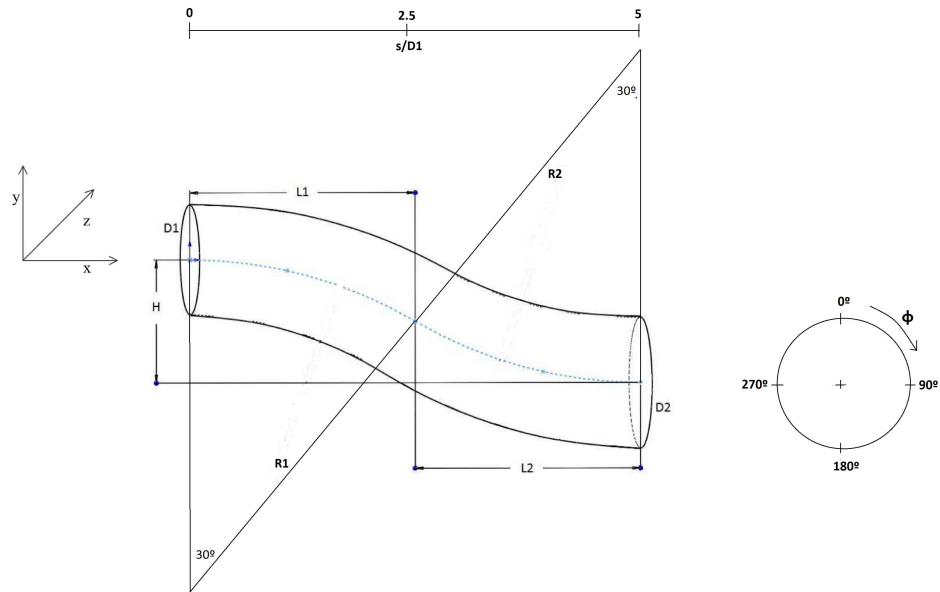


Figure 3.1: S-shaped duct. Geometry taken from Wellborn [1]. Symbols denote:  $H$  = vertical offset;  $D1$  = inlet diameter,  $D2$  = outlet diameter;  $L1$  = horizontal distance to inflection point from inlet;  $L2$  = horizontal distance to outlet from inflection point;  $R1$  = radius of first arc;  $R2$  = radius of second arc. Figure taken from [8].

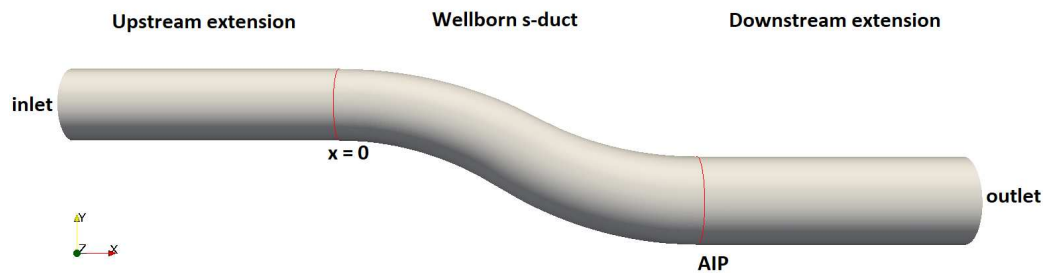


Figure 3.2: Representation of full numerical domain used for CFD simulations.

for  $0 \leq \theta \leq 30^\circ$ .

And:

$$x_{cl} = 2.042 \sin\left(\frac{\theta_{max}}{2}\right) - 1.021 \sin(\theta_{max} - \theta), \quad (3.11)$$

$$y_{cl} = 2.042 \cos\left(\frac{\theta_{max}}{2}\right) - 1.021 \cos(\theta_{max} - \theta) - 1.021, \quad (3.12)$$

$$z_{cl} = 0, \quad (3.13)$$

for  $30^\circ \leq \theta \leq 60^\circ$ .

The variation of the radius,  $r$ , along the duct centreline is given by the following equation:

$$\frac{r}{r_{inlet}} = 1 + 3\left(\frac{r_{outlet}}{r_{inlet}} - 1\right)\left(\frac{\theta}{\theta_{max}}\right)^2 - 2\left(\frac{r_{outlet}}{r_{inlet}} - 1\right)\left(\frac{\theta}{\theta_{max}}\right)^3, \quad (3.14)$$

where  $r_{inlet} = 0.1021m$  and  $r_{outlet} = 0.1257m$ .

It is important to note that the variation of radius along the centreline of the duct is not uniform. The radius varies by design more rapidly closer to the inflection point where the two  $\frac{\theta_{max}}{2}$  arc sectors meet, thus creating a non-uniform diffusion ratio inside the duct.

### 3.2.2 Computational grid

The computational mesh is a multiple block, structured, high quality grid. It was generated with the OpenFOAM blockMesh tool utilising spline curves for a smooth curvature definition of the geometry. Prism layers are used to resolve the near wall flow region. Important quality parameters were checked with a maximum skewness of 2.93, cell aspect ratios well below 1000, and a mean non-orthogonality level of 12 degrees. Additionally, a grid independence study was conducted to find a suitable mesh refinement. Figure 3.3 shows the results of a grid independence study conducted on different meshes with RANS simulations. The total pressure recovery was chosen as the figure of merit. The grid independence study is presented with average  $Y+$  values and total cell size of the mesh. Results clearly show an increasing level of mesh independence with finer computational grids. The  $Y+$  values in the computational domain are calculated based on equations 3.15 to 3.16:

$$Y_+ = \frac{yu_\tau}{\nu}, \quad (3.15)$$

where  $y$  is the distance to the nearest wall,  $u_\tau$  is the friction velocity at the nearest wall, and  $\nu$  is the local kinematic viscosity of the fluid.

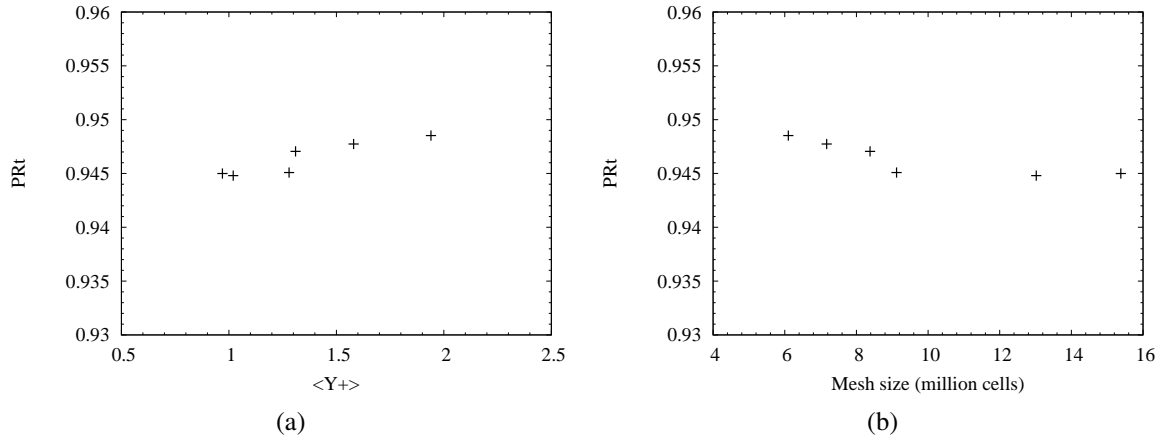


Figure 3.3: RANS simulations mesh convergence study with total pressure recovery: (3.3a) with average  $Y+$  value of mesh; (3.3b) with total cell size of mesh.

$$u_{\tau} = \left( \frac{\tau_{\omega}}{\rho} \right)^{\frac{1}{2}}, \quad (3.16)$$

where  $\tau_{\omega}$  is the wall shear stress, and  $\rho$  is the fluid density at the wall.

The final, total mesh size has  $15.4 \times 10^6$  cells. The final mesh is presented in Figure 3.4 cut along the symmetry plane of the geometry.  $Y+$  values at the viscous walls of the computational domain are presented in Figure 3.5a along with the convergence history of steady state RANS calculations in Figure 3.5b. The average  $Y+$  value at the walls for the whole domain is 0.97. The local differences in  $Y+$  values are due to a varying velocity field. This can be seen particularly well for the  $Y+$  values in the circumferential direction at a fixed streamwise location. For the RANS calculations a residual drop of 12 orders of magnitude was achieved. The spikes in the convergence history are due to restarts of the case on the high performance computer which has a limited job run time of two weeks. Spikes occur due to the write precision of 8 digits which is less than the internal 16 figures in memory. Upon restarting the simulation, there is a relatively large difference when it switches back to 16 figures. However, as is evident from the Figure the convergence recovers its previous level quickly.

### 3.2.3 CFD code

The open source CFD tool box OpenFOAM [92] is used for this study, with all presented data computed with OpenFOAM v1712 (OpenFOAM.com).

For the RANS, URANS, and DDES calculations the  $k-\omega$  SST turbulence model, as first proposed by Menter [93] is used. This model improves on the freestream sensitivity of the initial  $k-\omega$  model. Fiola [94] showed that for the Wellborn test case the  $k-\omega$  SST turbulence model matched experimental results better than the Spalart-Allmaras or the  $k-\varepsilon$  models. The

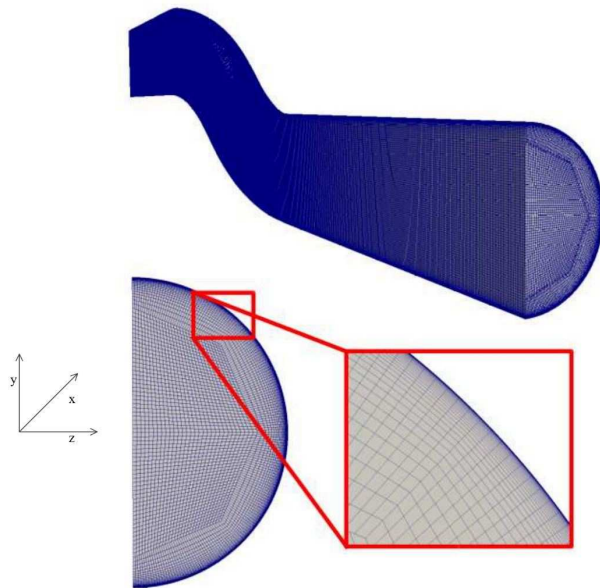


Figure 3.4: Computational mesh: structured, multi block grid cut along the symmetry plane of the geometry with a close up view of the prism layers near the wall.

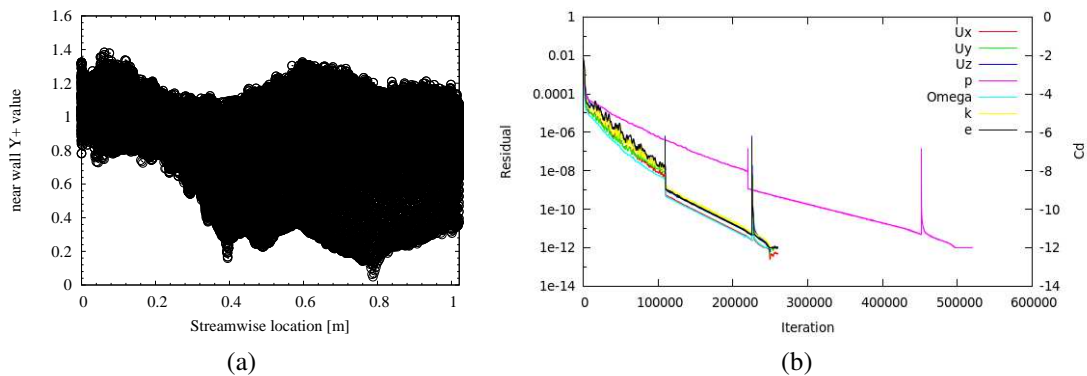


Figure 3.5: Wall  $Y^+$  values in computational domain for final mesh (3.5a) with corresponding convergence history for steady state RANS simulation with two iterations for pressure correction (3.5b) in OpenFOAM.

delayed DES formulation is chosen instead of DES so that mesh induced separation problems do not occur in the region where RANS is applied [95–97].

For the DDES formulation, the model put forward by Gritskevich [98] is used. This DDES model had its model coefficients tuned for the  $k$ - $\omega$  SST turbulence model and builds on prior work completed by Spalart [95] for the SA turbulence model. To prevent grid induced separation (GIS) the near wall boundary layer RANS model is shielded from switching to the DES model through the SST blending function. This shielding is the mechanism behind the delayed DES model. Gritskevich [98] refine the SST blending function coefficients to only depend on the eddy viscosity and wall distance. The DDES computations are carried out with the same model coefficients and proposed by Gritskevich [98]. No spectral content is added to the simulation set up. That is, there is no prescribed inlet turbulence profile.

Simulations were conducted with the rhoSimpleFoam and rhoPimpleFoam solvers for steady state and transient cases, respectively. Those are pressure based, compressible Navier-Stokes solvers utilising second order schemes and the SIMPLE or PIMPLE algorithms. The PIMPLE algorithm is derived from both the PISO (pressure implicit with splitting of operator) algorithm detailed by Issa [99] and the SIMPLE (semi implicit method for pressure linked equations) algorithm given by Patankar [100]. Each PIMPLE timestep calculation was solved with 200 subiterations or until a drop of residuals of 6 orders of magnitude was reached. The Sutherland law was used to model the relation of temperature and viscosity [101].

A geometric agglomerated algebraic multi grid pressure solver (GAMG) is used with a face area pair agglomerator. The GAMG solver coarsens the computational grid initially to achieve faster run times, smoothes high frequency errors out with a Gauss Seidel smoother, and generates a starting solution for the final mesh defined by the user. Other flow properties like the internal energy, velocity components, and turbulent kinetic energy are solved with the OpenFOAM smoothSolver. The smoothSolver iteratively solves the symmetric and asymmetric matrices with a run time selected Gauss Seidel smoother.

### 3.2.4 Boundary conditions, initial conditions, and numerical schemes

RANS simulations were performed with turbulence properties prescribed for kinetic energy and specific dissipation rate ( $\omega$ ) based on a 2.5% turbulence intensity. Equations 3.17 to 3.20 were used for calculating the specific dissipation based on the turbulence intensity  $I_{turb}$ , turbulent kinetic energy  $k_{turb}$ , and turbulent dissipation rate  $\varepsilon$ .

$$I_{turb} = 0.16Re_{in}^{-\frac{1}{8}}, \quad (3.17)$$

$$k_{turb} = 1.5(I_{turb}U_{in})^2, \quad (3.18)$$

$$\varepsilon = C_{\mu}^{\frac{3}{4}} k_{turb}^{\frac{3}{2}} l_{mix}^{-1}, \quad (3.19)$$

$$\omega = \frac{\varepsilon}{k_{turb} C_{\mu}} = \frac{C_{\mu}^{-\frac{1}{4}} k_{turb}^{\frac{1}{2}}}{l_{mix}}, \quad (3.20)$$

where  $Re_{in} = 2.6 \times 10^6$ ,  $U_{in} \approx 200$  m/s is the centreline streamwise velocity at the s-duct inlet,  $C_{\mu} = 0.09$ , and  $l_{mix} = 0.07 D_{in}$  is the mixing length based on the inlet diameter of the duct.

The total mass flow was set at the inlet, with the outlet being at atmospheric pressure. The no slip wall boundary condition was employed. Second order Gauss linear upwind schemes were used for gradient and divergence schemes. The scheme is based on Gaussian integration, linear interpolation with upwind differencing. The temporal derivative scheme is an implicit, second order, backward difference scheme. No wall functions are employed due to the low  $Y^+$  values.

It has been shown that there is an impact of inlet boundary layer characteristics on pressure distortion in the duct [102]. However, no such experimental data were available to match the boundary layer from the numerical studies to. Therefore, no inlet boundary layer profile was prescribed to the numerical domain.

### 3.3 Steady flow properties and performance criteria

Numerical simulations are compared to and validated against experimental data from literature. The data set from Wellborn [1] is chosen due to the availability of both qualitative and quantitative data. The experimental campaign was conducted in the early 1990's at a NASA research facility. The case is a benchmark study, but there are some limitations. Recorded data does not show transient features of the throughflow including unsteadiness levels and flow non-uniformity.

Wall static pressure coefficient plots are presented along streamwise and cross-stream locations in Figures 3.6a and 3.6b, respectively. The trends and gradients of the wall static pressure coefficients are extremely well captured by the RANS simulation throughout the duct domain from the inlet to the AIP both at cross-stream planes and streamwise locations. Most previous numerical studies reported in literature do not show a comparison of  $C_p$  values with Wellborn's benchmark, experimental data. In studies where this comparison is made, the results do not match the trends shown in experiments, see Delot [103]. Cross-stream pressure coefficients match experimental results very well at three planes along the duct ( $\frac{s_c}{D_1} = 0.96, 2.97, \text{ and } 4.01$ ) capturing the separated flow region. Streamwise pressure coefficients also exhibit the expected trends and only slightly underpredict pressure coefficients downstream of the separation region ( $4.0 < \frac{s_c}{D_1} < 5.0$ ) towards the end of the Wellborn s-duct.

The separation extent is visualised through streamlines at the inflection point in Figures 3.8

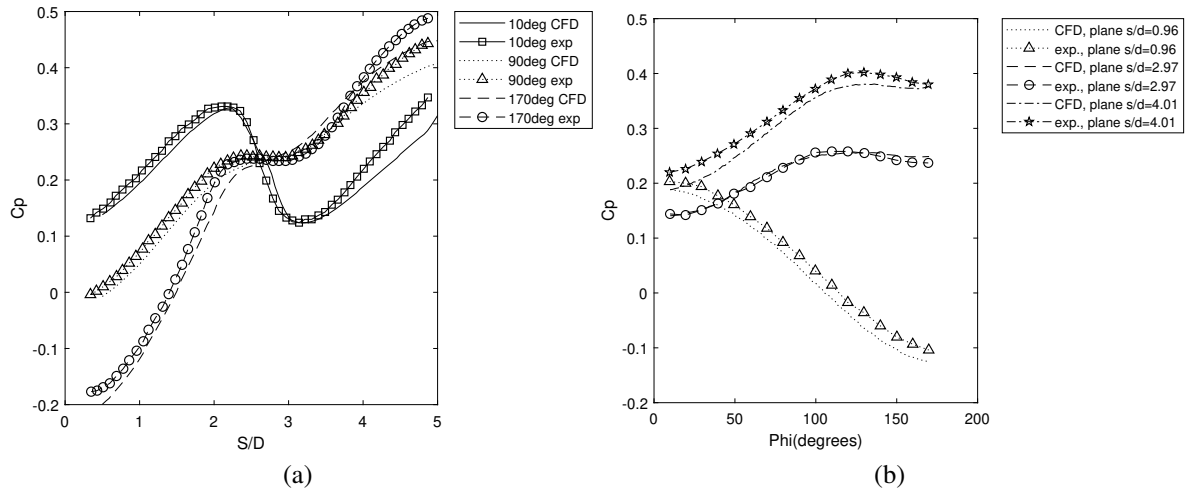


Figure 3.6: Wall static pressure coefficient along (3.6a) three streamwise lines of 10, 90, and 170 degrees and (3.6b) three cross-stream planes for Wellborn's experimental results ([1]) and OpenFOAM rhoSimpleFoam CFD results.

and 3.7. All streamlines are seeded from the same point source in paraview and displayed in the same style and colour scheme. For Figure 3.8 the view is from the bottom of the convoluted duct with the positive  $y$  direction into the page. The separated region consists of two saddle points, occurring on the duct split line ( $z = 0$ ), and two spiral nodes, lying in each symmetric duct half. The entire separated region is located on the lower wall of the s-duct.

There are key differences between the separation region of RANS, time averaged URANS, and time averaged DDES simulations. Firstly, it is evident that time averaged transient DDES simulation differs considerably from Reynolds averaged simulations of RANS and URANS. The separation region for DDES simulations seems more elongated in the streamwise direction with RANS results showing a much more confined separated flow region. Moreover, the flow following reattachment displays a much stronger vortical structure in the DDES case as compared to RANS and URANS simulations. Reversed flow is twice as high, however, with RANS and URANS simulations.

Quantitatively, the axial extent of the separation onset is located at  $\frac{s_c}{D_1} = 1.96$  for all three CFD simulation studies. The reattachment point varies, however, and moves further downstream from the RANS, to the URANS, and to the DDES flow field data. For RANS simulation the downstream saddle point occurs at  $\frac{s_c}{D_1} = 4.12$ , while URANS and DDES predict the reattachment point at  $\frac{s_c}{D_1} = 4.28$  and  $\frac{s_c}{D_1} = 4.39$ , respectively. This matches experimental data reported in [1] closely though not exactly. Experimental flow visualisations showed the onset to occur at  $\frac{s_c}{D_1} = 2.02$  with the reattachment position being at  $\frac{s_c}{D_1} = 4.13$ . RANS matches the recorded experimental reattachment point of the separation region closest. This is, however, only one aspect of the validation so definitive conclusions can not yet be drawn.

Time averaged total pressure and streamwise component of Mach number contour plots at the AIP are compared to Wellborn's experimental data in Figure 3.9. The figure shows that

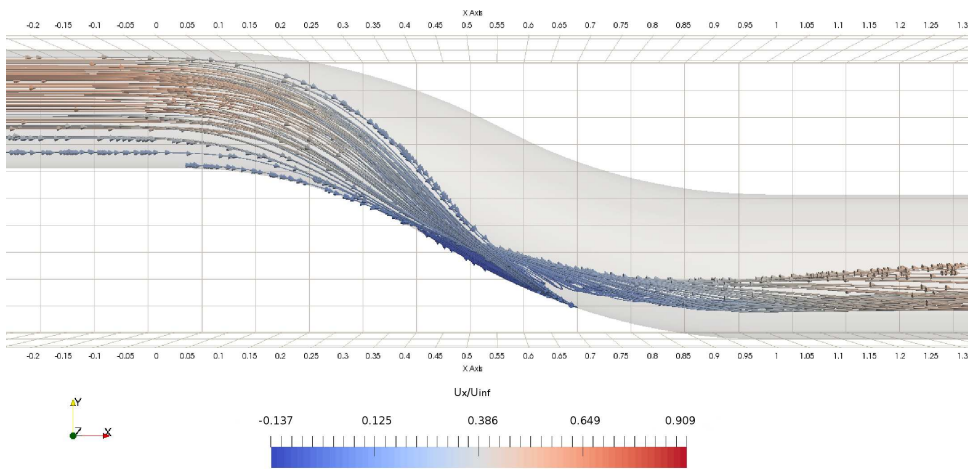
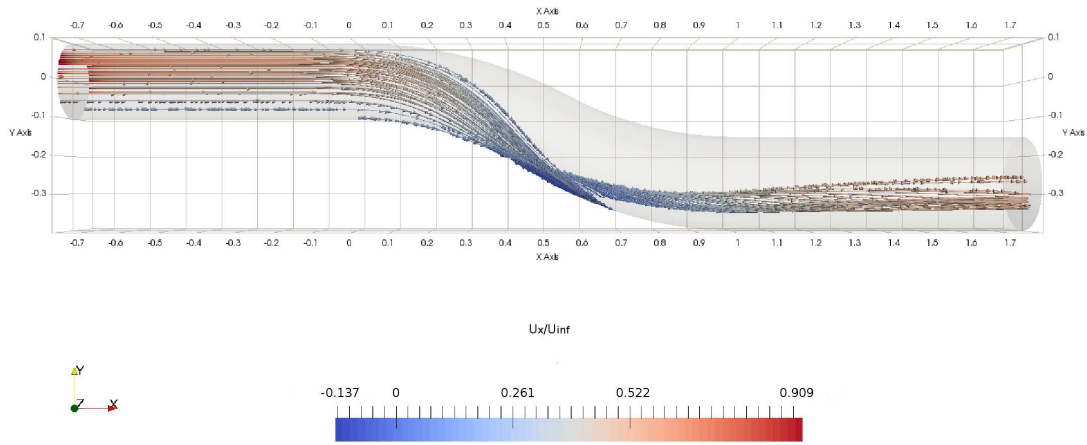
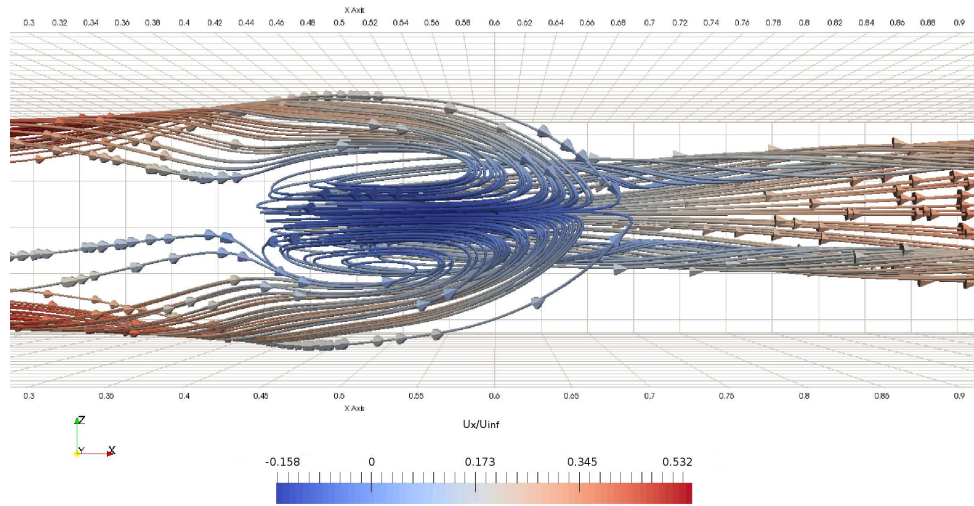
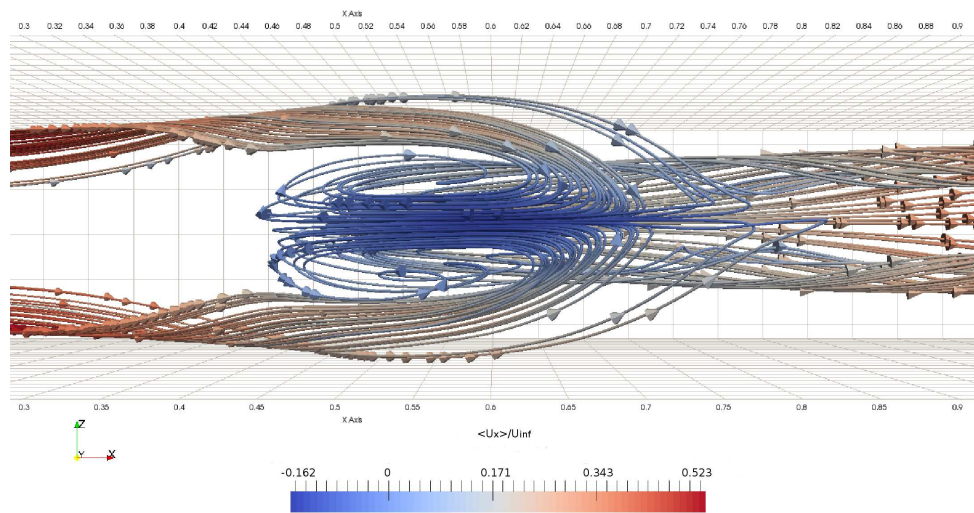


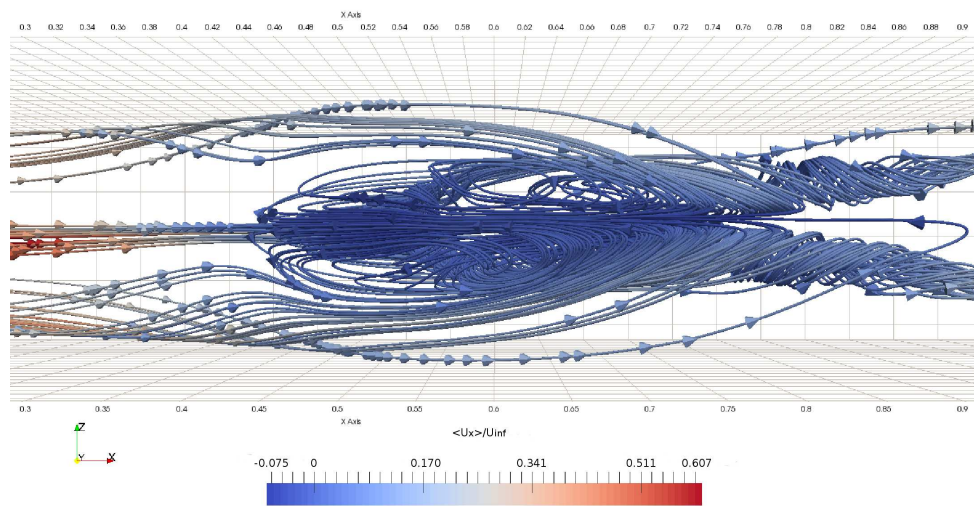
Figure 3.7: Streamlines for RANS simulations of (3.7a) baseline s-duct throughflow and (3.7b) a close up view on the inflection point. Colour legend describes the streamwise velocity component in ( $ms^{-1}$ ).



(a)



(b)



(c)

Figure 3.8: Streamlines at inflection point of s-duct for: (3.8a) RANS simulation; (3.8b) time averaged URANS simulation; and (3.8c) time averaged DDES simulation. Colour legend describes the streamwise velocity component in ( $ms^{-1}$ ).

RANS and URANS simulations capture the flow properties in the upper AIP region just as closely as DDES simulations. Based on experimental findings it is accepted that the smaller, second bend flow separation is already reattached in the AIP plane. Both URANS and DDES simulations capture the reattachment position accurately as is evident from the contour plots at the AIP. It seems the  $k-\omega$  SST turbulence model does capture the reattachment location well. This is shown in the corresponding plots in Figure 3.9.

Pressure distortion coefficients for URANS and DDES simulations are presented in Figure 3.10 for different sector extents and compared to experiments by Reichert and Wendt [2, 3]. The maximum total pressure distortion of the DDES simulation is only about half as high as the distortion recorded in experiments. It is believed that the turbulence modelling is responsible for the mismatch in distortion values. It is possible that full LES and DNS simulations are required to match experimental pressure distortion values at the AIP. URANS distortion coefficients are still lower. RANS and URANS pressure distortion coefficients vary only very slightly.

Time averaged flow properties at the AIP for transient simulations are presented in Figure 3.11 for URANS and DDES formulations. The flow properties in Figure 3.11 show the well known, distinctive low velocity, low pressure area in the centre of the bottom half of the AIP region evident in both URANS and DDES simulations. Cross-stream flow exhibits a high velocity upwards motion in the centre of the AIP and flow down the sides of the region for vertical velocity component,  $v$ . The horizontal flow pattern,  $w$ , moves fluid from the centre to the sides in the upper region of the AIP and then from the sides towards the centre in the lower region facilitating the vortical fluid flow pattern.

Statistical confidence in the time averaged properties presented in Figure 3.11 is established with a 95% confidence interval (CI). The CI is calculated with equation 3.21 for every face point at the AIP separately based on the snapshot time series of data collected. Figure 3.12 shows the CI normalised by the inlet centreline velocity for each face point at the AIP based on the URANS and DDES simulation results.

$$CI_{95\%_i} = \frac{Z_{value} \sigma_{SD_i}}{n_{samples}^{\frac{1}{2}}}, \quad (3.21)$$

where  $Z_{value}$  is taken as 1.96,  $\sigma_{SD_i}$  is the standard deviation at each face point at the AIP, and  $n_{samples}$  is the number of samples the standard deviation is based on.

For the presented flow properties of total pressure and the three velocity components  $u, v, w$  the maximum values of the 95% CI at the AIP for the DDES simulation snapshot data are 690 Pascals, and 4.4, 4.5, and 3.8  $\frac{m}{s}$ , respectively. Hence, there is a 95% confidence that the flow properties are within the calculated interval off the time averaged properties presented. The URANS data confidence intervals show an even smaller uncertainty with the limits being much closer to the time averaged properties.

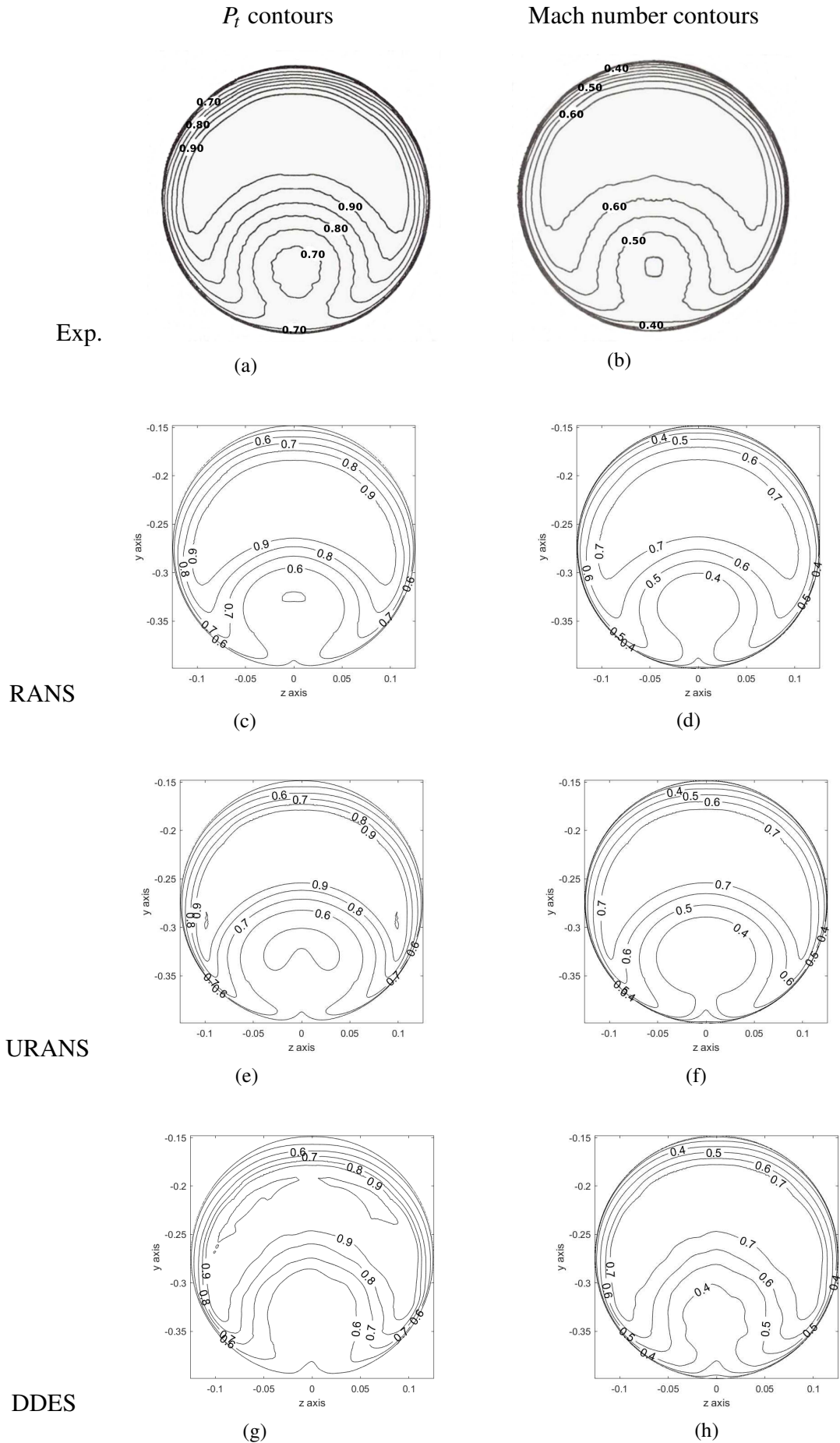


Figure 3.9: Contour plots: (3.9a-3.9b) Wellborn’s data, (3.9c-3.9d) RANS rhoSimpleFoam, time mean rhoPimpleFoam CFD of (3.9e-3.9f) URANS, and (3.9g-3.9h) DDES.

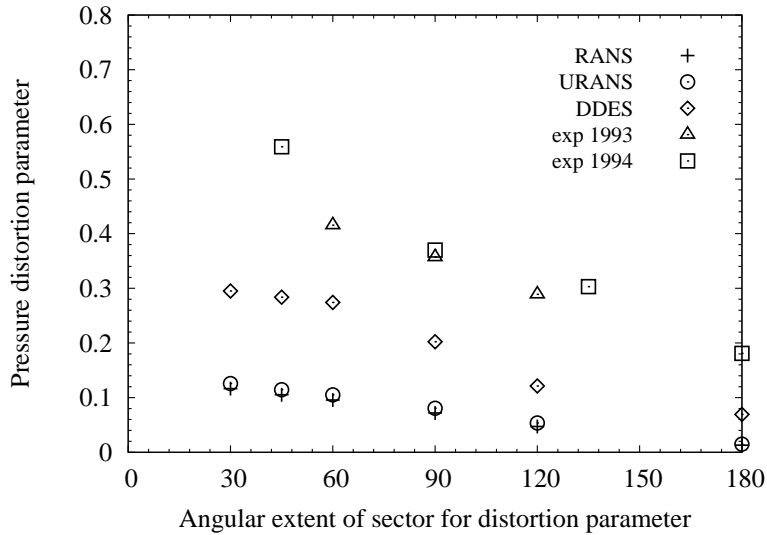


Figure 3.10: Total pressure distortion coefficient with sectors of 30, 45, 60, 90, and 120 degrees for RANS, URANS, and DDES simulations compared to experiments by [2, 3].

Steady state RANS and time averaged URANS and DDES simulation data show a very similar flow picture in terms of the wall static pressure distribution as well as Mach number and total pressure contours at the AIP. In that respect, RANS, URANS, and DDES all match experimental data closely.

### 3.4 Unsteady flow properties and performance criteria

Standard deviation maps of flow properties at the AIP for transient URANS and DDES simulations are presented in Figure 3.13. There is a distinct and substantial difference in standard deviation of all flow properties presented as is evident from Figure 3.13. The standard deviation with DDES simulations for velocity components  $u$ ,  $v$ , and  $w$  is 30, 50, and 55 times as high as with URANS modelling, respectively. URANS standard deviation levels are much lower than would be expected from an oscillating shear layer in a flow field with strong, secondary pressure gradients. Being based on the average of computed Reynolds stresses, it is clear that URANS modelling does not produce realistic unsteadiness levels of separated flow regions for flows through the Wellborn convoluted duct. The inability of URANS to predict the high unsteadiness levels seen in s-ducts is attributed to its averaging nature which does not allow large-scale dynamics in the separated shear layer to be captured and hence has to be expected.

The DDES standard deviation maps depict the more realistic picture, with the central area of the AIP region seeing the greatest fluctuations. The total pressure standard deviation at the AIP as a percentage of the inlet total pressure value has fluctuations up to 4.3%. This compares well with previous findings [29, 38]. Experiments were conducted on a scaled version of the Wellborn s-duct in [38] and report total pressure standard deviation at the AIP with fluctuations

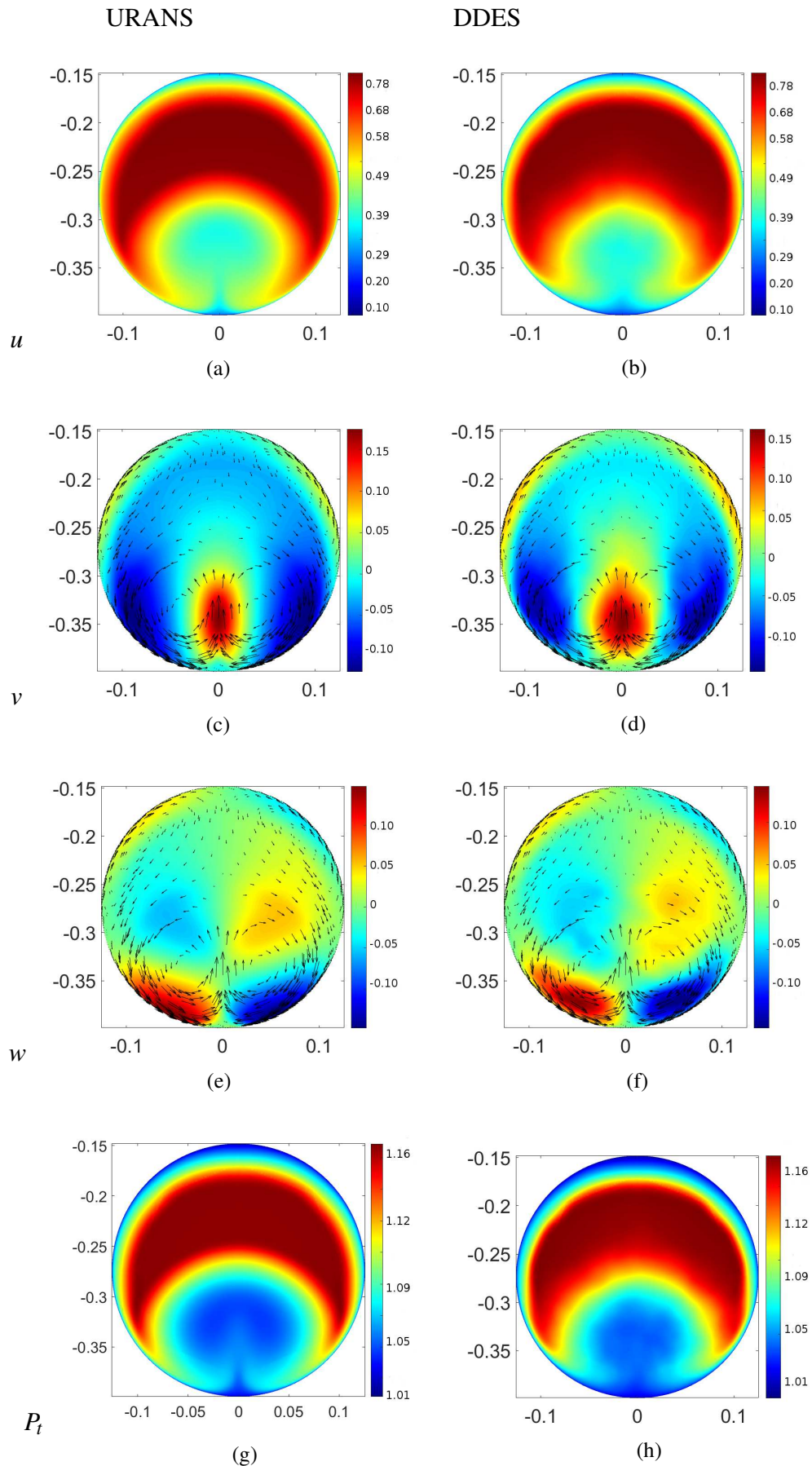


Figure 3.11: Time averaged flow properties at AIP showing velocity components  $u$ ,  $v$ ,  $w$  normalised by the inlet centreline velocity, and total pressure (Pa) normalised by the atmospheric pressure for URANS and DDES simulations.

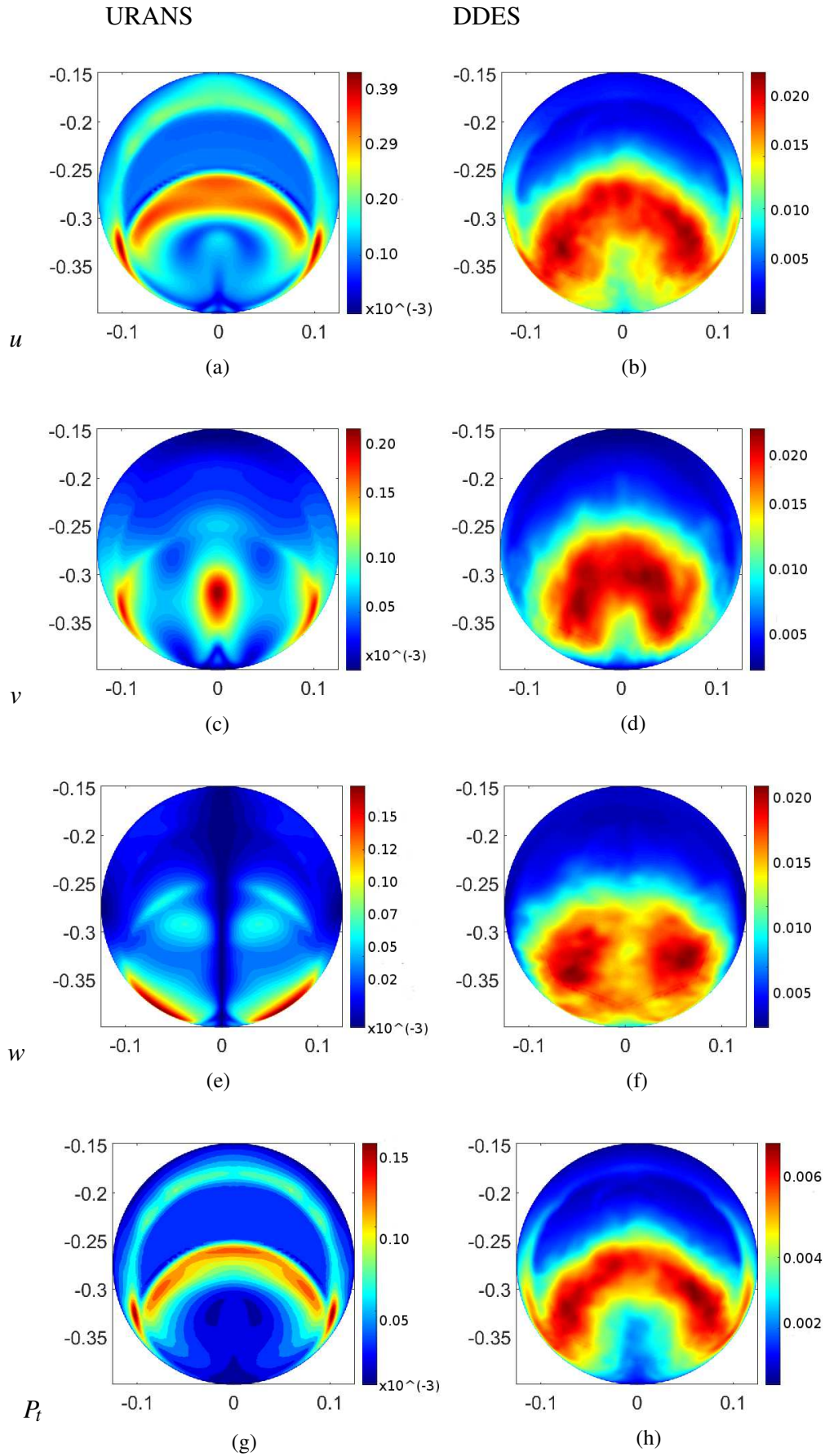


Figure 3.12: 95% confidence interval plots of the velocity components  $u$ ,  $v$ ,  $w$  normalised by the inlet centreline velocity, and the total pressure (Pa) normalised by the atmospheric pressure at the AIP region for URANS and DDES simulations.

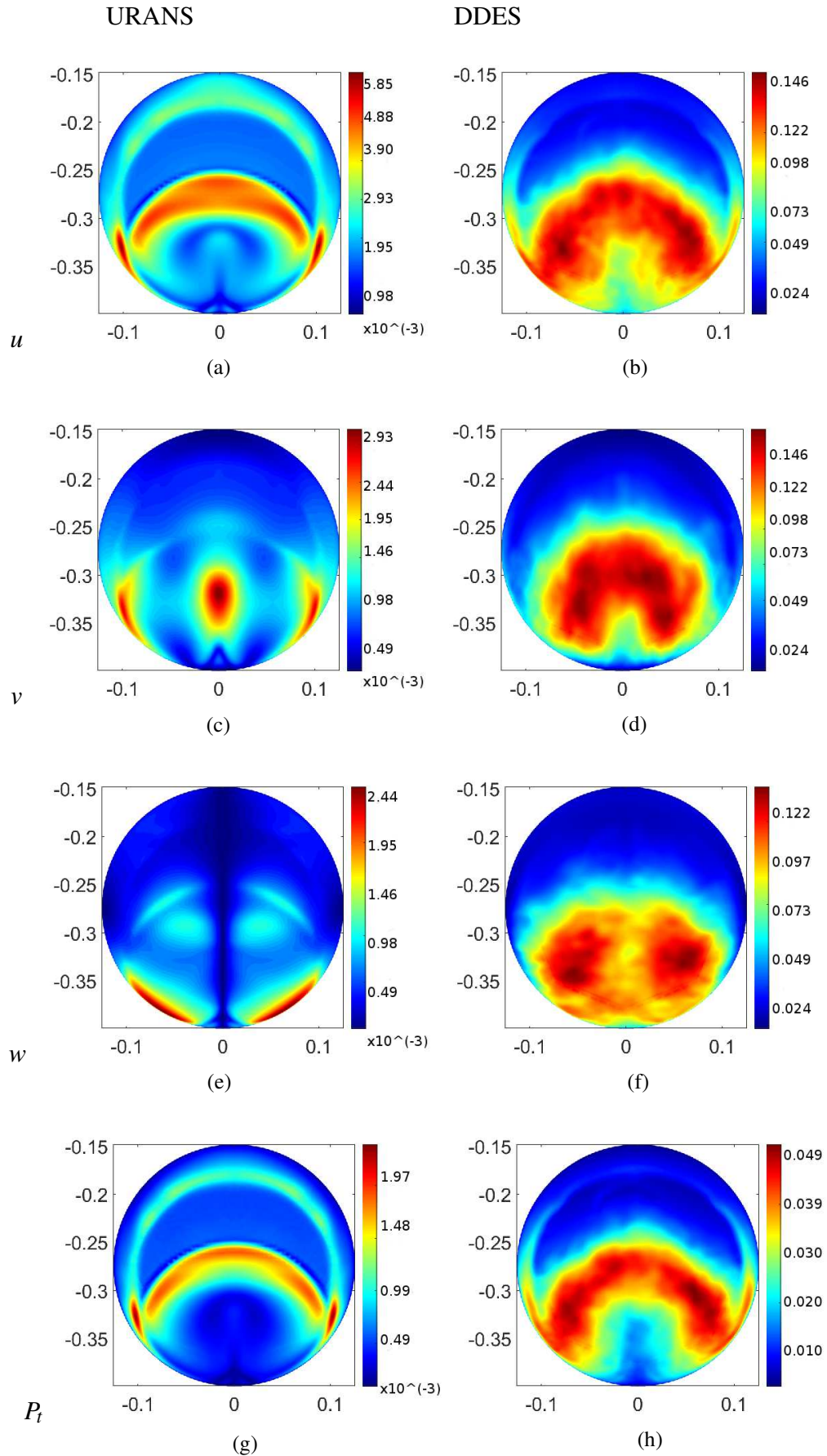


Figure 3.13: Standard deviation maps of flow properties at AIP showing velocity components  $u$ ,  $v$ ,  $w$  normalised by the inlet centreline velocity, and total pressure (Pa) normalised by the atmospheric pressure for URANS and DDES simulations.

of up to 3.5% of the intake total pressure.

The higher level of unsteadiness and flow fluctuations in DDES simulations, as compared to URANS, is also obvious from the snapshot based static and total pressure recovery data. Figure 3.14 shows the total and static pressure recovery for URANS and DDES simulations for each snapshot as well as the time averaged values. Pressure recovery values show a healthy variation between snapshots for DDES simulations emphasising the transient nature of the throughflow. OpenFOAM results are presented against experimental findings from [2, 3], and numerical results from [4] who computed the throughflow with DDES formulation in Ansys Fluent. The total pressure recovery is underpredicted by URANS and DDES simulations. However, the mean  $PR_t$  is less than 2.07% off the values recorded by Reichert and Wendt in their experiments for both transient simulation cases. In comparison, results by MacManus et al. overpredict the total pressure recovery by a margin of 0.8%.

The static pressure at the AIP indicates how efficiently the diffusing s-duct decelerates the flow field. The instantaneous values of the static pressure recovery in Figure 3.14d at the interface plane are yet another indicator of the unsteady nature of the flow field. The difference compared to Figure 3.14b is striking and clearly demonstrates the effect of the simulation fidelity on the results.

### 3.5 Modal decomposition and frequency spectrum

The proper orthogonal decomposition method of Sirovich [86] was applied to the DDES streamwise velocity snapshots at the AIP. Figure 3.15 shows the recreation of the secondary flow statistics, i.e. the fluctuations of the streamwise velocity component  $U_{x_i} - U_{x_{avg}}$ , at the AIP with a varying number of modes. Evidently, the decomposition works as intended, since the target flow field is reconstructed with greater detail the more modes are being used for its reconstruction.

The most dominant mode of the streamwise velocity snapshot data set carries an energy content of 4.35%. All the modal energy contents are shown in Figure 3.16.

POD modes of the velocity field show a number of dominant modes. The two most distinct modes are a vertical and horizontal shifting mode. Those result in a shifting motion of the central, low velocity region at the AIP. The horizontal mode shows the low velocity, low pressure region at the AIP switching periodically from left to right. The vertical mode, in contrast, shows the same low velocity region moving up and down at the AIP. Data suggests there is only one horizontal mode but two interacting vertical modes. Figure 3.17 shows the extreme cases of the horizontal mode, with the bottom two images showing the combined flow field of the mode shift and the mean flow superimposed. Extreme cases of modes are determined based on the maximum and minimum values of temporal coefficients for the corresponding mode. Similarly, the vertical shifting modes are presented in Figures 3.18 and 3.19.

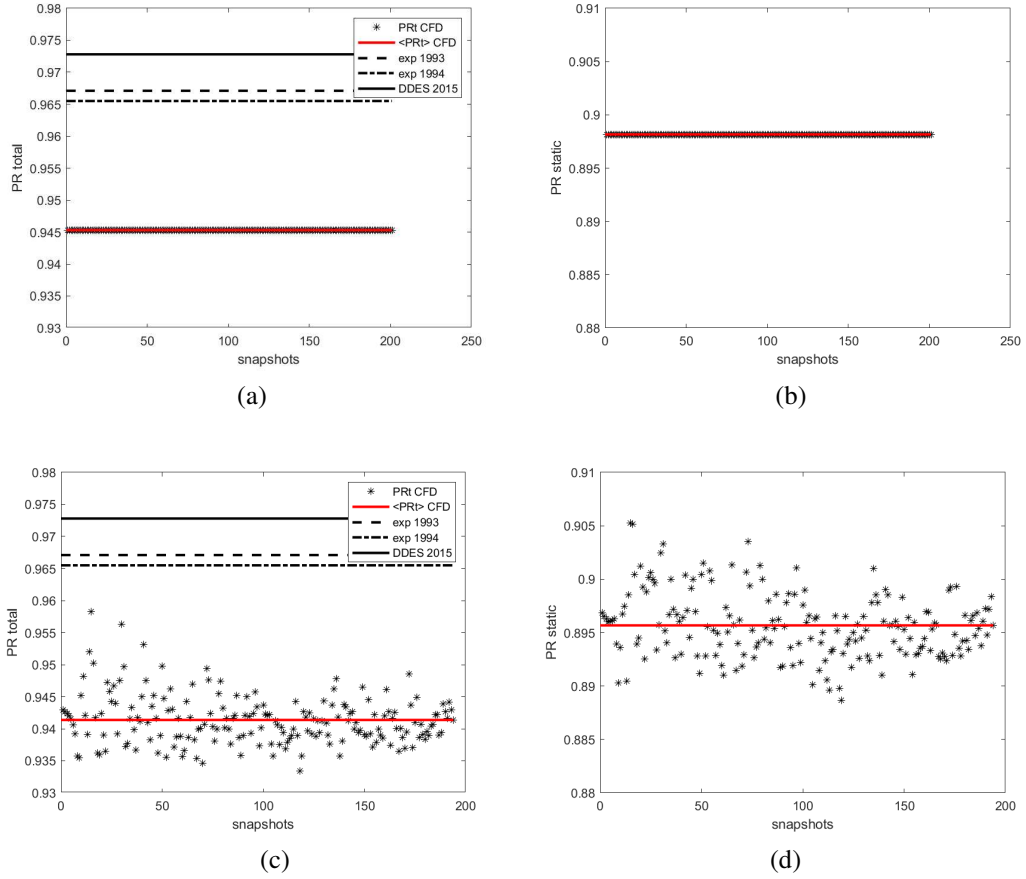


Figure 3.14: Total and static pressure recovery with snapshots of URANS (3.14a-3.14b) and DDES (3.14c-3.14d) simulations. The average PR is shown by the continuous line. Results are compared to experimental data recorded by [2, 3]. Numerical DDES results published by [4] are also presented.

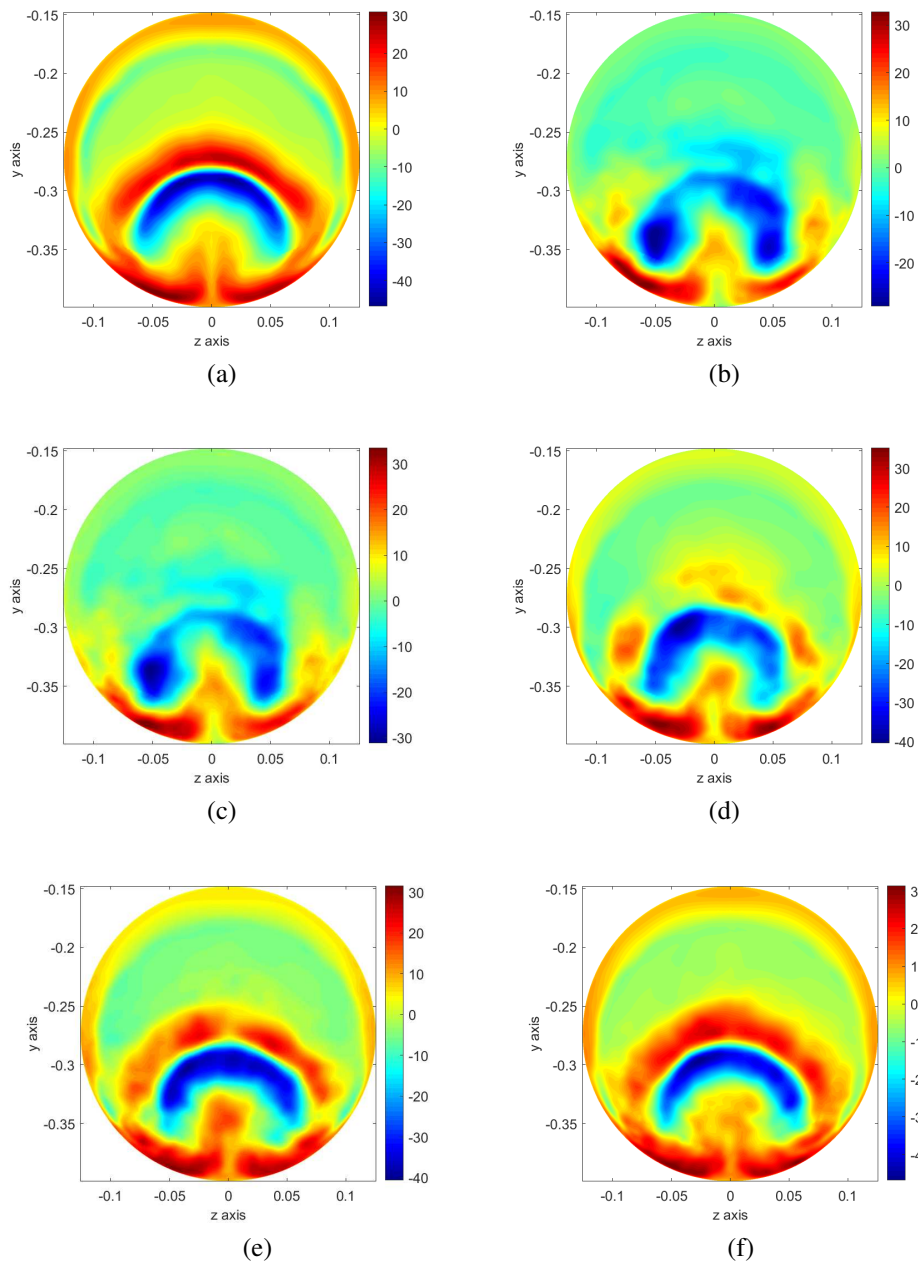
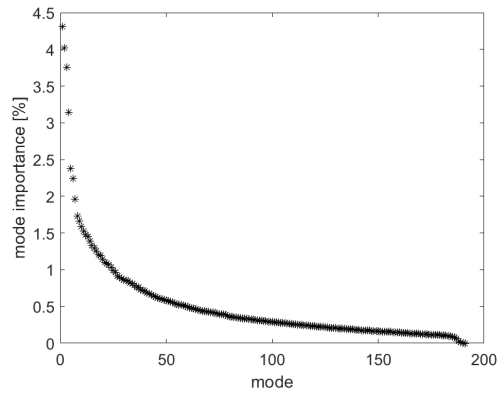
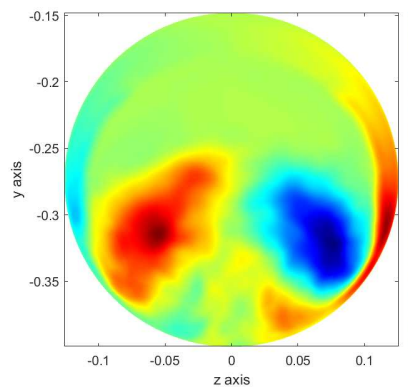


Figure 3.15: Reconstruction of flow statistics ( $m s^{-1}$ ) at AIP with POD modes: (3.15a) target snapshot secondary flow statistics; (3.15b) reconstruction based on first 5 modes; (3.15c) reconstruction based on first 10 modes; (3.15d) reconstruction based on first 20 modes; (3.15e) reconstruction based on first 40 modes; (3.15f) reconstruction based on first 60 modes.

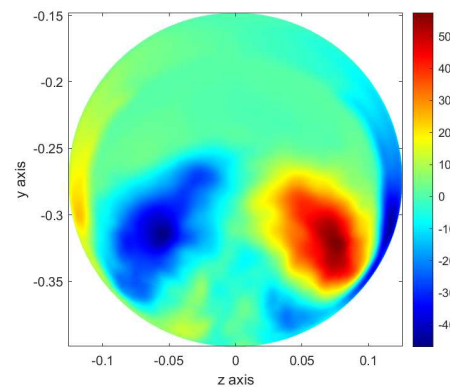


(a)

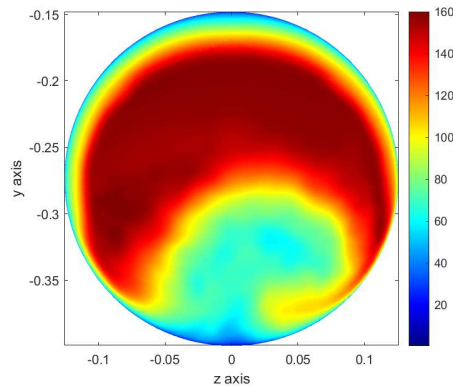
Figure 3.16: POD energy content for modes of the streamwise velocity component snapshot data set from DDES computations.



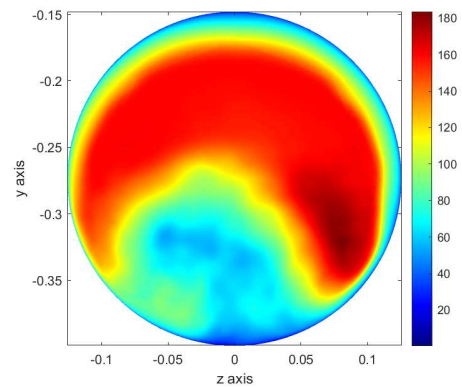
(a)



(b)



(c)



(d)

Figure 3.17: Horizontal shedding mode: (3.17a) mode for maximum temporal coefficient; (3.17b) mode for minimum temporal coefficient; (3.17c) mode for maximum temporal coefficient with superimposed average flow field; (3.17d) mode for minimum temporal coefficient with superimposed average flow field ( $ms^{-1}$ ).

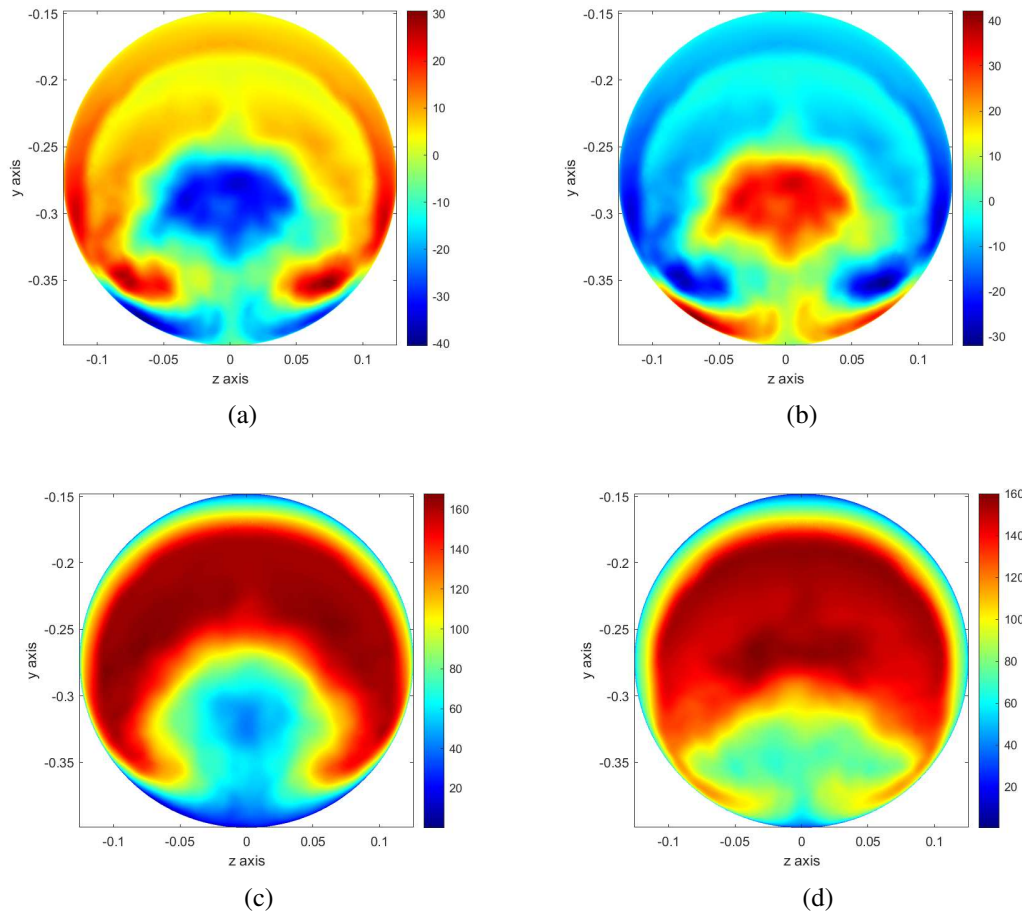


Figure 3.18: First vertical shedding mode: (3.18a) mode for maximum temporal coefficient; (3.18b) mode for minimum temporal coefficient; (3.18c) mode for maximum temporal coefficient with superimposed average flow field; (3.18d) mode for minimum temporal coefficient with superimposed average flow field ( $ms^{-1}$ ).

The vertical shifting mechanism of the velocity field at the AIP is probably driven by the oscillating shear layer related to the main separation in the s-duct. This oscillating shear layer is also responsible for the high standard deviation values in the central AIP region. The horizontal shifting mechanism is postulated to be caused by instabilities in the flow driven by secondary flow patterns and cross-stream, in-plane velocity profiles. Frequencies of the vertical and horizontal shifting modes were established through their respective occurrence rate over the simulation time. The horizontal shift occurs with a frequency of 215 Hz, while the first and second vertical modes' frequencies are 420 and 94 Hz, respectively.

DMD manipulates data sets to highlight coherent patterns as a low dimensional representation in time and space. It can be thought of as an operator that combines static mode extraction in the spatial domain and discrete Fourier transform (DFT) in the time domain. Unlike DFT, dynamic mode decomposition also provides information about growth/decay rates.

Dynamic mode decomposition of snapshots of the flow properties at the AIP are performed

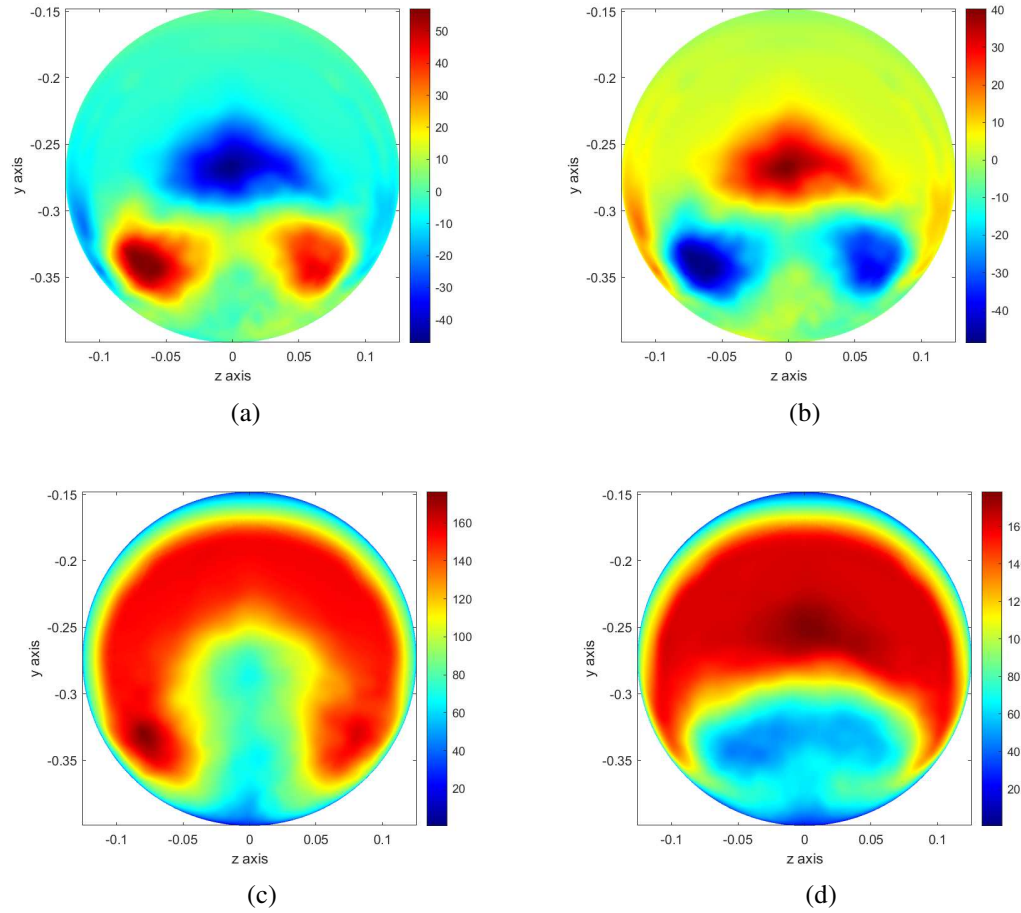


Figure 3.19: Second vertical shedding mode: (3.19a) mode for maximum temporal coefficient; (3.19b) mode for minimum temporal coefficient; (3.19c) mode for maximum temporal coefficient with superimposed average flow field; (3.19d) mode for minimum temporal coefficient with superimposed average flow field ( $ms^{-1}$ ).

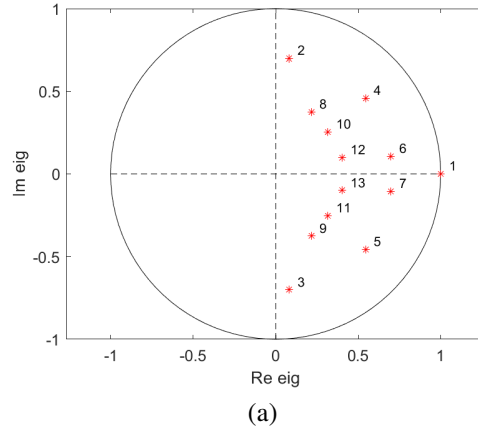


Figure 3.20: Eigenvalue unit circle plot for dynamic mode decomposition of streamwise velocity DDES data.

to get insight into phase information. Spatio-temporal coherent structures have characteristic frequency of oscillation and growth/decay rate. Depending on their imaginary and real parts, the unit circle of eigenvalues ( $\lambda$ ), Figure 3.20, reveals if a mode is stable, decaying (imaginary part of  $\lambda$  within unit circle) or exhibits growing, unstable (imaginary part of  $\lambda$  outwith unit circle) dynamics as defined by [104, 105].

Based on the unit circle plot it is clear that all DMD modes are stable as their imaginary parts are located within the unit circle. Mode 1, positioned on the unit circle, is steady and represents the mean flow field. Modes occur in coupled pairs with the same real part and different imaginary values. DMD modes 2 and 3, and 4 and 5 are coupled and represent the same dynamic features as POD modes 1 and 2, i.e. the vertical and horizontal shifting modes. The first three coupled DMD modes are shown in Figure 3.21.

The frequency of occurrence,  $f_i$ , is determined through the equation given in [106] and presented here:

$$f_i = \frac{\text{imag}(\omega_i)}{2\pi}, \quad (3.22)$$

where  $\omega_i$  is the imaginary part of the eigenvalue of the corresponding mode. Frequency values for the first and second vertical modes are 460 and 70 Hz. The DMD horizontal shifting mode has a frequency of 230 Hz. Those frequencies match remarkably well to the frequencies deduced from the mode occurrence of the POD decomposition. Interestingly, analysis of both DMD and POD decomposition suggests that the vertical mode is a combination of two vertical shifting mechanisms with a slower and faster frequency.

Frequency plots are obtained by running the snapshot DDES data set through a fast fourier transform function and extracting the dominant frequencies. This analysis is conducted for every mesh face at the AIP, of which there are over 17000. Once the frequency spectrum is obtained, it is normalised by its highest value. Next the Matlab peak detection function is used to extract

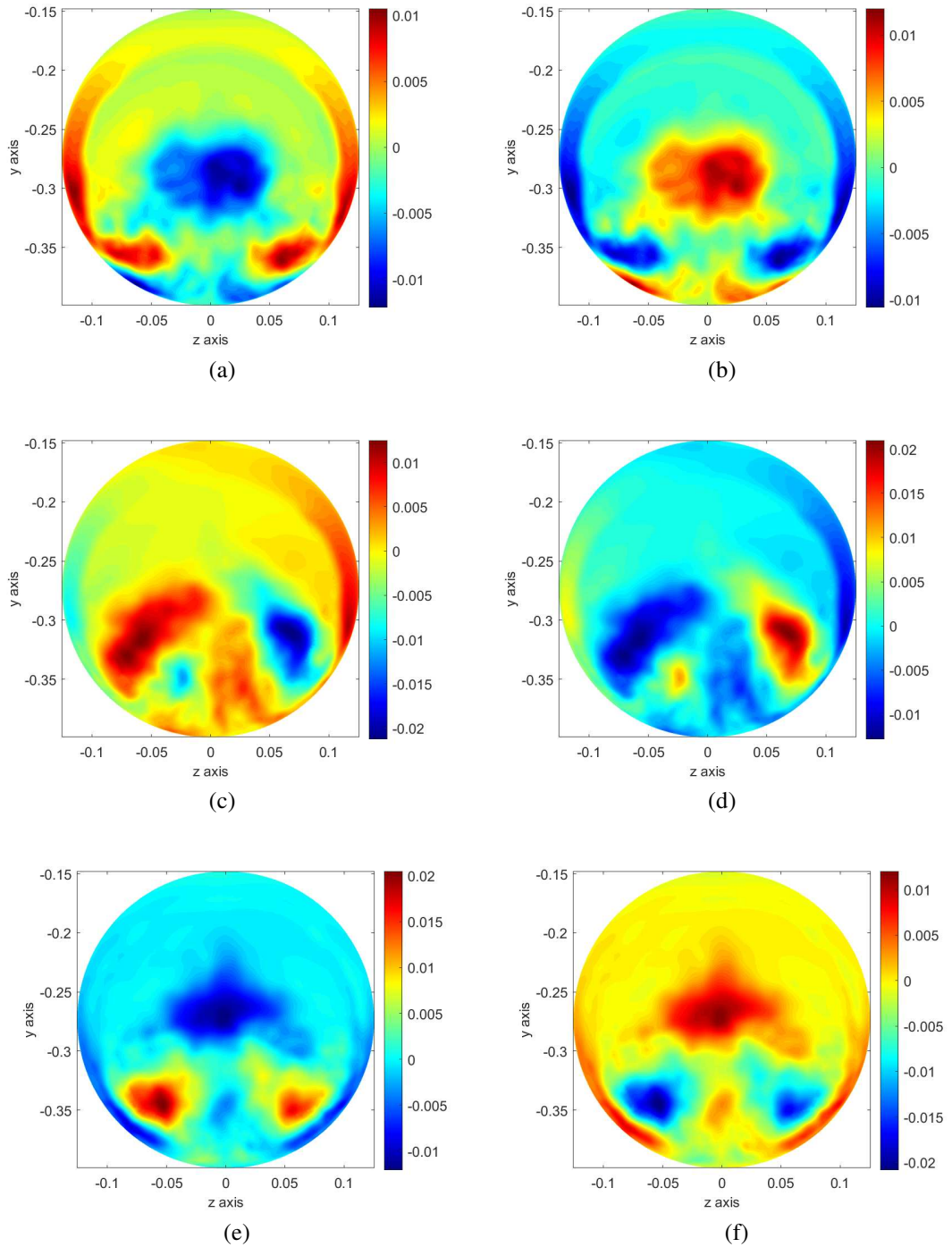


Figure 3.21: DMD first vertical mode (coupled DMD modes 2 and 3 in 3.21a and 3.21b, respectively) representing same dynamics as POD first vertical shifting mode. DMD horizontal mode (coupled DMD modes 4 and 5 in 3.21c and 3.21d, respectively) representing same dynamics as POD horizontal shifting mode. DMD second vertical mode (coupled DMD modes 6 and 7 in 3.21e and 3.21f, respectively) representing same dynamics as POD second vertical shifting mode.

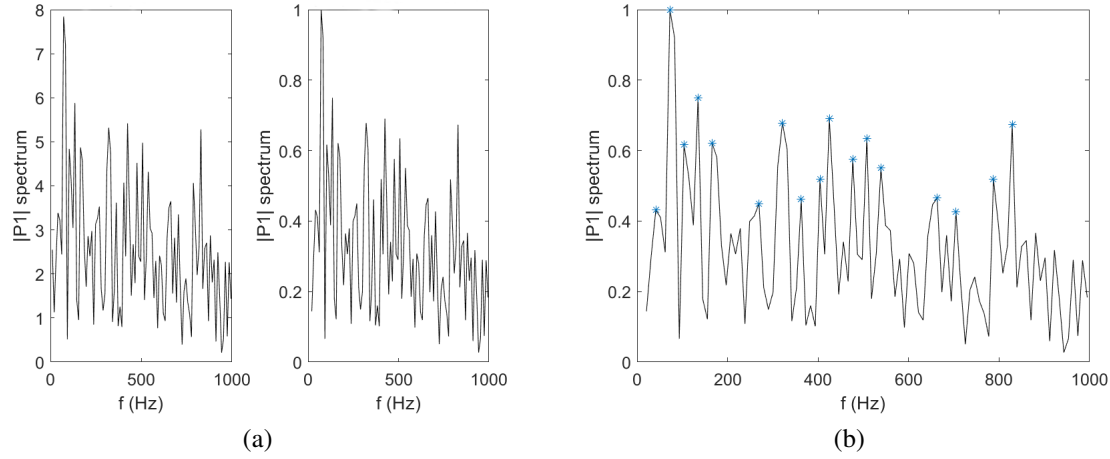


Figure 3.22: Example of dominant frequency extraction process: (3.22a) non-normalised and normalised FFT spectrum for point 14700; (3.22b) peak detection on normalised FFT spectrum.

dominant frequencies for each point location of the AIP. This process is shown in Figure 3.22. The data signal is neither smoothed nor are its frequency peaks sorted. Frequency values are nondimensionalised and presented as the Strouhal number:

$$St_i = \frac{f_i L}{U_{cl}}, \quad (3.23)$$

where  $f_i$  is the frequency at a specific mesh point  $i$ ,  $L$  is the inlet diameter, and  $U_{cl}$  is the centreline inlet velocity magnitude.

Dominant frequency maps of the streamwise velocity component and the static pressure at the AIP for DDES simulations are presented in Figure 3.23. For the static pressure, the highest frequencies are concentrated in the central region of the AIP. This corresponds to the fluctuating, highly dynamic region of the flow identified in the standard deviation plots. The first dominant frequency for static pressure reaches up to 450 Hz. Second and third dominant frequencies are higher still. In contrast, the area of the highest dominant frequencies for the streamwise velocity component is located in the upper central region of the AIP and more towards the walls of the interface plane. The frequencies for the first, second, and third dominant frequencies in those regions are 150 to 200, 200 to 250, and 250 to 300 Hz, respectively.

The first dominant frequency extracted from the FFT analysis of streamwise velocity data at the AIP is of the same order of magnitude as the oscillating frequency of the horizontal shifting modes obtained with the POD and DMD decomposition methods.

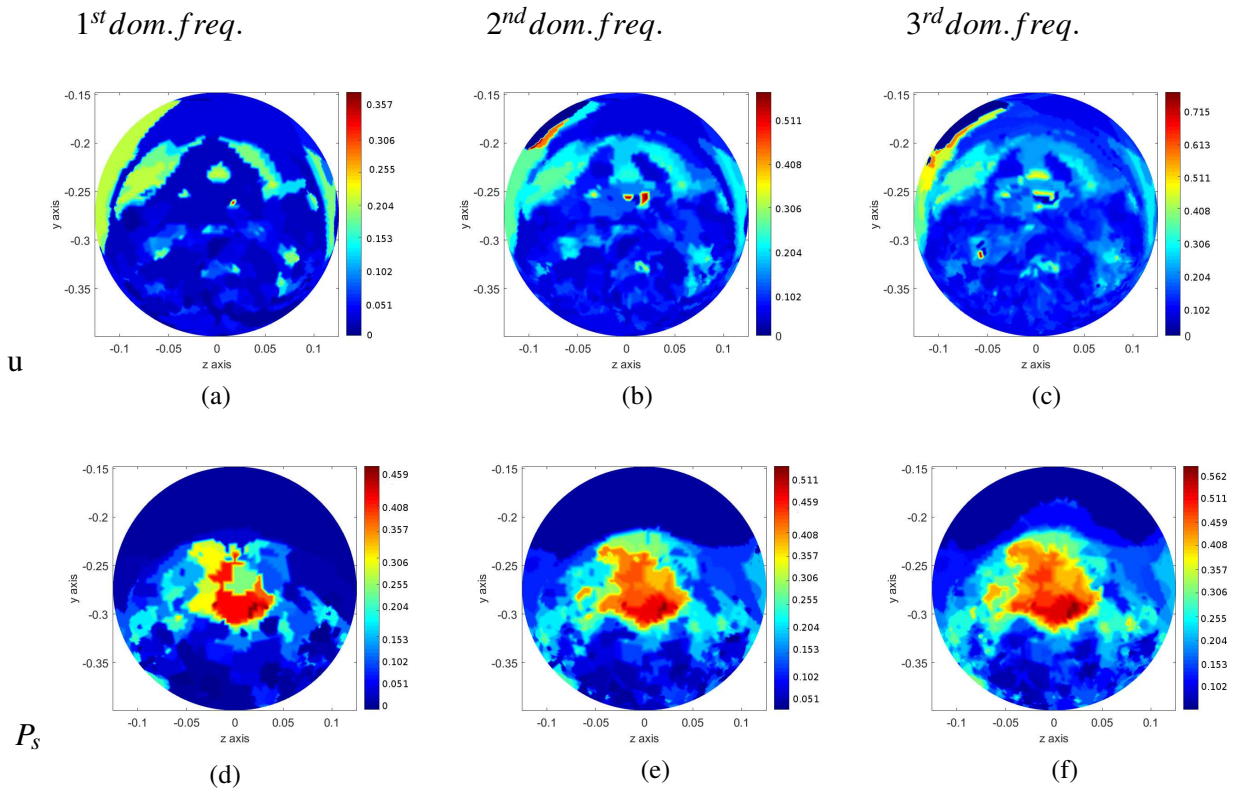


Figure 3.23: Maps of dominant frequency represented by the Strouhal number. Top row: stream-wise velocity component; and bottom row: static pressure at the AIP.

### 3.6 Conclusions

Numerical simulations in OpenFOAM have matched experimental data on the Wellborn s-duct remarkably well for steady state performance parameters generally and, especially, wall static pressure coefficients as well as contour plots at the AIP.

As expected, URANS results show an unrealistic unsteadiness level of the flow past the separation point with an almost static shear layer. Standard deviation values for flow properties at the AIP are massively underpredicted. URANS simulations are not adequate to capture important transient flow phenomena. DDES simulations depict a much more realistic picture of the throughflow. Total pressure recovery is within 2.07% of values recorded in experiments. Standard deviation values of velocity components are realistic and capture the fluctuation of the shear layer in the central region of the AIP. Fluctuations are located in the well known low velocity, low pressure central region of the AIP where the highest unsteadiness of the flow occurs.

The separation extent is captured well by the DDES CFD simulations also. The onset of the separation is very slightly underpredicted with the upstream saddle point occurring at  $\frac{s_c}{D_I} = 1.96$  in the numerical simulations as compared to  $\frac{s_c}{D_I} = 2.02$  in experiments. The reattachment position is overpredicted, however, so that the separated flow region from CFD has a greater axial extent than recorded in experimental flow visualisations.

Modal decomposition revealed dominant modes that exhibit a horizontal and vertical switch-

ing mechanism of the low velocity, low pressure region in the centre of the AIP. Their dynamics and frequency of occurrence were established with dynamic mode decomposition and the frequency domain analysis. Data suggests there are two vertical shifting modes with very different occurrence rates of 460 and 70 Hz. Static pressure and streamwise velocity component frequencies reach 350 and 450 Hz respectively for the first dominant frequencies.

In the bigger picture, results of the modal decomposition analysis and frequency domain might be useful to inform an active flow control strategy to counteract the undesirable flow features within the Wellborn convoluted duct. It is believed that information on the dynamic nature of the flow through s-ducts will be particularly useful to execute active flow control techniques successfully. This is further explored in Chapter 6.

# Chapter 4

## Dielectric barrier discharge plasma actuators

This chapter focuses on experimental campaigns to characterise plasma actuators. Each experiment is stand alone and designed to advance the understanding in the field of plasma actuation by answering research questions. However, the main purpose of this work in context of this thesis is to gather experimental data for validation of numerical plasma models. Numerical plasma models are discussed in detail in the next chapter and applied to the convoluted duct geometry in subsequent chapters.

### 4.1 Introduction

Plasma actuators (PA) have been studied extensively for a number of years, advancing the understanding of the underlying physics and showcasing their potential as flow control devices in many applications. The benefits of plasma actuators are manifold. They are low-power, lightweight devices with no moving parts, which makes them appealing as weight is a key cost factor in many industries. Being flush mounted on the surface, PA do not carry a drag penalty with them as is common in passive devices. The active nature of their operation means they can be utilised at different flow conditions and either turned off or operated with varied parameters to match off design conditions. It is no surprise, therefore, that PA were employed as flow control devices on bluff bodies [107–109], backwards facing steps [110, 111], and aerofoils [112, 113] to reduce wake losses, promote mixing, delay separation, and increase the stall angle. The use of PA for turbomachinery has been reported in [114–119].

A typical dielectric-barrier-discharge (DBD) plasma actuator consists of two electrodes, one exposed to the free stream and one covered by a dielectric layer [120], see Figure 4.1. Dependent on the signal fed to the electrodes, two distinct characteristics of DBD plasma actuation are common: alternate-current (ac) and pulsed nanosecond (ns) - with different operating principles and mechanisms to influence the fluid in the vicinity of the PA. The DBD plasma is formed when

a high, ac or ns, voltage is supplied across the electrodes, ionising the surrounding gas. In this region, it is known that DBD actuators partially ionise the fluid with the resulting electric field giving a body force to the ionised particles during DBD annihilation [121, 122]. In literature, this body force is also called ionic wind or induced velocity.

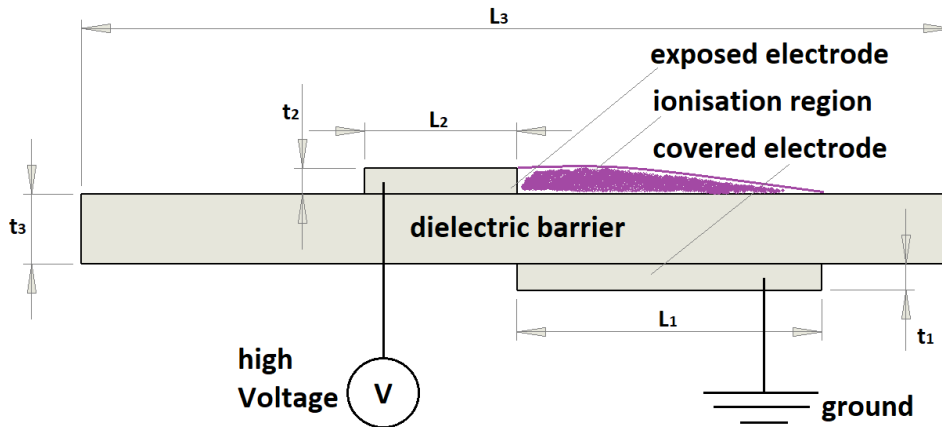


Figure 4.1: Schematic representation of typical dielectric barrier discharge plasma actuator configuration for ac and ns operation. Figure taken from [123].

Langmuir [124] first coined the term plasma to describe a region of ionised gas “containing ions and electrons in about equal numbers” in 1928. The plasma is generated by increasing the amplitude of the electric field above the breakdown electric field,  $E_b$ , which is the value needed to sustain electron-ion pairs in the gas [125, 126]. The minimum breakdown electric field is a function of the driving frequency, among other parameters. At atmospheric pressure,  $E_b$  is generally lower for an ac input. When the voltage amplitude is large enough that the electric field exceeds the breakdown electric field, the air ionizes. The ionised air is always observed to form towards the grounded electrode and over the dielectric material [127]. Time-resolved images of the ionization process, however, indicate it to be a highly dynamic, spatially evolving, non-equilibrium process [128–131], with features that develop on the timescale of the ac voltage period i.e. milliseconds or less [129].

Orlov [132] and Thomas et al. [121] investigated the effects of voltage and ac frequency on the extent and propagation velocity of the discharge. The study found that the maximum extent increased linearly with increasing ac voltage amplitude, and that it is independent of its frequency. However, the velocity of the plasma front increased linearly with both voltage amplitude and frequency. At the lower voltages, the induced thrust is proportional to the power law  $V^{3.5}_{AC}$ . This was first observed by Enloe et al. [133] and is represented in Figure ???. Thomas et al. [121] verified the consistency between the reaction force and the fluid momentum by integrating the velocity profiles downstream of the actuator. Post et al. [134] and others [127, 133] showed that, with increasing ac amplitude, the maximum velocity induced by the plasma actuator was limited by the area (extent for a unit span-wise width) of the covered electrode. Thus, the dielectric area needed to store charge can be too small to take full advantage of the

applied voltage. This is known as the self-limiting factor of ac-DBD plasma actuators with the highest recorded induced velocities reaching  $10 \text{ ms}^{-1}$  [135–137].

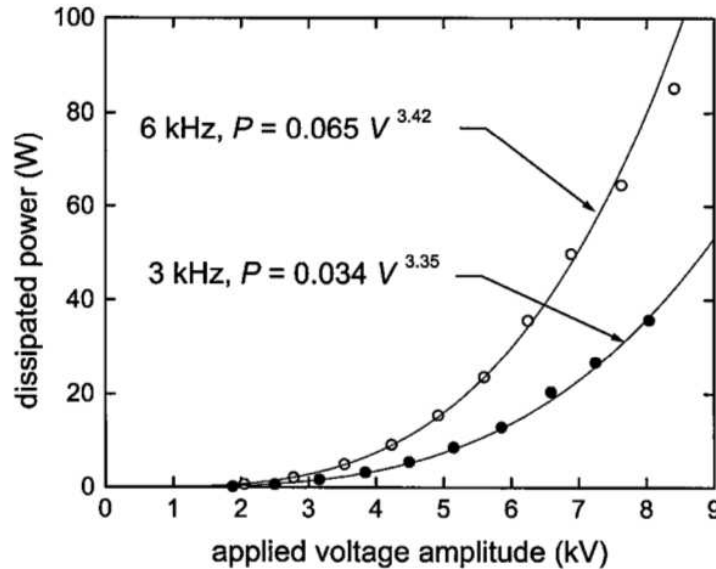


Figure 4.2: Power law of ac-DBD plasma actuators based on work from Enloe et al. Figure taken from [133].

Effects of different dielectric constants or the relative permittivity ( $\epsilon_r$ ) as it is also known, were studied, among others, by Roth and Dai [138] and Kozlov [139]. Pons et al. [140, 141] found that maximal ionic wind velocity varies with the permittivity of the material used. Experiments by Forte et al. [142] conducting velocity measurements for glass ( $\epsilon_r = 10.0$ ) and Polymethyl-methacrylate (PMMA) ( $\epsilon_r = 3.0$ ) show higher induced velocities with glass as the dielectric material for a given voltage input. A similar conclusion is reached by Thomas et al. [121] after studying Teflon ( $\epsilon_r = 2.1$ ), Delrin ( $\epsilon_r = 3.7$ ), Quartz ( $\epsilon_r = 4.3$ ), Macor ( $\epsilon_r = 6.0$ ), and Kapton ( $\epsilon_r = 3.7$ ). Results show higher thrust values with higher dielectric constants for fixed voltage input values.

Actuators tend to have higher saturation points with lower dielectric constants. Saturation occurs when an increase in voltage input does not translate to higher induced velocities. This was found to coincide with streamer formation on the actuator surface and give increased power dissipation [121]. Streamer formation is shown in Figure 4.3. A lower dielectric constant corresponds to a smaller capacitance value which scales with  $\epsilon_r / t_3$ , where  $t_3$  is the dielectric thickness. This decreases the local concentration of the electric field strength allowing higher voltage input before saturation is reached [120]. Hence, higher induced velocities are reached. As pointed out by Cattafesta et al. [137], it is generally beneficial to use thicker dielectric materials with lower  $\epsilon_r$  values.

Pressure dependency of ac-DBD plasma actuators was studied by Valerioti et al. [143] for pressures from 17 to 900 kPa and others [144–146]. Their studies conclude that the body force produced by ac-DBD actuators has two maxima - one at sub-atmospheric pressures and one

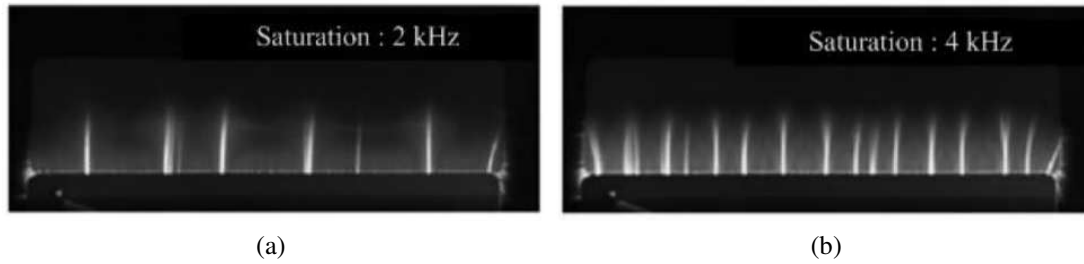


Figure 4.3: Plasma streamer formation for ac-DBD plasma actuators based on work from Thomas et al. Figure taken from [121].

at super-atmospheric pressures. These peaks depend on voltage input and occur at pressures further away from atmospheric conditions with increasing voltage input levels.

For the ns-DBD PA operation, the electrodes are fed with very high voltage nanosecond pulses. During each pulse the gas between the electrodes is ionised and charged particles are attracted to the high voltage electrode, traveling along the dielectric as close to the electrode as possible [71]. As the pulse ends, the electrons are released moving in a direction opposite to the relative position of the high voltage electrode. Plasma streamers are formed and induce local changes to the temperature, density, and viscosity fields. Ultra-fast gas heating occurs in the region of plasma streamers [147] which dictate the effective heating region. The highest temperature is generated locally at the exposed electrode edge. As the streamer propagates along the dielectric it is accompanied by a surface heating rise [70, 73]. Figure 4.4 shows the gas temperature field after a ns-DBD actuator discharge at  $t=40$  ns.

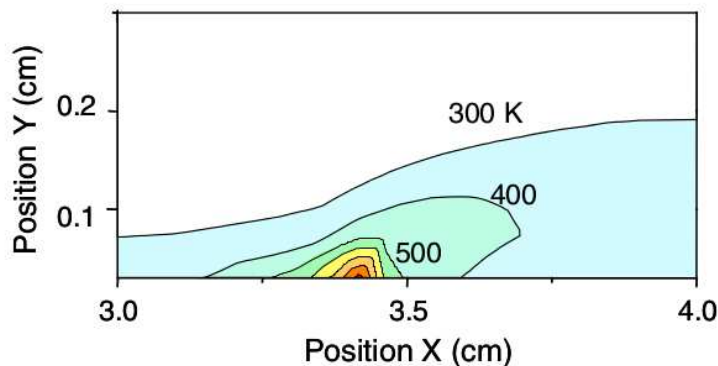


Figure 4.4: Gas temperature field after discharge of ns-DBD plasma actuator. Figure taken from [70].

Electrons collide with air molecules with enough energy to dissociate them. Their recombination is an exothermal process releasing large amounts of thermal energy [148, 149] over very short time periods (about  $1 \mu s$ ). Popov [148] found that the fluid is heated mainly by chemical reactions of dissociation of highly excited oxygen molecules.

The release of thermal energy in a short time period increases the local volume temperature by an approximate factor of ten [72]. Temperature increase of hundreds of degrees Kelvin in

a few dozen nanoseconds have been recorded [150–153]. Due to the short time frame the gas does not expand, resulting in an increase of both pressure and temperature. The gas expands adiabatically, generating a shock wave. The main mechanism of impact is the energy transfer to the near-wall gas in the form of a heat plume [72, 73, 154], which results in a shock wave. Strong local changes in temperature and viscosity accompanied by shock waves are the main method of interaction of the ns-DBD plasma actuator with the fluid. This offers both a very high flow control authority potential and low power consumption [72]. Unlike ac-DBD plasma actuators there is very weak ionic wind/momentum generated by ns-DBD plasma actuation [155].

The effect of geometry on shock wave strength was investigated in a previous study [156], with the results indicating that a thinner dielectric results in a stronger shock wave for a given voltage and pulse frequency input. This was also shown in studies by Van den Broecke and Avallone [157, 158].

Thermal effects of ns-DBD actuators and more specifically their ability to mitigate aircraft icing, was investigated by Lui and Chen [159, 160]. Winkel and others [157, 161] looked at the energy deposition of plasma actuators. Do Nascimento et al. [162] investigated the behaviour of DBD actuators in different gasses using argon, helium, and nitrogen while helium was also used by Nastuta and Liu [163, 164]. A novel method to measure the temperature field was designed and tested on ns-DBD plasma actuators by Ukai et al. [165].

## 4.2 Experimental set-up

Experiments were conducted at the University of Glasgow. The same equipment and basic set up as in the work by Ukai et al. [165] was used for characterising the ns-DBD plasma actuator. Ac-DBD measurements were taken in the National Wind Tunnel Facility.

Reasons for conducting experiments are twofold. The primary reason to characterise ns and ac DBD plasma actuators is to obtain experimental data that could be used to validate numerical models of plasma actuation. Furthermore, each investigation was aimed at extending the understanding of plasma actuation and form a stand alone research outcome. The ns-DBD PA measurements look into the effect of ambient pressure on the resulting discharge. For the ac-DBD PA the dielectric thickness and material as well as the frequency of voltage input are investigated.

### 4.2.1 ns-DBD experiments

The ns-DBD PA used in the study is shown in Figure 4.5. The exposed high-voltage and ground electrodes were 5 and 10 mm wide, respectively. The electrodes were made of 35  $\mu\text{m}$  thick copper. The electrodes are separated by a dielectric material known as glass reinforced epoxy (GRE FR-4: Flame Retardant Type 4) with three different thicknesses of 0.4, 0.8, and 1.6 mm.

There is no discharge gap between the electrodes. The lateral length of all electrodes is 85 mm. The ground electrode was fully covered by three layers of polyimide film, approximately 210  $\mu\text{m}$  in total. The polyimide film covered the exposed electrode 7.5 mm from both lateral side edges to prevent plasma arcing on the sides of the actuator.

The actuators were made using double-sided photolithography. The masks, shown in Figure 4.5, for the process were created using CAD software. The copper comes with a photo-resist coating, which is exposed under a UV light for 30 seconds. It is then submerged in a developer bath that removes the resist that was exposed to the UV light. The developer is Seno 4006, a solution of Potassium hydroxide, and Disodium metasilicate. The board is next sprayed with a ferric chloride solution to remove the exposed copper. The whole process is usually concluded in about 1 minute for each side of the actuator. Once the copper is removed, the remaining photo resist is cleaned with acetone.

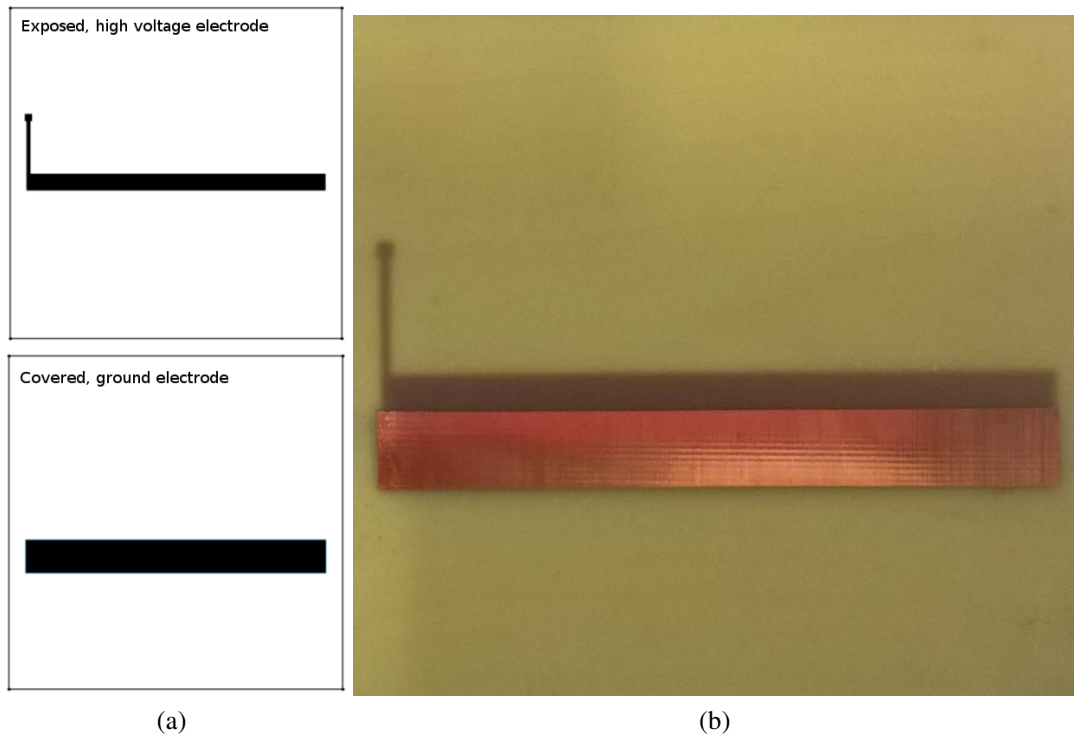


Figure 4.5: Example of the actuator used (not to scale): masks used for etching process (4.5a). Top: exposed, high voltage electrode. Bottom: covered, ground electrode. Image of actuator (4.5b) made of GRE dielectric with copper electrodes.

The discharge is driven by a high-voltage nanosecond pulse generator (Megaimpulse, model: NPG18/3500(N)) that supplies negative pulse polarity at a pulse rise time of approximately 4 ns. In the present study, an input voltage of 12 kV (negative polarity) was used with a pulse frequency of 1 kHz controlled by a function generator (AIM & THURLBY THANDAR INSTRUMENTS, model: TG2000). The negative polarity produces large gross energy related

to strong gas heating [166], thus negative polarity was used in this study. The supplied high-voltage pulses were transferred from the pulse generator to the exposed electrode by a  $75 \Omega$  coaxial cable. The ambient temperature was monitored using a K-type thermocouple with a data acquisition module system (National Instruments Corp., model: NI-9213, 24 bit) driven by LabVIEW. The pressure in a quadrilateral, stainless steel vacuum chamber with volume of  $0.138 \text{ m}^3$  was controlled through a vacuum pump and was measured through a pressure transducer (Kulite, model XTE-190M, pressure range: 0 to 170 kPA Absolute).

The Schlieren technique with a standard Z-type optical arrangement was employed to visualise the qualitative density gradient above the ns-DBD plasma actuator. Figure 4.6 shows a schematic of the experimental set up. The Schlieren system consists of a continuous light source (Newport, model: 66921) with a 450 W Xe arc lamp, a condenser lens with a focal length of 70 mm, a pinhole, a pair of 203.3 mm diameter concave mirrors with a focal length of 1829 mm, a circular dot cut-off plate, an imaging lens, and a high-speed camera. The pinhole in front of the condenser lens creates a light spot that illuminates the first concave mirror. The light beam is then collimated by the first mirror. The collimated beam passes through a 137 mm diameter quartz window of the vacuum chamber and the test section where the ns-DBD PA is located. A second parabolic mirror reflects the beam onto optics and the camera. The circular dot plate is positioned at the focal point of the second mirror.

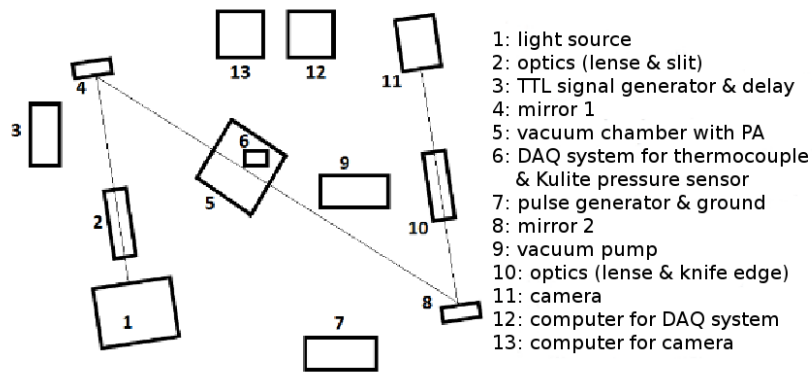


Figure 4.6: Schematic representation of experimental Schlieren set up.

Two high speed cameras, HPV-1 (Shimadzu) and Fast cam SA 1.1 (Photon), were used to capture the effect of pressure on the shock propagation speed and the shock strength. The images were required at a frame rate of 75 kfps (Photon) and 500 kfps (Shimadzu) with an exposure time of 1 second.

In order to measure the high voltage signal provided by the nanosecond pulse generator, the back-current shunt technique was used [158]. Due to the high voltage levels experienced through the core of the supply cable, the signal is instead measured from the current generated in the shielding of the coaxial cable. This is done using a series of resistors, connected in parallel to form a shunt resistor. This resistor is placed across a break in the ground of the coaxial cable

and the voltage across this shunt resistor is measured. The current generated in the ground connection can be related to the voltage using Equation 4.1 from transmission line theory:

$$V_{supply} = \frac{L_{characteristic}}{I}, \quad (4.1)$$

where  $V_{supply}$  is the supply voltage,  $I$  is the current through the transmission line and  $L_{characteristic}$  is the characteristic impedance of the transmission line. For the coaxial cable used in this work, the characteristic impedance is 75  $\Omega$ . The resistance of the shunt resistor is designed to be low, in the order of milliohms in order for the generated voltage to be measured directly through an oscilloscope. The voltage measured can then be converted to the actual voltage supplied,  $V_{actual}$ , to the DBD plasma actuator using Equation 4.2:

$$V_{actual} = V_{shunt} \cdot \frac{L_{characteristic}}{R_{shunt}}, \quad (4.2)$$

where  $V_{shunt}$  is the voltage measured across the current shunt and  $R_{shunt}$  is the known current shunt resistance.

## 4.2.2 ac-DBD experiments

This study discusses the characterisation of ac-DBD plasma actuators to optimise the use of existing plasma generating equipment (PGE) with respect to actuator performance. Parameters considered were the dielectric material, dielectric thickness, and the operating voltage frequency. For the channel PA design, the distance from the exposed, high voltage wire to the encapsulated, grounded electrodes was also varied. Constant inputs included the voltage waveform (sinusoidal) and an input voltage of 20 V to the Minipuls system. Both surface PA and channel PA are used.

The equipment used to generate the high voltage consisted of the Minipuls 4 system manufactured by GBS Elektronik [167]. It takes direct current (DC) voltage from a Voltcraft VSP2410 power supply. The power supply converts a standard (20 V) input to a square-wave AC voltage waveform. Thereafter, the transformer steps up the voltage to the desired value, before producing a sinusoidal waveform as an output. The specifications quoted by the datasheet by Brutscher [168] are voltages up to 40 kV peak to peak or 14 kV Root Mean Square (RMS) at a frequency range of 5-20 kHz. A custom LabVIEW program was used to control the required AC operating frequency (plasma frequency). Figure 4.7 shows the system components and their set-up.

The materials selected were polyimide Kapton, Polytetrafluoroethylene (PTFE), and Glass Reinforced Epoxy (GRE). Kapton was selected as extensive research has been carried out using

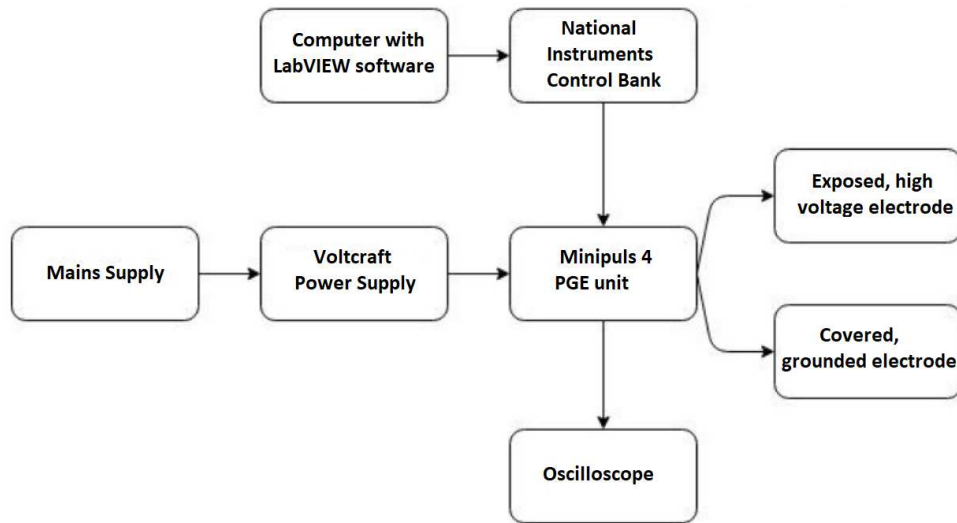


Figure 4.7: Schematic representation of experimental set up.

Table 4.1: Dielectric materials used with corresponding physical properties.

Dielectric material	Kapton	PTFE	GRE
Dielectric strength [kV/m]	16535	11220	15000
Dielectric constant $\epsilon_r$	3.70	2.10	4.48
Glass transition temperature $T_g$ [K]	635	390	400

Kapton tape as the dielectric material, therefore it would provide a good baseline result. GRE and PTFE have dielectric constants higher and lower than Kapton, respectively. See Table 4.1 for dielectric properties of the selected materials.

For the surface PA, the exposed high-voltage and ground electrodes were  $L_2 = 6$  mm and  $L_1 = 18$  mm wide, respectively. The electrodes were made of  $35 \mu\text{m}$  thick copper tape ( $t_1$  and  $t_2$ ). The electrodes are separated by a dielectric material of various thicknesses,  $t_3$ , of 0.5, 1.0, 1.5, 2.0, and 3.0 mm. There is no discharge gap between the electrodes. The overlapping, lateral length of the electrodes is 100 mm - the length over which plasma is expected to form. Surplus copper was put in place to attach the high voltage and ground connections to the electrodes. These regions were covered with dielectric, polyimide film. The ground electrode was fully covered by three layers of polyimide film, approximately  $210 \mu\text{m}$  thick in total. The polyimide film covered the exposed electrode 7.5 mm from both lateral side edges to prevent plasma arcing on the sides of the actuator, see Figure 4.8.

Plasma actuator performance was characterised with induced velocity data acquired via a traversable pitot tube connected to a FC012 micromanometer from Furness Controls and particle image velocimetry (PIV) flow field measurements. The manometer has a precision better than  $\pm 0.5\%$ . The glass pitot tube was manufactured to a specification of 100 mm straight section with a 90 degree bend followed by a 60 mm long straight section. Glass was the material of

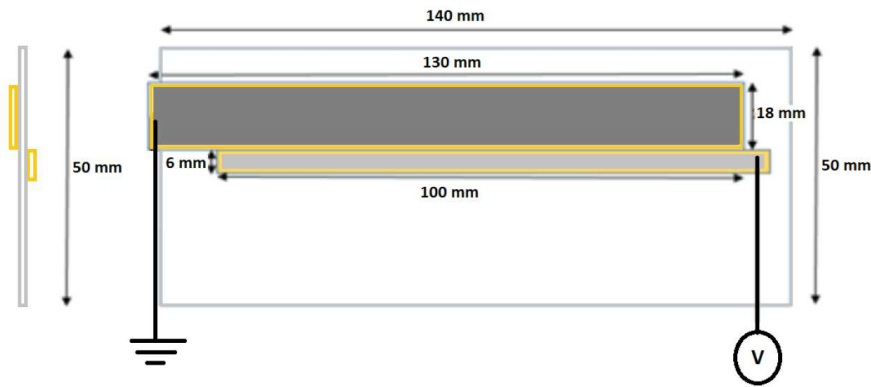


Figure 4.8: Design and layout of surface plasma actuator used. Left: side view, right: top view.

choice in order to prevent arcing from the discharge region to the pitot tube. The inner and outer radii were 0.3 mm and 1.2 mm, respectively. These dimensions allowed for measurement of the actuator jet velocity without the pitot tube affecting the flow field. Pitot tube readings were time averaged over 5 seconds and the mean of three consecutive readings is presented in this paper. An Agilent Technologies DSO3102A oscilloscope was used to record the current and voltage signals passed to the plasma actuator from the Minipuls system.

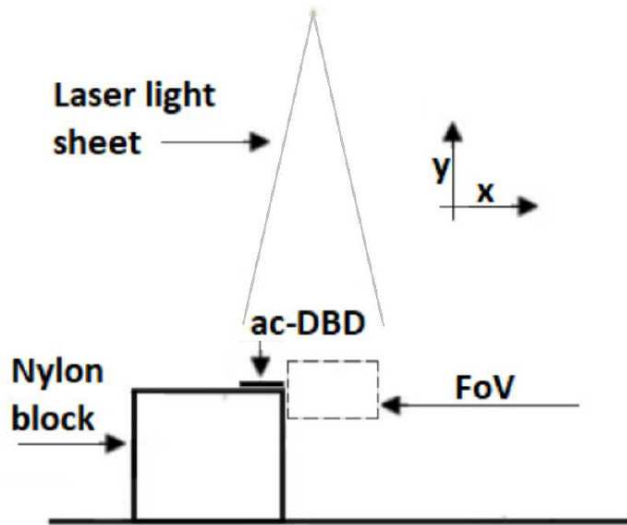


Figure 4.9: Schematic representation of PIV set up including field of view (FoV) and plasma actuator positioning.

PIV was conducted in a closed return wind tunnel at the National Wind Tunnel Facility (NWTF) at the University of Glasgow. The wind tunnel was run to disperse the seeding particles uniformly in the test section but turned off until quiescent conditions set in. The plasma actuator was positioned on a nylon block to allow optical access. The PIV set up is given in Figure 4.9.

The velocity jet produced by plasma actuators is three dimensional. However, two dimensional PIV is used to capture the velocity of the ionic wind. The highest velocities are generated close to the exposed electrode edge. The jet diffuses and slows down downstream from this

Table 4.2: Set up for PIV flow field measurements.

laser wavelength [nm]	pulse duration [ns]	flash lamp rate [Hz]	delta t [ $\mu$ s]	f#
535	8	10	60	2.8

point. The aim is to take measurements along the centreline of the actuator as close as possible to the electrode edge where the jet velocities are highest. It is assumed that the jet is uniform off centre along the exposed electrode edge hence 2D PIV is conducted.

Seeding particles were generated with a smoke machine that generates a fine mist. A spectra-Physics, Lab 130-10 Nd: YAG, single cavity, double pulsed, frequency-doubled laser produced the laser light sheet. The field of view was 110 by 110 mm with a spatial resolution of 2048 by 2048 pixels. Post processing of PIV images was performed using a tested cross correlation based procedure implemented with a vector validation scheme [169]. Results shown here were obtained using a forward/reverse tile testing (FRTT) correlation algorithm. A two-pass cross correlation analysis was used. The first with a 64 by 64 pixel window size and 50% overlap, and the second with a 32 by 32 pixel window size and 25% overlap.

Other PIV parameters are given in Table 4.2. The time delay between image pairs was set to  $60\mu$ s based on the expected plasma jet velocities and the desired displacement of particles between two consecutive images. The f# of the camera was chosen so that the depth of field is small enough to focus on particles at one distance away only. That is on particles that are passing along the laser light sheet.

An often encountered issue when dealing with high voltage equipment is electromagnetic interference (EMI) [170, 171]. This well known problem has the potential to affect electronic devices and cause system failures. In the NWTF laboratory this was avoided with measures including limiting the high voltage wire length, using aluminium foil shielding, and increasing the physical distance between sensitive devices such as the PIV and DAQ systems and the high voltage equipment.

## 4.3 Results & discussion

### 4.3.1 ns-DBD plasma actuators

The voltage supplied to the actuators is shown in Figure 4.10 which also shows the 20% and 80% treshhold lines. Those were used to evaluate the pulse width, rise time, and fall time of the signal. Measurements show a triangular signal with a pulse width of 6 ns, a rise time of 3.8 ns, and a peak, negative polarity voltage of 9.45 kV. The fall time seems to be longer than the rise time, lasting 9 ns based on the 20% and 80% threshhold values of the peak voltage. Current measurements were not taken during experiments.

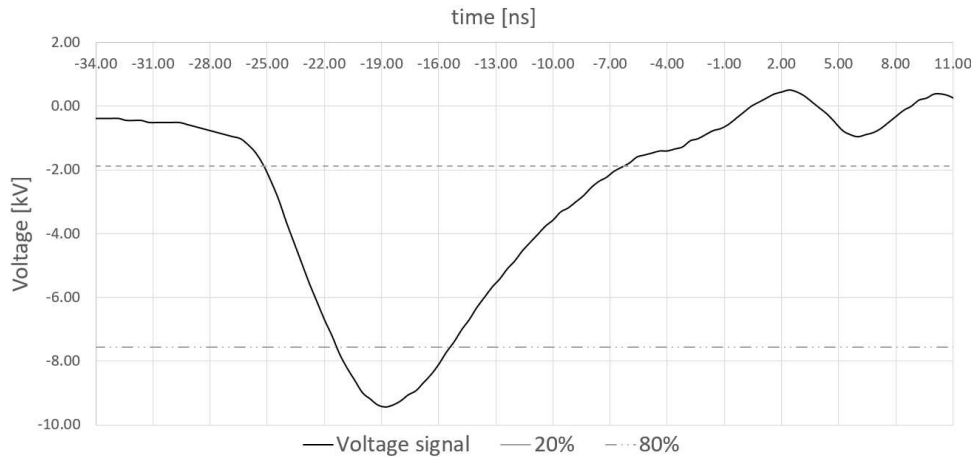


Figure 4.10: Voltage signal supplied to plasma actuators with the 20% and 80% threshold lines used to evaluate the pulse width, its rise and fall time.

The ns-DBD actuator generates a distinct, cylindrical shock wave with a tail which propagates from the actuator surface as is evident from the Schlieren images shown in Figure 4.11. There is also a clear planar wave which has been previously recorded in an experiment by Takashima [172]. These two waves are shown for the case of an ambient atmospheric pressure and temperature within the experimental domain and an actuator thickness of 0.8 mm. The shock wave is shown for two times after actuation: 13.3  $\mu\text{s}$  and 26.7  $\mu\text{s}$  respectively.

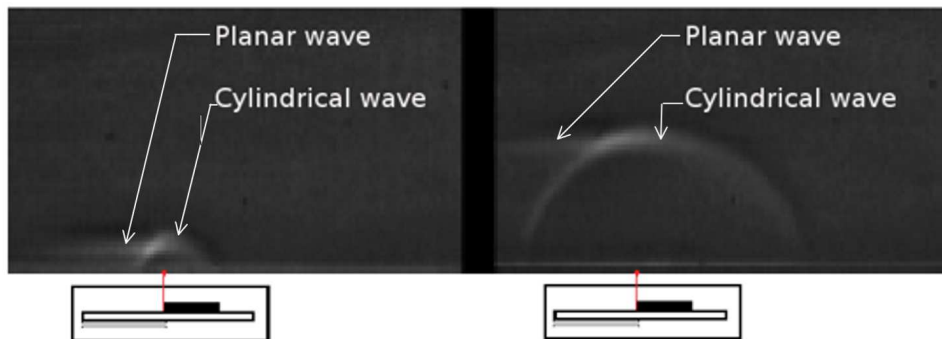


Figure 4.11: Schlieren image of distinct, cylindrical and planar shock wave generated from the ns-DBD actuator of 0.8 mm thickness at ambient (atmospheric) conditions. The location of the plasma actuator is shown with the ground electrode coloured grey, the dielectric barrier coloured white, and the high voltage electrode coloured black.

### Shock propagation

Propagation speed of the shock wave is calculated based on the location of the shock front in consecutive Schlieren images and the time between these images. The location of the shock front

is estimated by analysing the profile of the image intensity values across it and then searching for the maximum value in a purpose written post-processing code.

The following plots in Figures 4.12 to 4.14, show the shock propagation speed and the distance travelled by the shock front with time for the three actuator thicknesses ( $t = 0.4, 0.8,$  and  $1.6$  mm).

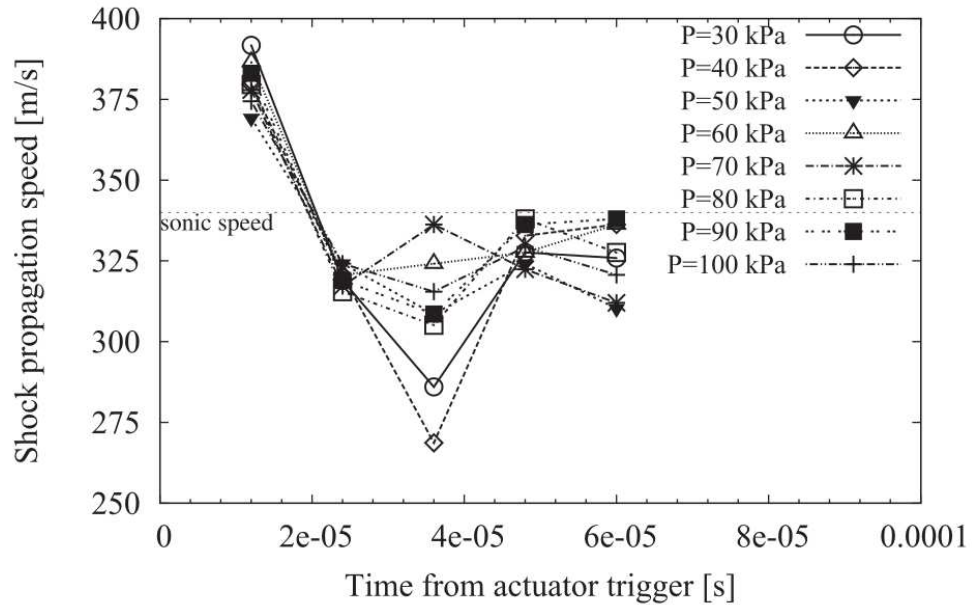


Figure 4.12: Shock propagation based on shock front location: time vs velocity. Actuator thickness: 0.4 mm.

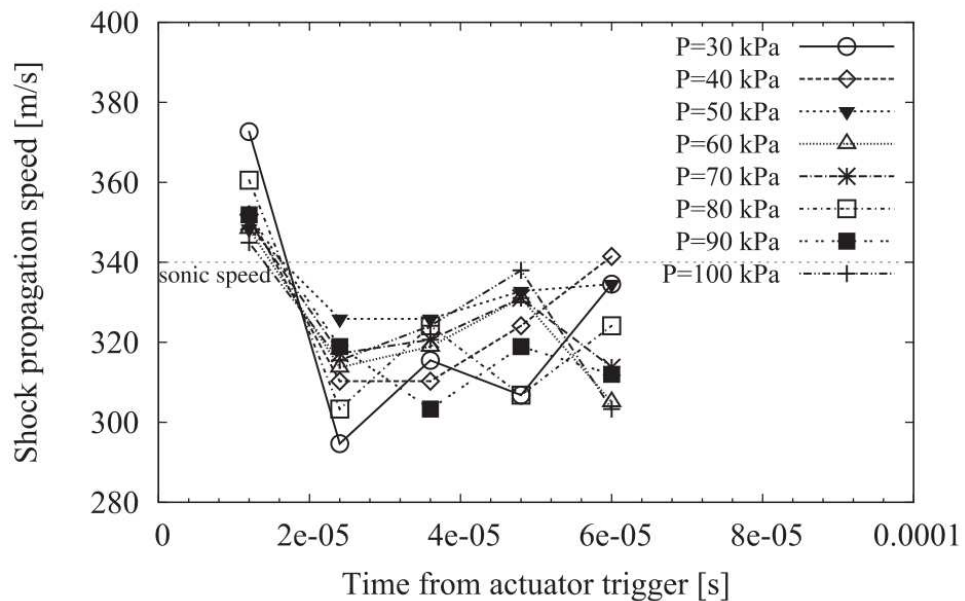


Figure 4.13: Shock propagation based on shock front location: time vs velocity. Actuator thickness: 0.8 mm.

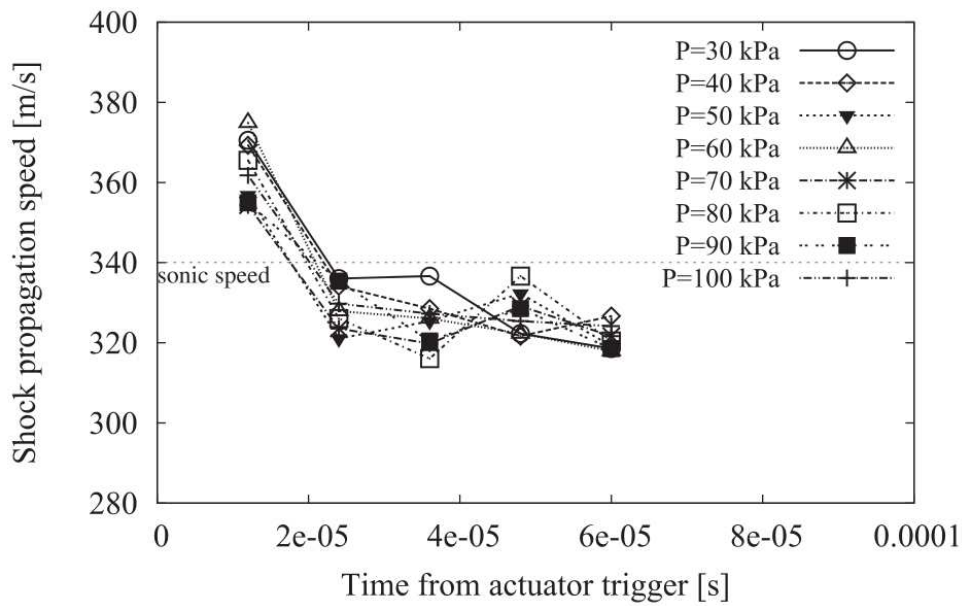


Figure 4.14: Shock propagation based on shock front location: time vs velocity. Actuator thickness: 1.6 mm.

### Shock strength

The shock strength was estimated based on the intensity values of the captured Schlieren images. An image processing software was used to combine a number of Schlieren images showing the propagation of a single shock wave in one image. Next, a purpose written Matlab code analysed the intensity of each pixel on the image along a vertical line from the centre of the actuator surface to the top of the image. Peak values of intensities and their corresponding vertical location are also extracted. Peak intensity values,  $I$ , are normalised by the background intensity,  $I_b$ , of each image. Image intensity was obtained from ten images of shock propagation. Normalised shock intensity,  $I/I_b$ , has a mean value of 5.11 (for a pressure of 60 kPa and a dielectric thickness of 0.4 mm) with a standard deviation of 0.243. The standard deviation is significantly smaller (below 5%) than the mean, therefore there is a high degree in repeatability. An example of this process is shown in Figure 4.15.

Figure 4.16 shows the intensity profiles of ten instances of recorded shock waves. Profiles indicate little spread in shock strength and wave front speed for recorded shock waves. The intensity values closest to the actuator region,  $230 < Y < 250$  pixels, show strong gradients in the vicinity to the discharge in what is known as the generated heat plume [149].

For the three actuator thicknesses used, 0.4, 0.8, and 1.6 mm, the process above was repeated for Schlieren images capturing ten separate shock waves for each pressure value in the vacuum chamber. The results presented below are the average of all ten instances. The plots in Figures 4.17 to 4.19, show the normalised shock strength,  $I/I_b$ , with vertical distance from the actuator surface. The pressure ranges from 30 to 100 kPa.

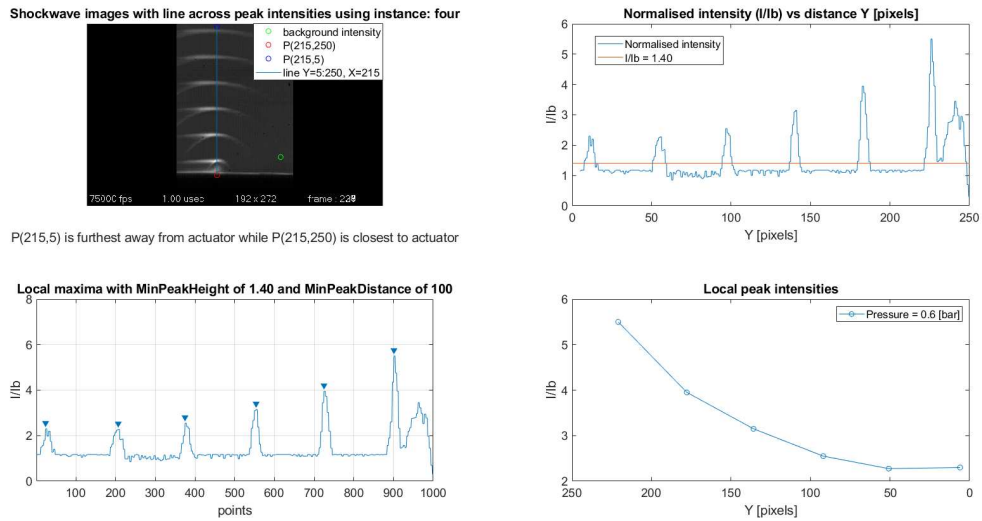


Figure 4.15: Example of output from Matlab code. Top left: Combined Schlieren images of the propagation of a single shock wave with the vertical line (from 215:5 to 215:250) indicating the position intensities are extracted from. Top right: Pixel intensity profile along line from 215:5 to 215:250. Bottom left: Pixel intensity profile with identified peak values that correspond to the shock wave fronts. Bottom right: Normalised shock strength  $I/I_b$  vs vertical distance [pixels] from actuator surface.

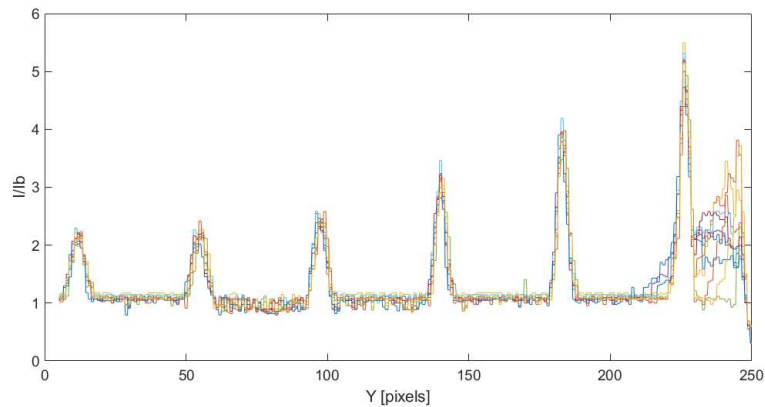


Figure 4.16: Normalised intensity profiles,  $I/I_b$ , along vertical line across ten shock wave propagation images.

## Discussion

Previous studies by Roupasov et al. [72] and Takashima et al. [172] showed that ns-DBD generated compression waves propagate with an approximately sonic velocity. This is confirmed by the shock propagation recorded through Schlieren images in this study. These results indicate that there is very little variation for different ambient pressures. However, from figs. 4.12 to 4.14, it is evident that the initial propagation velocity near the discharge is considerably higher though the waves remain sonic. The Mach number increases near the surface due to the high

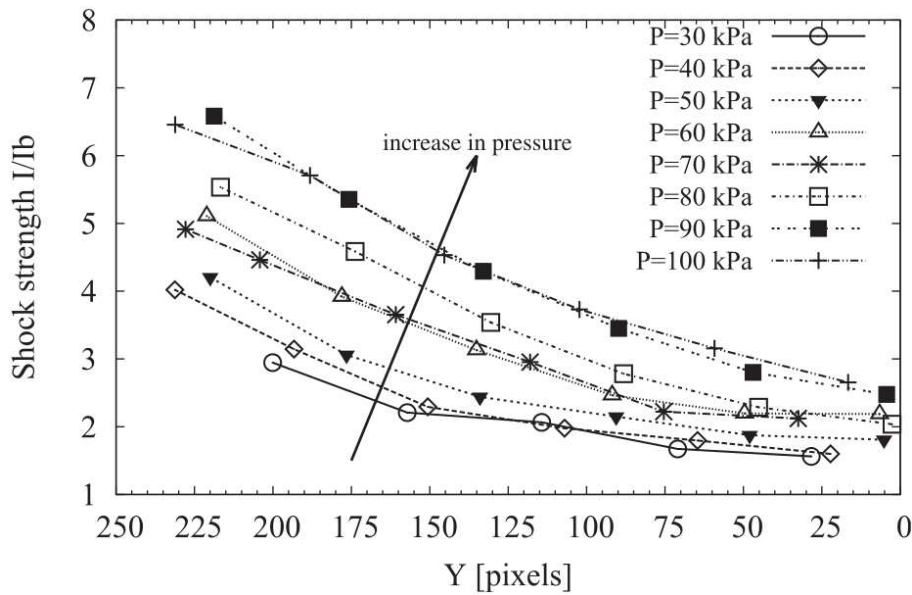


Figure 4.17: Normalised shock strength  $I/I_b$  vs vertical distance from actuator for a pressure range of 30 to 100 kPa. Actuator thickness is 0.4 mm.

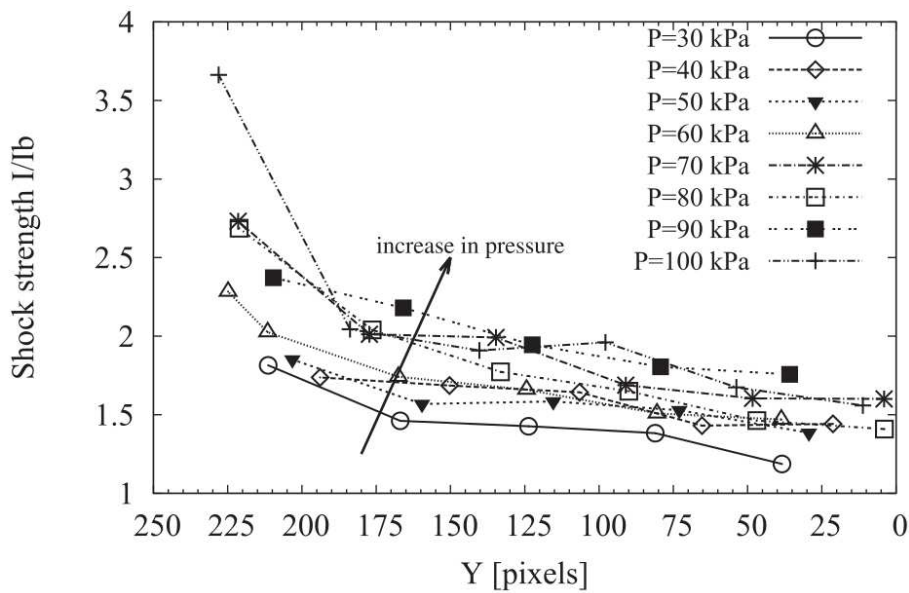


Figure 4.18: Normalised shock strength  $I/I_b$  vs vertical distance from actuator for a pressure range of 30 to 100 kPa. Actuator thickness is 0.8 mm.

temperature which results in higher wave speeds for Mach = 1. This has also been noted by other studies [72, 172].

From the results obtained, it is clear that a higher ambient pressure leads to a stronger shock strength. This has been observed for all three actuator thicknesses. With a higher pressure, the air density is greater, so that there are more particles being ionised by the electric field. Due to the higher number density of particles, it is believed that more exothermal recombination reactions take place which increases the shock strength of the generated shock wave. The effect

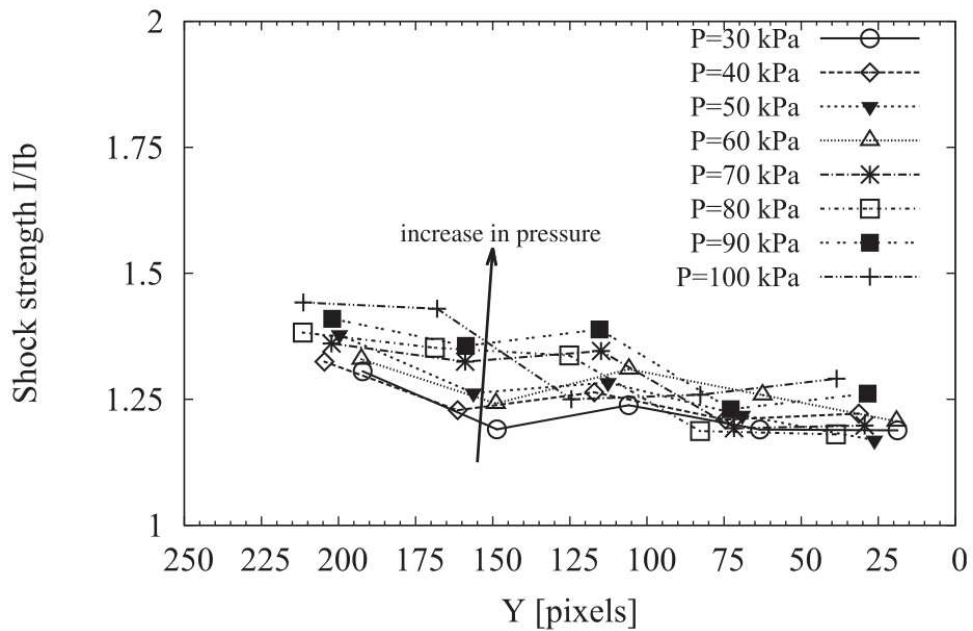


Figure 4.19: Normalised shock strength  $I/I_b$  vs vertical distance from actuator for a pressure range of 30 to 100 kPa. Actuator thickness is 1.6 mm.

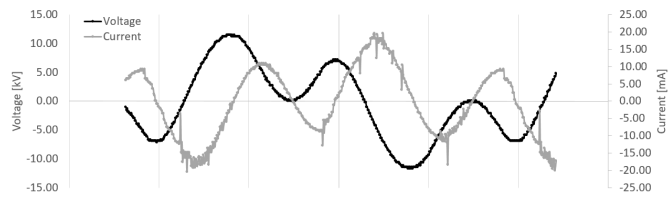
of ambient pressure on ultra-fast gas heating is not clear.

A second observation is that the actuator thickness also influences the shock strength considerably. As the resistance of the electric circuit is proportional to the actuator's thickness, this has a direct effect on the strength of the electric field generated by the ns-DBD PA. The electric field strength determines the rate/extent of the ionisation of air particles and hence the shock wave strength is enhanced. Therefore, the thinner actuator leads to a greater shock strength.

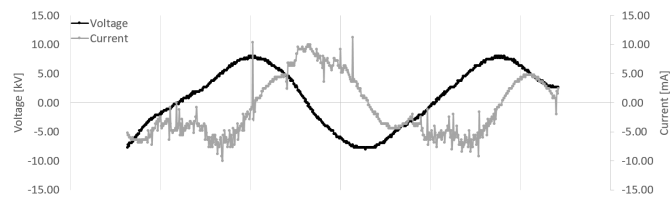
### 4.3.2 ac-DBD plasma actuators

Induced velocities from pitot tube and PIV measurements are presented for the surface PA. The power consumption of each plasma actuator is also shown. Voltage and current waveform plots passed to the actuator are presented in Figure 4.20 for frequencies of 5, 7, and 10 kHz with a 0.5 mm thick Kapton dielectric material. High-amplitude spikes of current are typical for plasma actuators [173] and indicate ionisation. They are the result of each micro-discharge and occur twice per cycle. Characteristically, the current and voltage are 90 degrees out of phase [142]. Based on the spike occurrence, it appears the 7 kHz case has more ionisation than the 5 kHz or 10 kHz cases. The impedance of PA, the electrostatic capacity, and the length of the high voltage cable can all influence the output voltage signal and hence the ionisation levels.

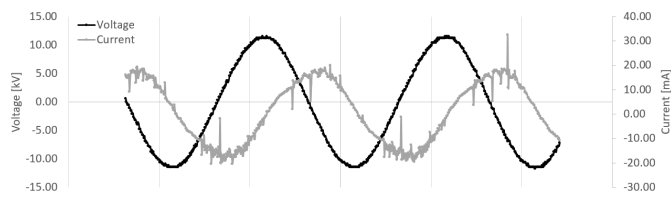
Initially, a study was conducted to establish the optimum location to measure plasma induced velocity downstream of the surface actuator. Figure 4.21 shows induced velocity measurements along the centreline of the actuator with streamwise and vertical positions of the Pitot tube. This exercise was performed with a PTFE plasma actuator of 1.0 mm thickness at a driving frequency



(a)



(b)



(c)

Figure 4.20: Measured voltage and current signal waveforms passed to the plasma actuator for a 0.5 mm thick Kapton dielectric with (4.20a) 5 kHz, (4.20b) 7 kHz, and (4.20c) 10 kHz signal frequency.

of 10 kHz. Results show a peak induced velocity at a downstream distance of 4 mm from the high voltage electrode edge and a vertical location of 0.6 mm. All measurements presented and discussed hereafter refer to data collected at this optimum position.

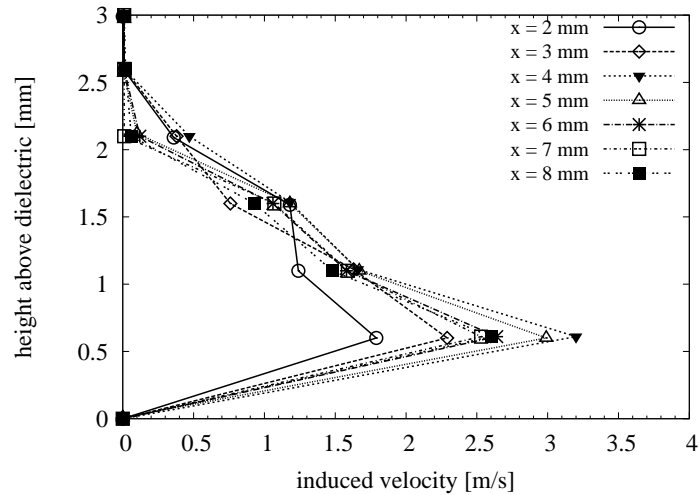


Figure 4.21: Induced velocity with x-y location along centreline ( $z = 0\text{mm}$ ) downstream of plasma actuator.

### Pitot tube measurements

Induced velocity measurements of the three dielectric materials and for five dielectric thicknesses for a frequency range of 5 to 10 kHz are presented in Figures 4.22a, 4.23a, and 4.24a. Higher frequencies resulted in the dielectric materials breaking down and the actuators becoming damaged with visible signs of degradation of the dielectric material due to arcing. Damaged actuators were replaced with spare ones. This did not effect measurement results as the GRE and PTFE dielectric material was machined to size in order to keep a consistent geometry of the actuators. Measurements were taken with a traversable pitot tube along the centreline of the exposed actuator. Each data point is the average of three measurements.

Plots of consumed power by the plasma actuators are given in Figures 4.22b, 4.23b, and 4.24b. Consumed power was calculated by multiplying the root mean square values of the voltage and current signals recorded over one period by the oscilloscope.

$$P_c = V_{RMS}I_{RMS}. \quad (4.3)$$

### PIV measurements

Two component PIV measurements were taken for two configurations of surface plasma actuators with PTFE and GRE as the dielectric material. Kapton could not be used due to excessive

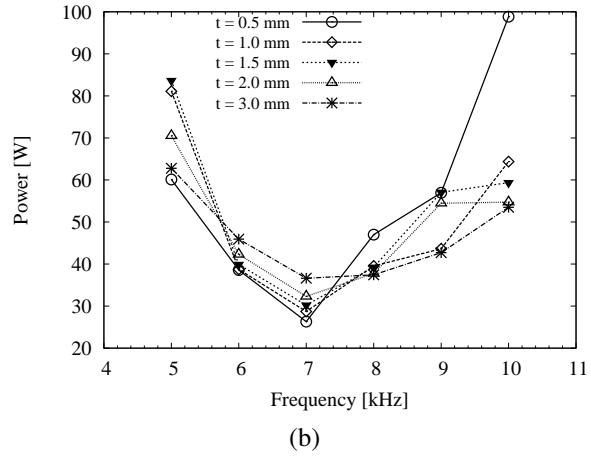
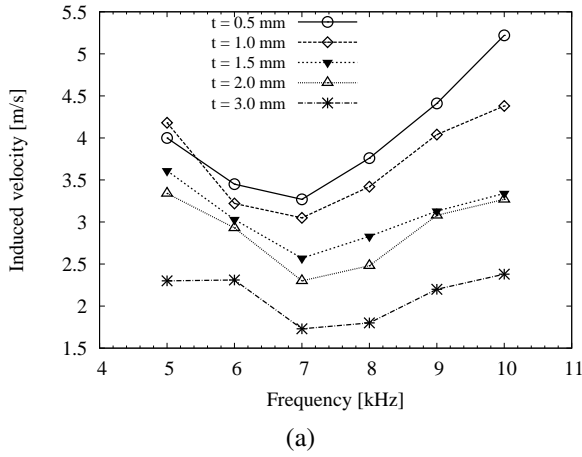


Figure 4.22: Induced velocity with frequency for varying thicknesses of Kapton dielectric material,  $\epsilon_r = 3.70$  (4.22a) and the corresponding power used (4.22b).

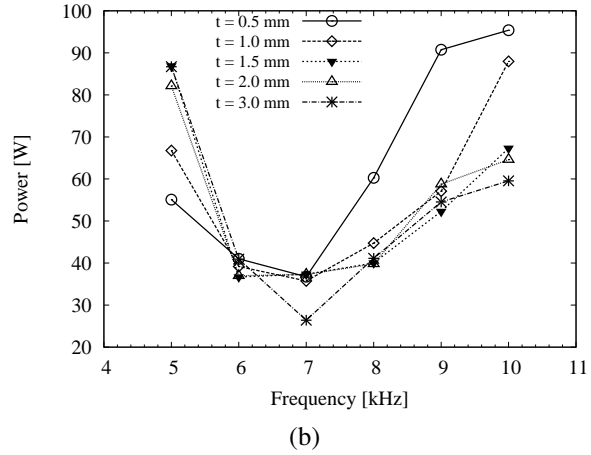
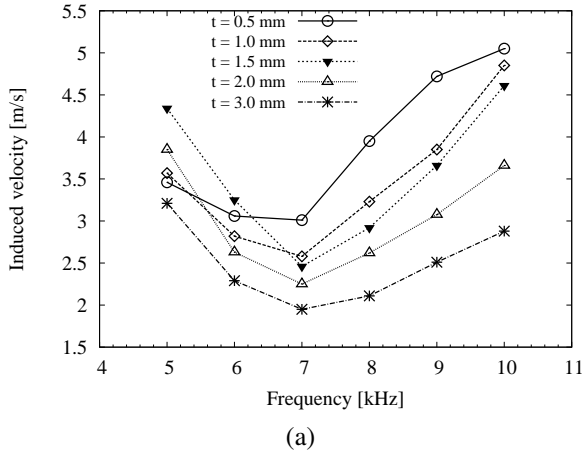


Figure 4.23: Induced velocity with frequency for varying thicknesses of GRE dielectric material,  $\epsilon_r = 4.48$  (4.23a) and the corresponding power used (4.23b).

Table 4.3: Best performing surface PA and their properties.

Dielectric material	Kapton	PTFE	GRE
Thickness [mm]	0.5	0.5	0.5
AC frequency [kHz]	10	10	10
Velocity [ $\text{ms}^{-1}$ ]	5.22	4.66	5.05

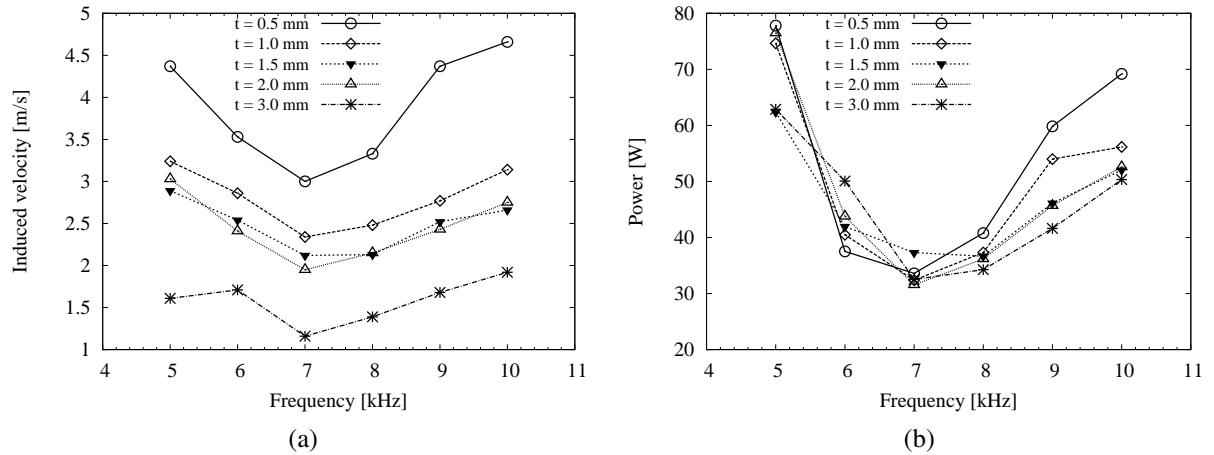


Figure 4.24: Induced velocity with frequency for varying thicknesses of PTFE dielectric material,  $\epsilon_r = 2.10$  (4.24a) and the corresponding power used (4.24b).

laser sheet reflections from its tape surface resulting in poor PIV data sets. The two cases correspond to the PTFE and GRE cases from Table 4.3. In total, three sets of 20 image pairs were recorded. Statistical convergence was established with fewer image pairs. Results obtained from processing fewer vector maps were qualitatively similar to those obtained by processing the full set of 60. The PIV error,  $E_u$ , estimate was calculated based on the magnification factor,  $M$  [pixel/m], and the time step  $\Delta t$  between image pairs assuming a maximum displacement error of 0.1 pixels as given by [174]:

$$E_u = \frac{0.1}{M * \Delta t} = \frac{0.1}{\frac{2048}{0.11} * 60 * 10^{-6}} = 0.0895 [m/s]. \quad (4.4)$$

The plasma actuators were positioned on the edge of a nylon support block to allow optical access to the region of interest i.e. the ionic jet coming off the plasma actuator. Due to reflections from surfaces, namely the actuator geometry itself, the field of view (FoV) of the camera had to be reduced and shifted to exclude the actuator geometry. The FoV captures the edge of the nylon block/actuator with the jet only visible from a distance of 18 mm (the length of the covered electrode) off the exposed electrode onwards i.e. not directly from the edge of the high voltage electrode where the induced flow is highest. The PIV region does not cover the peak velocity jet location.

Time averaged velocity vector fields for both cases are presented in Figures 4.25 and 4.26.

The averaged velocity profiles along horizontal and vertical planes are also shown in Figures 4.27 and 4.28, respectively.

## Discussion

The highest averaged induced velocity was achieved with Kapton tape as the dielectric. It was operating at an AC frequency of 10 kHz, and a material thickness of 0.5 mm yielding a velocity

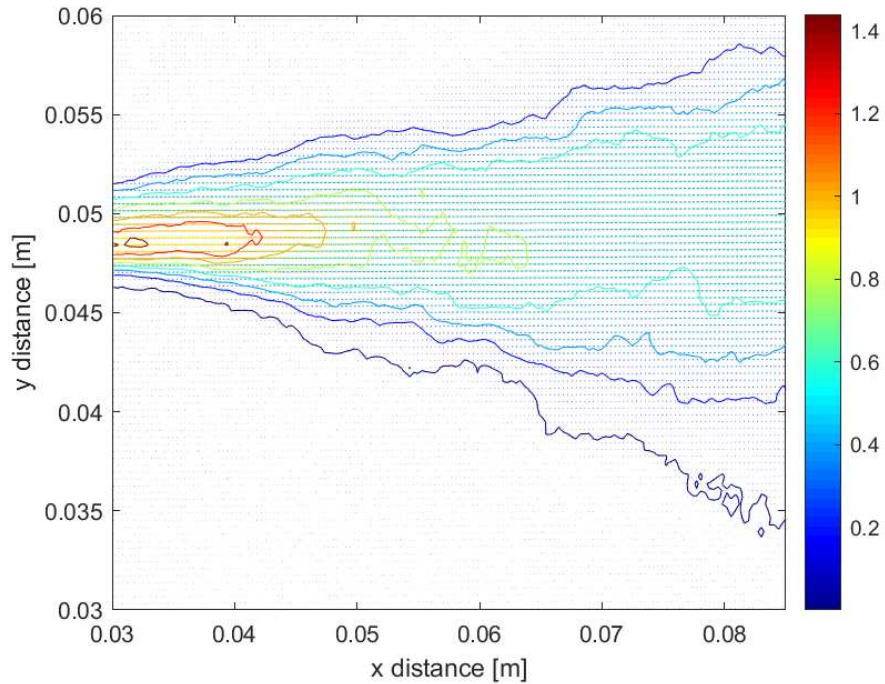


Figure 4.25: Time averaged velocity vector plot from PIV for surface PA with a 0.5 mm GRE dielectric material. Units are in  $\text{ms}^{-1}$  with the horizontal and vertical axes showing the FoV.

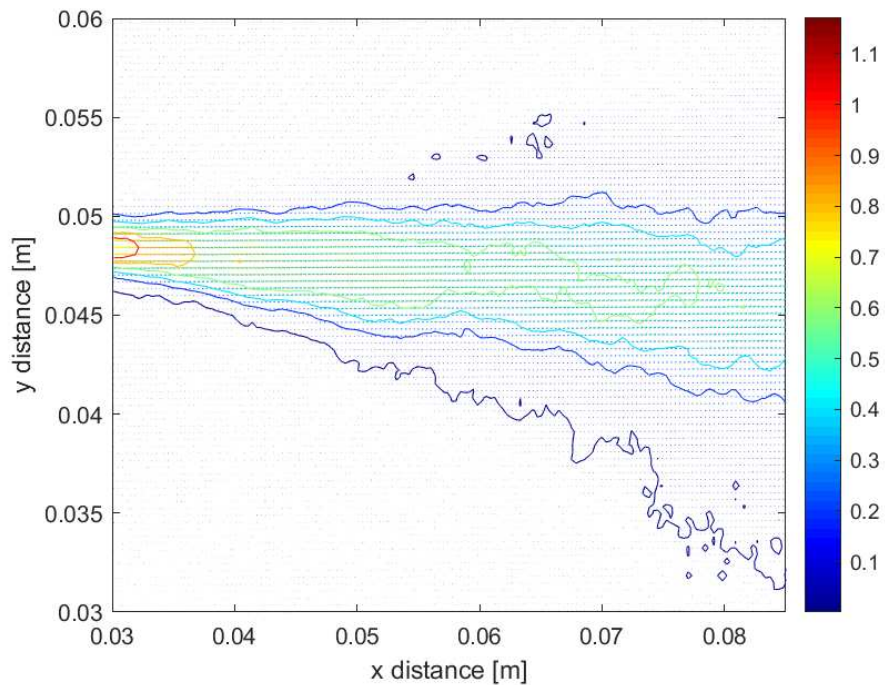


Figure 4.26: Time averaged velocity vector plot from PIV for surface PA with a 0.5 mm PTFE dielectric material. Units are in  $\text{ms}^{-1}$  with the horizontal and vertical axes showing the FoV.

of  $5.22 \text{ ms}^{-1}$ . GRE and PTFE both produced velocities over  $4.5 \text{ ms}^{-1}$ . For the set power supply input conditions of 20 V and 0.12 A, the thinnest dielectric performed best for all materials.

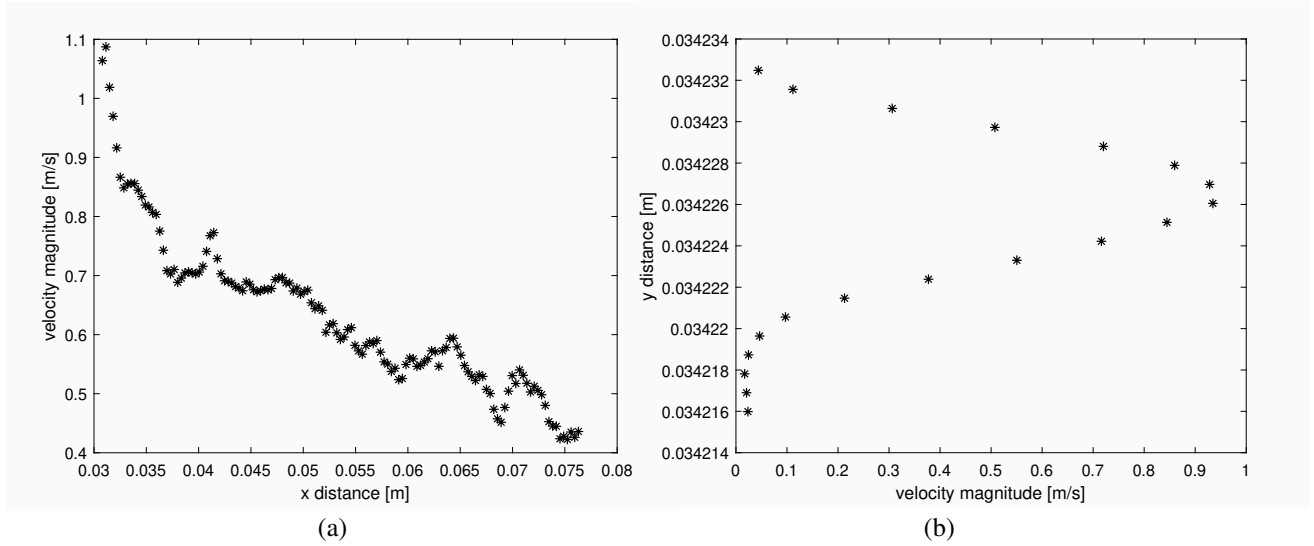


Figure 4.27: Induced flow air jet velocity profiles for PTFE surface PA: (4.27a) horizontal velocity profile along  $y=0.049$  m, (4.27b) vertical velocity profile along  $x=0.034$  m.

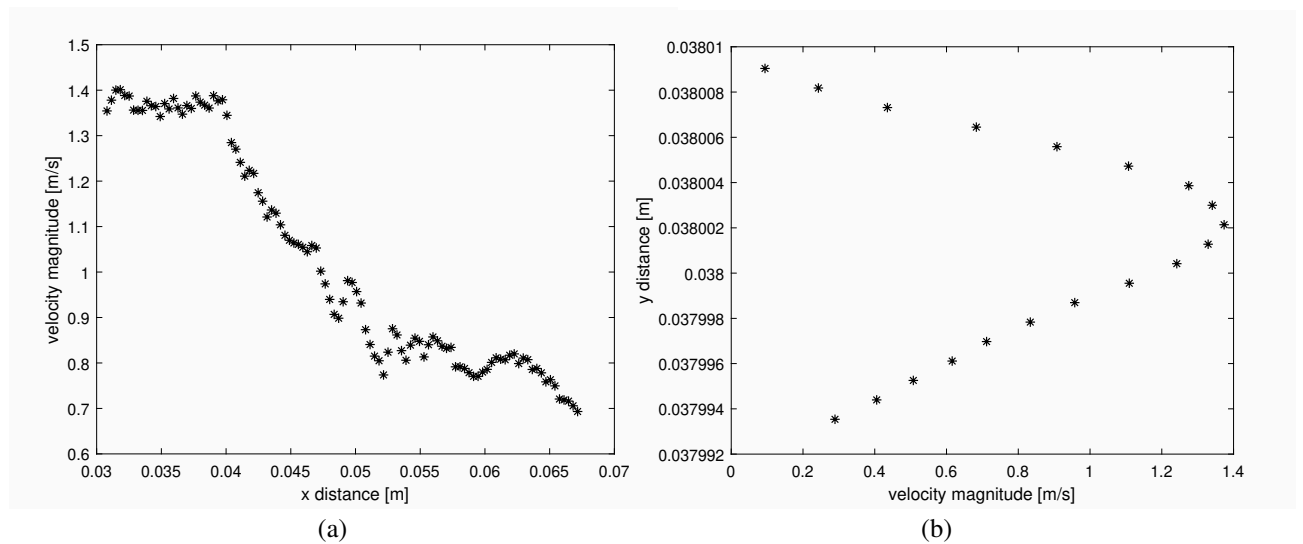


Figure 4.28: Induced flow air jet velocity profiles for GRE surface PA: (4.28a) horizontal velocity profile along  $y=0.049$  m, (4.28b) vertical velocity profile along  $x=0.038$  m.

As the material thickness increased, the induced velocity is reduced, due to the constant input voltage. Since the input voltage is constant, thicker dielectric materials perform worse as the electric field strength decreases. Operating frequencies of 5 and 10 kHz resulted in the highest measured induced velocities while the ionic wind was lower for other frequencies. A minimum induced flow was consistently recorded for a frequency of 7 kHz, irrespective of the dielectric material or its thickness. Table 4.3 summarises the best performing surface plasma actuators.

Power consumption was highest for frequencies of 5 and 10 kHz irrespective of the dielectric material. Those cases correspond to the highest induced velocities recorded. A minima of power consumption was consistently recorded at a frequency of 7 kHz. This is not expected as other studies show an increase in ionic wind with increasing signal frequencies [121, 175]. However, a change in plasma from a corona discharge to a streamer discharge can result in a decrease in the body force generated and hence lower consumed power levels. See Figure 4.20 for measured voltage and current waveforms with 5, 7, and 10 kHz frequency signals.

PIV measurements clearly show the jet of air formed by the plasma actuators. Peak velocities are, however, much smaller than recorded with the pitot tube. This is expected because the distance from the exposed electrode edge to the pitot tube was much smaller than in the PIV set-up. Reflections rendered the near actuator vector field useless and hence were excluded from the analysis. The error in velocity is only about 0.064% and 0.081% of the maximum velocities recorded for the GRE and PTFE vector fields.

The GRE surface PA produces an induced jet with more vertical spreading (diffusion) than the PTFE actuator which has a much more confined jet structure. This may be due to a buoyancy effect which is related to heat release within the dielectric materials. This would result in different surface temperatures between the two cases inducing a different convection of the induced jet.

The vertical induced jet profiles show more clearly the vertical spread of the two induced jets. Looking at the horizontal velocity profiles across the induced air jets, it is clear that there is a considerable drop off in velocity with distance from the exposed electrode. This is significant, as it limits the effects of the ionic flow to the vicinity of the PA. The total rate of velocity decrease is  $-14.8$  and  $-20.2 \text{ ms}^{-1}$  per metre for the PTFE and GRE surface PA, respectively.

Compared to the velocity magnitudes seen in the Wellborn s-duct which reach  $200 \text{ ms}^{-1}$  it is questionable whether the plasma jet strength is sufficient to have a meaningful impact on the duct throughflow. In relation to the freestream velocities the plasma induced jet strengths reaches only about 2.5 % of the freestream. However, the aim is to use the plasma jets to reenergize the near wall fluid within the boundary layer which is much slower.

## 4.4 Conclusions

For the ns-DBD plasma actuators shock wave propagation speed and strength were recorded showing clear trends with decreasing ambient pressure. Higher ambient pressures result in stronger shock waves; this has been observed irrespective of the actuator thickness. This might be explained with fewer air molecules to ionise at lower ambient pressures and hence a lower temperature from the exothermal recombination reactions which produce thermal energy. This finding has, potentially, implications on using plasma actuators at altitude i.e. on airborne vehicles where the ambient pressure is naturally lower than at sea level. Although, the effect of ambient temperature would also have to be considered. To the author's knowledge, no such experiment linking plasma actuator performance to altitude is available in the literature. The data further shows that the thickness of the dielectric barrier also influences the shock strength. In accordance with previous findings it was confirmed that a thinner dielectric barrier results in a greater shock strength.

For the ac-DBD plasma actuator, PTFE and GRE dielectric materials performed similarly, with Kapton producing the highest induced velocity jet of  $5.22 \text{ ms}^{-1}$ . Higher plasma ionisation tends to occur with operating frequencies of 5 and 10 kHz. Power consumption is also greater for frequencies of 5 and 10 kHz. Results show a clear minimum power consumption at 7 kHz for all tested cases. With the voltage input being constant, thinner dielectric materials outperformed thicker ones. For a given thickness, GRE, which has the smallest dielectric constant of the materials tested, resulted in higher induced velocities. However, the thinnest dielectric of 0.5 mm does not exhibit the same behavior. A high gradient of velocity reduction with streamwise distance was recorded. This is significant, as it shows plasma actuators have mostly localised effects. The GRE surface PA had a total rate of velocity decrease of  $-20 \text{ ms}^{-1}$  per metre.



# Chapter 5

## DBD plasma numerical models

### 5.1 ns-DBD model

Various models exist in the literature to numerically simulate ns-DBD plasma actuation. The most detailed models aim at modelling the chemistry of particle dynamics including reaction equations. On the other spectrum, phenomenological models try to reproduce the effects of an ns-DBD plasma actuator without resolving the chemistry of the discharge process. Both approaches have their merits with the former being more physical, producing insights into the discharge process while the latter is usually less computationally expensive and simpler in nature.

Many researchers chose to create a detailed physical model of ns-DBD plasma generation including near wall electric field equations, adding electron and ion densities in the gas, and solving drift diffusion equations [70, 176, 177]. Unfer and Boeuf [70] implemented a two dimensional ns-DBD model taking into account the drift diffusion and local field approximations. The latter is used to approximate the energy gained by charged particles from the electric field by locally balancing the gains with losses due to collisions with neutral molecules. The former assumes that a particle's momentum can be estimated by equating a particle's fluxes with the sum of a drift and a diffusion term.

However, most researchers agree that given the timescales involved there is no added benefit from adding ion motion, electron diffusion, and chemical recombination processes to plasma modelling unless the focus is on studying those interactions and the discharge mechanism. This is not the case in this thesis, so a phenomenological model is used instead.

Here a phenomenological model is selected hence the aim of this work is to apply a numerical ns-DBD model and determine its effect on the flow field within a convoluted duct. The model is adapted from the method proposed by Gaitonde [178, 179] and is based on a heated volume region. Similar approaches are used by Zhao and Kinefuchi [180, 181].

### 5.1.1 ns-DBD model implementation

A numerical model of ns-DBD PA was implemented in OpenFOAM for the use with transient, compressible computational fluid dynamics (CFD) calculations. A region of the mesh is selected for which a Gaussian temperature profile is prescribed to simulate the heat addition by the ns-DBD plasma actuators. See Figure 5.1 for the temperature profile prescribed to the heated region. The non-symmetric nature of the profile results in both a cylindrical and planar shock wave being generated. The length of the Gaussian profile was chosen based on the covered electrode width along which the plasma is generated. Discharge distance or streamer length, which actually govern the extent of the heated region, were not available from experiments to use.

The governing equation defining the heat addition is multiplied by a factor ( $\chi$ ) of the ambient temperature  $T_{amb}$ :

$$T = T_{amb} + \sqrt{\frac{\gamma}{2\pi x^3}} \exp\left(-\frac{\gamma}{2\beta^2 x}(x - \beta)^2\right) T_{amb} \chi \quad (5.1)$$

The symbols  $\gamma$  and  $\beta$  are parameters used to alter the Gaussian profile and its mean value, respectively. In this study,  $\gamma$  is set to 1 and  $\beta$  to 0.3.

Implementation is achieved through a local cell set temperature constraint that follows the desired Gaussian profile. To this end a new constraint functionality in OpenFOAM was created, called nsdbdTemperatureConstraint. This functionality uses a selected mesh region to prescribe temperature values to their cell centres based on the governing equation for temperature addition.

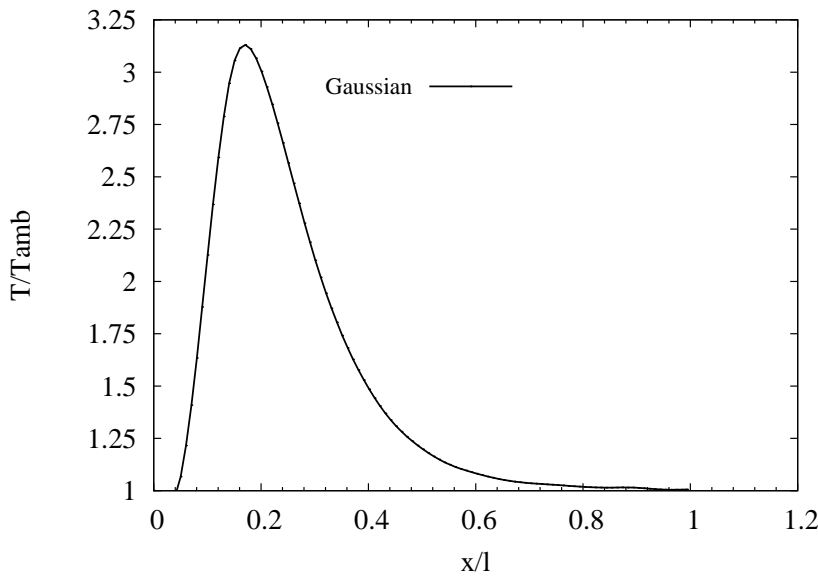


Figure 5.1: Gaussian distribution of temperature profile prescribed to heated region. Shape adapted from [178, 179].

The Gaussian temperature profile is essential to capture the shock structure while the uniform

and step profiles of temperature do not produce a good match [178]. In the current implementation, the pulse time, rest time, actuator length and width, and its starting point can all be set by the user. It is also possible to create multiple heated regions and investigate the effect of a number of actuators. The fvOptions file used to set up these parameters is included in the appendix.

### 5.1.2 Results

For this study, the sonicFoam solver in OpenFOAM was used due to its transient, compressible features. Calculations were performed with second order (Gauss limitedLinear) schemes and the PIMPLE algorithm in laminar, quiescent conditions. The PIMPLE algorithm derived from both the PISO (pressure implicit with splitting of operator) [99] and SIMPLE (semi implicit method for pressure linked equations) [100] algorithms. The time step was 2 nanoseconds with the pulse time of the ns-DBD model set to 100 nanoseconds. The simulation was performed for a total of 60 microseconds with a write interval of 2 microseconds. Initially a mesh independence study was conducted to ascertain that simulation results would not be affected by mesh density. Figure 5.2 shows the grid independence study with the shock front Mach number taken as the criteria for mesh convergence. The shock front Mach numbers are evaluated and presented for various times after the plasma model actuation. The ambient temperature was set to 293 K, corresponding to the ambient temperature during the experimental campaign. Wave transmissive boundary conditions were used along all domain boundaries but the bottom of the domain which was a solid surface. The wall boundary was assigned a no-slip condition.

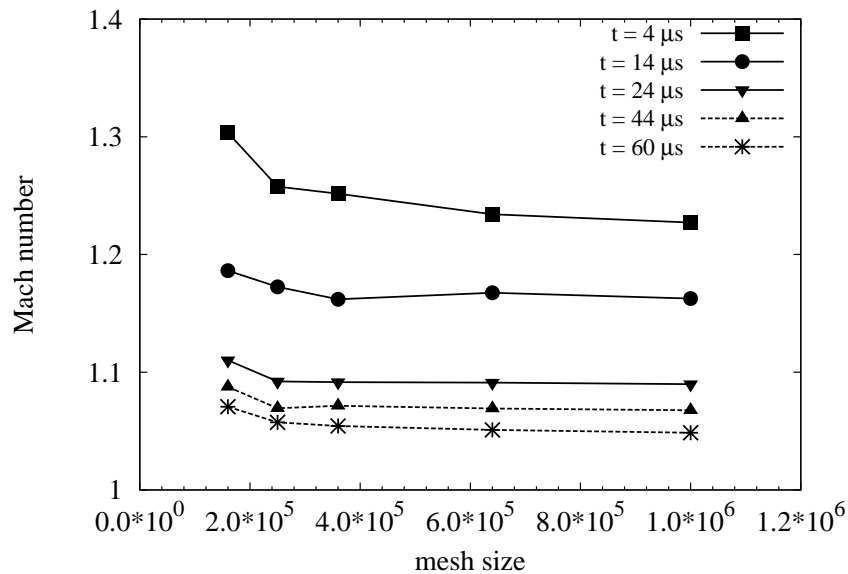


Figure 5.2: Mesh independence study.

The implementation was tested with a simple 2D case in a quiescent flow. The numerical domain was  $100 \times 50 \times 1$  mm in the  $x$ ,  $y$ , and  $z$  direction, respectively. Within this domain the

heated region was placed centrally at  $y = 50\text{mm}$ . The heated volume dimensions are  $10 \times 1 \times 10^{-5} \times 1$  mm in the  $x$ ,  $y$ , and  $z$  direction, respectively. The 10 mm length of the heated volume match the covered electrode width from the experiments described in the previous chapter.

Flow solutions show a shock wave propagating through the domain with the same distinct features observed from experiments. The results were post-processed with a purpose written code to determine the exact shock front location at different time steps. Figure 5.3 shows the shock wave structure at a time of 10 microseconds after discharge. The figure presents a strong pressure gradient (5.3a) and the density field (5.3b). The progression of the shock wave front through the numerical domain is depicted in Figure 5.4.

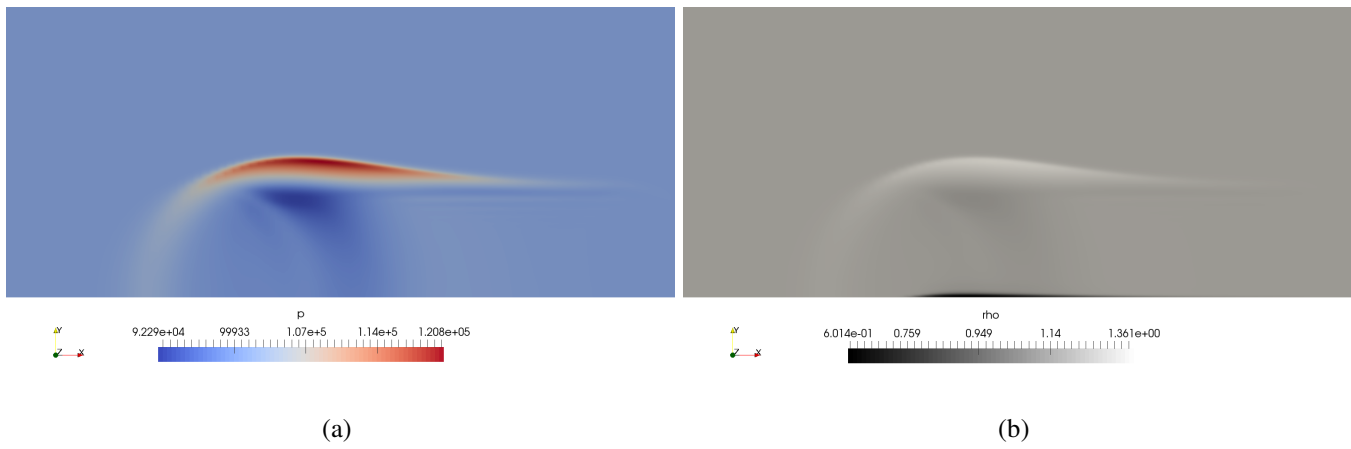


Figure 5.3: Numerically modelled ns-DBD plasma actuator: (a) pressure contours of shock front, (b) density contours of shock front.



Figure 5.4: Progression of shock wave with the ns-DBD model implemented in OpenFOAM. Black coloured region at the bottom of the computational domain schematically depicts the heated volume region. This is not to scale. Dimensions of the heated volume are  $10 \times 1 \times 10^{-5} \times 1$  mm in the  $x$ ,  $y$ , and  $z$  direction, respectively.

Figure 5.5 shows an instantaneous density field captured by the Schlieren imaging next to the density field produced by the numerical plasma model. Both flow structures show the same key features of a cylindrical and planar shock wave.

The parameter  $\chi$  controls the amount of the thermal energy being added to the heated region. Increasing  $\chi$  yields a stronger shock wave with higher velocities (Figure 5.6). The model is



Figure 5.5: Experimental density field from Schlieren imaging (a) and numerical density field from plasma model (b). Both flow structures show the same key features of a cylindrical and planar shock wave.

compared to experimental results obtained. Plots, in Figures 5.7 to 5.9, show the shock wave propagation speed as distance vs time, for pressures of 30, 70 and 100 kPa, respectively. The y axis represents the vertical distance travelled by the shock wave front from the actuator surface in the experiments and from the heated volume region in the numerical plasma simulations. This distance is non-dimensionalised by the heated volume length which is also equal to the covered electrode width in the experiments.

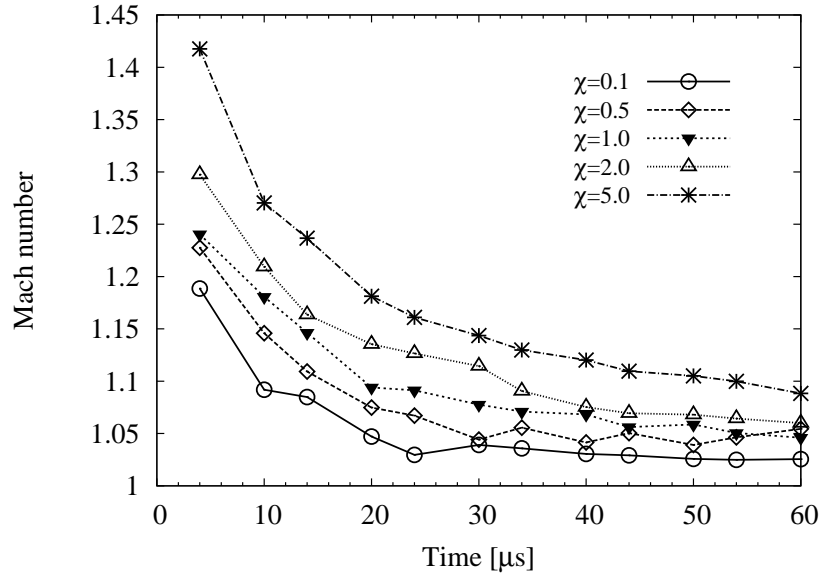


Figure 5.6: Effect of parameter  $\chi$  on Mach number of shock front at ambient conditions.

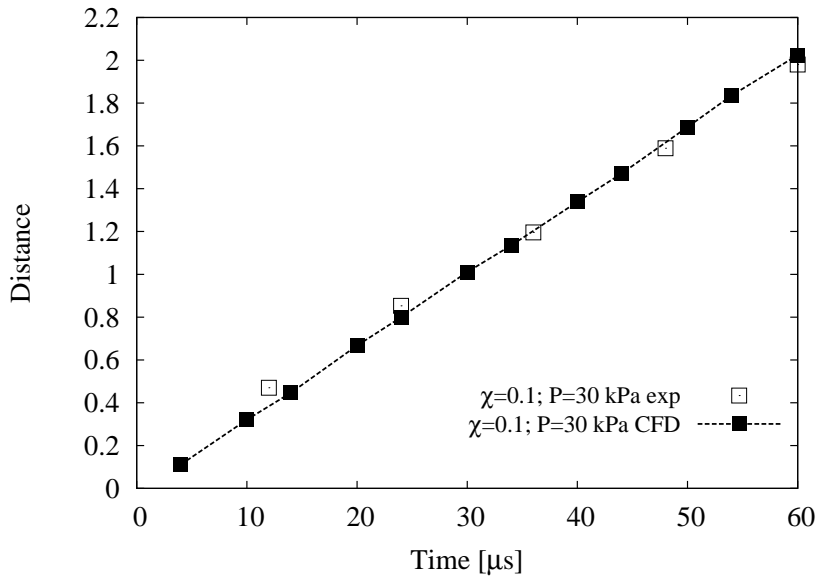


Figure 5.7: Comparison of experimental and numerical shock wave propagation for ambient pressure of 30 kPa.

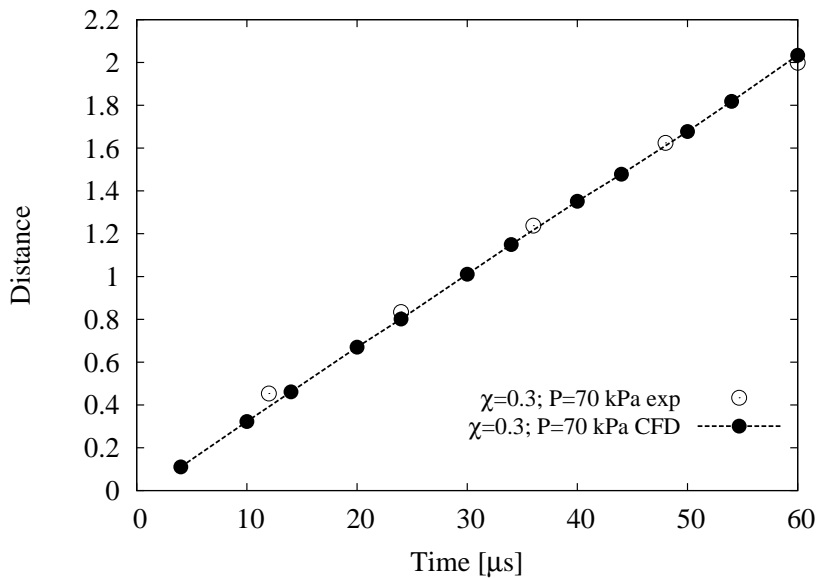


Figure 5.8: Comparison of experimental and numerical shock wave propagation for ambient pressure of 70 kPa.

### 5.1.3 Discussion

The numerical ns-DBD model captures the overall shock structure and propagation speed accurately. The numerical simulation results compare well with experiments, matching the shock front propagation determined from the Schlieren experiments. The amount of temperature addition required to match experimental results of shock propagation are given in Table 5.1. It outlines the temperature values added to the near wall region for the simulation of ns-DBD generated shock waves. Less added thermal energy is needed at lower pressure values to match

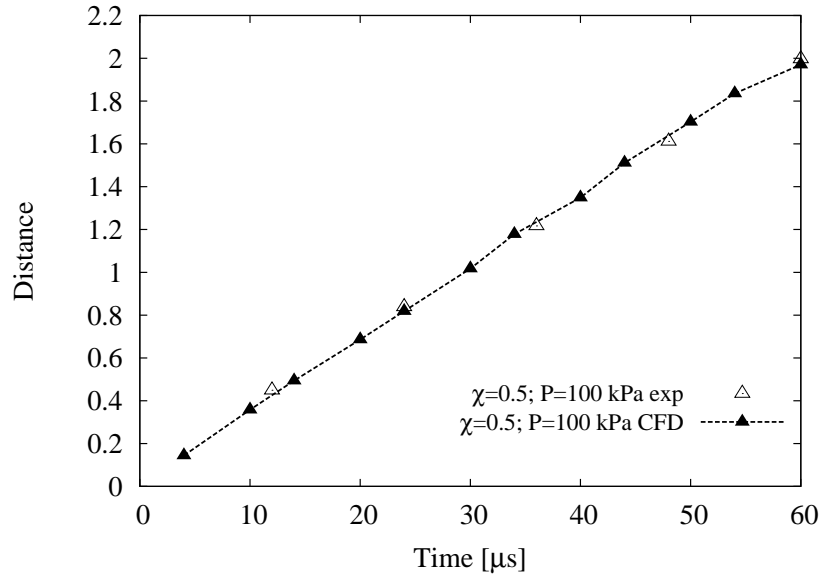


Figure 5.9: Comparison of experimental and numerical shock wave propagation for ambient pressure of 100 kPa.

Table 5.1: Temperature values added to the near wall region for the simulation of ns-DBD generated shock waves.

Pressure [kPa]	$\chi$	T max [K]	T avg [K]
30	0.1	410.319	295.214
70	0.3	654.657	299.642
100	0.5	898.995	304.071

Temperature values corresponding to  $\chi$  parameters used for CFD.

experimental results. This indicates that less flow control authority is available at lower ambient pressures.

The overall shock wave structure and propagation speed from CFD match well with conducted experiments, allowing the conclusion that a phenomenological plasma model is sufficient to capture the dominant features of ns-DBD plasma actuation. The heat addition required to reproduce experimental results varied with ambient pressure. Less heating of the near-wall region was needed with lower ambient pressures.

Finally, it is highlighted that there is a computational cost associated with the ns-DBD plasma model beyond the numerical calculations based on the heat addition. The model is based on a physical time step of nanoseconds and thus requires a time step small enough to capture the plasma actuation.

## 5.2 ac-DBD model

The ac-DBD plasma model is a combination of the electrohydrodynamic (EHD) body force proposed by Soloviev [182] and the EHD body force distribution by Singh [183]. Babou et al. first presented preliminary results of this approach [184].

### 5.2.1 ac-DBD model implementation

Soloviev's model is based on key parameters of plasma actuators: the dielectric thickness, the applied peak-to-peak voltage, and the driving frequency. This simplified model can produce qualitative thrust values in agreement with empirical data [182]. The actuator EHD force production is given by:

$$T_{Soloviev} = 2.4 \times 10^{-10} \beta^4 \frac{f_v}{d} \left( \frac{9V_0}{4\Delta V_c} \right)^4 \left( 1 - \frac{7\Delta V_c}{6V_0} \right)^4 \left( 1 - \exp\left(\frac{-1}{4f_v\Delta\tau_q}\right) \right) \quad (5.2)$$

where  $\beta = 1$  is a fitting parameter,  $f_v = 10$  is the frequency of voltage (kHz),  $d = 0.3$  is the thickness of dielectric (cm),  $V_0 = 20000$  is the applied voltage peak-to-peak (V),  $\Delta V_c = 600$  is the normal falldown of cathode voltage,  $\Delta\tau_q = 1e-4$  is the residence time of negative ions inside the acceleration volume.

The EHD force distribution presented by Singh is based on detailed computational studies of plasma discharge. From the CFD data, Singh et al. recorded spatial and temporal distribution statistics of electric potential and species densities [183]. Singh et al. noted that the force magnitude from their approximation does not match experimental body force measurements. However, the spatial distribution is based on direct measurements and is adopted for this combined model. The force distribution was then expressed by an analytical relation:

$$F_{Sing,x}(V, x, y, x_0, y_0) = \frac{F_{x_0}}{F_{y_0}} \exp\left(-\sqrt{(ccX - x_0 - (ccY - y_0))ccY} - \gamma_x \sqrt{ccY - y_0}\right) \quad (5.3)$$

$$F_{Sing,y}(V, x, y, x_0, y_0) = \frac{F_{x_0}}{F_{y_0}} * \exp\left(-\sqrt{\frac{ccX - x_0}{ccY}} - \gamma_y \sqrt{ccY - y_0}\right) \quad (5.4)$$

where  $F_{x_0}$  is the force in the horizontal direction,  $F_{y_0}$  is the force in the vertical direction,  $ccX$  and  $ccY$  are the cell centers in the x and y directions,  $x_0$  and  $y_0$  are the actuator (cell region) start points,  $\gamma_x$  and  $\gamma_y$  are constants set to  $8 \times 10^5$  and  $1 \times 10^7$  respectively.

The resulting numerical model for ac-DBD plasma actuation EHD force production and distribution is used as a source term in the momentum equation for fluid simulations in Open-

FOAM. The model has been generalised to allow for three dimensional computational domains and transient simulations where the on/off time of the actuation can be specified based on the timestep of the simulation. The momentum source term is implemented through the fvOptions utility in OpenFOAM. A full fvOptions file is included as an appendix.

### 5.2.2 Results

The implementation of the ac-DBD body force model was tested with OpenFOAM in a quiescent flow numerical domain. The computational domain was a flat plate with no slip condition at the wall. Different model parameters were varied to assess the model EHD force production. Figures 5.10 and 5.11 show the resultant, horizontal wall bounded jet streamwise velocity from the ac DBD model with dielectric thickness and driving frequency. Varying the input peak-to-peak voltage level in the model parameters affects the resultant wall bounded jet strength. Figure 5.12 shows the streamwise velocity component of the wall bounded jets for a range of voltage values with dielectric thickness. As expected, with lower input peak-to-peak voltage level the streamwise velocity decreases.

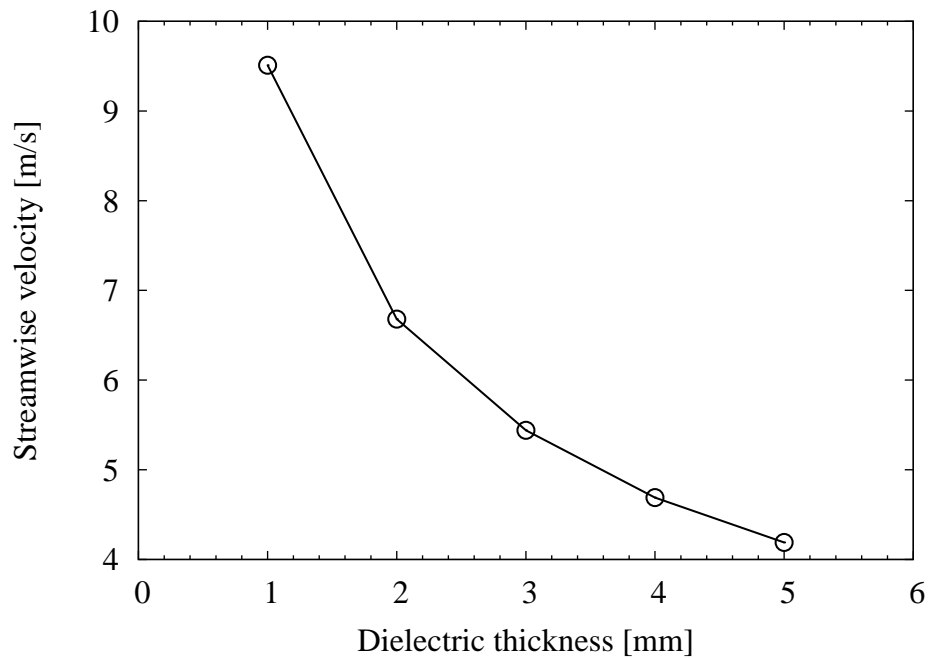


Figure 5.10: Numerically modelled ac-DBD plasma actuator: resultant horizontal jet velocity with dielectric thickness used in numerical model.

The flow field around the numerical ac-DBD plasma actuator in quiescent air is presented in Figure 5.13. The wall bounded jet diffuses downstream as expected and entrains fluid downwards towards the wall at the beginning of the actuated region.

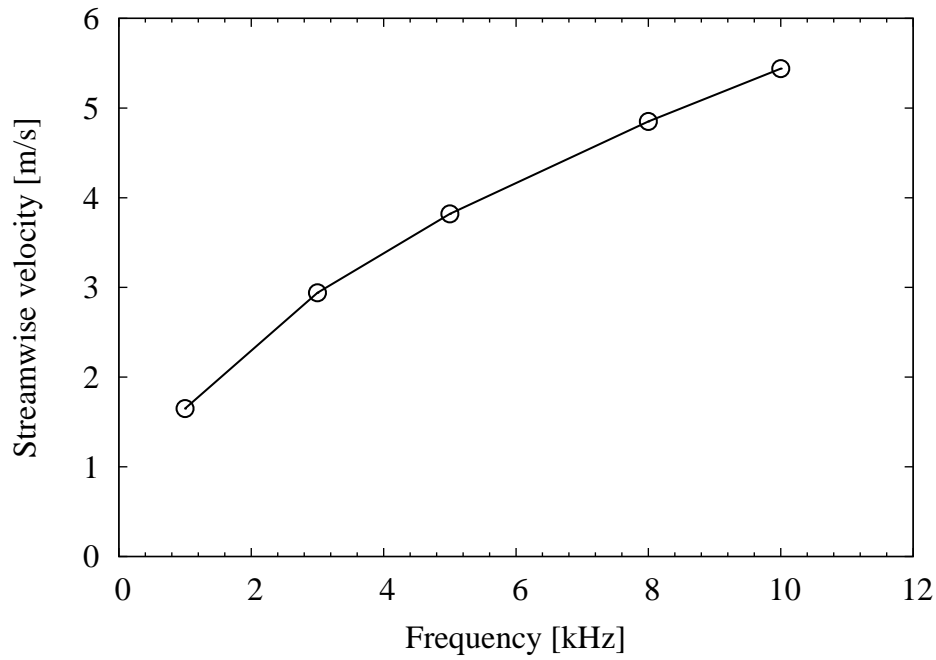


Figure 5.11: Numerically modelled ac-DBD plasma actuator: resultant horizontal jet velocity with driving frequency ( $f_v = 10$  kHz) used in numerical model.

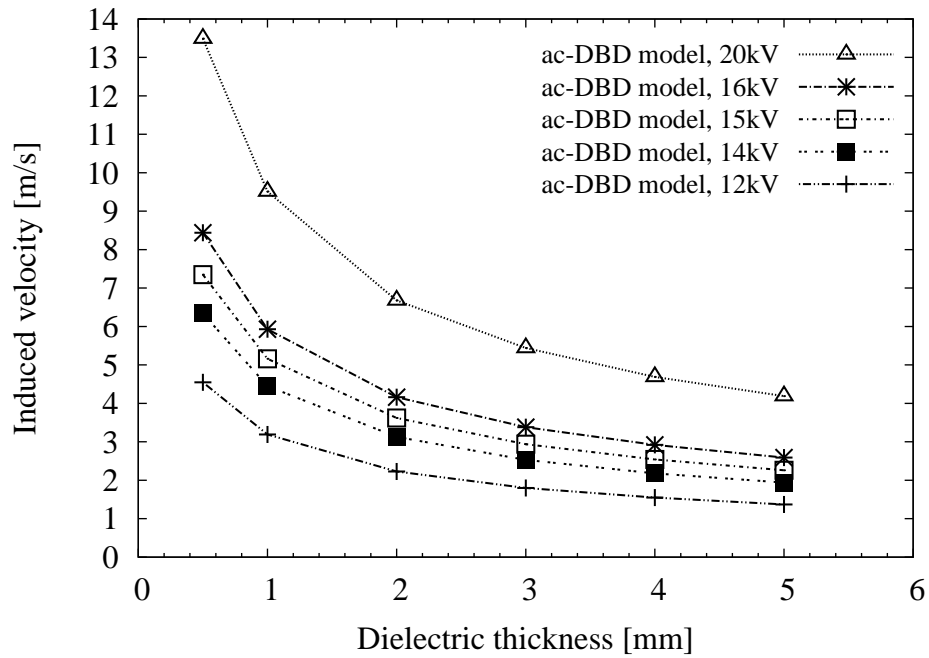


Figure 5.12: Resulting streamwise jet velocities with peak-to-peak voltage input for ac-DBD numerical model.

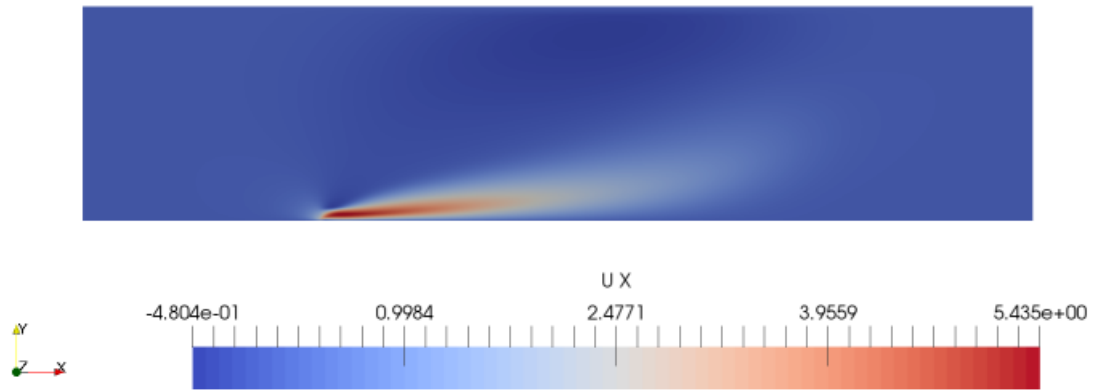


Figure 5.13: Horizontal velocity component ( $ms^{-1}$ ) of resultant wall bounded jet.

### 5.2.3 Discussion

Wall bounded jet velocity magnitudes of the ac-DBD model and experiments are plotted in Figure 5.14 with dielectric thickness. The body force produced by the numerical model follows the same trend as the experiments, generating smaller magnitudes of ionic jet velocities with increasing dielectric thickness. However, the magnitudes of the body force do not match experimental values for the same dielectric thickness, driving frequency, and peak-to-peak voltage inputs. This might be due to the fact that the numerical model does not take into account the properties of the dielectric material such as the dielectric constant and the breakdown voltage.

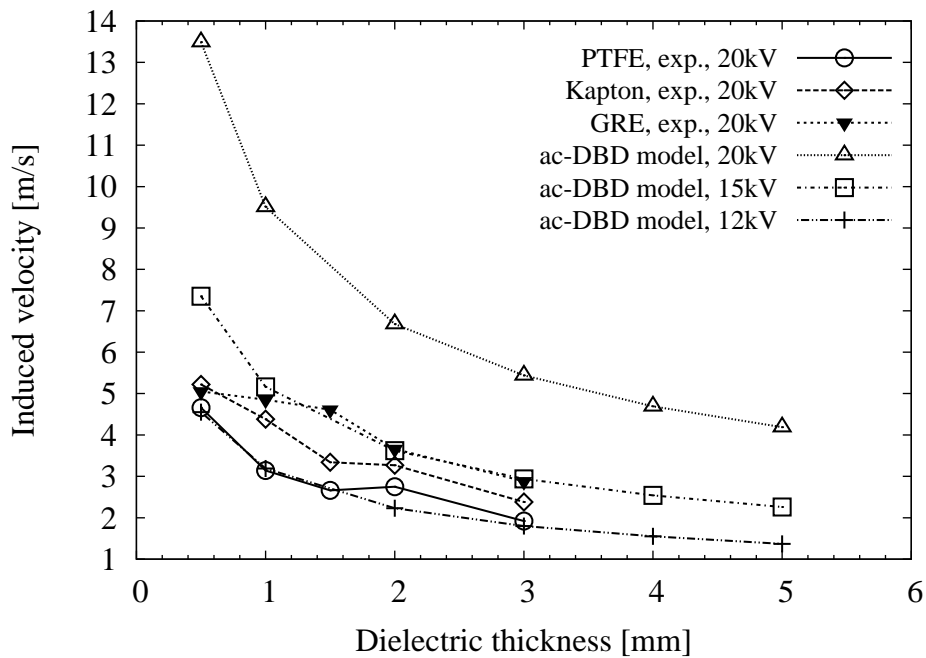


Figure 5.14: Experiments compared to ac-DBD model body force with dielectric thickness.

The numerical model is tuned by using a lower input voltage level than in experiments to match the resultant wall bounded jet velocities to the experimental values. Wall bounded jet ve-

locity magnitudes of the tuned ac-DBD model and experimental data are plotted in Figure 5.14 with dielectric thickness. Lower input peak-to-peak voltage levels than in the experiments cover the range of ionic jet velocities recorded for the PTFE, GRE, and Kapton dielectric plasma actuators. Figures 5.15 to 5.17 show more clearly how the ac-DBD numerical model matches experimental data from PTFE, Kapton, and GRE plasma actuators, respectively. An input peak-to-peak voltage of 12 kV matches numerically the experimental data recorded for a PTFE dielectric actuator operated at 20kV, while to match the GRE dielectric actuator an input peak-to-peak voltage level of 15kV is needed.

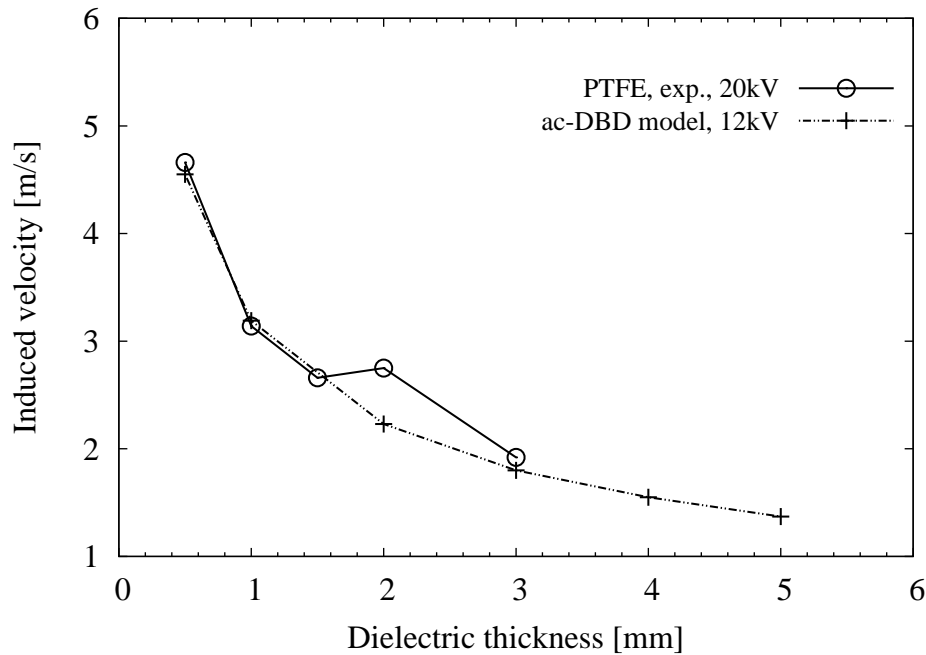


Figure 5.15: PTFE dielectric experiments compared to tuned ac-DBD model body force with dielectric thickness.

### 5.3 Conclusions

The ns-DBD numerical model matches experimental results well capturing qualitatively and quantitatively experimental results. This model is phenomenological in nature and based on the thermal energy input to a near wall volume where the plasma discharge takes place. This model captures the overall shock structure and propagation speed accurately. However, this model suffers from the required time step it is based on increasing the computational cost of the simulation. The ns-DBD model applies the plasma pulses at very short time frames, usually nanoseconds. Therefore, the computational cost is high as the time step needs to be small enough to capture the individual pulses of actuation.

The numerical model presented for ac-DBD plasma actuation captures qualitatively the wall bounded jet. However, the velocity of the ionic jet produced exceeds experimental values by

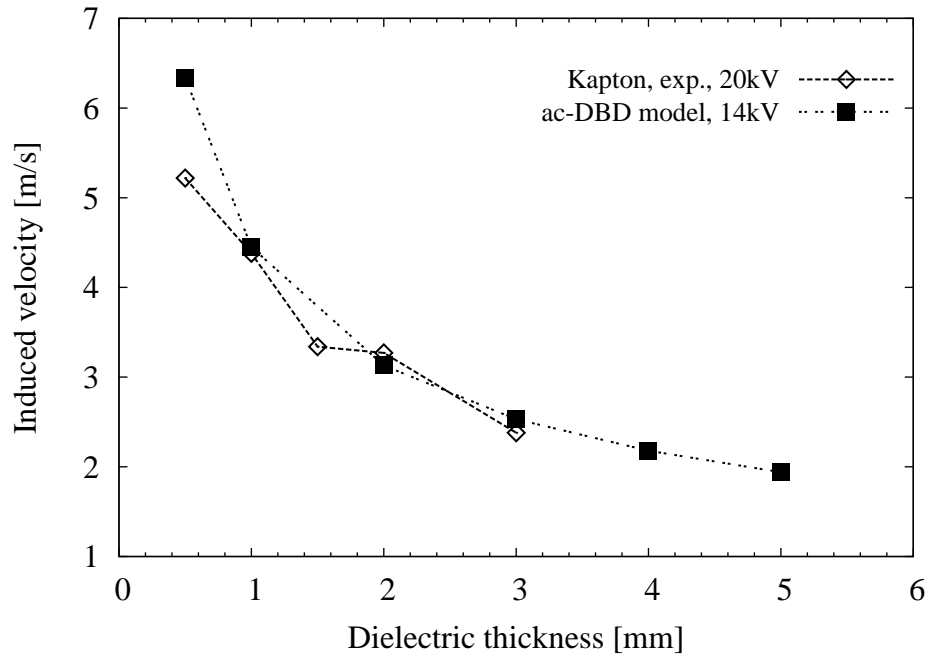


Figure 5.16: Kapton dielectric experiments compared to tuned ac-DBD model body force with dielectric thickness.

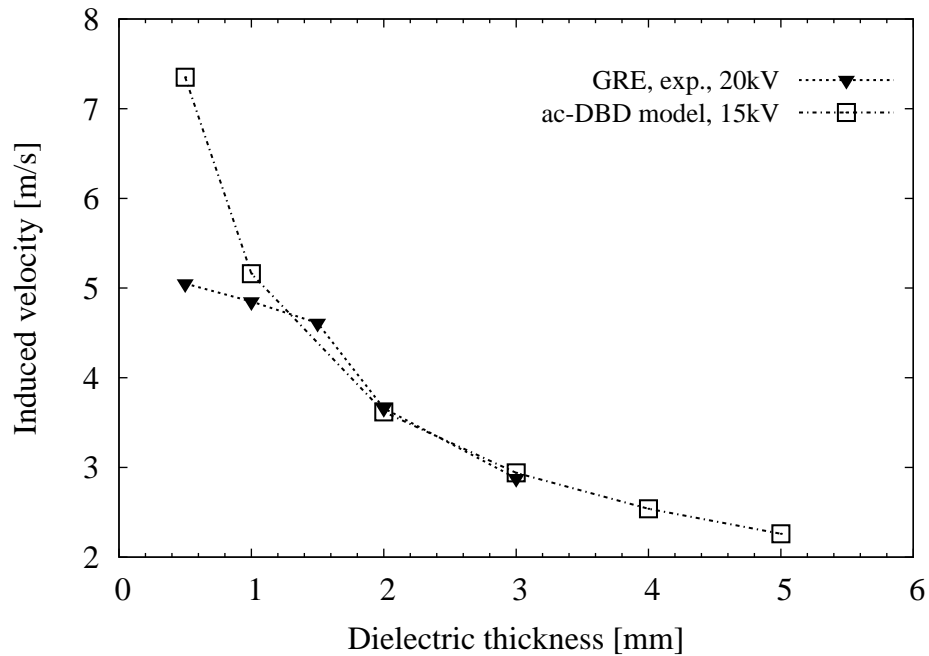


Figure 5.17: GRE dielectric experiments compared to tuned ac-DBD model body force with dielectric thickness.

up to a factor of two. This could possibly be addressed by incorporating physical properties of the dielectric material into the numerical model. For the purpose of demonstrating the effects of ac-DBD plasma actuation on the flow in a convoluted duct, the numerical model is tuned successfully by using a lower input voltage level than in experiments to match the resultant wall

bounded jet velocity. It was shown in this chapter that, when tuned, the ac-DBD model matches experimental results well. The ac-DBD model can be applied in steady state and transient simulations. Therefore, unlike the ns-DBD model, the additional computational cost is negligible.

# Chapter 6

## Plasma flow control

### 6.1 Plasma flow control in convoluted ducts

In chapter 5, experimental data of ac and ns DBD plasma actuators was used to model their effect numerically with separate functionalities implemented in OpenFOAM. The baseline flow physics and throughflow characteristics of the convoluted duct were analysed in chapter 3. This chapter combines the two main aspects of the work undertaken in chapters 3 and 5 with the aim of determining the effect plasma actuation has on the throughflow in a convoluted duct. To this end, lower and higher fidelity numerical simulations are conducted within the convoluted duct with the new plasma functionalities.

The ac-DBD plasma actuators were characterised experimentally for highest induced jet velocity to help influence the near wall fluid the most. The ns-DBD plasma actuation was intended to be pulsed with a frequency based on the baseline flow features extracted in chapter 3. However, the frequencies extracted for dominant flow features varied from 94, to 215, to 420 Hz. As a result, the ns-DBD plasma pulse was set to 100 Hz for the flow control study.

#### 6.1.1 Meshing: new cell set for plasma functionality

In OpenFOAM cell sets are used to select and group mesh regions. Usually, cell sets are defined so that a particular operation can be performed on the whole set as a group rather than on individual cells. A new cell set class in OpenFOAM was developed to select a cell region based on a target circular arc sector called `radialStripToCell`. This cell set class complements other, existing OpenFOAM classes such as `boxToCell` that work with simpler geometries. The functionality of `radialStripToCell` is key to apply the phenomenological plasma models in the convoluted duct due to its circular cross-section.

The `topoSet` functionality in OpenFOAM was used to create mesh regions for the DBD plasma models to be applied to. First, the selected mesh region was refined into smaller cells in order to better represent the prescribed Gaussian temperature profile of the DBD code in a

given physical length of the actuation region. For this, the refineMesh utility was used. Next, based on this finer defined mesh region a cellSet source function called radialStripToCell was implemented. This radialStripToCell function selects cells with their respective cell centers in a circular arc volume as defined by input parameters. The user needs to define an inner and outer radius along with the arc centre point, as well as the axial and angular extent of the arc volume. With this information, the function groups all cells that fall within the arc volume into one cell set. Figure 6.1 shows one such circular arc volume selected from the total numerical domain of the s-shaped duct. An example topoSetDict file is included in the appendix for reference. The radialStripToCell function code files radialStripToCell.C and radialStripToCell.H are also included of the appendix.

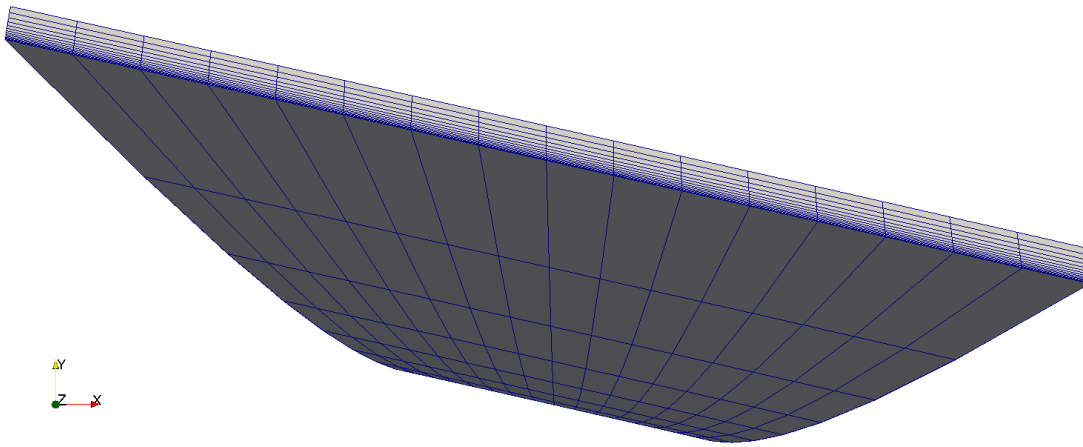


Figure 6.1: Mesh of heated region at  $x = 0.18\text{m}$  in numerical domain of s-shaped duct.

### 6.1.2 CFD code

The open source CFD tool box OpenFOAM ([92]) is used, with all presented data computed with OpenFOAM v1712 (OpenFOAM.com). For the RANS and DDES calculations the  $k-\omega$  SST turbulence model, as first proposed by [93] is used. The simulation set up is kept consistent with the baseline CFD computations conducted. Further details about the turbulence model are discussed in chapter 3.

Simulations were conducted with the rhoSimpleFoam and rhoPimpleFoam solvers for steady state and transient cases, respectively. Those are pressure based, compressible solvers utilising second order schemes and the SIMPLE or PIMPLE algorithms. Each PIMPLE timestep calculation was solved with 200 subiterations or until a drop of residuals of 6 orders of magnitude was reached. For more details refer to the CFD set up section in chapter 3.

Due to the volume of data generated, flow solutions were saved every  $500 \mu\text{s}$  of physical time for the ac-DBD case and  $250 \mu\text{s}$  for the ns-DBD case. For faster run times transient simulations were initialised from a converged RANS calculation. The ARCHIE-WeST high performance computing machine in Glasgow was used to run the simulations in parallel on 40 cores. ARCHIE-WeST uses Intel Xeon Gold 6138 20 core 2.0 GHz CPU chips. Being computationally expensive simulations, two weeks of run time of DDES on the HPC generate only 25 snapshots for the ac-DBD plasma model in the convoluted duct. The ns-DBD plasma model is even more computationally expensive as its time step is 50 times smaller.

### **Boundary conditions, initial conditions, and numerical schemes**

RANS simulations were performed with turbulence properties prescribed for kinetic energy and specific dissipation rate ( $\omega$ ) based on a 2.5% turbulence intensity. Equations 3.17 to 3.20 were used for calculating the specific dissipation based on the turbulence intensity  $I_{turb}$ , turbulent kinetic energy  $k_{turb}$ , and turbulent dissipation rate  $\varepsilon$ .

The total mass flow was set at the inlet, with the outlet being at atmospheric pressure. The no slip wall boundary condition was employed. Second order Gauss linear upwind schemes were used. No wall functions are employed due to the low  $Y^+$  values.

### **6.1.3 ac-DBD flow control**

Compressible flow solvers are used for both steady and transient simulations given the flow is subsonic with an inlet Mach number of 0.6. Consistent with the baseline flow calculations of chapter 5, for transient simulations a timestep of  $1 \mu\text{s}$  was used resulting in a maximum Courant number of 0.24 in the domain with a mean value of 0.06.

Initially, steady state RANS simulations are conducted before transient simulations with DDES are set up.

#### **Flow control cases**

To find an optimum placement of plasma actuation within the convoluted duct four locations were chosen for the initial steady state simulations. Steady state simulations were kept to four cases only due to constraints on computational resources and the time frame of the project.

The optimum location of flow control devices is upstream of the separation point as pointed out in chapter 2 based on analysis of existing literature on flow control studies in convoluted ducts. The actual optimum position can not be defined for a general case, however. For instance, in literature, recommendations range from 5 to 30 device heights upstream of the separation location for submerged vortex generators [43]. Therefore, four locations upstream of the separation onset were chosen to determine any effect of the actuator placement. Those locations are all upstream of the separated flow region and the duct inflection point. The separated flow

region is well defined from the baseline flow study in chapter 5 and the experimental data from Wellborn [1]. In the duct the separated flow region extends from  $2.0 < \frac{s_c}{D_1} < 3.7$ . Based on this, the four actuation locations were set at  $\frac{s_c}{D_1} = 0.88575, 1.13619, 1.38928, \text{ and } 1.64584$ .

The circumferential extent of the heated regions is based on findings in literature which suggest that actuation along the centre of the duct is more beneficial to actuation along the whole cross-stream surface [7]. The actuators' circumferential extent was fixed to span from 160 to 200 degrees in the cross-stream plane of the duct, i.e. the actuators are centred at the symmetry plane of the duct at  $z = 0$  m. Their streamwise extent was modelled on the length of physical plasma actuators and was set to 5 mm.

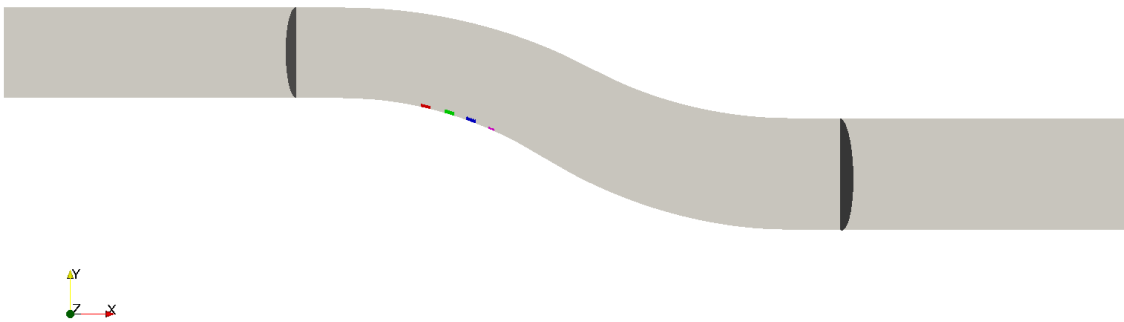


Figure 6.2: Flow control locations in s-shaped duct with inlet and AIP cross-stream planes shaded. Flow direction is in the positive x-direction.

Figures 6.2 and 6.3 show the four actuation locations within the convoluted duct and the four cell sets selected for actuation. Figure 6.2 shows the heated regions at four locations within the numerical domain, while the heated regions are shown in more detail in Figure 6.3.

The four cell regions were refined first and next selected with the `radialStripToCell` function discussed earlier. In Figure 6.2 the Wellborn s-duct inlet and AIP cross-stream planes are shaded. As is evident from the Figure there are constant diameter duct sections upstream and downstream of the Wellborn duct. The numerical domain is identical to the one described in chapter 3 for the baseline s-duct CFD calculations.

Table 6.1 provides details of the four cell set regions selected for the DBD plasma actuation. Their axial location is given in terms of the streamwise coordinate the cell set regions start at and the corresponding non-dimensionalised distance  $\frac{s_c}{D_1}$  along the duct centreline. There are slight variations in the number of cells each cell region encompasses, however, this is of little overall effect as their volume is of the same order of magnitude. This becomes more evident once the resultant plasma jets are compared between the four placements. To this end, test runs with quiescent boundary conditions were conducted. Figure 6.4 shows the streamwise velocity component produced by the ac-DBD plasma model in the convoluted duct for quiescent RANS

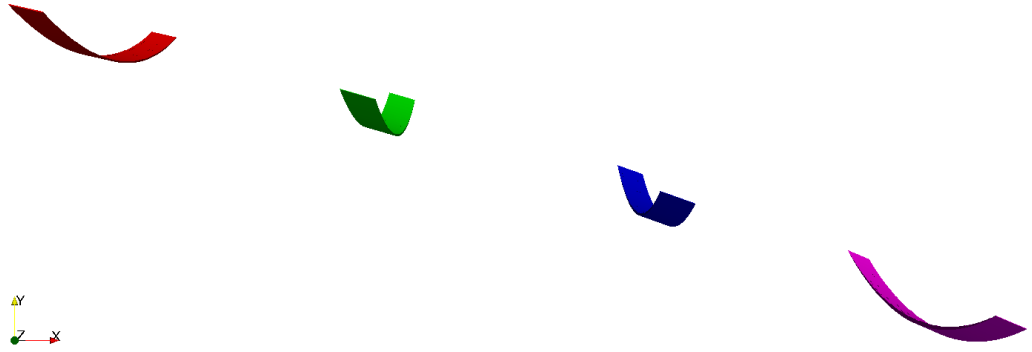


Figure 6.3: Heated regions in numerical domain of s-shaped duct.

simulations. The refined mesh region at the respective cell sets are also included with clearly visible finer mesh region. The maximum streamwise velocity of the generated plasma jets across the four locations is constant for all practical purposes and only varies very slightly from  $5.486$  to  $5.610 \text{ ms}^{-1}$ . This is important so that a fair comparison between the actuator placements can be conducted. The thickness of the resulting jet profiles looks to be increasing from the most upstream to the most downstream actuation region. This is the case as the curvature of the duct comes into play. The jet direction is parallel to the surface at the point of actuation with the curvature of the convoluted duct moving away downstream of that point.

Table 6.1: Details of cell set regions for flow control cases.

axial location [m]	0.18	0.23	0.28	0.33
centreline location $\frac{s_c}{D_1}$	0.88575	1.13619	1.38928	1.64584
circumferential extent [ $^\circ$ ]	160-200	160-200	160-200	160-200
number of cells	9030	8838	9734	10074
volume $\times 10^{-7} [m^3]$	1.06781	0.96667	1.38127	1.89639

As mentioned in chapter 5 on the phenomenological model of ac-DBD plasma actuators, the numerical model requires tuning to match expected ionisation levels. Without tuning the ac-DBD model overpredicts the resulting ionic jet strength. Therefore, the input parameters for the four actuator placement regions were adjusted in the fvOptions file. Table 6.2 shows the driving frequency, dielectric thickness, and voltage levels taken for the simulations. The voltage level was adjusted while monitoring the resulting plasma jet profile. The driving frequency is kept the same as for the plasma experiments presented in chapter 5 and is set to 10 kHz. Values presented in Table 6.2 provide an equal actuation strength across all four plasma placements in the numerical domain.

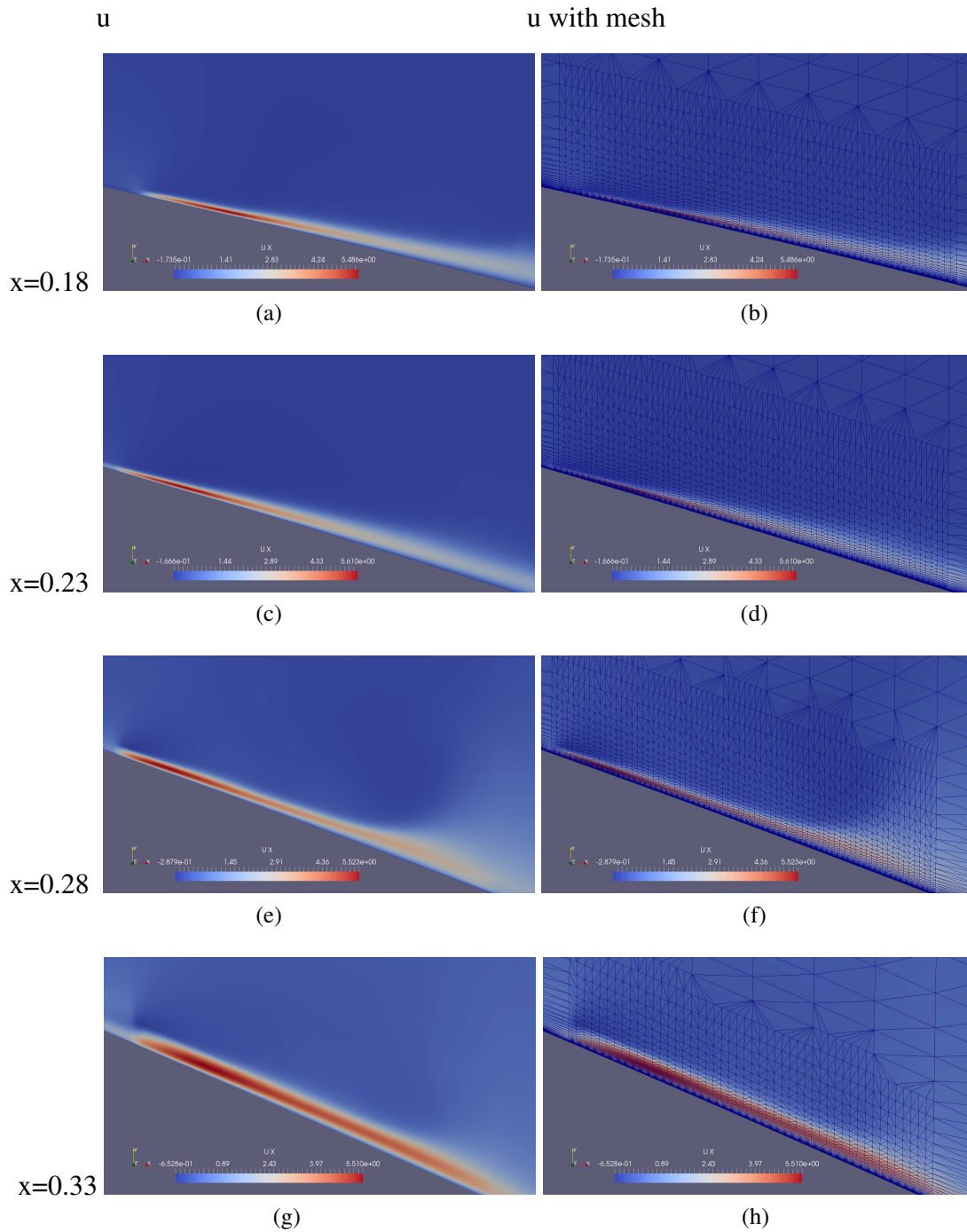


Figure 6.4: Streamwise velocity component produced by ac-DBD plasma model in convoluted duct for quiescent RANS simulations.

Table 6.2: Input details of numerical ac-DBD model.

axial location [m]	0.18	0.23	0.28	0.33
centreline location $\frac{s_c}{D_1}$	0.88575	1.13619	1.38928	1.64584
voltage [kV]	16.00	17.00	20.00	17.35
driving frequency [kHz]	10	10	10	10
dielectric thickness [mm]	3	3	3	3

## RANS

Numerical simulations with ac-DBD plasma flow control are analysed and compared against the baseline CFD simulations. First, entropy in the flow at the AIP is calculated based on the flow snapshots and presented in Figure 6.5 for all cases. Entropy,  $s$ , is calculated at each face point at the AIP based on the time averaged values of temperature and static pressure, the specific gas constants,  $R$ , and the specific heat capacity at constant pressure,  $C_p$ :

$$s_i = C_p \log(T_{avg_i}) - R \log(P_{s_{avg_i}}). \quad (6.1)$$

Entropy is a measure of randomness and, being an irreversible quantity, can be directly related to the losses generated in a system. For both the baseline and the actuated cases the entropy profile at the AIP is most prominent in the lower central region. This is the lower velocity region most influenced by the oscillating shear layer from the separation region where there are the biggest fluctuations in flow properties. Though the changes are subtle, the baseline case shows a higher maximum value of entropy at the AIP than the four actuated cases suggesting higher localised losses in the baseline case. However, the distribution of entropy fields for the actuated cases show a larger area of high entropy. Overall, the differences are marginal with the entropy level decreasing by less than 1% from the baseline case.

For a quantitative analysis the area averaged entropy values at the AIP face are calculated. Baseline RANS simulation results in an average entropy level of  $2420.4 \frac{J}{K}$  at the AIP while the ac-DBD actuated cases produce a lower entropy level of  $2419.1 \frac{J}{K}$ .

Differences between the four ac-DBD plasma actuation cases are even less pronounced. Based on the entropy plots at the AIP there is no clear variation between them and no optimum location of actuation can be singled out.

Figure 6.6 shows plots of stagnation pressure at the AIP for the four actuated cases and the baseline simulations. Differences between the plots are even smaller than for the entropy fields presented earlier. The only spottable difference is in the extent of the highest pressure region. This region extents slightly further towards the bottom of the AIP in the baseline case.

The separation extent of the baseline and four ac-DBD model RANS studies are shown in Figures 6.7 and 6.8 by streamlines around the inflection point of the s-duct. All streamlines

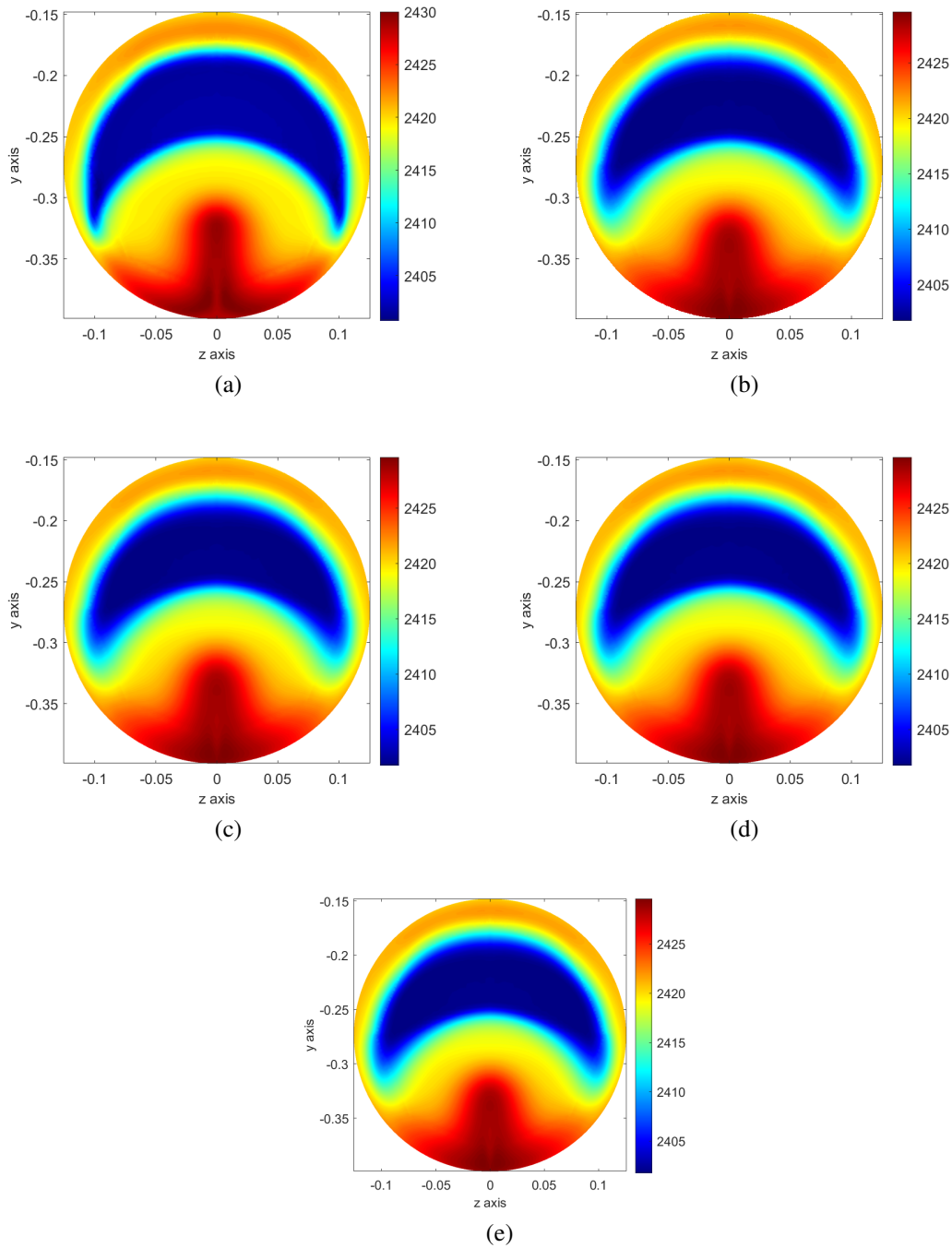


Figure 6.5: Entropy ( $\frac{J}{K}$ ) plots at the AIP for the (6.5a) baseline s-duct throughflow and plasma model simulations at: (6.5b)  $x = 0.18$  m, (6.5c)  $x = 0.23$  m, (6.5d)  $x = 0.28$  m, (6.5e)  $x = 0.33$  m.

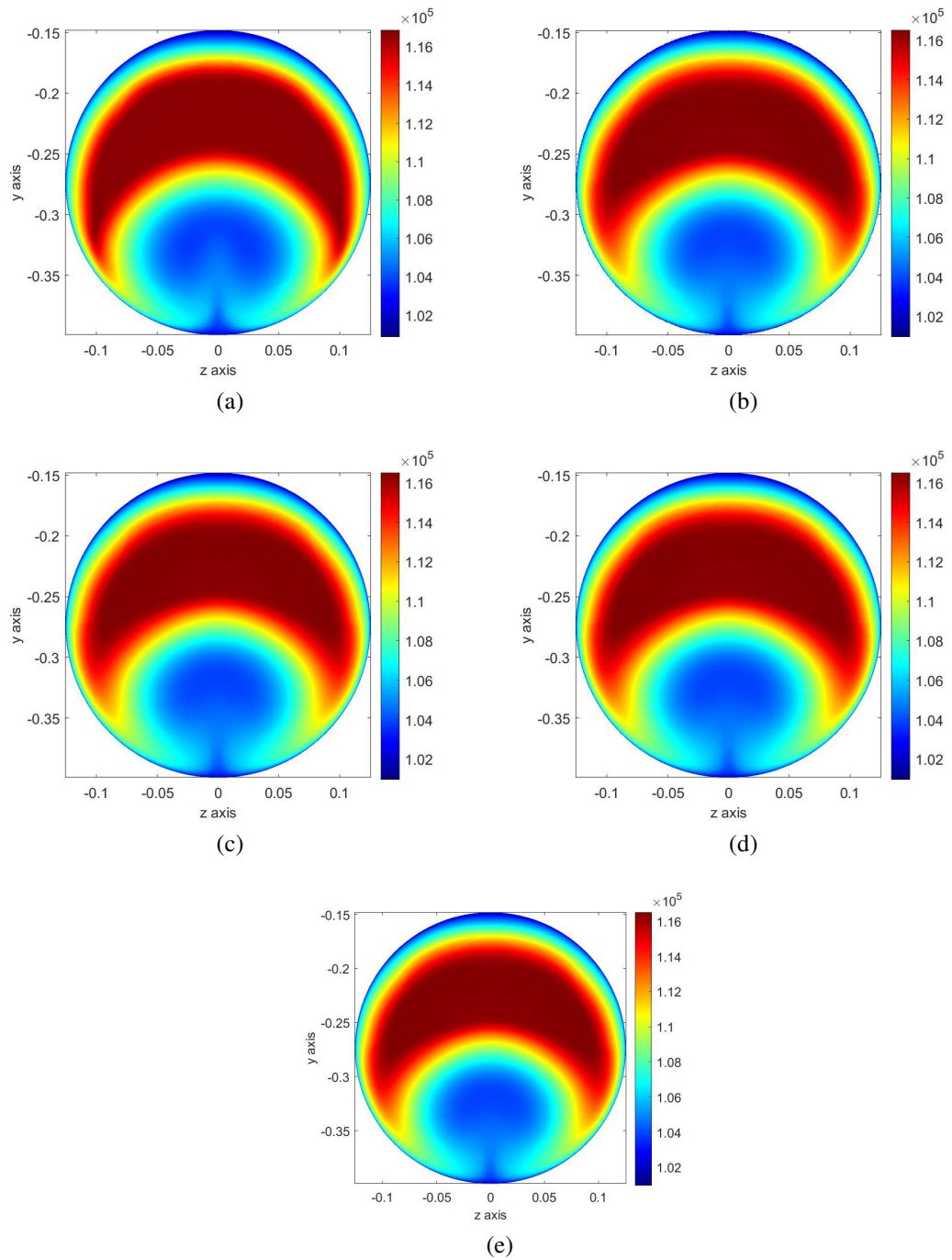


Figure 6.6: Plots of stagnation pressure at the AIP for the (6.6a) baseline s-duct throughflow and plasma model simulations at: (6.6b)  $x = 0.18$  m, (6.6c)  $x = 0.23$  m, (6.6d)  $x = 0.28$  m, (6.6e)  $x = 0.33$  m.

are seeded from the same point source in paraview and displayed in the same style and colour scheme. The view is from the bottom of the convoluted duct with the positive y direction into the page. The separated flow region is clearly visible in all plots with its extent only changing marginally between the different flow control cases and the baseline flow. In chapter 3, the flow separation region and its key features are described in detail. From the four ac-DBD model simulations there is no clear delay of separation onset in the convoluted duct.

Wall static pressure coefficients at three internal planes,  $\frac{s_c}{D_1} = 0.96, 2.97, \text{ and } 4.01$ , of the convoluted duct are extracted and presented in Figure 6.9. There is no evidence in the data that the plasma actuation affected the static pressure distribution at these three cross-planes in the duct. Wall static pressure coefficients along three stream-wise lines are shown in Figure 6.10 and also do not show any influence on the wall static pressure distribution by the actuation.

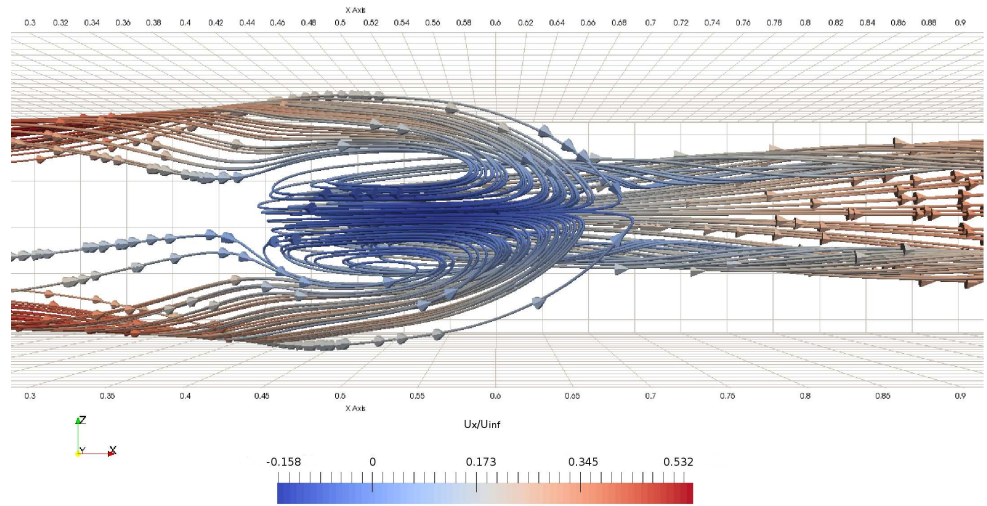
Comparing the wall static pressure coefficients at the cross-stream planes and the three streamwise lines of the four actuated cases, there is no distinguishable difference between them. Based on this data, two possible conclusions can be made. Firstly, there is no optimum placement of actuation. Secondly, the actuation is not having any effect on the flow field. This could be due to the modelling method or point to a fundamental problem with plasma actuation in this specific application.

Pressure recovery values for both total and static pressure data at the AIP is also recorded. The total pressure recovery for the baseline and actuated cases is 0.9446 with a small variation around that number. However, the differences are not significant with variations starting after 4 decimal places. The static pressure recovery also does not vary significantly between the baseline and actuated cases and is calculated to be 0.8990.

Figure 6.11 shows the pressure distortion coefficients for various sector extents at the aerodynamic interface plane for both the baseline and actuated cases with the ac-DBD plasma model. Pressure distortion coefficients do not vary significantly between the baseline and actuated cases. However, with the scale of the figure no clear distinction between the various cases can be made for any one sector extent. Therefore, the cases were split up for each sector size. Pressure distortion coefficients for sectors of 30, 45, 60, and 90 degrees are presented in Figure 6.12. The baseline distortion is lower than than the distortion with the ac-DBD actuation. The differences are marginal, however, with far less than 1% variation between the various cases. There is also no clear optimum location of actuation that would outperform other actuation placements in the convoluted duct yet alone better the baseline case throughflow performance.

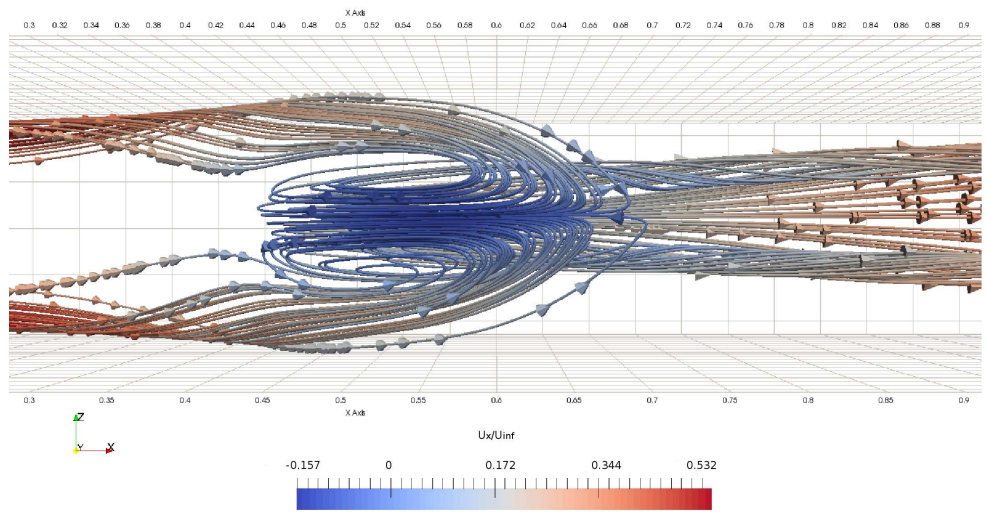
Unsurprisingly, with all performance parameters staying unchanged or varying only very slightly, the separation extent is not changed by the four actuation cases with the ac-DBD model either. As is the case for the baseline throughflow, the separation onset for the actuated cases also occurs upstream of the inflection point in the geometry and lies between  $2.0 < \frac{s_c}{D_1} < 3.7$ .

It is expected, to some degree, that the ac-DBD actuators have a low flow control authority due to their relatively low induced velocities compared to the free stream velocity. This is



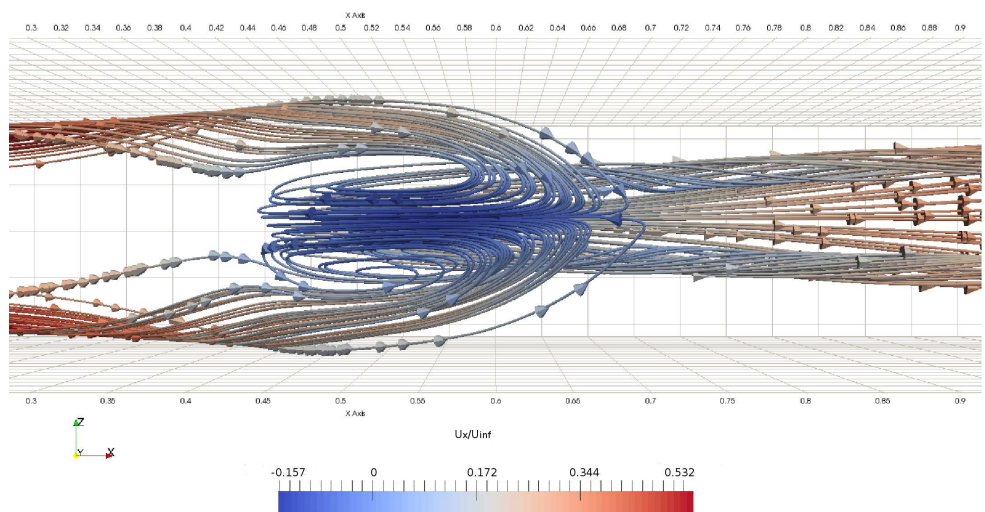
Baseline

(a)



$x = 0.18\text{m}$

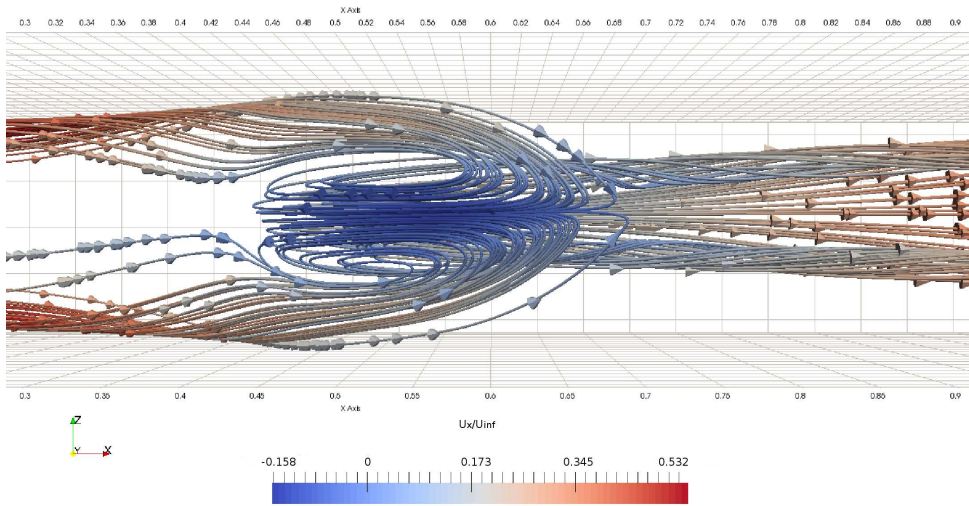
(b)



$x = 0.23\text{m}$

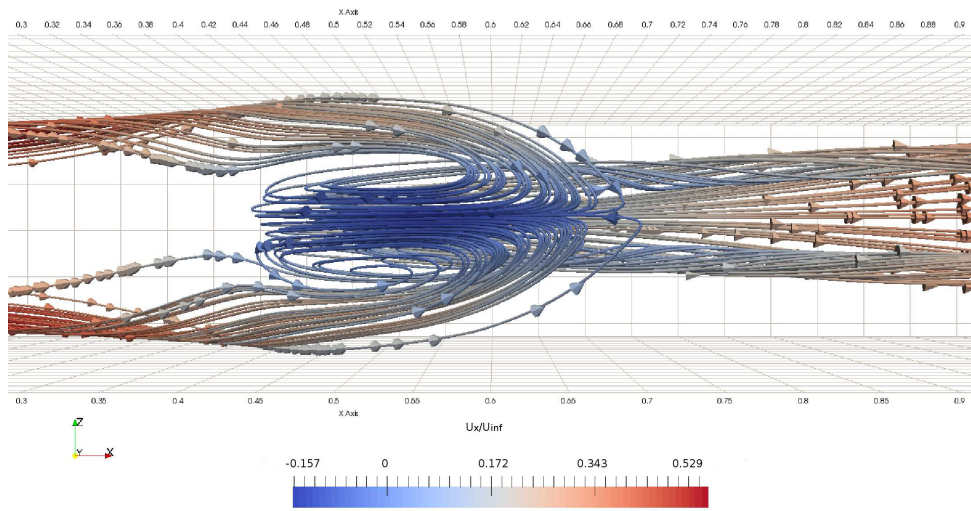
(c)

Figure 6.7: Streamlines at inflection point of s-duct for (6.8a) the baseline flow and ac-DBD model at: (6.7b)  $x = 0.18\text{ m}$  and (6.7c)  $x = 0.23\text{ m}$ . Colour legend describes the streamwise velocity component in ( $\text{ms}^{-1}$ ).



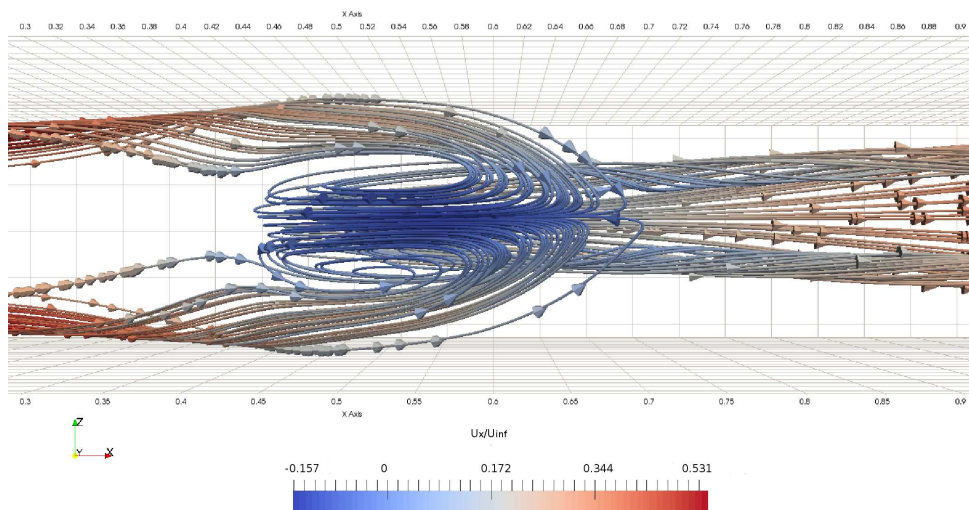
Baseline

(a)



$x = 0.28\text{m}$

(b)



$x = 0.33\text{m}$

(c)

Figure 6.8: Streamlines at inflection point of s-duct for (6.8a) the baseline flow and ac-DBD model at: (6.8b)  $x = 0.28\text{ m}$  and (6.8c)  $x = 0.33\text{ m}$ . Colour legend describes the streamwise velocity component in ( $\text{ms}^{-1}$ ).

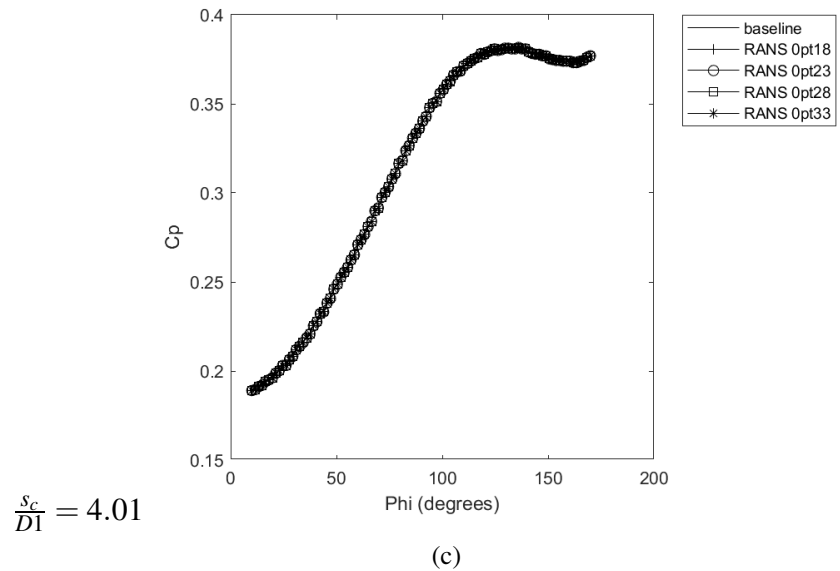
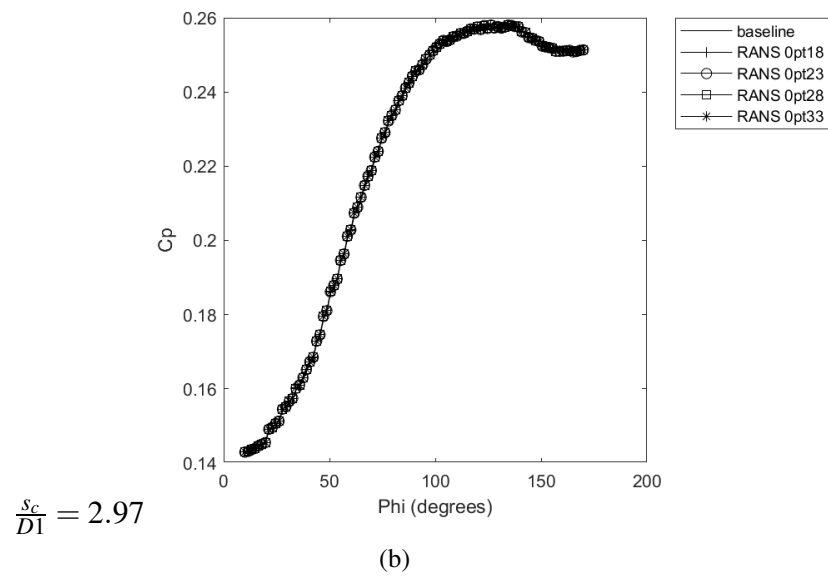
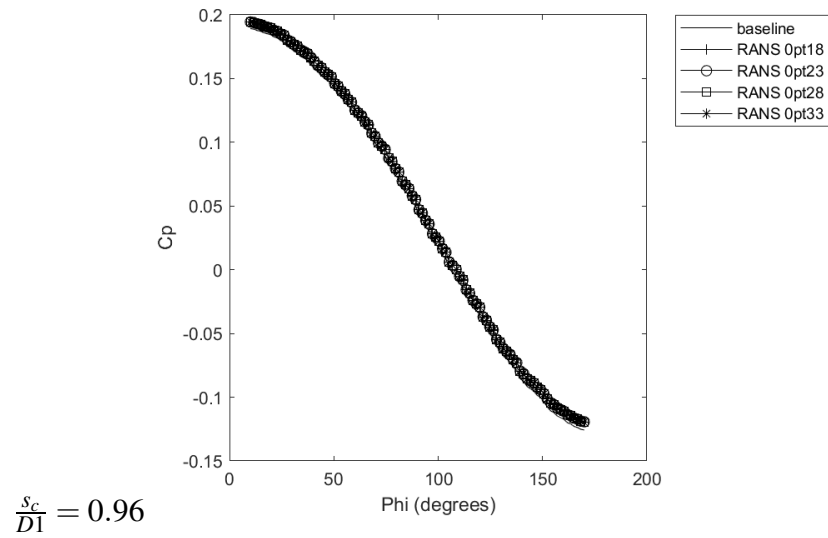


Figure 6.9: Wall static pressure contours at three cross-stream planes.

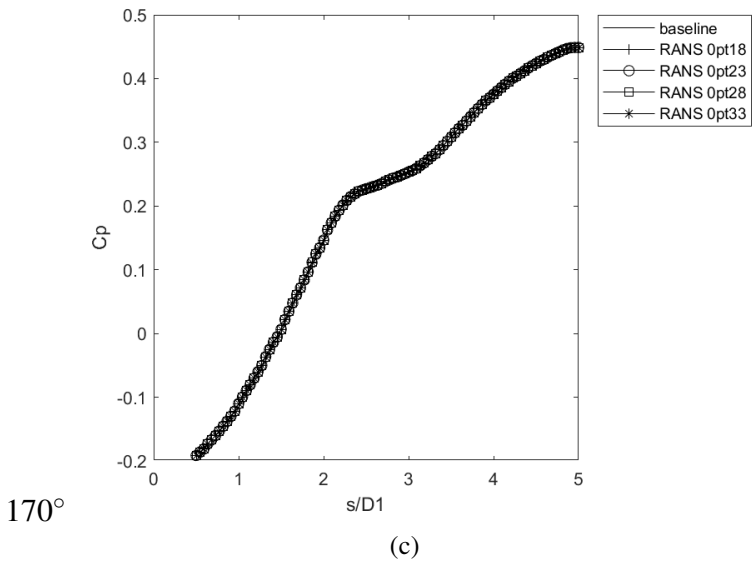
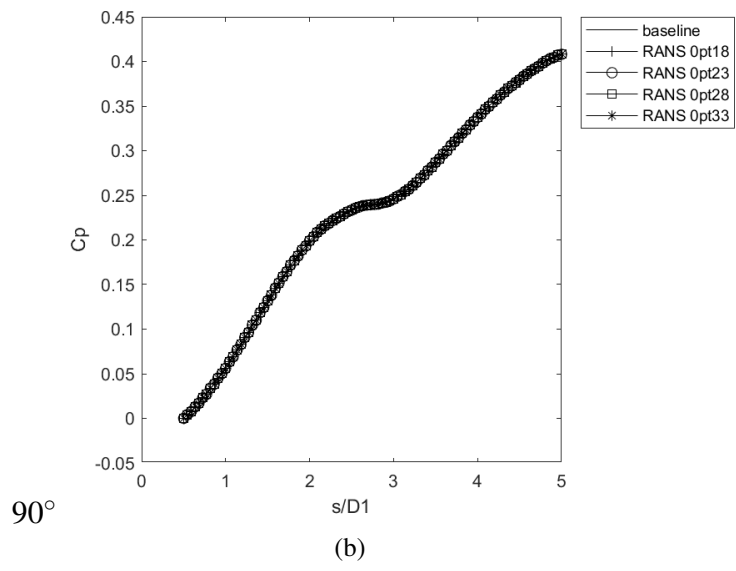
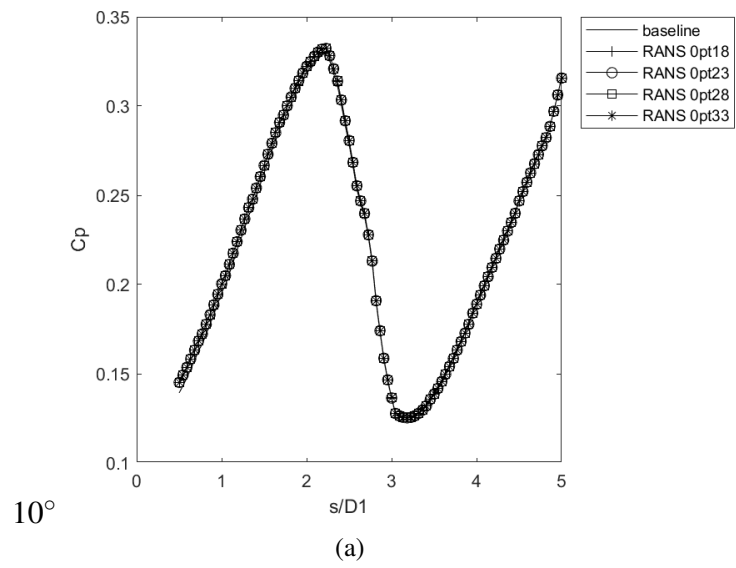


Figure 6.10: Wall static pressure contours along three streamwise lines.

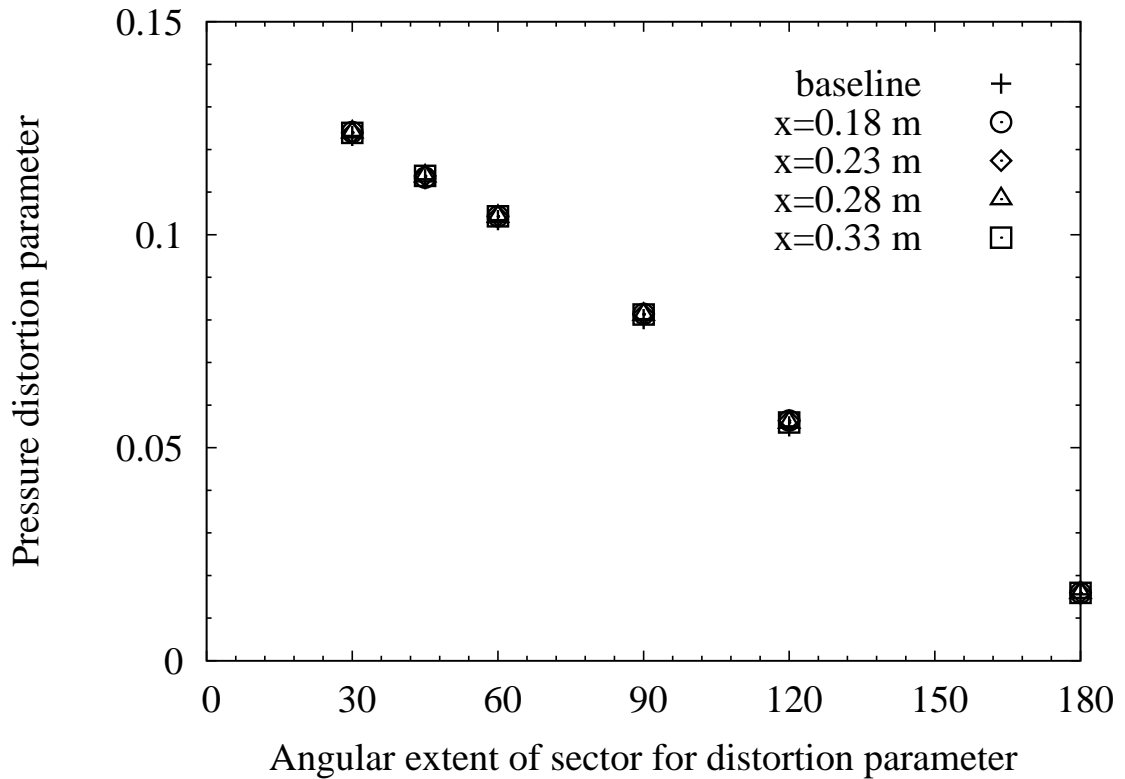


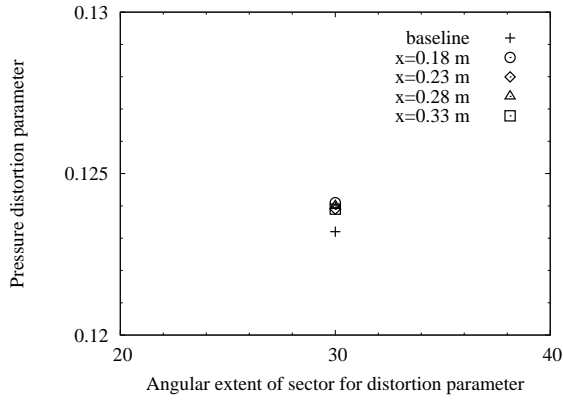
Figure 6.11: Pressure distortion coefficient at AIP for various sector extents.

reported in literature for other flows also. Zheng et al. [185] come to the same conclusion when investigating plasma flow control on bi-stable vortices over a cone-cylinder. Controlling free turbulent jets, Labergue et al. [186] also noticed a lower flow control authority with an increased free stream.

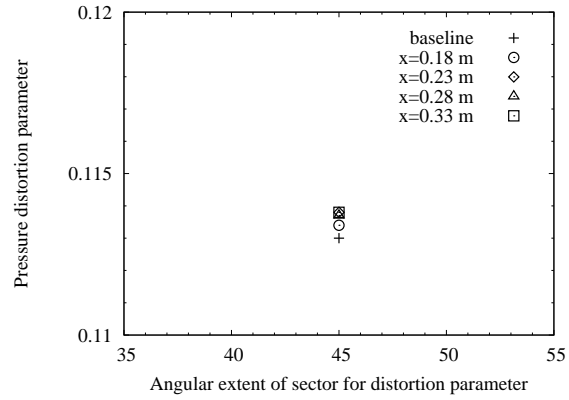
With no clear benefit of ac-DBD plasma actuation computed with RANS simulations and no clear difference in performance between the four actuation placements it is unlikely transient simulations will change that initial conclusion. With limited computational resources available and keeping in mind the considerable run time of DDES simulations, no transient CFD is conducted for the ac-DBD model. Transient simulations are still recommended as they form a key part of analysing flow control techniques in convoluted ducts. However, to justify the computational expense a performance benefit in steady state computations is needed to have confidence in the overall viability of the flow control technique and its application in the desired flow field.

#### 6.1.4 ns-DBD flow control

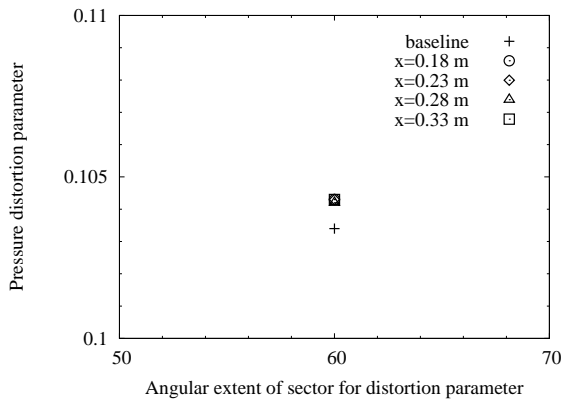
Unlike the ac-DBD actuated cases, ns-DBD actuation does not generate a continuous ionisation as it is operated in very short duration pulses. Steady state simulations are thus not employed with plasma pulse actuation being achieved through time step control. The ns-DBD flow control simulations require a much smaller time step than the baseline numerical computations due



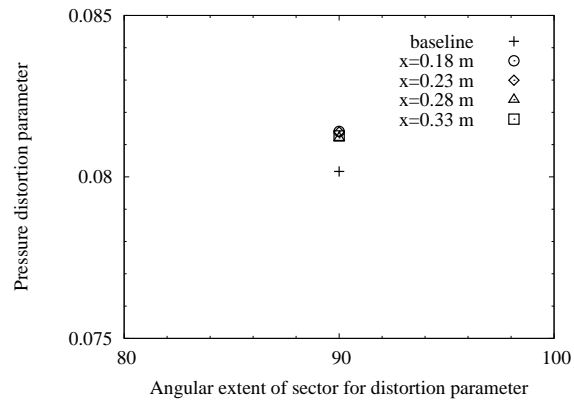
(a)



(b)



(c)



(d)

Figure 6.12: Pressure distortion coefficients for baseline and ac-DBD actuated cases: (6.12a) 30° sector; (6.12b) 45° sector; (6.12c) 60° sector; (6.12d) 90° sector.

to the nature of the actuation mode and timescales involved in the physical plasma ionisation mechanism. Therefore, the time step was reduced significantly and set at 20 nano seconds. An undesirable consequence of this necessity is the prolonged computational expense of any numerical study and extended run time. A further drawback is that no first estimates of performance criteria can be obtained of steady state simulations that can serve as a guidance for transient simulations. For those reasons, only one placement of actuation was chosen and set at  $x = 0.23$  m or  $\frac{x_c}{D_1} = 1.13619$ .

Table 6.3: Input details of numerical ns-DBD model.

axial location [m]	0.23
centreline location $\frac{x_c}{D_1}$	1.13619
pulse time [ $\mu$ s]	1.0
ambient temperature [K]	288.15
rest time [ms]	9.999
$\chi$	0.7
actuator start point	0.23
actuator length	0.006

Table 6.3 shows the input parameters for the ns-DBD model simulation specified in the fvOptions file. The pulse time of  $1\mu$ s and rest time of 9.999 ms are used to define an occurrence of actuation every 0.01 seconds. Hence, the simulation operates with actuation activated at a frequency of 100 Hz.

## DDES

Time averaged data is compared to the baseline DDES simulations. Similarly to the ac-DBD cases, entropy generation is looked at first. Figure 6.13 shows the entropy profile at the AIP for both the baseline and ns-DBD actuated cases. In absolute values, there is a higher total entropy level in the ns-DBD plasma model case. However, qualitatively the baseline case has a larger region of high entropy in the lower half of the AIP. For a quantitative comparison the entropy values across the AIP face are area averaged. This shows that the ns-DBD actuation results in a higher average entropy level across the AIP face. The baseline DDES produces an entropy level of  $2420.7 \frac{J}{K}$  which is only slightly higher than for the baseline RANS simulation. The ns-DBD actuated case, however, has an area averaged entropy level of  $2421.1 \frac{J}{K}$ . Caution has to be taken though when analysing entropy levels. The ns-DBD model adds heat to the selected cell region and thus increases the entropy in the system of the convoluted duct throughflow.

The separation extent of the baseline DDES simulations and the ns-DBD plasma model DDES simulations is shown in Figure 6.14 through the streamwise velocity profile along the symmetry plane of the convoluted duct at  $z = 0$  m. The upper limits of the streamwise velocity in the figure are set at  $0 \text{ m s}^{-1}$  so that the reverse flow region is highlighted. Based on those two

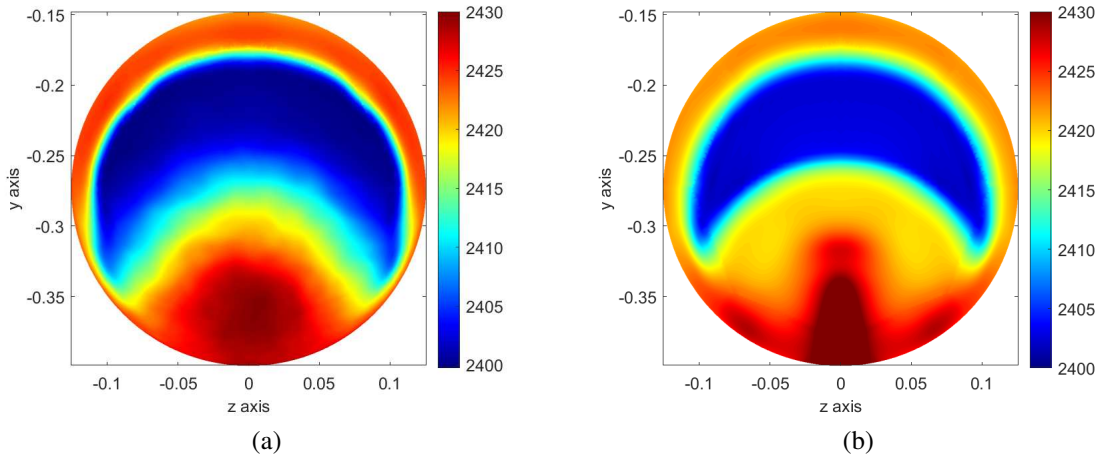


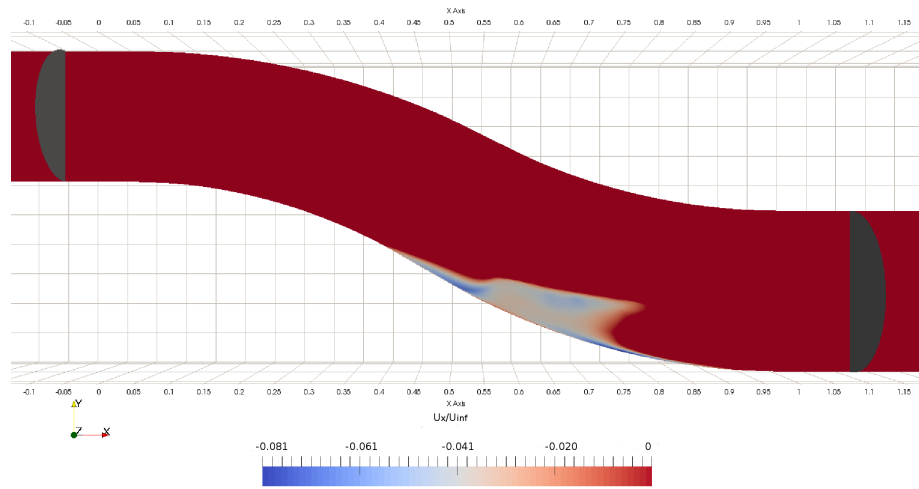
Figure 6.13: Entropy plots at the AIP for the (6.13a) baseline s-duct throughflow and ns-DBD plasma model simulation at (6.13b)  $x=0.23$  for time averaged DDES computations.

extents of reverse flow region the separated flow area for the baseline and actuated cases are very similar. Neither the onset of reversed flow nor the extent seems to be changed. The magnitude of the reverse flow varies between the two cases, however, with the actuated reverse flow being a few  $ms^{-1}$  higher than the baseline case.

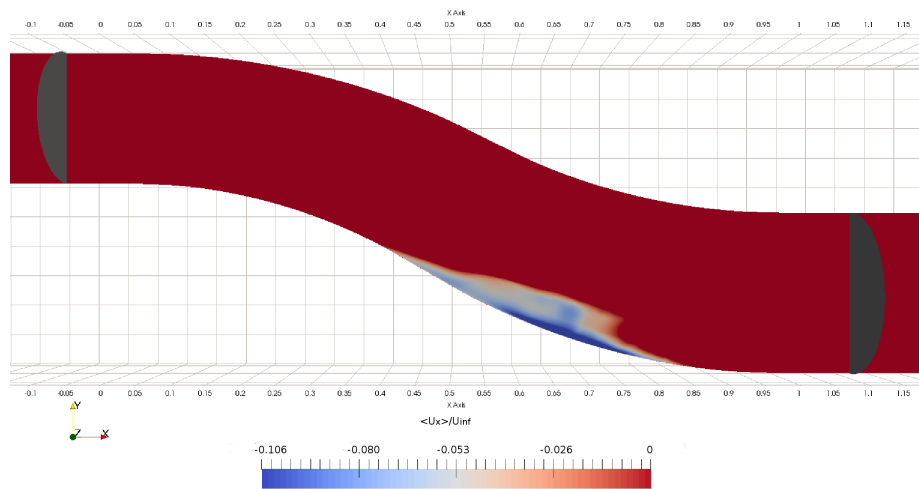
Streamlines at the inflection point in the duct show the separation region in more detail in Figure 6.15. The extent of the separation region does only vary marginally between the baseline simulation and the ns-DBD numerical model.

The total and static pressure recovery of the convoluted duct did not change from the baseline DDES computations to the actuated plasma model DDES computations. Therefore, the total efficiency and performance of the convoluted duct stayed the same with no visible effect of the plasma actuation with the ns-DBD model.

Figure 6.16 shows the standard deviation maps of flow properties at the AIP for the baseline and ns-DBD actuated transient DDES computations. The standard deviation values for the three velocity components are normalised by the centreline velocity magnitude at the s-duct inlet and the total pressure standard deviation values are non-dimensionalised by the atmospheric pressure. The standard deviation levels of the in-plane velocity components,  $v$  and  $w$ , for the ns-DBD actuated case are lower than for the baseline case. The difference is low, however, with  $4.5 ms^{-1}$  and  $1.8 ms^{-1}$ , respectively. Contrary, the streamwise velocity standard deviation is higher with the ns-DBD model than for the baseline case. The difference here is  $3.8 ms^{-1}$ . The total pressure standard deviation reaches the same maximum value for both the baseline and ns-DBD actuated case. Figure 6.16 also shows that the baseline standard deviation maps have a larger region of peak values than the actuated simulation. This data seems to suggest that the plasma actuation, though not influencing traditional performance metrics, has an effect on the transient features of the flow.

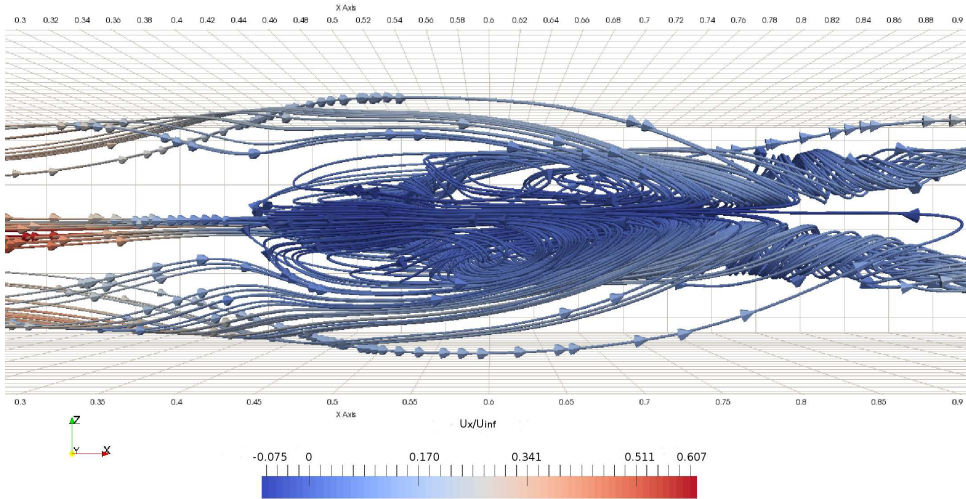


(a)

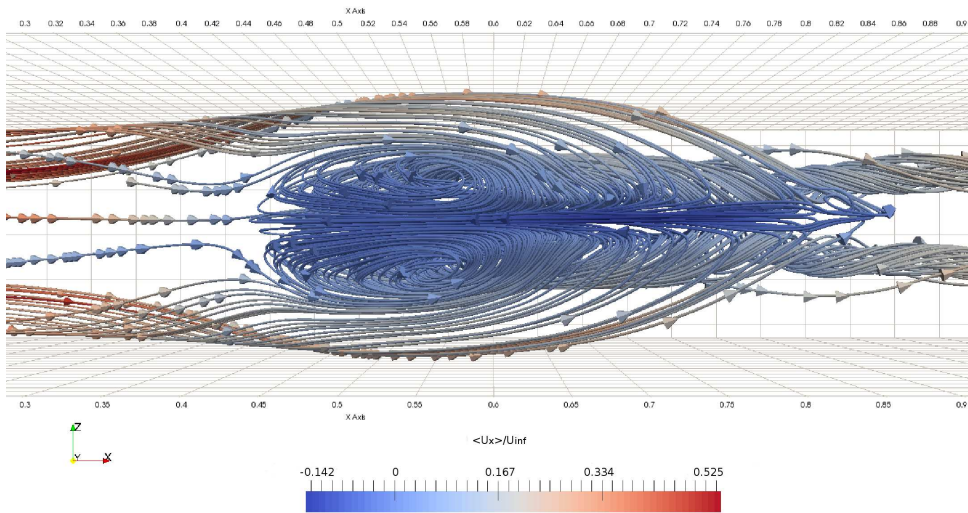


(b)

Figure 6.14: Reversed flow region with streamwise velocity normalised by the inlet centreline velocity for time averaged DDES simulations of (6.14a) baseline s-duct throughflow and (6.14b) ns-DBD plasma model simulation at  $x = 0.23$  m. Upper limit of colour map was set to 0.



(a)



(b)

Figure 6.15: Streamlines for time averaged DDES simulations of (6.15a) baseline s-duct throughflow and (6.15b) ns-DBD plasma model simulation at  $x = 0.23$  m. Colour legend describes the streamwise velocity component normalised by the inlet centreline velocity.

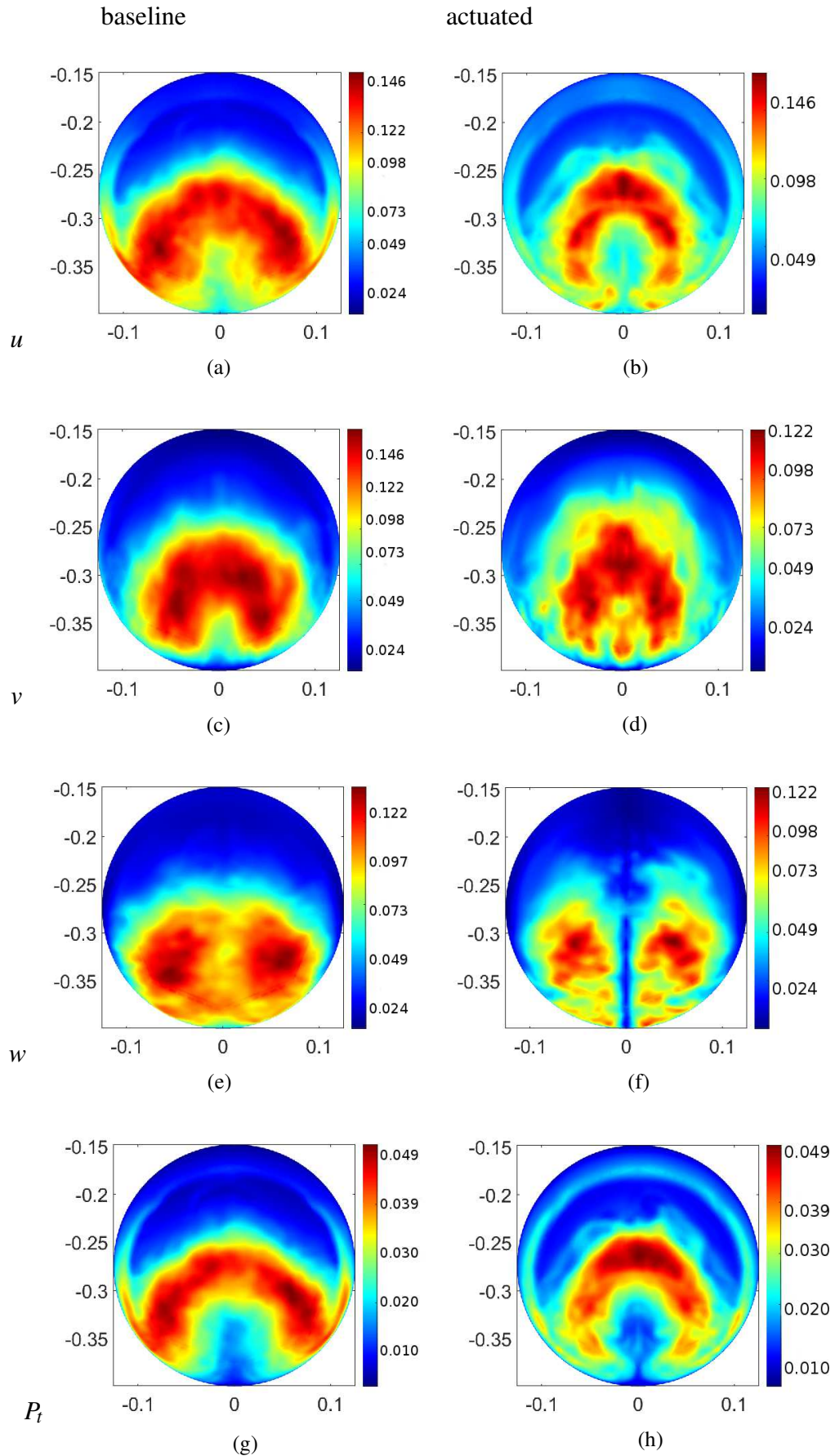


Figure 6.16: Standard deviation maps of flow properties at AIP showing velocity components  $u$ ,  $v$ ,  $w$  normalised by the inlet centreline velocity, and total pressure normalised by the atmospheric pressure for DDES simulations of the baseline and actuated cases.

This is to some degree unexpected, as in literature the high speed flow control authority of ns-DBD plasma actuators is well documented. For instance Littel et al. [187] applied ns-DBD plasmas to control stall on an aerofoil at Reynolds number of 1 million. However, Russell [187] also found ns-DBD plasma actuators not to be effective as high speed flow control devices in supersonic cavity flows. Neither a reduction nor an amplification in the amplitude of the resonant tones were observed within the cavity investigated.

Pulsed operation of ns-DBD plasmas for flow control is believed to be the reason for its effective application to other high speed, high Reynolds number flows. However an explanation of the limited effect might be that the vorticity generated by discrete lengths of plasma actuators is in fact the key to the influence on the surrounding fluid. This was recently postulated by Russell [187]. Following this line of thought it is the small vortices created rather than the pulsed forcing that makes the ns-DBD plasmas effective as high speed flow control devices. The phenomenological model, however, is applied to a whole cell set of the numerical domain and not to discrete patches in the mesh region. Therefore, the same effect does not transpire here.

### **6.1.5 Conclusions**

Flow control studies in the convoluted duct did not show a clear benefit in terms of performance improvement. The initial RANS computations with the ac-DBD numerical model applied at four streamwise locations did not answer the question which actuation placement is best suited for flow control. To answer this question fully, an optimisation study would be best equipped with incremental changes to the placement being driven by a cost function based on previous iterations. Such an approach does, however, require a considerable amount of time and computational resources as oftentimes hundreds of iterations are needed for an optimiser to find an optimum solution. This is outwith the scope of this thesis and hence this question remains unanswered.

Time averaged properties of plasma actuation did produce limited performance benefits at best. Therefore, transient phenomena were not computed in the case of the ac-DBD model. For the ns-DBD model, transient results show a mixed picture with lower standard deviation values for in-plane velocity components, but a higher value for the streamwise component. Both ac and ns DBD flow control studies did not produce the results hoped for. Other flow control studies in convoluted ducts did record more performance benefits as pointed out in the literature review. On the other hand, some flow control studies recorded in the public domain were detrimental to the overall throughflow performance increasing non-uniformity and distortion parameters.

## 6.2 Practical considerations

In light with the many benefits plasma actuators offer it is no surprise that they were employed as flow control devices on bluff bodies [107–109], backwards facing steps [110], and aerofoils to reduce wake losses, promote mixing, delay separation, and increase the stall angle. The use of plasma actuators for turbomachinery has been reported in [114, 115, 118, 119]. A number of researchers report higher aerodynamic efficiencies through increased lift to drag ratios on airfoils [71, 134, 188–191]. Others show the flow attachment at post-stall angles of attack for plasma actuated cases [192, 193].

### 6.2.1 Control authority

There is, however, a question mark over the control authority of plasma actuators at normal, cruise flight conditions. From the aforementioned studies, the highest free stream velocity in experiments was used by Correale [71] at  $80 \text{ ms}^{-1}$  and a  $\text{Re}_{\text{chord}}$  of  $3.2 \times 10^6$ , while the second highest  $\text{Re}_{\text{chord}}$  used was  $1 \times 10^6$  [193] with a free stream velocity of  $62 \text{ ms}^{-1}$ . Typical cruise conditions of civil aircraft, however, range from Mach numbers of 0.5 to 0.8 and a Reynolds number in the tens of millions. It follows that working principle in compressible flow fields have yet to be demonstrated. To the author's knowledge, no studies of successful plasma flow control at realistic Mach and Reynolds numbers have been published to date.

Moreover, flow control authority in adverse pressure gradients and off-design conditions needs to be demonstrated for this technology to be considered in practical applications in the aviation industry.

### 6.2.2 Effect of ambient conditions

It has been shown that plasma actuator are capable to operate in both low temperature and low pressure environments. Thermal effects and the ability to mitigate aircraft icing was demonstrated in two studies by Liu and Chen [159, 160]. Nanosecond plasma performance with ambient pressure has been investigated in [123]. With lower pressures and hence fewer air molecules to ionise, the plasma actuator ionisation was shown to be weaker with less flow control authority. AC plasma actuators pressure dependency also varies with ambient pressure [143]. Based on those results, the body force (ionic wind) produced has two maxima - one at subatmospheric and one at superatmospheric pressures. The combined effect, if any, of ambient temperature and pressure on plasma actuators is yet to be investigated. This is key to gain confidence in the practical operation of plasma actuators at altitude or within the challenging environment of modern jet engines.

### **6.2.3 Power source**

Further practical considerations include the energy source for the active actuation. Plasma actuators require very high voltage input signals (typically 5-40 kV) and high frequency (typically 1-20 kHz) waveforms to operate. This is of little concern, however, as the current being drawn is low in the order of milliamps, resulting in generally low power requirements. Voltage levels can be achieved from a mains supply if an electrical step up converter is used. This could possibly be drawn from the propulsion system i.e. the gas turbine engine or from batteries on board the aircraft. Both the voltage converter and the batteries mean additional weight, however. Therefore, the overall benefits due to the plasma actuator flow control have to be evaluated with the extra system complexity and mass taken into consideration.

With the given voltage levels, electromagnetic interference is an issue that has to be addressed. It is beneficial to place the power source as close to the actuator as possible and reduce the high voltage cable length that connects to the plasma actuator. Some kind of shielding is advised to protect other electrical systems in the vicinity of the plasma actuator as some electromagnetic noise will still be generated. The actuator should also be separated from other metal surfaces with a dielectric barrier. Note, that these issues will have to be solved for the 'all-electric' aircraft of the future also.

### **6.2.4 Control system**

Active actuation requires a control system operated manually or an autonomous feedback loop based on sensor readings of the incoming flow. Such systems were shown to work by Segawa et al. and Kwan et al. for low speed plasma flow control with free stream velocity values of 20  $\text{ms}^{-1}$  and 30  $\text{ms}^{-1}$ , respectively [194, 195]. Concepts are yet to be translated to higher velocity environments and industrial scale.

### **6.2.5 Conclusions**

A multidisciplinary effort including power electronics, control systems, and plasma actuator development is essential to make plasma actuator flow control viable for industrial scale, commercial applications. Power supply and electromagnetic noise considerations pose problems that are solvable. The overall benefit of using plasma actuators has first to become apparent, in order to make the exercise worthwhile. Therefore, the main push in research ought to go towards increasing the flow control authority of plasma actuators. Attention is also required to reduce the size and mass of step up converters and minimise the overall energy use of PA increasing their efficiency. Experiments at realistic flow conditions are key to demonstrate that ability.

# Chapter 7

## Conclusions & Future work

Combining both numerical and experimental aspects, the work presented in this thesis covers a broad range of topics within the fields of aerodynamics, fluid dynamics, and flow control. Background information, details, and explanations are kept concise due to the complexity and depth of every one of those research fields.

The common denominator in this research project is the convoluted duct. In the literature review, the current accepted knowledge about s-shaped ducts is established and categorised, comparing and contrasting different approaches and methods. The main findings are summarised in a published review article which should be beneficial to the research community.

### 7.1 Conclusions

Separate parts of this thesis are summarised in turn and conclusions drawn on the outcomes of each section. Those include i) OpenFOAM CFD validation for convoluted duct test case; ii) analysis of transient phenomena and coherent structures in convoluted ducts; iii) ac and ns DBD plasma characteristic; iv) numerical models of ac and ns DBD plasma actuation; v) flow control studies with plasma actuators.

#### 7.1.1 OpenFOAM CFD validation for convoluted duct test case

Validation of CFD simulations in the open source tool OpenFOAM were conducted against experimental data from literature. Results show that the throughflow was captured accurately as various flow features and performance criteria were matched to experiments. Numerical data compares well qualitatively and quantitatively with experimental findings. Well known flow features like the separation extent, the double vortex pattern, and the location of the low velocity region at the AIP were captured. Wall static pressure profiles along streamwise lines and in cross-stream planes matched experimental data very closely.

## **7.1.2 Analysis of transient phenomena and coherent structures**

Transient data confirmed the existence of dominant shifting modes in the vertical and horizontal directions. In addition, a second vertical shifting mode was extracted from the snapshot CFD data time series. Rate of occurrence of modes and phase information were also discussed.

## **7.1.3 ac- and ns-DBD plasma characteristic**

Experimental campaigns for ac and ns DBD plasma actuators were designed with two purposes. Each study was stand alone so that it would answer a specific research question. However, the main aim was to gather data for the validation of numerical plasma models. The ns-DBD experimental campaign established the effect ambient pressure has on the resulting shock strength, while the ac-DBD experiments analysed parameters such as frequency, dielectric material and thickness, and actuator geometry.

## **7.1.4 Numerical models of ac and ns DBD plasma actuation**

Numerical models of ac and ns DBD plasma actuators were adopted from literature. Those models were implemented in OpenFOAM and tested in 2D and 3D computational domains with quiescent boundary conditions. The models were found to phenomenologically capture the plasma actuators but not quantitatively. Therefore, with the experimental data collected, the models were tuned to match the experimental findings more accurately.

## **7.1.5 Flow control studies with plasma actuators**

Numerical plasma flow control in the convoluted duct did not show any significant performance improvement. Analysis shows marginal differences between the baseline case and actuated cases. However, with the current flow control authority of plasma actuators the effects are small.

Transient features showcased some effect of the actuation on the s-duct through-flow. Standard deviation values of transient flow properties are slightly different. Those paint a mixed picture with lower maximum fluctuations of the in-plane velocities, but a higher standard deviation of the streamwise velocity component.

## **7.2 Future work**

Recommendations for future work are given in bullet points below. Different aspects of the work are grouped individually.

The proposed work on flow physics in convoluted ducts is intended to provide greater insight into flow structures. Higher fidelity data would also be useful for validation of numerical models and create a reference for other studies.

With regards to the flow control aspect, work is required on the authority of the ac-DBD plasma actuators in higher velocity flow fields in order to see performance benefits. Moreover, a tailored control strategy could easier be formulated for the specific case of the s-duct with detailed phase information on important flow features. This ties in with the previous point.

On a separate note, the performance of plasma actuators in high altitude is of very practical interest. Those experiments need a controlled environment of ambient temperature and pressure. Results would complement the data collected for effect of ambient pressure variation.

- Flow physics in convoluted ducts
  - determine exact mechanism, cause, and effect of unsteadiness and flow phenomena (such as flow separation, diffusion, swirl formation, secondary flows)
  - conduct benchmark LES and DNS numerical studies to complement literature
  - extract phase information for modal analysis from experimental data at AIP
- ns-DBD experimental campaign
  - establish combined effect of ambient temperature and pressure on actuation performance
- ac-DBD experimental campaign
  - explore options to increase flow control authority of actuation
- Numerical plasma flow control in convoluted ducts
  - demonstrate flow control authority on lower Reynolds number test case
  - use optimisation algorithms to define optimum actuation location
  - compare steady actuation to pulsed operation of plasma actuator
  - collect experimental data with plasma actuation
- Experimental flow control studies in convoluted ducts
  - collect experimental data with plasma actuation in convoluted duct



# Appendix A

## A.1 fvOption file ns-DBD numerical model

Example fvOption file for the ns-DBD numerical model.

```
/*-----* C++ *-----*/
=====
\ \ \ \ \ F i e l d           OpenFOAM: The Open Source CFD Toolbox
\ \ \ \ \ O p e r a t i o n       Version: 2.4.0
\ \ \ \ \ A n d                   Web: www.OpenFOAM.org
\ \ \ \ \ M a n i p u l a t i o n
-----*/
FoamFile
{
    version     2.0;
    format      ascii;
    class       dictionary;
    location    "system";
    object      fvOptions;
}
// ***** //

nsdbdTemperature
{
    type        nsdbdTemperatureConstraint;
    active      true;

    nsdbdTemperatureConstraintCoeffs
    {
        selectionMode    cellSet;
        cellSet          heatedRegion;
        ambientTemperature 293;
        pulseTime        100e-9;
        restTime         4e-3;
        actuatorLength   0.010;
        actuatorStartPoint 0.050;
        chi               0.2;
    }
}
// ***** //
```

## A.2 fvOption file ac-DBD numerical model

Example fvOption file for the ac-DBD numerical model.

```
/*-----* C++ -*-----*/
=====
Field      | OpenFOAM: The Open Source CFD Toolbox
Operation  | Version: 2.4.0
And       | Web: www.OpenFOAM.org
Manipulation
-----*/
FoamFile
{
    version      2.0;
    format       ascii;
    class        dictionary;
    location     "system";
    object       controlDict;
}
// ***** //

momentumSource
{
    type          vectorCodedSource;
    active        on;
    selectionMode cellSet;
    cellSet       ionicWindRegion;
    name          actuator1;

    vectorCodedSourceCoeffs
    {
        fields      (U); //fields (U);
        redirectType velocitySource;
        selectionMode cellSet;
        cellSet     ionicWindRegion;
        scalar ccX = mesh_.cellCentres()[cells[t]].x();
        scalar ccY = mesh_.cellCentres()[cells[t]].y();
        scalar ccZ = mesh_.cellCentres()[cells[t]].z();
    }

    codeCorrect
    #{
        Pout<< "***codeCorrect**" << endl;
    #};

    codeAddSup
    #{
        Pout << "***codeAddSup***" << endl;
        cellSet selectedCells(mesh_, cellSetName_);
        labelList cells = selectedCells.toc();
        vectorField values(cells.size());

        volVectorField Su
        (
            IOobject
            (
                "Su",
                mesh_.time().timeName(),
                mesh_,
                IOobject::NO_READ,
                IOobject::AUTO_WRITE
            ),
            mesh_,
            dimensioned<vector>
            (
                "zero",
                eqn.dimensions()/dimVolume,
                pTraits<vector>::zero
            )
        );

        scalar V = 0.0;
        forAll (cells, t)
        {
            V += mesh_.V()[cells[t]];
        }
        reduce (V, sumOp<scalar>());

        forAll(cells, t)
        {
            scalar ccX = mesh_.cellCentres()[cells[t]].x();
            scalar ccY = mesh_.cellCentres()[cells[t]].y();
            scalar ccZ = mesh_.cellCentres()[cells[t]].z();
            //inputs
            scalar fv= 10; //frequency of voltage (kHz)
            scalar d = 0.1; //thickness of dielectric (cm)
            scalar V0 = 16000; //V0 the applied voltage peak-to-peak (V)
            scalar delta_vc = 600; //the normal falldown of cathode voltage
            scalar delta_tq = 1e-4; //is the residence time of negative ions inside the acceleration volume
            scalar Fx_0 = 2.0; //constant
            scalar Fy_0 = 2.0; //constant
            scalar beta_x = 8e5; //constant
            scalar beta_y = 1e7; //constant
            scalar f_mod = 7.5359e-6; //constant
            scalar alpha = 1;
            scalar theta = 1;
            scalar y0 = 0.0; //actuator start point y
            scalar x0 = 0.02; //actuator start point x
            scalar yref = 0;
        }
    }
}
```

```

//Equations
scalar thrust_soloviev=2.4e-10*pow(alpha,4.0)*(fv/d)*pow((9.0/4.0)*V0/delta_vc,4.0)*pow(1.0-((7.0/6.0)*delta_vc/V0),4.0)*(1.0 - exp(-1.0/(4.0*fv*delta_tq)));
scalar distribution_singh_x = (Fx_0/Fy_0)*exp(-1.0*sqr((ccX - x0 - (ccY - yref - y0) )/ccY) - beta_x*sqr(ccY - yref - y0));
scalar distribution_singh_y = (Fx_0/Fy_0)*exp(-1.0*(sqr(((ccX - x0)/ccY))) - beta_y*sqr((ccY - yref - y0)));
vector distribution_singh = vector::zero;
distribution_singh.x() = distribution_singh_x;
distribution_singh.y() = distribution_singh_y;

vector total_thrust =(thrust_soloviev)*(distribution_singh/f_mod);

    Su[cells[t]] = total_thrust;
}

eqn += Su;
#};

codeSetValue
#{
    Pout<< "**codeSetValue**" << endl;
#};

// Dummy entry. Make dependent on above to trigger recompilation
code
#{
    $codeInclude
    $codeCorrect
    $codeAddSup
    $codeSetValue
#};
}

// sourceTimeCoeffs
velocitySourceCoeffs
{
    // Dummy entry
    selectionMode    cellSet;
    cellSet          ionicWindRegion;
}
}

```



```

edges
(
  //outer circle
  arc 4 9 (0 0.0943355 -0.039075) //22.5 degrees
  arc 15 20 (1.02 -0.1574383264 -0.04811478795)
  arc 26 31 (-0.762 0.0943355 -0.039075)
  arc 37 42 (1.782 -0.1574383264 -0.04811478795)

  arc 9 10 (0 0.039075 -0.0943355) //67.5 degrees
  arc 20 21 (1.02 -0.225482912 -0.1161593736)
  arc 31 32 (-0.762 0.039075 -0.0943355)
  arc 42 43 (1.782 -0.225482912 -0.1161593736)

  arc 10 5 (0 -0.039075 -0.0943355) //112.5 degrees
  arc 21 16 (1.02 -0.321712488 -0.1161593736)
  arc 32 27 (-0.762 -0.039075 -0.0943355)
  arc 43 38 (1.782 -0.321712488 -0.1161593736)

  arc 5 0 (0 -0.0943355 -0.039075) //157.5 degrees
  arc 16 11 (1.02 -0.3897570736 -0.04811478795)
  arc 27 22 (-0.762 -0.0943355 -0.039075)
  arc 38 33 (1.782 -0.3897570736 -0.04811478795)

  spline 0 11
  (
    ( 0.0800532185 -0.1060679855 0 )
    ( 0.1592740463 -0.1177924582 0 )
    ( 0.2368922868 -0.1369864146 0 )
    ( 0.3122124787 -0.1632837343 0 )
    ( 0.3846193187 -0.1962616849 0 )
    ( 0.4535997092 -0.2354556494 0 )
    ( 0.5401725974 -0.2838274679 0 )
    ( 0.6309427483 -0.3244117493 0 )
    ( 0.7252193084 -0.3566859876 0 )
    ( 0.8222427052 -0.3801819626 0 )
    ( 0.9211697924 -0.3945008131 0 )
  )
  spline 4 15
  (
    ( 0.0979328292 0.0982969435 0 )
    ( 0.1953434666 0.0867674326 0 )
    ( 0.2915578356 0.0574914407 0 )
    ( 0.3862476643 0.0401263122 0 )
    ( 0.4784351368 0.0049270339 0 )
    ( 0.5674996877 -0.0381421411 0 )
    ( 0.6389337408 -0.0720334621 0 )
    ( 0.7127579025 -0.0996264098 0 )
    ( 0.7883913628 -0.1209246196 0 )
    ( 0.8653005756 -0.1359885929 0 )
    ( 0.9430049536 -0.144923726 0 )
  )
  spline 10 21
  (
    ( 0.0808930238 -0.003885521 -0.1025727847 )
    ( 0.1773087565 -0.0155125128 -0.1038577778 )
    ( 0.2642750612 -0.0347924869 -0.1057989375 )
    ( 0.3492300715 -0.061578711 -0.1082322222 )
    ( 0.4315272278 -0.0956673255 -0.1109935903 )
    ( 0.5105401984 -0.1367988953 -0.1139190000 )
    ( 0.5895531691 -0.177930465 -0.1168444097 )
    ( 0.6718503254 -0.2120190795 -0.1196057778 )
    ( 0.7568053356 -0.2388053036 -0.1220390625 )
    ( 0.8437716404 -0.2580852777 -0.1239802222 )
    ( 0.9320087370 -0.2697122695 -0.1252652153 )
  )
  spline 9 20
  (
    ( 0.0934629265 0.0686443906 -0.0725299116 )
    ( 0.1863261115 0.0579260261 -0.0734385389 )
    ( 0.2779664484 0.0400186592 -0.0748111461 )
    ( 0.3677388679 0.0149530273 -0.0765317383 )
    ( 0.4549811823 -0.0171830052 -0.0784843204 )
    ( 0.5390199431 -0.0562459979 -0.0805528974 )
    ( 0.6142434550 -0.0953809906 -0.0826214745 )
    ( 0.6923041139 -0.127445023 -0.0845740565 )
    ( 0.7725983492 -0.1525186549 -0.0862946487 )
    ( 0.8545361080 -0.1704180219 -0.0876672559 )
    ( 0.9375461633 -0.1811363864 -0.0885758832 )
  )
  spline 5 16
  (
    ( 0.0845231212 -0.0764154326 -0.0725299116 )
    ( 0.1682914014 -0.0889510518 -0.0734385389 )
    ( 0.2505836740 -0.1096036331 -0.0748111461 )
    ( 0.3307212751 -0.1381104493 -0.0765317383 )
    ( 0.4080732732 -0.1741516459 -0.0784843204 )
    ( 0.4820604538 -0.2137517927 -0.0805528974 )
    ( 0.5648628833 -0.2605519395 -0.0826214745 )
    ( 0.6513965368 -0.2965931361 -0.0845740565 )
    ( 0.7410123220 -0.3250999523 -0.0862946487 )
    ( 0.8330071728 -0.3457525336 -0.0876672559 )
    ( 0.9266285827 -0.3582881527 -0.0885758832 )
  )
)

```

```

spline 3 14
(
  ( 0.0934629265 0.0786872637 0 )
  ( 0.1863261115 0.0683452650 0 )
  ( 0.2779664484 0.0510064506 0 )
  ( 0.3677388679 0.0266535112 0 )
  ( 0.4549811823 -0.0046737352 0 )
  ( 0.5390199431 -0.0428798953 0 )
  ( 0.6142434550 -0.0810860553 0 )
  ( 0.6923041139 -0.1124133017 0 )
  ( 0.7725983492 -0.1367662411 0 )
  ( 0.8545361080 -0.1541050555 0 )
  ( 0.9375461633 -0.1644470543 0 )
)
spline 1 12
(
  ( 0.0845231212 -0.0864583057 0 )
  ( 0.1682914014 -0.0993702906 0 )
  ( 0.2595836740 -0.1205914244 0 )
  ( 0.3307212751 -0.1498109332 0 )
  ( 0.4080732732 -0.186609158 0 )
  ( 0.4820604538 -0.2307178953 0 )
  ( 0.5648628833 -0.2747748748 0 )
  ( 0.6513965368 -0.3116248573 0 )
  ( 0.7410123220 -0.3408443661 0 )
  ( 0.8330071728 -0.3620654999 0 )
  ( 0.9266285827 -0.3749774848 0 )
)
spline 7 18
(
  ( 0.0889930238 -0.003885521 -0.0825727847 )
  ( 0.1773087565 -0.0155125128 -0.0838577778 )
  ( 0.2642750612 -0.0347924869 -0.0857989375 )
  ( 0.3492300715 -0.061578711 -0.0882322222 )
  ( 0.4315272278 -0.0956673255 -0.0909935903 )
  ( 0.5105401984 -0.1367988953 -0.0939190000 )
  ( 0.5895531691 -0.177930465 -0.0968444097 )
  ( 0.6718503254 -0.2120190795 -0.0996057778 )
  ( 0.7560953356 -0.2380853036 -0.1020390625 )
  ( 0.8437171604 -0.2580852777 -0.1039002222 )
  ( 0.9320873730 -0.2697122695 -0.1052652153 )
)
spline 8 19
(
  ( 0.0912279752 0.0545022550 -0.0583877760 )
  ( 0.1818174340 0.0437838905 -0.0592964033 )
  ( 0.2711207548 0.0258765236 -0.0606690105 )
  ( 0.3584844697 0.0008108916 -0.0623896027 )
  ( 0.4432542050 -0.0313251408 -0.0643421847 )
  ( 0.5247800707 -0.0703881335 -0.0664107618 )
  ( 0.6018983120 -0.1094511262 -0.0684793308 )
  ( 0.6820772197 -0.1415871506 -0.0704319209 )
  ( 0.7647018424 -0.1666527906 -0.0721525130 )
  ( 0.8491538742 -0.1845601575 -0.0735251202 )
  ( 0.9348167682 -0.195278522 -0.0744337475 )
)
spline 6 17
(
  ( 0.0867580725 -0.062273297 -0.0583877760 )
  ( 0.1720007079 -0.0740393281 -0.0592964033 )
  ( 0.2574293676 -0.0934806126 -0.0606690105 )
  ( 0.3399756733 -0.1204494901 -0.0623896027 )
  ( 0.4198002505 -0.1547411731 -0.0643421847 )
  ( 0.4963003261 -0.1960952986 -0.0664107618 )
  ( 0.5772080262 -0.2374679832 -0.0684793388 )
  ( 0.6616234311 -0.2718153439 -0.0704319209 )
  ( 0.7489080288 -0.2988770173 -0.0721525130 )
  ( 0.8383894066 -0.3184482162 -0.0735251202 )
  ( 0.9293579779 -0.3303812801 -0.0744337475 )
)
spline 2 13
(
  ( 0.0889930238 -0.003885521 0 )
  ( 0.1773087565 -0.0155125128 0 )
  ( 0.2642750612 -0.0347924869 0 )
  ( 0.3492300715 -0.061578711 0 )
  ( 0.4315272278 -0.0956673255 0 )
  ( 0.5105401984 -0.1367988953 0 )
  ( 0.5895531691 -0.177930465 0 )
  ( 0.6718503254 -0.2120190795 0 )
  ( 0.7560953356 -0.2380853036 0 )
  ( 0.8330071728 -0.2580852777 0 )
  ( 0.9266285827 -0.2697122695 0 )
)
);

```

```

boundary
(
  symmetry
  {
    type symmetryPlane;
    faces
    (
      (2 3 25 24)//front
      (3 4 26 25)
      (1 2 24 23)
      (0 1 23 22)
      (2 3 14 13)//s-duct
      (3 4 15 14)
      (1 2 13 12)
      (0 1 12 11)
      (13 14 36 35)//aft
      (14 15 37 36)
      (12 13 35 34)
      (11 12 34 33)
    );
  }
  outlet
  {
    type patch;
    faces
    (
      (35 36 41 40)//extension outlet
      (36 37 42 41)
      (40 41 42 43)
      (38 39 40 43)
      (33 34 39 38)
      (34 35 40 39)
    );
  }
  inlet
  {
    type patch;
    faces
    (
      (22 23 28 27)//extension inlet
      (23 24 29 28)
      (24 25 30 29)
      (25 26 31 30)
      (27 28 29 32)
      (29 30 31 32)
    );
  }
  duct
  {
    type wall;
    faces
    (
      (4 9 20 15)//s-duct
      (9 10 21 20)
      (10 5 16 21)
      (5 0 11 16)
      (4 9 31 26)//front
      (9 10 32 31)
      (10 5 27 32)
      (5 0 22 27)
      (20 15 37 42)//aft
      (21 20 42 43)
      (16 21 43 38)
      (11 16 38 33)
    );
  }
);
mergePatchPairs
(
);
// ***** //

```

## A.4 controlDict file

Example of controlDict file for the Wellborn s-duct CFD simulations with rhoPimpleFoam in OpenFOAM.

```
/*-----* C++ -*-----*\
|=====| Field | OpenFOAM: The Open Source CFD Toolbox
| \ \ \ | O peration | Version: plus
| \ \ \ | A nd | Web: www.OpenFOAM.com
| \ \ \ | M anipulation |
|=====|
FoamFile
{
  version 2.0;
  format ascii;
  class dictionary;
  location "system";
  object controlDict;
}
// ***** //

application rhoPimpleFoam;
startFrom latestTime;
startTime 92800;
stopAt endTime;
endTime 92800.5;
deltaT 1e-6;
writeControl timeStep; //runTime;
writeInterval 500; //5e-4; //1000 time directories
purgeWrite 0;
writeFormat ascii;
writePrecision 8;
writeCompression off;
timeFormat general;
timePrecision 18;
runTimeModifiable true;
adjustTimeStep no;
maxCo 10; //0.01;
maxDeltaT 1; //1e-8;
// ***** //
```

## A.5 fvSchemes file

Example of fvSchemes file for the Wellborn s-duct CFD simulations with rhoSimpleFoam in OpenFOAM.

```

/*-----* C++ *-----*/
=====
Field      | OpenFOAM: The Open Source CFD Toolbox
Operation  | Version: 3.0.1
And        | Web: www.OpenFOAM.org
Manipulation
-----*/
FoamFile
{
  version      2.0;
  format       ascii;
  class        dictionary;
  location     "system";
  object       fvSchemes;
}
// ***** //

ddtSchemes
{
  default      steadyState;
}

gradSchemes
{
  default      Gauss linear;
}

divSchemes
{
  default      none;

  div(phi,U)      bounded Gauss upwind linear;
  div(((rho*nuEff)*dev2(T(grad(U))))      Gauss linear;
  div(phi,e)      bounded Gauss upwind linear;
  div(phi,epsilon) bounded Gauss upwind linear;
  div(phi,k)      bounded Gauss upwind linear;
  div(phi,omega)  bounded Gauss upwind linear;
  div(phi,d,p)    Gauss upwind linear;
  div(phi,Ekp)    bounded Gauss upwind linear;
  div(phi|interpolate(rho),p) Gauss upwind linear;
}

laplacianSchemes
{
  default      Gauss linear corrected;
}

interpolationSchemes
{
  default      linear;
}

snGradSchemes
{
  default      corrected;
}

wallDist
{
  method meshWave;
  nRequired false;
}
// ***** //

```







```

{
  name   heatedRegion6;
  type   cellSet;
  action new;
  source radialStripToCell;
  sourceInfo
  {
    centre (0.1819 -0.01640 0);
    outerRadius 0.1200;
    innerRadius 0.10588;
    axialStart 0.1817;
    axialEnd 0.1828;
    angularStart 160;
    angularEnd 200;
  }
}
{
  name   heatedRegion7;
  type   cellSet;
  action new;
  source radialStripToCell;
  sourceInfo
  {
    centre (0.1822 -0.01640 0);
    outerRadius 0.1200;
    innerRadius 0.10595;
    axialStart 0.1820;
    axialEnd 0.1823;
    angularStart 160;
    angularEnd 200;
  }
}
{
  name   heatedRegion8;
  type   cellSet;
  action new;
  source radialStripToCell;
  sourceInfo
  {
    centre (0.1825 -0.01640 0);
    outerRadius 0.1200;
    innerRadius 0.10602;
    axialStart 0.1823;
    axialEnd 0.18265;
    angularStart 160;
    angularEnd 200;
  }
}
{
  name   heatedRegion9;
  type   cellSet;
  action new;
  source radialStripToCell;
  sourceInfo
  {
    centre (0.1828 -0.01640 0);
    outerRadius 0.1200;
    innerRadius 0.10610;
    axialStart 0.18265;
    axialEnd 0.18295;
    angularStart 160;
    angularEnd 200;
  }
}
{
  name   heatedRegion10;
  type   cellSet;
  action new;
  source radialStripToCell;
  sourceInfo
  {
    centre (0.1831 -0.01640 0);
    outerRadius 0.1200;
    innerRadius 0.10617;
    axialStart 0.18295;
    axialEnd 0.1833;
    angularStart 160;
    angularEnd 200;
  }
}
{
  name   heatedRegion11;
  type   cellSet;
  action new;
  source radialStripToCell;
  sourceInfo
  {
    centre (0.1834 -0.01640 0);
    outerRadius 0.1200;
    innerRadius 0.10625;
    axialStart 0.1833;
    axialEnd 0.1836;
    angularStart 160;
    angularEnd 200;
  }
}
}

```

```
{
  name heatedRegion12;
  type cellSet;
  action new;
  source radialStripToCell;
  sourceInfo
  {
    centre (0.1837 -0.01640 0);
    outerRadius 0.1200;
    innerRadius 0.10632;
    axialStart 0.1836;
    axialEnd 0.18395;
    angularStart 160;
    angularEnd 200;
  }
}
{
  name heatedRegion13;
  type cellSet;
  action new;
  source radialStripToCell;
  sourceInfo
  {
    centre (0.1841 -0.01640 0);
    outerRadius 0.1200;
    innerRadius 0.10640;
    axialStart 0.1840;
    axialEnd 0.1843;
    angularStart 160;
    angularEnd 200;
  }
}
{
  name heatedRegion14;
  type cellSet;
  action new;
  source radialStripToCell;
  sourceInfo
  {
    centre (0.1844 -0.01640 0);
    outerRadius 0.1200;
    innerRadius 0.10647;
    axialStart 0.1843;
    axialEnd 0.1846;
    angularStart 160;
    angularEnd 200;
  }
}
{
  name heatedRegion15;
  type cellSet;
  action new;
  source radialStripToCell;
  sourceInfo
  {
    centre (0.1847 -0.01640 0);
    outerRadius 0.1200;
    innerRadius 0.106545;
    axialStart 0.1846;
    axialEnd 0.1849;
    angularStart 160;
    angularEnd 200;
  }
}
{
  name heatedRegion16;
  type cellSet;
  action new;
  source radialStripToCell;
  sourceInfo
  {
    centre (0.1850 -0.01640 0);
    outerRadius 0.1200;
    innerRadius 0.10662;
    axialStart 0.1849;
    axialEnd 0.1853;
    angularStart 160;
    angularEnd 200;
  }
}
};
// ***** //
```

## A.9 radialStripToCell.C

Cell set code radialStripToCell.C file.

```

/*-----*/
=====
\ \ \ \ \ F i e l d      | OpenFOAM: The Open Source CFD Toolbox
  \ \ \ \ \ O peration  |
    \ \ \ \ \ A nd      | Copyright (C) 2011-2012 OpenFOAM Foundation
      \ \ \ \ \ M anipulation
-----*/

License
This file is part of OpenFOAM.

OpenFOAM is free software: you can redistribute it and/or modify it
under the terms of the GNU General Public License as published by
the Free Software Foundation, either version 3 of the License, or
(at your option) any later version.

OpenFOAM is distributed in the hope that it will be useful, but WITHOUT
ANY WARRANTY; without even the implied warranty of MERCHANTABILITY or
FITNESS FOR A PARTICULAR PURPOSE. See the GNU General Public License
for more details.

You should have received a copy of the GNU General Public License
along with OpenFOAM. If not, see <http://www.gnu.org/licenses/>.

/*-----*/

#include "radialStripToCell.H"
#include "polyMesh.H"
#include "addToRunTimeSelectionTable.H"

// ***** Static Data Members ***** //

namespace Foam
{
    defineTypeNameAndDebug(radialStripToCell, 0);
    addToRunTimeSelectionTable(topoSetSource, radialStripToCell, word);
    addToRunTimeSelectionTable(topoSetSource, radialStripToCell, istream);
}

Foam::topoSetSource::addToUsageTable Foam::radialStripToCell::usage_
(
    radialStripToCell::typeName,
    "\n Usage: radialStripToCell (centreX centreY centreZ) \n\n"
    " outerRadius innerRadius \n\n"
    " Select all cells with cellCentre within bounding region\n\n"
);

// ***** Private Member Functions ***** //

void Foam::radialStripToCell::combine(topoSet& set, const bool add) const
{
    const pointField& ctrs = mesh_.cellCentres();

    forAll(ctrs, cellI)
    {
        scalar offset = sqrt(
            sqr(centre_.y() - ctrs[cellI].y()) +
            sqr(centre_.z() - ctrs[cellI].z())
        );

        scalar cellAngle = atan(
            (centre_.z() - ctrs[cellI].z()) /
            (centre_.y() - ctrs[cellI].y())
        ) * 57.2958;

        vector offsets = ctrs[cellI] - centre_;

        if(offsets.z() >= 0)
        {
            if(offsets.y() >= 0) //1st quadrant
            {
                //ok
            }
            else //2nd quadrant
            {
                cellAngle = 180 + cellAngle; //ok
            }
        }
        else
        {
            if(offsets.y() <= 0) //3rd quadrant
            {
                cellAngle = 180 + cellAngle; //ok
            }
            else //4th quadrant
            {
                cellAngle = 360 + cellAngle; //ok
            }
        }
    }
}

```

```

        if(offset <= outerRadius_ && offset >= innerRadius_)
        {
            if(ctrs[cellI].x() >= axialStart_ && ctrs[cellI].x() <= axialEnd_)
            {
                if(cellAngle >= angleStart_ && cellAngle <= angleEnd_)
                {
                    addOrDelete(set, cellI, add);
                }
            }
        }
    }
}

// ***** Constructors ***** //

// Construct from components
Foam::radialStripToCell::radialStripToCell
(
    const polyMesh& mesh,
    const vector& centre,
    const scalar outerRadius,
    const scalar innerRadius,
    const scalar axialStart,
    const scalar axialEnd,
    const scalar angleStart,
    const scalar angleEnd
)
:
    topoSetSource(mesh),
    centre_(centre),
    outerRadius_(outerRadius),
    innerRadius_(innerRadius),
    axialStart_(axialStart),
    axialEnd_(axialEnd),
    angleStart_(angleStart),
    angleEnd_(angleEnd)
{}

// Construct from dictionary
Foam::radialStripToCell::radialStripToCell
(
    const polyMesh& mesh,
    const dictionary& dict
)
:
    topoSetSource(mesh),
    centre_(dict.lookup("centre")),
    outerRadius_(readScalar(dict.lookup("outerRadius"))),
    innerRadius_(readScalar(dict.lookup("innerRadius"))),
    axialStart_(readScalar(dict.lookup("axialStart"))),
    axialEnd_(readScalar(dict.lookup("axialEnd"))),
    angleStart_(readScalar(dict.lookup("angularStart"))),
    angleEnd_(readScalar(dict.lookup("angularEnd")))
{}

// Construct from Istream
Foam::radialStripToCell::radialStripToCell
(
    const polyMesh& mesh,
    Istream& is
)
:
    topoSetSource(mesh),
    centre_(checkIs(is)),
    outerRadius_(readScalar(checkIs(is))),
    innerRadius_(readScalar(checkIs(is))),
    axialStart_(readScalar(checkIs(is))),
    axialEnd_(readScalar(checkIs(is))),
    angleStart_(readScalar(checkIs(is))),
    angleEnd_(readScalar(checkIs(is)))
{}

// ***** Destructor ***** //

Foam::radialStripToCell::~radialStripToCell()
{}

// ***** Member Functions ***** //

void Foam::radialStripToCell::applyToSet
(
    const topoSetSource::setAction action,
    topoSet& set
) const
{
    if ((action == topoSetSource::NEW) || (action == topoSetSource::ADD))
    {
        Info<< "    Adding cells within defined region " << endl;

        combine(set, true);
    }
    else if (action == topoSetSource::DELETE)
    {
        Info<< "    Removing cells within defined region " << endl;

        combine(set, false);
    }
}

// ***** //

```



```
// Constructors

//- Construct from components
radialStripToCell
(
    const polyMesh& mesh,
    const vector& centre,
    const scalar outerRadius,
    const scalar innerRadius,
    const scalar axialStart,
    const scalar axialEnd,
    const scalar angleStart,
    const scalar angleEnd
);

//- Construct from dictionary
radialStripToCell
(
    const polyMesh& mesh,
    const dictionary& dict
);

//- Construct from Istream
radialStripToCell
(
    const polyMesh& mesh,
    Istream&
);

//- Destructor
virtual ~radialStripToCell();

// Member Functions

virtual sourceType setType() const
{
    return CELLSETSOURCE;
}

virtual void applyToSet
(
    const topoSetSource::setAction action,
    topoSet&
) const;

};

// ***** //
} // End namespace Foam
// ***** //
#endif
// ***** //
```

---

# Bibliography

- [1] S. R. Wellborn, B. A. Reichert, and T. H. Okiishi, *An experimental investigation of the flow in diffusing s-duct*. PhD thesis, NASA Technical Memorandum 105809, 1992.
- [2] B. A. Reichert and B. J. Wendt, “An experimental investigation of s-duct flow control using arrays of low profile v<sub>g</sub>,” tech. rep., NASA 106030, 1993.
- [3] B. A. Reichert and B. J. Wendt, “Improving diffusing s-duct performance by secondary flow control,” tech. rep., NASA Technical Memorandum 106492, 1994.
- [4] D. G. MacManus, N. Chiereghin, D. Gil-Prieto, and P. Zachos, “Complex aero-engine intake ducts and dynamic distortion,” in *33rd AIAA Applied Aerodynamics Conference*, no. 2015-3304, (Dallas, TX), AIAA Aviation, 2015.
- [5] Y. Hui, L. Feng, S. Yaoying, and S. Baigang, “Numerical investigation of electrohydrodynamic (EHD) flow control in an s-shaped duct,” *Plasma Science and Technology*, vol. 14, no. 10, pp. 897–904, 2012.
- [6] J. C. Vaccaro, Y. Elimelech, Y. Chen, O. Sahni, K. E. Jansen, and M. Amitay, “Experimental and numerical investigation on steady blowing flow control within a compact inlet duct,” *International Journal of Heat and Fluid Flow*, vol. 54, pp. 1143–152, 2015.
- [7] Z. J. Chen and J. J. Wang, “Numerical investigation on synthetic jet flow control inside an s-inlet duct,” *Science China Technological Sciences*, vol. 55, no. 9, pp. 2584–2578, 2012.
- [8] M. M. Wojewodka, C. White, S. Shahpar, and K. Kontis, “A review of flow control techniques and optimisation in s-shaped ducts,” *International Journal of Heat and Fluid Flow*, vol. 74, pp. 223–235, 2018.
- [9] S. A. E. Standard, “1419b: Inlet total pressure distortion considerations for gas turbine engines,” 2013.
- [10] S. A. E. Standard, “1420b: Gas turbine engine inlet flow distortion guidelines,” 2011.
- [11] N. C. Bissinger and T. Breuer, *Encyclopedia of Aerospace Engineering, Chapter EAE487; Basic principles, Gas turbine compatibility, intake aerodynamic aspects*. 2010.

- [12] R. W. Guo and J. Seddon, "The swirl in an s-duct of typical air intake proportions," *Aeronautical Quarterly*, vol. 34, no. 2, pp. 99–129, 1983.
- [13] P. K. Zachos, D. G. MacManus, and N. Chiereghin, "Flow distortion measurements in convoluted aero engine intakes," in *33rd AIAA Applied Aerodynamics Conference*, 2015.
- [14] J. C. Vaccaro, Y. Elimelech, Y. Chen, O. Sahni, K. E. Jansen, and M. Amitay, "Experimental and numerical investigation on the flow field within a compact inlet duct," *International Journal of Heat and Fluid Flow*, vol. 44, pp. 478–488, 2013.
- [15] A. D. Vakili, J. M. Wu, P. Liver, and M. K. Bhat, "Compressible flow in a diffusing s-duct with flow separation," tech. rep., SEE A87-45831, 1987.
- [16] D. Gil-Prieto, D. G. MacManus, P. K. Zachos, G. Tanguy, and K. R. Menzies, "Convoluted intake distortion measurements using stereo particle image velocimetry," in *34th AIAA Applied Aerodynamics Conference*, no. AIAA 2016-3560, 2016.
- [17] A. R. Paul, K. Kuppa, M. S. Yadav, and U. Dutta, "Flow improvement in rectangular air intake by submerged vortex generators," *Journal of Applied Fluid Mechanics*, vol. 4, no. 2, pp. 77–86, 2011.
- [18] A. Asghar, R. Stowe, W. Allan, and D. Alexander, "Entrance aspect ratio effect on s-duct inlet performance at high-subsonic flow," *Journal of Engineering for Gas Turbines and Power*, vol. 139, May 2017.
- [19] G. Tanguy, D. G. MacManus, P. Zachos, and D. Gil-Prieto, "Passive flow control study in an s-duct using stereo particle image velocimetry," *AIAA Journal*, vol. 55, June 2017.
- [20] P. Bansod and P. Bradshaw, "The flow in s-shaped ducts," *Aeronautical Quarterly*, vol. 23, no. 2, pp. 131–140, 1972.
- [21] A. M. K. P. Taylor, J. H. Whitelaw, and M. Yianneskis, "Developing flows in s-shaped ducts: square cross-section duct," tech. rep., NASA 3550, 1982.
- [22] A. M. K. P. Taylor, J. H. Whitelaw, and M. Yianneskis, "Developing flows in s-shaped ducts: circular cross-section duct," tech. rep., NASA 3759, 1984.
- [23] A. D. Vakili, J. M. Wu, P. Liver, and M. K. Bhat, "Flow control in a diffusing s-duct," in *AIAA Shear Flow Conference*, 1985.
- [24] T. Berens, A. Delot, M. Chevalier, and J. V. Muijden, "Numerical simulations for high offset intake diffuser flows," *AIAA Journal*, no. 2014-0371, 2014.
- [25] R. W. Guo and J. Seddon, "An investigation of the swirl in an s-duct," *Aeronautical Quarterly*, vol. 33, no. 1, pp. 25–58, 1982.

- [26] Y. T. Ng, S. C. Luo, T. T. Lim, and Q. W. Ho, "On the relation between centrifugal force and radial pressure gradient in flow inside curved s-shaped ducts," *Physics of Fluids*, vol. 20, no. 5 (055109), 2008.
- [27] R. K. Sullerey, S. Mishra, and A. M. Pradeep, "Application of BL fences and VG in improving performance of s-duct diffuser," *Transactions of ASME*, vol. 124, pp. 136–142, 2002.
- [28] M. J. Brear, Z. Warfield, J. F. Mangus, C. S. Braddom, J. D. Paduano, and J. S. Philhower, "Flow separation within the engine inlet of an uninhabited combat air vehicle," *Transactions of ASME*, vol. 126, pp. 266–272, 2004.
- [29] D. G. MacManus, N. Chiereghin, D. Gil-Prieto, and P. Zachos, "Complex aero-engine intake ducts and dynamic distortion," *AIA Journal*, vol. 55, no. 7, 2017.
- [30] A. S. Luers, "Flow control techniques in a serpentine inlet: an enabling technology to increase the military viability of unmanned air vehicles," Master's thesis, MIT, 2003.
- [31] D. Gil-Prieto, D. G. MacManus, P. K. Zachos, G. Tanguay, and K. R. Menzies, "Convolute intake distortion measurements using stereo particle image velocimetry," *AIAA Journal*, vol. 55, no. 6, pp. 1878–1892, 2017.
- [32] J. C. Lin, "Review of research on low-profile vortex generators to control boundary-layer separation," *Progress in Aerospace Sciences*, vol. 38, pp. 389–420, 2002.
- [33] D. M. Rao and T. T. Kariya, "Boundary-layer submerged vortex generators for separation control - an exploratory study," in *AIAA/ASME/SIAM/APS 1st National Fluid Dynamics Congress*, 1988.
- [34] J. C. Lin, "Control of turbulent boundary-layer separation using micro-vortex generators," in *30th AIAA Fluid Dynamics Conference*, 1999.
- [35] R. W. Guo and J. Seddon, "Swirl characteristics of an s-shaped air intake with both horizontal and vertical offsets," *Aeronautical Quarterly*, vol. 34, no. 2, pp. 130–146, 1983.
- [36] P. Ashill, J. Fulker, and K. Hackett, "Research at DERA on sub boundary layer vortex generators (SBVGs)," in *39th AIAA Aerospace Sciences Meeting and Exhibit*, 2001.
- [37] B. J. Wendt, G. I., and H. W.R., "The structure and development of streamwise vortex arrays embedded in a turbulent boundary layer," *AIAA Journal*, no. 92-0551, 1992.
- [38] A. L. Delot, E. Garnier, and D. Pagan, "Flow control in a high-offset subsonic air intake," in *47th AIAA/ASME/SAE/ASEE Joint Propulsion conference*, 2011.

- [39] Y. T. Ng, S. C. Luo, T. T. Lim, and Q. W. Ho, "Three techniques to control flow separation in an s-shaped duct," *AIAA*, vol. 49, no. 9, pp. 1825–1832, 2011.
- [40] Y. Zhang, S. Hu, X. F. Zhang, M. Benner, A. Mahallati, and E. Vasic, "Flow control in an aggressive interturbine transition duct using low profile vortex generators," *Journal of Engineering for Gas Turbines and Power*, vol. 136, no. 11 (112604), 2014.
- [41] A. Gissen, B. Vukasinovic, M. McMillan, and A. Glezer, "Distortion management in a boundary layer ingestion inlet diffuser using hybrid flow control," *Journal of Propulsion and Power*, vol. 30, no. 3, pp. 834–844, 2014.
- [42] A. R. Paul, P. Ranjan, V. K. Patel, and A. Jain, "Comparative studies on flow control in rectangular s-duct diffuser using submerged vortex generators," *Aerospace Science and Technology*, vol. 28, pp. 332–343, 2013.
- [43] L. Jenkins, S. A. Gorton, and A. S., "Flow control device evaluation for an internal flow with an adverse pressure gradient," in *40th AIAA Aerospace Sciences Meeting and Exhibit*, 2002.
- [44] J. B. Parham, M. Fitzgerald, and E. de la Rosa Blanco, "Flow control for boundary layer ingestion in an s-duct diffuser," in *9th AIAA Aerospace Science Meeting*, 2011.
- [45] J. W. Hamstra, D. N. Miller, P. P. Truax, B. A. Anderson, and B. J. Wendt, "Active inlet flow control technology demonstration," *The Aeronautical Journal*, vol. 104, no. 1040, pp. 473–479, 2000.
- [46] A. Jirasek, "Design of vortex generators flow control in inlets," *Journal of Aircraft*, vol. 43, no. 6, pp. 1886–1892, 2006.
- [47] B. Anderson, D. Miller, G. Addington, and J. Agrell, "Optimal micro-vane flow control for compact air vehicle inlets," *NASA/TM-2014-212936*, 2004.
- [48] J. S. Yi, C. Kim, and B. J. Lee, "Adjoint based design optimisation of vortex generator in an s-shaped subsonic inlet," *AIAA Journal*, vol. 50, no. 11, pp. 2492–2507, 2012.
- [49] W. L. Zhang, D. D. Knight, and D. Smith, "Automated design of a three dimensional subsonic diffuser," *Journal of Propulsion and Power*, vol. 16, no. 6, pp. 1132–1139, 2000.
- [50] S. Lefantzi and D. D. Knight, "Automated design optimisation of a three dimensional s-shaped subsonic diffuser," *Journal of Propulsion and Power*, vol. 18, no. 4, pp. 913–921, 2002.
- [51] A. Aranake, J. G. Lee, D. Knight, R. M. Cummings, J. Cox, M. Paul, and A. R. Byerley, "Automated design optimisation of a three dimensional subsonic diffuser," *Journal of Propulsion and Power*, vol. 27, no. 4, pp. 838–846, 2011.

- [52] D. Ghate, A. Isaacs, K. Sudhakar, P. M. Mujumdar, and A. G. Marathe, “3D duct design using variable fidelity method,” in *10th AIAA/ISSMO Multidisciplinary Analysis and Optimization Conference*, no. AIAA 2004-4427, 2004.
- [53] A. E. Eiben and J. E. Smith, *Introduction to evolutionary computing - Natural Computing Series*. Springer, 2015.
- [54] S. Shahpar, “High fidelity multi-stage design optimisation of multi-stage turbine blades using a mid-range approximate method (MAM),” in *13th AIAA/ISSMO Multidisciplinary Analysis Optimization Conference*, 2010.
- [55] S. Shahpar, S. Caloni, and L. de Prieelle, “Automatic design optimisation of profiled endwalls including real geometrical effects to minimise turbine secondary flows,” *Journal of Turbomachinery*, vol. 139, no. 7, 2017.
- [56] A. Polynkin, V. Toropov, and S. Shahpar, “Multidisciplinary optimisation of turbomachinery based on metamodel built by genetic programming,” in *13th AIAA/ISSMO Multidisciplinary Analysis optimisation Conference*, no. AIAA 2010-9397, 2010.
- [57] S. Shahpar, “Challenges to overcome for routine usage of automatic optimisation in the propulsion industry,” *The Aeronautical Journal*, vol. 115, October 2011.
- [58] Y. Korolev, V. Toropov, and S. Shahpar, “Large-scale CFD optimization based on the FFD parametrization using the multipoint approximation method in an HPC environment,” *AIAA 2015-3234*, 2015.
- [59] Y. Korolev, V. Toropov, and S. Shahpar, “Design optimization under uncertainty using the multipoint approximation method,” *AIAA 2017-1934*, 2017.
- [60] P. T. Boggs and J. W. Tolle, “Sequential quadratic programming,” *Acta Numerica*, vol. 4, pp. 1–51, 1995.
- [61] W. H. Ball, “Tests of wall suction and blowing in highly offset diffusers,” *Journal of Aircraft*, vol. 22, no. 3, pp. 161–167, 1985.
- [62] P. F. Weng and R. W. Guo, “New method of swirl control in a diffusing s-duct,” *AIAA Journal*, vol. 30, no. 7, pp. 1918–1919, 1991.
- [63] M. Amitay, D. Pitt, and A. Glezer, “Separation control in duct flows,” *Journal of Aircraft*, vol. 39, no. 4, pp. 616–620, 2002.
- [64] A. M. Pradeep and R. K. Sullerey, “Active flow control in circular and transitioning s-duct diffusers,” *Transactions of ASME*, vol. 128, pp. 1192–1203, 2006.

- [65] J. C. Vaccaro, Y. Elimelech, and M. Amitay, "Experimental investigation of actuators for flow control in short inlet ducts," in *48th AIAA Aerospace Science Meeting*, 2010.
- [66] E. Garnier, M. Leplat, J. C. Monnier, and J. Delva, "Flow control by pulsed jet in highly bended s-duct," in *6th AIAA flow control conference*, 2012.
- [67] E. Garnier, "Flow control by pulsed jet in a curved s-duct: a spectral analysis," *AIAA Journal*, vol. 53, no. 10, pp. 2813–2827, 2015.
- [68] R. Mathis, D. Duke, V. Kitsios, and J. Soria, "Use of zero-net-mass-flow for separation control in diffusing s-duct," *Experimental Thermal and Fluid Science*, vol. 33, pp. 169–172, 2008.
- [69] X. Xu, *Plasma actuation for boundary layer separation control in engine ducts*. PhD thesis, University de Montreal, 2011.
- [70] T. Unfer and J. P. Boeuf, "Modelling of a nanosecond surface discharge actuator," *Journal of Physics*, vol. 42, no. 19 (194017), 2009.
- [71] G. Correale, "Preliminary investigation on ns-DBD plasma actuator for active flow separation control," Master's thesis, TU Delft, 2011.
- [72] D. V. Roupasov, A. A. Nikipelov, M. M. Nudnova, and A. Y. Starikovskii, "Flow separation control by plasma actuator with nanosecond pulsed-periodic discharge," *AIAA Journal*, vol. 47, no. 1, pp. 168–185, 2009.
- [73] J. Little, K. Takashima, M. Nishihara, I. Adamovich, and M. Samimy, "Separation control with nanosecond-pulse-driven dielectric barrier discharge plasma actuators," *AIAA Journal*, vol. 50, no. 2, pp. 350–365, 2012.
- [74] A. Gissen, B. Vukasinovic, and A. Glezer, "Dynamics of flow control in a nemulated boundary layer ingesting offset diffuser," *Experiments in Fluids*, vol. 55, no. 1794, 2014.
- [75] L. Owens, B. Allan, and S. Gorton, "Boundary-layer-ingesting inlet flow control," *Journal of Aircraft*, vol. 45, no. 4, pp. 1431–1440, 2008.
- [76] G. J. Harloff, B. A. Reichert, and S. R. Wellborn, "Navier-stokes analysis and experimental data comparison of compressible flow in a diffusing s-duct," *AIAA*, no. 92-2699, 1992. NASA Technical Memorandum 105683.
- [77] C. F. Smith, J. E. Bruns, G. J. Harloff, and J. R. Debonis, "Three dimensional compressible turbulent computations for a diffusing s-duct," Tech. Rep. NASA-CR-4392, NASA, 1992.

- [78] S. R. Wellborn, T. H. Okiishi, and B. A. Reichert, "A study of the compressible flow through a diffusing s-duct," Technical Memorandum 106411, Nasa, 1993.
- [79] S. R. Wellborn, B. A. Reichert, and T. H. Okiishi, "Study of the compressible flow in a diffusing s-duct," *AIAA Journal of Propulsion and Power*, vol. 10, pp. 668–675, 1994.
- [80] A. L. Delot, T. M. Berens, M. Tormalm, M. Saterskog, and N. Ceresola, "Des computations for a subsonic uav configuration with a highly integrated s-shaped intake duct," in *52nd Aerospace Sciences Meeting*, no. AIAA2014-0723, AIAA, January 2014.
- [81] A. Kalpakli Vester, R. ÅŰrlÅij, and P. H. Alfredsson, "Pod analysis of the turbulent flow downstream a mild and sharp bend," *Experiments in Fluids*, vol. 56, no. 3, 2015.
- [82] M. J. Tunstall and J. K. Harvey, "On the effect of a sharp bend in a fully developed turbulent pipe flow," *Journal of Fluid Mechanics*, vol. 34, no. 3, pp. 595–608, 1968.
- [83] D. Gil-Prieto, D. G. MacManus, P. K. Zachos, T. G., F. Wilson, and N. Chiereghin, "Delayed detached eddy simulation and particle image velocimetry investigation of s-duct flow distortion," *AIAA Journal*, vol. 55, no. 6, 2017.
- [84] A. Seifert, T. Bachar, D. Koss, M. Shepshelovich, and I. Wygnanski, "Oscillatory blowing: a tool to delay boundary-layer separation," *AIAA Journal*, vol. 31, p. 2052–2060, 1993.
- [85] I. Wygnanski, "Some observations affecting the control of separation by periodic excitation," in *Fluids Conference and Exhibit*, no. AIAA2000-2314, 2000.
- [86] L. Sirovich and M. Kirby, "Turbulence and dynamics of coherent sstructure. part 1: Coherent structures," *Quarterly of Applied Mathematics*, vol. 45, no. 3, pp. 561–571, 1987.
- [87] J. L. Lumley, "Stochastic tools in turbulence," *Dover Books on Engineering*, 2007.
- [88] P. J. Schmid, "Dynamic mode decomposition of numerical and experimental data," *Journal of Fluid Mechanics*, vol. 656, pp. 5–28, 2010.
- [89] P. J. Schmid, "Application of the dynamic mode decomposition to experimental data," *Experiments in Fluids*, vol. 50, no. 4, pp. 1123–1130, 2011.
- [90] J. H. Tu, C. W. Rowley, D. M. Luchtenburg, S. L. Brunton, and J. N. Kutz, "On dynamic mode decomposition: theory and applications," *arXiv*, no. 13120041, 2013.
- [91] G. Tanguy, D. G. MacManus, P. K. Zachos, D. Gil-Prieto, and E. Garnier, "Passive flow control study in a convoluted intake using stereo particle image velocimetry," in *34th AIAA Applied Aerodynamics Conference*, no. AIAA 2016-3563, 2016.

- [92] H. G. Weller, G. Tabor, H. Jasak, and C. Fureby, "A tensorial approach to computational continuum mechanics using object-oriented techniques," *Computers in Physics*, vol. 12, no. 620, 1998.
- [93] F. R. Menter, "Two-equation eddy-viscosity turbulence models for engineering applications," *AIAA Journal*, vol. 32, no. 8, pp. 1598–1605, 1994.
- [94] C. Fiola and R. K. Agarwal, "Simulation of secondary and separated flow in diffusing s ducts," *Journal of Propulsion and Power*, vol. 31, no. 1, 2015.
- [95] P. R. Spalart, S. Deck, M. L. Shur, K. D. Squires, M. K. Strelets, and A. Travin, "A new version of detached eddy simulation, resistant to ambiguous grid densities," *Theoretical and Computational Fluid Dynamics*, vol. 20, pp. 181–195, 2006.
- [96] P. R. Spalart, "Detached eddy simulation," *Annual Review Fluid Mechanics*, vol. 41, pp. 181–202, 2008.
- [97] M. Chevalier and S. H. Peng, "Detached eddy simulation of turbulent flow in a highly offset intake diffuser," *Progress in Hybrid RANS-LES Modelling NNFM 111*, Springer-Verlag Berlin, pp. 111–121, 2010.
- [98] M. S. Gritskevich, A. V. Garbaruk, J. Schuetze, and F. R. Menter, "Development of DDES and IDDES formulations for the k-w shear stress transport model," *Flow Turbulence and Combustion*, vol. 88, p. 431–449, 2011.
- [99] R. I. Issa, "Solution of the implicitly discretised fluid flow equations by operator splitting," *Journal of Computational Physics*, vol. 62, pp. 40–65, 1985.
- [100] S. V. Patankar and D. B. Spalding, "A calculation procedure for heat, mass and momentum transfer in three dimensional parabolic flows," *International Journal of Heat and Mass Transfer*, vol. 15, pp. 1787–1806, 1972.
- [101] W. Sutherland, "The viscosity of gases and molecular force," *Philosophical Magazine*, vol. 5, no. 36, pp. 507–531, 1893.
- [102] J. E. Giuliani and J. P. Chen, "Fan response to boundary layer ingesting inlet distortions," *AIAA Journal*, vol. 54, no. 10, 2016.
- [103] A. L. Delot and R. K. Scharnhorst, "A comparison of several CFD codes with experimental data in a diffusing s-duct," in *49th AIAA/ASME/SAE/ASEE Joint Propulsion Conference*, no. AIAA 2013-3796, 2013.
- [104] M. Jovanovic, P. J. Schmid, and J. W. Nichols, "Sparsity-promoting dynamic mode decomposition," *Physics of Fluids*, vol. 26, no. 2, 2013.

- [105] Z. Bai, E. Kaiser, J. L. Proctor, J. N. Kutz, and S. L. Brunton, "Dynamic mode decomposition for compressive system identification," *AIAA Journal*, 2019. 10.2514/1.J057870.
- [106] B. W. Brunton, L. A. Johnson, J. G. Ojemann, and J. N. Kutz, "Extracting spatial-temporal coherent patterns in large-scale neural recordings using dynamic mode decomposition," *Journal of Neuroscience Methods*, vol. 258, pp. 1–15, 2016.
- [107] F. Thomas, A. Koslov, and T. Corke, "Plasma actuator for bluff body flow control," in *AIAA meeting*, no. 2006-2845, (San Francisco, California, USA), 2006.
- [108] T. N. Jukes and K. S. Choi, "Flow control around a circular cylinder using pulsed dielectric barrier discharge surface plasma," *Physics of Fluids*, vol. 21, no. 8, pp. 1–12, 2009.
- [109] S. Roy, P. Zhao, A. Das Gupta, and J. Soni, "Dielectric barrier discharge actuator for vehicle drag reduction at high speeds," *American Institute of Physics, Advances* 6, no. 025322, 2016.
- [110] J. D'Adamo, R. Sosa, and G. Artana, "Active control of a backwards facing step flow with plasma actuator," *Journal of Fluids Engineering*, vol. 136, 2014.
- [111] A. Das Gupta, P. Zhao, and S. Roy, "Plasma assisted turbulent flow separation control over a backwards facing step," in *54th AIAA Aerospace Sciences Meeting*, 2016.
- [112] M. Riherd, S. Roy, D. P. Rizzetta, and M. R. Visbal, "Study of transient and unsteady effects of plasma actuation in transitional flow over an SD7003 airfoil," in *49th AIAA Aerospace Sciences Meeting*, no. AIAA2011-1075, (Orlando, Florida), 2011.
- [113] S. Mukherjee and S. Roy, "Enhancement of lift and drag characteristics of an oscillating airfoil in deep dynamic stall using plasma actuation," in *50th AIAA Aerospace Sciences Meeting*, no. AIAA2012-702, 2012.
- [114] J. Huang, T. C. Corke, and F. O. Thomas, "Plasma actuators for separation control of low pressure turbine blades," *AIAA Journal*, vol. 44, no. 1, pp. 51–57, 2006.
- [115] D. P. Rizzetta and M. R. Visbal, "Numerical investigation of plasma based flow control for transitional highly loaded low pressure turbine," *AIAA Journal*, vol. 45, no. 10, 2007.
- [116] C. C. Wang and S. Roy, "Electrodynamic enhancement of film cooling of turbine blades," *Journal of Applied Physics*, vol. 104, no. 073305, 2008.
- [117] C. C. Wang and S. Roy, "Active cooling of turbine blades using horse-shoe plasma actuator," in *47th AIAA Aerospace Sciences Meeting*, no. AIAA2009-679, (Orlando, Florida), 2009.

- [118] J. E. Stephens, T. C. Corke, and S. Morris, "Blade mounted single dielectric barrier discharge plasma actuator in turbine cascade," *Journal of Propulsion and Power*, vol. 27, no. 3, pp. 692–699, 2011.
- [119] X. Zhao, Y. Li, Y. Wu, T. Zhu, and Y. Li, "Numerical investigation of flow separation control on a highly loaded compressor cascade by plasma aerodynamic actuation," *Chinese Journal of Aeronautics*, vol. 25, pp. 349–360, 2012.
- [120] T. C. Corke, C. L. Enloe, and S. P. Wilkinson, "Dielectric barrier discharge plasma actuators for flow control," *Annual Review Fluid Mechanics*, vol. 42, pp. 505–529, 2010.
- [121] F. O. Thomas, T. C. Corke, M. Iqbal, A. Kozlov, and D. Schatzman, "Optimisation of dielectric barrier discharge plasma actuators for active aerodynamic flow control," *AIAA Journal*, vol. 47, no. 9, pp. 2169–2178, 2009.
- [122] M. Kotsonis, S. Ghaemi, L. Veldhuis, and F. Scarano, "Measurement of the body force field of plasma actuators," *Journal of Applied Physics*, vol. 44, no. 4, 2011.
- [123] M. M. Wojewodka, C. White, T. Ukai, A. Russell, and K. Kontis, "Pressure dependency on a nanosecond pulsed dielectric barrier discharge plasma actuator," *Physics of Plasmas*, 2019.
- [124] I. Langmuir, "Oscillations in ionized gases.," *Proceedings of the National Academy of Sciences of the United States of America*, vol. 14, pp. 627–637, 1928.
- [125] E. E. Kunhardt and L. H. Luessen, "Electric breakdown and discharges in gases," *Wiley, New York*, 1981.
- [126] Y. P. Raizer, "Gas discharge physics," *Springer-Verlag Berlin Heidelberg*, 1991.
- [127] C. L. Enloe, T. E. McLaughlin, R. D. VanDyken, K. D. Kachner, E. J. Jumper, and T. C. Corke, "Mechanisms and responses of a single-dielectric barrier plasma actuator: plasma morphology," *AIAA Journal*, vol. 42, no. 3, pp. 589–594, 2004.
- [128] C. L. Enloe, T. E. McLaughlin, G. I. Font, and J. W. Baughn, "Parametrization of temporal structures in the single dielectric barrier aerodynamic plasma actuator," *AIAA Journal*, vol. 44, no. 6, 2006.
- [129] C. L. Enloe, M. G. McHarg, and T. E. McLaughlin, "Time-correlated force production measurements of the dielectric barrier discharge plasma aerodynamic actuator," *Journal of Applied Physics*, vol. 103, no. 073302, 2008.
- [130] J. P. Boeuf, Y. Lagmich, and L. C. Pitchford, "Contribution of positive and negative ions to the electrohydrodynamic force in a dielectric barrier discharge plasma actuator operating in air.," *Journal of Applied Physics*, vol. 106, no. 023115, 2009.

- [131] M. Kotsonis and L. Veldhuis, "Experimental study on dielectric barrier discharge actuators operating in pulse mode," *Journal of Applied Physics*, vol. 108, no. 113304, 2010.
- [132] D. M. Orlov, *Modelling and simulation of single dielectric barrier discharge plasma actuators*. PhD thesis, Univ. Notre Dame, 2006.
- [133] C. L. Enloe, T. E. McLaughlin, R. D. VanDyken, K. D. Kachner, and E. J. Jumper, "Mechanisms and responses of a single-dielectric barrier plasma actuator: geometric effects," *AIAA Journal*, vol. 42, no. 3, pp. 595–604, 2004.
- [134] M. L. Post, *Plasma actuators for separation control on stationary and unstationary airfoils*. PhD thesis, Univ. Notre Dame, 2004.
- [135] X. Huang and X. Zhang, "Streamwise and spanwise plasma actuators for flow induced cavity noise control," *Physics of Fluids*, vol. 20, no. 3, 2008.
- [136] B. Dong, J. M. Bauchire, J. M. Pouvesle, P. Magnier, and D. Hong, "Experimental study of a BDB surface discharge for the active control of subsonic flows," *Journal of Applied Physics*, vol. 41, no. 15, 2008. 155201.
- [137] L. N. Cattafesta and M. Sheplak, "Actuators for active flow control," *Annual Review Fluid Mechanics*, vol. 43, pp. 247–272, 2011.
- [138] J. R. Roth and X. Dai, "Optimisation of the aerodynamic plasma actuator as an electrohydrodynamic EHD electrical device," in *44th AIAA Aerospace Sciences Meeting and Exhibit*, 2006.
- [139] A. V. Kozlov, *Plasma actuators for bluff body flow control*. PhD thesis, Univ. Notre Dame, 2007.
- [140] J. Pons, E. Moreau, and G. Touchard, "Asymmetric surface dielectric barrier discharge in air at atmospheric pressure: electrical properties and induced airflow characteristics," *Journal of Applied Physics*, vol. 38, no. 19, pp. 3635–3642, 2005.
- [141] J. Pons, E. Moreau, and G. Touchard, "Electrohydrodynamic properties of surface dielectric barrier discharges in ambient air for aerodynamic airflow control," in *28th ICPIG*, (Prague, Czech Republic), pp. 953–956, 2007.
- [142] M. Forte, J. Jolibois, J. Pons, E. Moreau, G. Touchard, and M. Cazalens, "Optimisation of a dielectric barrier discharge actuator by stationary and non-stationary measurements of the induced flow velocity: application to airflow control," *Experiments in Fluids*, vol. 43, no. 6, pp. 917–928, 2007.

- [143] J. A. Valerioti and T. C. Corke, "Pressure dependence of dielectric barrier discharge plasma flow actuators," *AIAA Journal*, vol. 50, pp. 1490–1502, July 2012.
- [144] N. Benard, N. Balcon, and E. Moreau, "Electric wind produced by a surface dielectric barrier discharge operating in air at different pressures: Aeronautical control insights," *Journal of Physics D: Applied Physics*, vol. 41, no. 4, 2008.
- [145] P. Versailles, V. Gingras-Gosselin, and H. Vo, "Impact of pressure and temperature on the performance of plasma actuators," *AIAA Journal*, vol. 48, no. 4, pp. 859–863, 2010.
- [146] C. Y. Schuele and T. Corke, "Characteristics of single dielectric barrier discharge plasma actuators at subatmospheric pressures," in *61st Annual American Physical Society Fluid Dynamics Meeting*, (San Antonio, Texas), 2008.
- [147] K. Kourtzanidis and L. L. Raja, "Three electrode sliding nanosecond dielectric barrier discharge actuator: modeling and physics," *AIAA Journal*, vol. 55, no. 4, pp. 1393–1404, 2017.
- [148] N. A. Popov, "Investigation of the mechanism for rapid heating of nitrogen and air in gas discharges," *Plasma Physics Reports*, vol. 27, no. 10, pp. 886–896, 2001.
- [149] G. Correale, T. Michelis, D. Ragni, M. Kotsonis, and F. Scarano, "Nanosecond-pulsed plasma actuation in quiescent air and laminar boundary layer," *J. Appl. Phys.*, vol. 47, no. 105201, 2014.
- [150] D. Z. Pai, D. A. Lacoste, and C. O. Laux, "Nanosecond repetitively pulsed discharges in air at atmospheric pressure - the spark regime," *Plasma Sources Sci. Tech.*, vol. 19, no. 065015, 2010.
- [151] M. S. Bak, W. Kim, and M. Cappelli, "On the quenching of excited electronic states of molecular nitrogen in nanosecond pulsed discharges in atmospheric pressure air," *Applied Physics Letters*, vol. 98, no. 011502, 2011.
- [152] A. Lo, G. Cleon, P. Vervisch, and A. Cessou, "Spontaneous raman scattering: a useful tool for investigating the afterglow of nanosecond scale discharges in air," *Applied Physics B*, vol. 107, pp. 229–42, 2012.
- [153] D. L. Rusterholtz, D. A. Lacoste, G. D. Stancu, D. Z. Pai, and C. O. Laux, "Ultrafast heating and oxygen dissociation in atmospheric pressure air by nanosecond repetitively pulsed discharges," *Journal of Applied Physics*, vol. 46, no. 464010, 2013.
- [154] T. Michelis, G. Correale, I. B. Popov, M. Kotsonis, D. Ragni, S. Hulshoff, and L. Veldhuis, "Disturbance introduced into a laminar boundary layer by ns-DBD plasma actuator," in *51st AIAA Aerospace Sciences Meeting*, (Grapevine, TX), January 2013.

- [155] D. V. Roupasov, A. A. Nikipelov, M. M. Nudnova, and A. Y. Starikovskii, "Boundary layer separation control by nanosecond plasma actuator," in *44th AIAA/ASME/SAE/ASEE Joint Propulsion Conference & Exhibit*, (Hartford, CT), July 2008.
- [156] A. Russell, H. Zare-Behtash, and K. Kontis, "Characterisation of ns-DBD plasma actuators for supersonic flow control," in *Proceedings of 30th International Council of the Aeronautical Sciences*, 2016.
- [157] J. Van den Broecke, G. Correale, and F. Avallone, "Characteristics of efficiency of energy deposition of a ns-DBD plasma actuator," in *54th AIAA Aerospace Sciences Meeting, AIAA Sci Tech Forum, San Diego, California, USA*, AIAA, 2016.
- [158] F. Avallone and G. Correale, "Method to quantify the electrical efficiency of a ns-DBD plasma actuator," *Pacific Symposium on Flow Visualisation and Image processing*, vol. 10, pp. 1–10, 2015.
- [159] Y. Liu, C. Kolbakir, H. Hu, A. Y. Starikovskiy, and R. Miles, "An experimental investigation on the thermal effects of ns-DBD and ac-DBD plasma actuators for aircraft icing mitigation," *Plasma Sources Sci. Tech.*, 2018. in press.
- [160] J. Chen, H. Liang, Y. Wu, B. Wei, G. Zhao, M. Tian, and L. Xie, "Experimental study on anti-icing performance of ns-DBD plasma actuator," *Applied Sciences*, vol. 8, no. 10.3390, p. 1889, 2018.
- [161] R. Winkel, "Experimental study on the energy deposition of an ns-DBD plasma actuator and its effect on a laminar boundary layer," Master's thesis, TU Delft, 2015.
- [162] F. do Nascimento, S. Moshkalev, and M. Machida, "Experimental analysis of DBD plasma jet properties using different gases and two kinds of transfer plate," *arXiv*, no. 1512.03712, 2016.
- [163] A. V. Nastuta, V. Pohoata, I. Mihaila, and I. Topala, "Diagnosis of a short-pulse DBD at atmospheric pressure in helium with hydrogen-methane admixtures," *Physics of Plasmas*, vol. 25, no. 4, 2018.
- [164] Y. Liu, Y. Hao, and B. Zheng, "Plasma formation in atmospheric pressure helium discharges under different background air pressures," *Physics of Plasmas*, vol. 19, no. 9, 2012.
- [165] T. Ukai, A. Russell, H. Zare-Behtash, and K. Kontis, "Temporal variation of the spatial density distribution above a nanosecond pulsed dielectric barrier discharge plasma actuator in quiescent air," *Physics of Fluids*, vol. 30, November 2018.

- [166] R. A. Dawson and J. Little, "Effects of pulse polarity on nanosecond pulse driven dielectric barrier discharge plasma actuators," *Journal of Applied Physics*, vol. 115, no. 043306, 2014.
- [167] S. D. I. A. Ramirez, "Incompressible cavity flow control using plasma actuators," Master's thesis, Univ. of Glasgow, 2016.
- [168] J. Brutscher, "Datasheet Minipuls 4," 2013.
- [169] R. B. Green, C. J. Doolan, and R. Cannon, "Measurements of the orthogonal blade vortex interactions using a particle image velocimetry technique.," *Experiments in Fluids*, vol. 29, no. 4, pp. 369–379, 2000.
- [170] M. Kaur, S. Kakar, and D. Mandal, "Electromagnetic interference," in *3rd International Conference on Electronics Computer Technology (ICECT)*, no. 10.1109/ICECTECH.2011.5941844, 2011.
- [171] S. Shihab, K. Debnath, Z. Giu, and V. Rao, "EMI and EMC in high voltage energy systems," in *Regional Symposium on Electromagnetic Compatibility*, no. 10.1109/ISEMC.1992.257558, 1992.
- [172] K. Takashima, Y. Zuzeeq, W. Lempert, and I. Adamovich, "Characterization of a surface dielectric barrier discharge plasma sustained by repetitive nanosecond pulses," *Plasma Sources Sci. Tech.*, vol. 20, no. 055009, 2011.
- [173] F. F. Rodrigues, J. C. Pascoa, and M. Trancossi, "Experimental analysis of alternative dielectric materials for DBD plasma actuators," in *ASME 2018 International Mechanical Engineering Congress and Exposition*, IMECE2018-87455, 2018.
- [174] A. K. Prasad, "Stereoscopic particle image velocimetry," *Experiments in Fluids*, vol. 29, no. 2, pp. 103–116, 2000.
- [175] R. E. Hanson, N. M. Houser, and P. Lavoie, "Dielectric material degradation monitoring of dielectric barrier discharge plasma actuators," *Journal of Applied Physics*, vol. 115, no. 4, 2014.
- [176] K. Takashima, Z. Y. Yin, and I. V. Adamovich, "Measurements and kinetic modeling of energy coupling in volume and surface nanosecond pulse discharges," *Plasma Sources Sci. Tech.*, vol. 22, 2013. 015013.
- [177] J. G. Zheng, Z. J. Zhao, J. Li, Y. D. Cui, and B. C. Khoo, "Numerical simulation of nanosecond pulsed dielectric barrier discharge actuator in a quiescent flow," *Physics of Fluids*, vol. 26, no. 3, 2014.

- [178] D. V. Gaitonde and M. H. McCrink, “A semi-empirical model of a nanosecond pulsed plasma actuator for flow control simulations with LES,” in *50th AIAA Aerospace Sciences Meeting*, no. AIAA 2012-0184, January 2012.
- [179] D. V. Gaitonde, “Analysis of plasma-based flow control mechanisms through large-eddy simulations,” *Computers and Fluids*, vol. 85, pp. 19–26, 2013.
- [180] Z. Zhao, J. Li, J. Zheng, Y. d. Cui, and B. C. Khoo, “Study of shock and induced flow dynamics by nanosecond dielectric-barrier-discharge plasma actuators,” *AIAA Journal*, vol. 53, no. 5, pp. 1336–1348, 2015.
- [181] K. Kinefuchi, A. Y. Starikovskiy, and R. B. Miles, “Numerical investigation of nanosecond pulsed plasma actuators for control of shock-wave/boundary-layer separation,” *Physics of Fluids*, vol. 30, no. 10, 2018.
- [182] V. Soloviev, “Analytical estimation of the thrust generated by a surface dielectric barrier discharge,” *Journal of Physics D: Applied Physics*, vol. 45, no. 2, 2011.
- [183] K. P. Singh and S. Roy, “Force approximation for a plasma actuator operating in atmospheric air,” *Journal of Applied Physics*, vol. 103, no. 1, 2008.
- [184] Y. Babou, E. Nieto Martin, and P. Fajardo Pena, “Simple body force model for dielectric barrier discharge plasma actuator,” in *7th European conference for aeronautics and aerospace sciences (EUCASS)*, no. 10.13009/EUCASS2017-122, 2017.
- [185] B. Zheng, C. Gao, Y. Li, F. liu, and S. Luo, “Flow control over a conical forebody by periodic pulsed plasma actuation,” *Plasma Science and Technology*, vol. 15, no. 4, 2013.
- [186] A. Labergue, E. Moreau, N. Zouzou, and G. Touchard, “Separation control using plasma actuators: application to a free turbulent jet,” *Journal of Physics D: Applied Physics*, vol. 40, pp. 674–684, 2007.
- [187] A. Russell, *Directed energy deposition flow control for high speed intake applications*. PhD thesis, University of Glasgow, 2020.
- [188] M. L. Post and T. C. Corke, “Separation control in high angle of attack airfoil using plasma actuators,” *AIAA Journal*, vol. 42, no. 11, pp. 2177–2184, 2004.
- [189] A. Sidorenko, B. Y. Zanin, and B. V. Postnikov, “Pulsed discharge actuators for rectangular wing separation control,” in *45th AIAA Aerospace Sciences Meeting and Exhibit*, (Reno, Nevada, USA), 2007.
- [190] A. Gross and H. F. Fasel, “Flow control for nrel s822 wind turbine airfoil,” *AIAA Journal*, vol. 50, no. 12, 2012.

- [191] A. Salmasi, A. Shadaram, and A. S. Taleghani, "Effect of plasma actuator placement on the airfoil efficiency at post stall angles of attack," *IEEE Transactions on Plasma Science*, vol. 41, no. 10, 2013.
- [192] M. P. Patel and Z. H. Sowle, "Autonomous sensing and control of wing stall using a smart plasma slat," *Journal of Aircraft*, vol. 44, no. 2, 2007.
- [193] J. Little, K. Takashima, M. Nishihara, I. Adamovich, and M. Samimy, "High lift airfoil leading edge separation control with nanosecond pulsed dielectric barrier discharge plasma actuator," in *5th Flow Control Conference*, (Chicago, USA), AIAA, 2010.
- [194] T. Segawa, D. Suzuki, T. Fujino, T. Jukes, and T. Matsunuma, "Feplasma control of flow separation using plasma actuator and fbg sensor," *International Journal of Aerospace Engineering*, no. 8648919, 2016.
- [195] P. W. Kwan and X. Huang, "A pedagogical study of aerodynamic feedback control by dielectric barrier discharge plasma," *IEEE Transactions On Industrial Electronics*, no. 2897514, 2019.